IDENTIFICATION AND QUANTIFICATION OF RADIOACTIVE IMPURITIES IN MEDICAL RADIONUCLIDES

A thesis submitted in fulfilment of the requirement for the degree of Doctor of Philosophy in Medical Engineering and Medical Physics

By

ANSAM ABD ALRASOOL ALI AL-OBAIDI

B.Sc., M.Sc.

School of Engineering

Cardiff University

UK

2019

DECLARATION AND STATEMENTS

DECLARATION

This work has not previously been accepted in substance for any degree and is not concurrently submitted in candidature for any degree.

Signed ……..... Date …….

STATEMENT 1

This thesis is being submitted in partial fulfilment of the requirements for the degree of Doctor of Philosophy (PhD).

Signed ……..... Date …….

STATEMENT 2

This thesis is the result of my own independent work/investigation, except where otherwise stated. Other sources are acknowledged by explicit references.

Signed ……..... Date …….

STATEMENT 3

I hereby give consent for my thesis, if accepted, to be available for photocopying and inter-library loan, and for the title and summary to be made available to outside organisations.

Signed ……..... Date …….

Summary

The presence of radioactive impurities in radionuclides that are used for medical applications may adversely affect the quality of diagnostic images and increase radiation dose to the patient. The aim of this project was to identify and quantify such impurities in the following solutions: ^{99m}Tc generator eluates, commercial ^{123}I and ^{131}I sodium iodide and cyclotron-produced ^{68}Ga and ^{89}Zr. The work was done with a calibrated high-purity germanium (HPGe) detector and gamma spectroscopy system with the activity of the main radionuclides being measured with a radionuclide calibrator. Impurity activity was expressed as a percentage of the main radionuclide activity.

The parent ^{99}Mo was found in all the ^{99m}Tc generator eluates but with low relative activity (<3x10^{-3}%). There was no significant difference between the corresponding eluates of two generators having different reference activity. Overall, the relative activity decreased logarithmically with eluate number and this has not been reported previously. This suggests that as regards ^{99}Mo content, the later eluates are safer for patients than the earlier ones because they deliver lower additional radiation dose. The radionuclide ^{103}Ru was also identified as an impurity in some ^{99m}Tc generator eluates, but at a much lower relative activity (<2x10^{-5}%). This decreased rapidly after the first elution suggesting that, in effect, its presence may be eliminated by pre-elution of the generator.

For the Na^{123}I solution, the main contaminants were ^{125}I (<2x10^{-2}%) and ^{121}Te (<7x10^{-3}%). However, also observed were trace activities (<8x10^{-4}%) of ^{124}I, ^{126}I, ^{95m}Tc and ^{96}Tc, which have not been reported in the literature. As these impurities were found only in some samples with very low relative activity and as their half-lives are similar to or shorter than the half-life of the longer-lived main impurity (^{125}I), they do not present a significant hazard to patients. No impurities were identified in the Na^{131}I solution.

The radionuclides ^{68}Ga and ^{89}Zr were produced by a cyclotron at the Cardiff University Positron Emission Tomography Imaging Centre (PETIC), the former for the first time in the UK using a liquid target. For ^{68}Ga, the identified impurities were ^{67}Ga (<9x10^{-1}%), ^{66}Ga (<7x10^{-3}%) and ^{56}Co (<5x10^{-4}%), while for ^{89}Zr, the contaminants were ^{88}Zr

(<$2x10^{-3}$%), ^{88}Y ($4x10^{-4}$%) and ^{56}Co (<$3x10^{-3}$%). In both cases, the relative activities of the impurities were well within the goal of <2%. The results of this study may be used to optimise the irradiation conditions for the production of the two main radionuclides.

This work has confirmed the usefulness of a HPGe detector and high-resolution gamma spectroscopy for the analysis of the radionuclidic purity of medical radionuclides, and suggested several avenues for future research.

ACKNOWLEDGEMENTS

I am grateful to my God “ALLAH”, the Prophet Muhammad and Ahl al-Bayt and their relatives (the peace and blessings of Allah be upon them) for giving me the strength and the ability to attain this goal.

My sincere appreciation and gratitude go to my supervisor Professor William David Evans for his continuous valuable advice and guidance, and his constructive feedback on my thesis. Thank you for all the skills I learned from you and thank you for being a great supervisor.

I would like to thank my supervisor Prof Leonard Derek Nokes for providing me with necessary information and direction.

I would also like to thank all the members of the Medical Physics Department at the University Hospital of Wales for their help and kind assistance. I am especially grateful to Dr. Beth Jones, Mr. Paul Rabaiotti, Mr. Mike Robinson and Dr. Matthew Talboys. My thanks also go to Dr. Martin Hofmann of KETEK GmbH for detailed information about the efficiency of the radiation detector used in his work.

I deeply appreciate the financial support of my sponsor, HCED and the University of Kerbala. Without their support and immediate help, this work would not have been achievable.

I dedicate this work to my wonderful family: Mum, Dad, my lovely husband, my beautiful daughter, my amazing brothers and sisters. It is a blessing to have you in my life.

TABLE OF CONTENTS

LIST OF ABBREVIATIONS

HPGe	High-purity germanium
$t_{1/2}$	Half-life
NPL	National Physical Laboratory
NCR	Net count rate
CPS	counts per second
ADC	Analogue-to-digital converter
Bq	Becquerel
MBq	Mega Becquerel
ICRP	International Commission on Radiological Protection
MCA	Multichannel Analyser
PMT	Photomultiplier tube
No	Number
SD	Standard Deviation
EOB	End of bombardment
FWHM	Full Width at Half Maximum
PETIC	Positron Emission Tomography Imaging Centre

Chapter 1

Introduction

1.1 Motivation

Nuclear medicine is the science by which trace amounts of compounds labelled with radioactivity (radionuclides) are administered to the human body. The radiolabelled compound is called a radiopharmaceutical, or more commonly, a tracer or radiotracer. A tracer is a substance that follows ("traces") a physiologic or biochemical process.

Radiopharmaceuticals are used either for diagnostic or therapeutic purposes. In its most usual form, a diagnostic nuclear medicine study involves injecting a radiopharmaceutical, which is labelled with a gamma-ray-emitting or positron-emitting radionuclide, into the body. When the radionuclide decays, gamma radiation or high-energy annihilation photons are emitted. These are detected outside the body by equipment designed for planar radionuclide imaging, single photon emission tomography (SPECT) or positron emission tomography (PET). A disadvantage of these techniques is that they deliver an unwanted radiation dose to the patient. The magnitude of the dose depends on factors such as the physical properties of the radionuclide and the physiological properties of the radiopharmaceutical. In radionuclidic therapy, on the other hand, the goal is to deliver a relatively large targeted radiation dose to a specific organ or tissue such as a hyper-functioning thyroid gland or a cancerous tumour.

Radionuclides for diagnostic or therapeutic applications are chosen because their properties are suitable for the intended purpose. These properties include half-life ($t_{1/2}$), mode of decay, photon emission and type and energy of particle. They are produced in a nuclear reactor or a particle accelerator, usually a cyclotron, or by a radionuclide generator. However, in most if not all cases, radionuclidic contaminants are produced along with the desired radionuclides and these can be significant in some situations. The effect of these contaminants is to increase and redistribute the radiation dose to the patient, especially if these radioactive impurities have relatively long half-life. An example is ^{99}Mo ($t_{1/2}\approx$ 66 hrs) in ^{99m}Tc ($t_{1/2}\approx$ 6 hrs). They may also increase detector dead time, and if the energy of their emissions falls within the acceptance window of the detector system, contaminants may result in incorrect counting rate or pixel intensities in images. Thus, an important aspect of the quality control of radiopharmaceuticals is to obtain high radionuclidic purity to produce, in turn, good images and to avoid unnecessary dose to the patient.

In this study, the radionuclidic purity of ^{99m}Tc eluates, commercial sodium iodide solutions (^{123}I and ^{131}I) and locally produced ^{68}Ga solutions and ^{89}Zr solutions were evaluated.

1.2 Aim

The aim of this project was to identify and quantify radioactive contaminants in the previously mentioned radionuclides, which were produced by different methods: generator, reactor and cyclotron.

1.3 Objectives

- Reviewing previous work on the radionuclidic purity of ^{99m}Tc, ^{123}I, ^{131}I, ^{68}Ga and ^{89}Zr.
- Obtaining a series of ^{99m}Tc eluates and commercially produced ^{123}I and ^{131}I solutions from the radiopharmacy at the University Hospital of Wales, Cardiff.
- Co-operation with the Cardiff University Positron Emission Tomography Imaging Centre (PETIC) to analyse ^{68}Ga and ^{89}Zr produced by the centre's own cyclotron.
- Characterising the performance of a high-purity germanium (HPGe) detector, including energy and efficiency calibration, so that it could be used with a gamma spectroscopy system to identify and measure the activity of radionuclidic impurities.
- Using a secondary standard radionuclide calibrator to measure the activity of the primary radionuclides.
- Correcting the activity readings for factors such as radioactive decay, type of vial and volume of solution.
- Expressing radionuclidic impurity activities as a percentage of the primary radionuclide activities.

1.4 Thesis outline

The thesis chapters are organised into the following structure:

Chapter 1: This chapter highlights the motivation, aim and objectives of the research and outlines the structure of the thesis.

Chapter 2: This chapter introduces radioactivity and gives a review of background information including the following:

- Radiation, radioactive decay, modes of decay and rate of decay.
- Interaction of particles and photons: charged particles (electrons), gamma photons (photoelectric, Compton, and pair production).
- Radiation dose, biological effect of ionisation radiations, mechanisms of this effect.
- Detection of radiation: scintillation detectors, gas detectors, semiconductor detectors.
- Electronic components of a nuclear radiation counting instrument, multi-channel analyser (MCA), pulse height spectrum, dead-time and live-time.
- Energy calibration and efficiency calibration.

Chapter 3: This chapter reviews the methods of producing medical radionuclides and radiopharmaceuticals, including:

- Nuclear reactor: principles, fission fragment and neutron activation.
- Charged-particle accelerators: cyclotron principles.
- Generator: design of the generator, activity decay and growth in a $^{99}Mo/^{99m}Tc$ generator, the generator eluate.
- Impurities produced alongside medical radionuclides.
- Radiopharmaceuticals and radiation dose.

Chapter 4: This chapter, on the construction and performance of the HPGe detector at the University Hospital of Wales, introduces experimental work including the following:

- Electronic components.
- Energy calibration.
- Background spectrum.

- Peak area calculation.
- Detector stability.
- Counting efficiency.
- Energy resolution.

Chapter 5 This chapter is dedicated to the evaluation of the radionuclidic purity of ^{99m}Tc eluates based on the following:

- Activity measurement with a Fidelis secondary standard radionuclide calibrator.
- Correction of the ^{99m}Tc activity readings for the effect of different volumes and types of vial.
- Correction of the ^{99}Mo net count rate readings for the effect of different volumes and type of vial.
- Measuring the ratio of ^{99}Mo to ^{99m}Tc activity and comparing it with the limits recommended by the European Pharmacopeia.
- Evaluating the relationship between eluates of different generators.
- Evaluating the relationship between the ratio of ^{99}Mo to ^{99m}Tc activity and the eluate number.

Chapter 6: This chapter, on the radionuclidic purity of sodium iodide solution (^{123}I and ^{131}I), describes the following experimental work:

- Preparation of samples of both ^{123}I and ^{131}I sodium iodide solution in-house in a standard volume and type of vial.
- Using the Fidelis calibrator to measure the activity of the main radionuclide (^{123}I and ^{131}I).
- Using the HPGe detector to determine the presence and activity of radioactive impurities.
- Calculating the ratio of the radioactive contaminant activity to that of the main radionuclide.

Chapter 7: This chapter, on the radionuclidic purity of ^{68}Ga radioactive solutions, describes the following experimental work:

- The production of ^{68}Ga in PETIC, Cardiff University.
- Measuring the activity of the main radionuclide (^{68}Ga).

- Using the HPGe detector to determine the presence and activity of radioactive impurities.
- Calculating the ratio of the radioactive contaminant activity to that of the main radionuclide and determining the half-lives of the contaminants.

Chapter 8 This chapter, on the radionuclidic purity of ^{89}Zr radioactive solutions, describes the following experimental work:

- The production of ^{89}Zr in PETIC, Cardiff University.
- Measuring the activity of the main radionuclide (^{89}Zr).
- Using the HPGe detector to determine the presence and activity of radioactive impurities.
- Calculating the ratio of the radioactive contaminant activity to that of the main radionuclide and determining the half-lives of the contaminants.

Chapter 9 This chapter summarises the research outcomes and suggests future work.

1.5 Presentations

A poster entitled Radionuclide Impurities in Cyclotron-Produced Gallium-68 and Zirconium-89 For Positron Emission Tomography was presented at the All-Wales Medical Physics and Clinical Engineering Summer Meeting (June 2018) and it won a prize for the best poster.

An oral presentation entitled Radionuclide Impurities in Cyclotron-produced Gallium-68 and Zirconium-89 for Positron Emission Tomography was presented at the 17th International Workshop on Targetry and Target Chemistry (17WTTC) (August 2018) in Coimbra, Portugal.

Chapter 2

Radioactivity and its Measurement

2.1 Introduction

The phenomenon of radioactivity was discovered in France in 1896 by Henri Becquerel when he noticed the luminescence caused by uranium salts. Uranium is an example of a naturally occurring radionuclide; the other category is man-made or artificial radionuclides. The decay of naturally occurring radioactive materials, such as uranium and thorium that exist in the earth's crust, contributes to the terrestrial component of background radiation. Most of the naturally occurring radionuclides are very long-lived (e.g. ^{40}K, $t_{1/2} \sim 10^9$ years) and are isotopes of very heavy elements (e.g. uranium and radium) that are unimportant in metabolic or physiologic processes.

Some of the first applications of radioactivity for medical tracer studies in the 1920s and 1930s made use of natural radionuclides; however, because of their generally undesirable characteristics, they have found no use in medical diagnostic procedures since that time (Cherry et al. 2012). All the radionuclides used in modern nuclear medicine are of the manufactured or artificial variety. They are made by bombarding nuclei of stable atoms with nuclear particles (such as protons and neutrons) to cause nuclear reactions that change a stable nucleus into an unstable (radioactive) one (Cherry et al. 2012) or nuclear fission whose products are radioactive.

2.2 Radiation and radioactive decay

2.2.1 Modes of decay

Radiation is generally divided into two main types. These are:

- Charged particle radiation
- Uncharged particle radiation

The first category includes radiation such as fast electrons, protons and heavy charged particles, while the second category includes neutron radiation and electromagnetic radiation (Knoll 2010). The various modes of radioactive decay and associated processes act as sources of radiation.

2.2.1.1 Charged particle radiation sources

2.2.1.1.1 Fast electrons

A) Beta decay

Beta particle emissions have either positive or negative electric charge (Knoll 2010; Jones et al. 2013). The process of β-particle emission is accompanied by the emission of another particle called a neutrino or an neutrino. These are an uncharged particles with zero or negligible mass (Thrall et al. 2001; Knoll 2010; Jones et al. 2013).

The positive β-particle is called a positron (e^+). It behaves like a positively charged electron, and it has the same as an electron mass. The emission of a positive β-particle takes place in a radionuclide with too many protons the results in a decrease of the nuclear charge by one unit (Knoll 2010). However, the negative β-particle, sometimes called negatron, is an electron (e^-) and it is emitted in a radionuclide with too many neutrons (Thrall et al. 2001; Jones et al. 2013).

B) Internal conversion

The internal conversion process often competes with gamma emission. This process begins with an excited nuclear state. One of the common methods of de-excitation is to emit a gamma photon. For some excited states, the emission of a gamma photon is inhibited and the nucleus de-excites by transferring its energy directly to one of the

orbital electrons of the atom. This electron is called a conversion electron (Lilley 2001; Knoll 2010).

C) Auger electron emission

This takes place when the excitation energy originates in the atom rather than in the nucleus. This happens due to a process such as electron capture (sometimes called inverse β^- decay) in which an orbital electron is captured by the nucleus and combines with a proton to form a neutron. This creates a vacancy in an inner electron shell. This vacancy is normally filled by another electron from one of the outer shells of the atom, resulting in characteristic x-ray emission. Alternatively, the de-excitation happens through ejecting what is called an Auger electron. This happens when the excitation energy is directly transferred to another outer electron (Thrall et al. 2001; Knoll 2010).

2.2.1.1.2 Heavy charged particles

A) Alpha decay

Many natural heavy nuclei with $82 < Z \leq 92$ and artificially produced nuclei ($Z > 92$) decay by the emission of an alpha (α) particle. It was shown by Rutherford and his co-workers that this particle consisted of two protons and two neutrons and is equivalent to the nucleus of a helium atom ${}_2^4He$. One example of the α-decay process is the decay of radium-226 to its daughter radon-222 (Krane 1988).

B) Spontaneous fission

Fission is normally thought to occur under unnatural and artificial circumstances, such as in a nuclear reactor. However, there are some nuclei that undergo fission spontaneously (Krane 1988; Knoll 2010).

In the spontaneous fission process, a heavy nucleus with an excess number of neutrons splits into two lighter nuclei with roughly equal masses. This process results in the production of energetic charged particles with mass greater than that of the alpha particle (Krane 1988; Knoll 2010). During fission, one or more neutrons are also emitted, together with heat energy. An example of a nuclide that undergoes spontaneous nuclear fission is uranium-235, which is inherently unstable (Powsner et al. 2013).

2.2.1.2 Uncharged particulate radiation sources

2.2.1.2.1 Neutron sources

Neutrons can be created in three different ways: spontaneous fission, (α,n) nuclear reaction and photoneutron interaction. These processes will not be discussed in detail as they are out of the scope of this study.

2.2.1.2.2 Electromagnetic radiation sources

A) Annihilation radiation

Annihilation takes place when a electron (from an absorbing material) and a positron (from the decay of a parent nucleus) interact and are converted into two gamma photons that are emitted in opposite directions, each with an energy of 511 keV. These two photons may, in turn, interact in the material by either Compton scattering or photoelectric absorption (Thrall et al. 2001).

B) Bremsstrahlung radiation

When an electron or positron passes through matter, it may be deflected due to interaction with the atomic nucleus and suffer a change in velocity. These charged particles, therefore, will be decelerated and all decelerating charged particles radiate x-rays. Such radiation is normally called bremsstrahlung radiation (or braking radiation) (Krane 1988; Lilley 2001; Knoll 2010).

C) Gamma radiation (γ)

Gamma radiation is emitted by the transition of a nucleus from an excited state to a lower excited state or possibly the ground state. The energy of the γ radiation photon is equal to the energy difference between the initial and the final nuclear states. This kind of radiation normally follows α and β decay, which usually leave the daughter nucleus in an excited state.

There are two different types of excited nuclear states:

- Excited states that are very unstable and have only a transient existence before transforming into some other state.

- Metastable states that are also are unstable, but have relatively longer lifetimes than the other excited states; these also are called isomeric states.

Some metastable states are quite long-lived; in some cases they have average lifetimes of several hours. Therefore, metastable nuclear states are considered to have separate identities and are classified as nuclides. The ground state and metastable state of a particular nuclides are called isomers. Excited states are represented by an asterisk ($^{A}X^{*}$), while metastable states are denoted by the letter m (^{Am}X or X-Am). An example is ^{99m}Tc (or Tc-99m), which denotes the metastable state of ^{99}Tc, and ^{99m}Tc and ^{99}Tc are isomers (Cherry et al. 2012).

2.2.2 Rate of decay and half-life

Three years after the discovery of radioactivity in 1896, it was noticed that the decay rate of a pure radioactive material decreases with the passage of time. The decay rate of the radioactive source is known as the activity. The source activity is given by (Thrall et al. 2001; Knoll 2010):

$$\frac{-dN_t}{dt} \propto N_t \qquad \textbf{(2-1)}$$

where N_t represents the number of radioactive nuclei at time t and dN_t/dt represents the rate of change in the number of radioactive nuclei. The negative sign indicates that the number of unstable nuclei decreases with time.

$$\frac{-dN_t}{dt} = \lambda N_t \qquad \textbf{(2-2)}$$

where λ is the constant of proportionality and is known as the decay constant. Re-arrangement and integration of equation (2-2) results in the following mathematical expression:

$$N_t = N_o\, e^{-\lambda t} \qquad \textbf{(2-3)}$$

where N_o denotes the number of radioactive nuclei at time t=0. The sample activity A_t at the time t is proportional to the number of radioactive nuclei N_t, therefore:

$$A_t = A_o\, e^{-\lambda t} \qquad \textbf{(2-4)}$$

where A_o represents the activity at t=0.

The old unit of activity is called the curie (Ci), which is exactly equal to 3.7×10^{10} disintegrations per second . However, the curie was replaced by another unit called the becquerel (Bq), which has been became the standard unit to measure the activity of a radioactive source (Thrall et al. 2001; Knoll 2010). The Bq is one disintegration per second and so:

$$\mathbf{1\ Bq = 2.703 \times 10^{-11}\ Ci} \qquad \textbf{(2-5)}$$

The time required for half the nuclei to decay is called the half-life ($t_{1/2}$). The half-life value can be derived from the previous expressions, it is given by (Krane 1988; Pearson 1986; Thrall et al. 2001):

$$\frac{No}{2} = N_o\, e^{-\lambda t_{1/2}} \qquad \textbf{(2-6)}$$

$$\frac{1}{2} = e^{-\lambda t_{1/2}} \qquad \textbf{(2-7)}$$

Since $e^{-0.693}=1/2$, equation (2-7) can be simplified to yield the following expression:

$$\lambda\, t_{½} = 0.693 \qquad \textbf{(2-8)}$$

$$t_{½} = 0.693/\lambda \qquad \textbf{(2-9)}$$

2.3 Interaction of radiation with matter

Both types of radiation, charged particles (such as α and β particles) and electromagnetic radiation (such as γ photons), are emitted during radioactive decay. These types of radiation transfer their energy to matter as they pass through it, producing ionisation and excitation of atoms and molecules. Thus they are known as ionising radiation (Cherry et al. 2012).

As a charged particle passes through matter, it loses its energy through collisions when it interacts with orbital electrons or the nuclei of atoms it encounters. The amount of energy transferred from the charged particle to matter in each individual interaction is relatively small; thus the particle undergoes a large number of interactions before all of its kinetic energy is spent (Cherry et al. 2012).

Gamma (or x-ray) photons are uncharged particles and create little direct ionisation or excitation in the matter through which they pass. Gamma rays can interact with matter by three major mechanisms: photoelectric absorption, Compton scattering and pair

production. In the first two interactions, the energy of the gamma photon is partially or completely transferred to an atomic electron. In pair production, an electron-positron pair is created. The photon either disappears or is scattered at a specific angle (Knoll 2010).

When a photon passes through a material, the probability that it will interact depends on the photon energy and on the thickness and composition of the material. The dependence on thickness is relatively simple; the thicker the absorber material, the greater the probability that an interaction will happen. The dependence on material composition and photon energy, however, is more complicated (Cherry et al. 2012).

A reduction in the intensity of a photon beam as it passes through a material is called attenuation. The attenuation involves both absorption and scattering. The quantity linear attenuation coefficient (μ_l) has the dimensions of cm^{-1} and it represents the attenuating ability of the material. For a monoenergetic photon beam:

$$I_x = I_o\, e^{-\mu_l x} \qquad \textbf{(2-10)}$$

where I_o is the initial intensity, I_x is the intensity through thickness x of the material. The linear attenuation coefficient is affected by the radiation energy and the characteristics of the material and it is found to increase linearly with material density (ρ). The effect of density is factored out by dividing the linear attenuation coefficient by density, resulting in a quantity called mass attenuation coefficient (μ_m), which has the dimensions $cm^2\, g^{-1}$. It is affected by the atomic number (Z) and electron density of the material, and the energy (E) of the incident photon (Cherry et al. 2012).

As mentioned earlier, the main types of interaction between gamma rays and matter are photoelectric absorption, Compton scattering and pair production. The total mass attenuation coefficient can be split into components for all these interactions as follows (Cherry et al. 2012):

$$\mu_m = \tau + \kappa + \sigma \qquad \textbf{(2-11)}$$

where τ represents the component of the mass attenuation coefficient caused by the photoelectric process, σ stands for the component caused by Compton scattering and κ is the component caused by pair production. The probability of these three principal

interactions over a wide range of energy of the incident photon and atomic number of the attenuating material is shown in Figure 2-1.

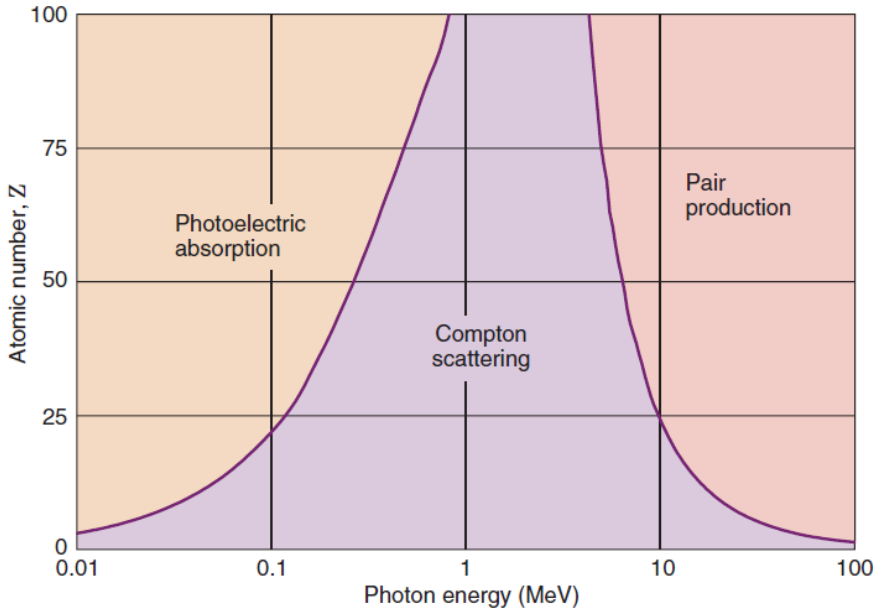

Figure 2-1: The most probable interactions versus photon energy for elements of different atomic numbers (Cherry et al. 2012)

2.3.1 Photoelectric absorption

Photoelectric absorption occurs when the energy of the incident photon is totally transferred to an orbital electron. Thus, that photon completely disappears. In its place, a photoelectron is ejected from the atom. The photoelectron loses its energy through multiple ionisations and excitations. As a consequence of the initial ionisation, an electron from a higher shell falls down to fill the vacancy. The de-excitation of the atom happens through the emission of Auger electrons or characteristic x-rays. In turn, these may interact with the medium (Lilley 2001; Thrall et al. 2001; Knoll 2010).

In order for this process to happen, the photon must have an energy greater than the binding energy (E_b) of the electron in its orbit. As the energy of the incident photon increases, the probability of the photoelectric process decreases. The energy of the ejected electron (E_e), which is commonly the K-shell electron (Figure 2-2), is given by:

$$E_e = h\nu - E_b \qquad \textbf{(2-12)}$$

where h is Plank's constant, ν is the frequency associated with the photon and hν represents the energy of the incident photon (Thrall et al. 2001; Knoll 2010).

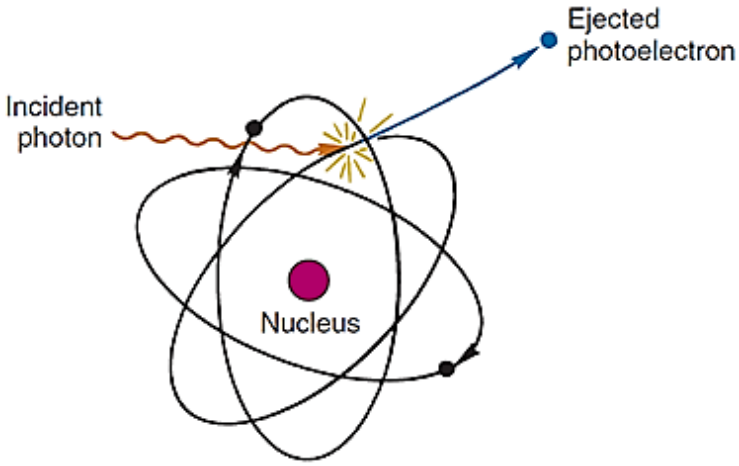

Figure 2-2: Photoelectric absorption (Cherry et al. 2012)

The photoelectric component τ decreases rapidly with increasing photon energy (E) and increases rapidly with increasing atomic number (Z) of the material (equation 2-13). Thus, the photoelectric effect is the dominant effect in heavy elements at low photon energies.

$$\tau \propto \frac{Z^3}{E^3} \qquad \textbf{(2-13)}$$

In diagnostic nuclear medicine, the photoelectric effect is undesirable in body tissues, but it is important in the detection of ionising radiation. This is why imaging systems are typically made of materials with high atomic number, in which the probability of the photoelectric process is high (Thrall et al. 2001).

2.3.2 Compton scattering

In Compton scattering, the incoming photon interacts with a weakly bound electron. The incident photon transfers part of its energy to that electron, which results in its ejection it as a recoil electron. The original photon is deflected from its original path with lower energy (Figure 2-3) (Thrall et al. 2001; Knoll 2010). The recoil electron produces further ionisations as it travels through matter. The amount of energy transferred to the electron depends on the angle of scattering (θ) with respect to the

direction of the incident photon, ranging from zero to a large fraction of the photon energy. Maximum energy transfer to the electron occurs at θ =180°, when the photon is scattered backwards, and the electron moves in the same direction as the incident photon. Minimum energy transfer occurs at θ =0, when the scattered photon moves in the same direction as the incident photon, just grazing the electron (Cherry et al. 2012).

The process of Compton scattering is undesirable in nuclear medicine imaging because it contributes to the loss of spatial resolution (Thrall et al. 2001; Knoll 2010).

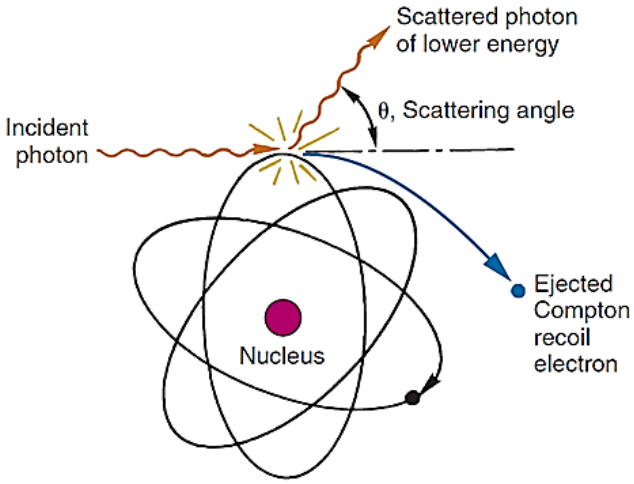

Figure 2-3: : The Compton scattering process (Cherry et al. 2012)

The Compton scatter component σ decreases slowly with increasing photon energy E and it is relatively independent of the atomic number Z. Compton scattering is the dominant interaction for intermediate values of Z and E (Cherry et al. 2012).

$$\sigma \propto \frac{Z}{A} . \frac{1}{E} \qquad \textbf{(2-14)}$$

where A is the mass number.

2.3.3 Pair production

Pair production is possible if the energy of the incoming photon exceeds twice the electron rest mass energy (1.02 MeV). In this interaction mechanisms the incident photon is replaced by an electron-positron pair. Both the electron and the positron lose their kinetic energy by ionisation and excitation. After it has lost its energy, the positron

is attracted to an electron and annihilates with it, emitting two annihilation photons each with an energy 511 keV and direction at 180^0 to each other (Figure 2-4) (Lilley 2001; Thrall et al. 2001; Knoll 2010).

The pair production component κ increases with increasing photon energy (E) and atomic number (Z) of the material as follows:

$$\kappa \propto (E-1.022\ MeV)\ Z \qquad \textbf{(2-15)}$$

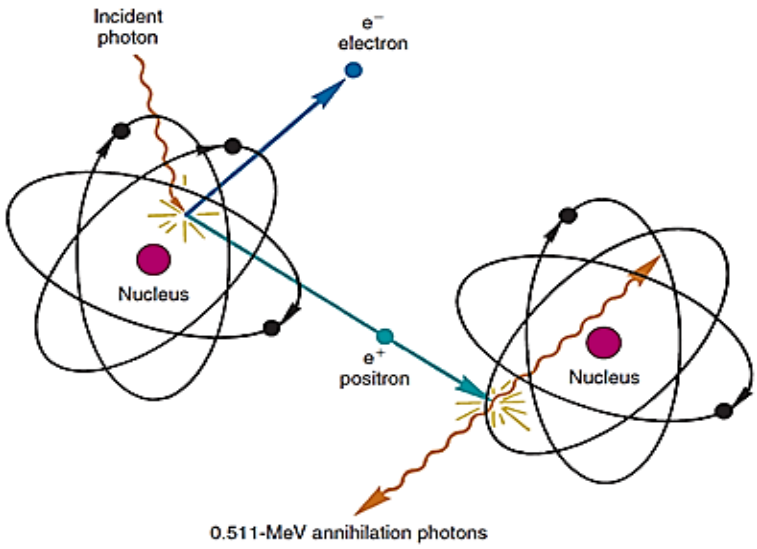

Figure 2-4: Pair production and positron annihilation (Cherry et al. 2012)

2.4 Radiation dose

'Dose' is a colloquial term that is often used to describe the activity of a radionuclide or radiopharmaceutical that is to be administered to a living subject. However, the term 'Radiation dose' refers to the energy deposited by ionising radiation in a material and its effect on living tissue. Absorbed dose is defined as the quantity of radiation energy deposited in an absorber per unit mass of absorber material. It is measured in gray (Gy), which is equal to one joule per kilogram (J kg^{-1}). The biological damage caused by radiation interacting with a particular tissue or organ depends on the type of ionising radiation. Alpha particles, for example, are densely ionising and have more effect than other ionising radiations. Therefore, the absorbed dose is weighted according to its

potential damage to biological tissues, and this quantity is called equivalent dose (Cherry et al. 2012).

The equivalent dose is a quantity that takes into account the relative biological damage caused by radiation interacting with a particular tissue or organ. Equivalent dose equals the absorbed dose multiplied by a radiation weighting factor. This factor is 20 for alpha particles, but 1 for beta particles, gamma rays and x-rays, which allows for the various effects of different ionising radiations in causing radiation damage to living tissue. Equivalent dose is measured in sievert (Sv). However, human tissues and organs are not equally sensitive to radiation damage; for example, the skin is relatively insensitive to damage whereas the bone marrow is particularly susceptible. Effective dose represents the whole-body dose that is the sum of the weighted equivalent doses in all the tissues and organs of the body. It considers the susceptibility of tissues and organs to radiation damage through a tissue weighting factor, and it is also measured in Sv (Cherry et al. 2012).

2.5 Biological effects of ionising radiation

The biological effects of ionising radiation have been known for many years. The first case of human injury was reported in 1895 after the discovery of x-rays by Roentgen, while the genetic effects of radiation were reported at the beginning of 1902. Early evidence of harmful biological effects due to exposure to high radiation dose was obtained for persons working in the radium industry in the 1920s and 1930s (Al-Musawi 2018). Knowledge of these effects increased through the atomic bombings of Hiroshima and Nagasaki in 1945, U.S. nuclear testing in 1952-1953 and nuclear accidents, such as the Goiania accident and the Chernobyl and the Fukushima Daiichi disasters.

The biological effects of radiation can be categorised depending on the timing after exposure (stochastic and deterministic) and the persons affected (genetic and somatic) (Figure 2-6) (Al-Musawi 2018).

Stochastic effects are unpredictable and random effects that occur after chronic exposure to a low radiation dose, and they include genetic effects and cancer. These effects have an increased probability of occurrence with increased dose. The International Commission on Radiological Protection (ICRP) has determined limits for

annual radiation dose at 20 mSv for workers and 1 mSv for members of the public to limit stochastic effects.

Deterministic effects are also called non-stochastic effects. They are non-random and have a predictable response to radiation. The severity of the effect and tissue damage increase with increasing dose. It has a dose threshold below which the effect does not occur; the threshold may vary from person to person. To prevent a particular deterministic effect, skin reddening (erythema), the ICRP has limited the annual radiation dose at 500 mSv for workers and 50 mSv for members of the public (Al-Musawi 2018). Radiation-induced burns, acute and chronic radiation syndrome and thyroiditis are all examples of deterministic effects.

The effects of radiation can also classified according to the subjects exposed. Somatic effects of radiation, for example, appear in the exposed person, either immediately after the exposure (e.g. skin damage), or a long period of time after exposure (e.g. damage to the reproductive system). However, genetic effects cause damage to the reproductive cells and may be transmitted to next generations (Figure 2-5) (Al-Musawi 2018).

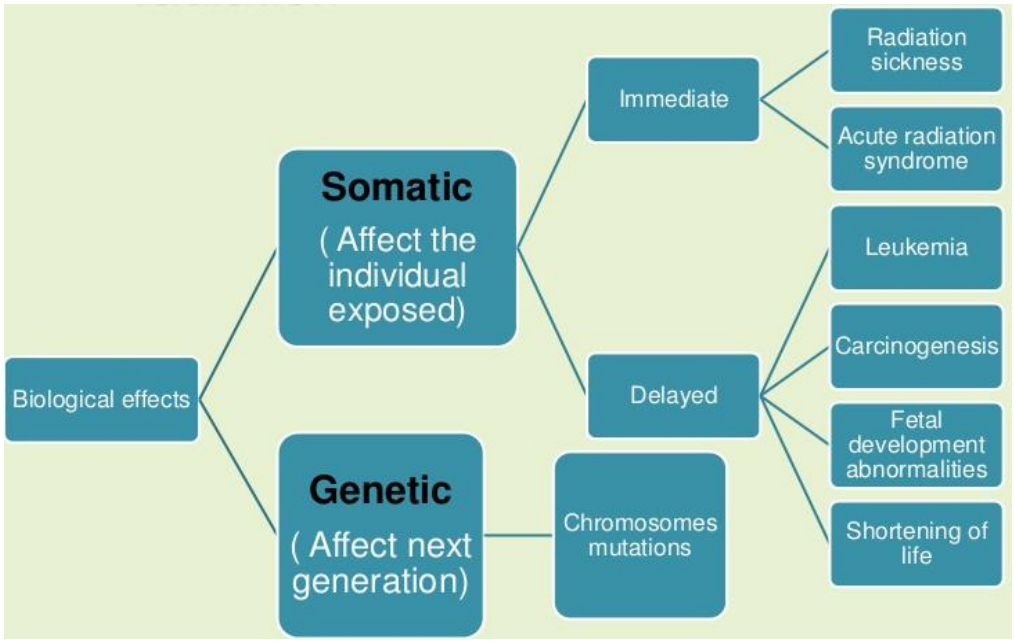

Figure 2-5: Somatic and genetic effects of ionising radiation (Al-Musawi 2018)

The biological effect of ionising radiation is due to the transfer of energy to cells and the production of ionisation and excitation in their constituent atoms. The effect can be acute, e.g. following the exposure of a subject to a high radiation dose, greater than 100

mGy, within a short period of time (a few days). This causes severe damage to skin and internal organs. The severity of the damage depends on the dose. Otherwise, the effect is considered to be chronic, which occurs when a relatively small radiation dose is delivered over a long period of time (several years). The latter is characteristic of occupational exposure, for which the biological effects may appear after many years. The interaction of ionising radiation with cells may damage the chromosomes, which are considered the most important parts of the cell as they carry the DNA, the genetic material of most living organisms. Potential damage to the chromosomes can cause cell mutations resulting in genetic effects and the development of cancer (Grupen 2010). The various stages of the physical and biological effects of radiation are shown in Figure 2-6.

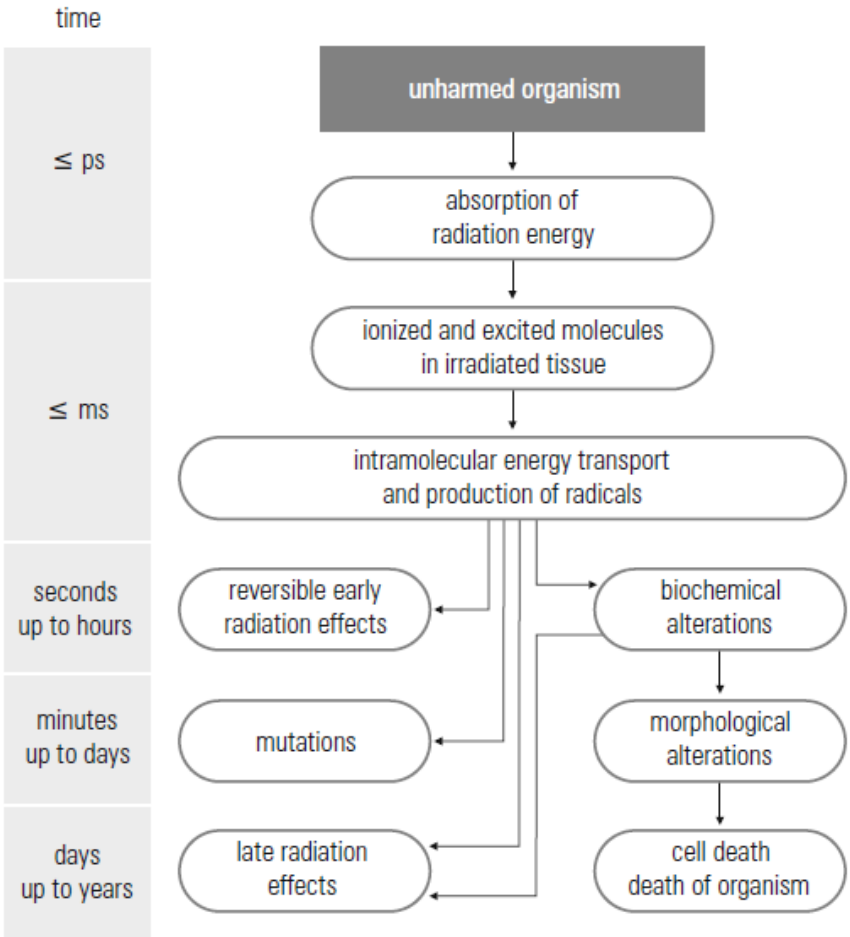

Figure 2-6: Stages of the physical-biological effects of absorbed radiation (Grupen 2010)

2.6 Detection of radiation

The detection of radiation is important to the practice of nuclear medicine because the activity of radiopharmaceuticals (this term is discussed in chapter 3) must be measured and documented. Furthermore, the working area must also be monitored for the presence of radioactivity to ensure the safety of both workers and patients. A detector may only record the existence of nuclear radiation, but more often it gives information about the energy of that radiation and its type. There are different types of detectors, which use different detecting media. These are gas-filled detectors, scintillation detectors and semiconductor detectors. The basic operating principle of all detectors is the conversion of ionising energy into electrical energy. Electronic circuits are used in association with the detectors to determine the intensity of this radiation (Thrall et al. 2001).

2.6.1 Gas-filled detectors

In its basic form, this type of detector comprises a gas-filled chamber with positive and negative electrodes across which a voltage is applied (Figure 2-7). When the gas is exposed to radiation, ionisation will create positive and negative ions (ion pairs), which then move towards the electrodes and produce an electrical current. There are two ways in which an ion pair is formed: by direct interaction between the incident radiation and the gas molecules or by a secondary process in which the electron that left its original atom may possess enough kinetic energy to generate further ions. Those energetic electrons are usually called delta rays.

There are three sub-types of gas-filled detectors that are used in nuclear medicine applications: ionisation chamber, proportional counter and Geiger-Müller counter (Thrall et al. 2001). Just the first type of detector (ionisation chamber) was used in this study and so it is the only one discussed in detail.

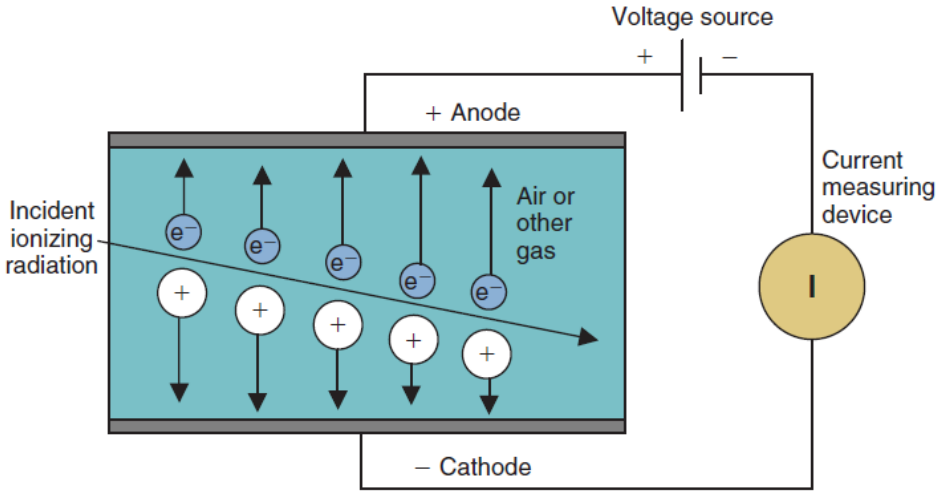

Figure 2-7: Operating principles of a gas-filled detector (Cherry et al. 2012)

2.6.1.1 Ionisation chamber

In most ionisation chambers, the gas between the electrodes is air. Many different designs have been utilised for the electrodes, but basically they consist of a wire along the central axis of a cylinder or a pair of concentric cylinders. For maximum efficiency of operation, the voltage between the electrodes must be sufficient to ensure complete collection of ions and electrons produced by the interaction of the radiation with the gas in the chamber. If the voltage is too low, some of the ions and electrons simply recombine with each other without producing an electrical current. As the voltage rises, the probability of recombination decreases and the resulting electrical current increases. The correct choice of the voltage applied between the electrodes is crucial to ensure that it is high enough to avoid recombination but insufficient to cause further secondary ionisations. This ensures that there is a direct proportionality between the ionisation current produced and the energy deposited per unit time via primary ionisations in the chamber (Cherry et al. 2012).

The amount of electrical charge released in an ionisation chamber by a single ionising radiation event is small. Thus, ionisation chambers normally are not used to record or count individual radiation events, but they are used to measure the total current passing through the chamber caused by the radiation. Small amounts of electrical current (usually of the order of pA to μA) are measured using a sensitive current-measuring device called an electrometer. A single electrometer may not be able to accommodate

very small currents and thus a number of electrometers may be used for measurement, with electronics used to switch between them (Cherry et al. 2012).

There are two devices consisting of ionisation chambers and electrometers that are used in nuclear medicine applications: survey meters and activity calibrators. Survey meters are used to monitor radiation dose rates for protection purposes (Cherry et al. 2012). However, it is the activity calibrators that were used in this study.

The purpose of an activity calibrator is to measure the activity of a radionuclide in a syringe or vial before it is administered to a patient. The basic components of a radionuclide calibrator are shown in Figure 2-8. Unlike other types of ionisation chamber, an activity calibrator consists of a sealed and pressurised chamber that is normally filled with argon gas. This reduces the effect of changing atmospheric pressure on output readings. Activity calibrators assay the total amount of activity present by measuring the total amount of ionisation produced (Cherry et al. 2012). Once the ionisation current is measured, a chosen calibration factor is applied to convert it to activity for the particular radionuclide assayed. The calibration factor depends on several factors, one of the main ones being the energy of the radionuclide. After the application of the calibration factor, the display unit is configured to show the activity in an appropriate unit (GBq to kBq). Activities lower than the order of kBq involve high statistical variations due to the poor sensitivity of the electrometer to measure low currents. In such cases, a radionuclide calibrator would not be the ideal device to measure activity. It would be more appropriate to use an alternative detection system, such as a scintillation detector or semiconductor detector (Talboys 2016).

Ionisation chambers have no inherent ability for energy discrimination and so they cannot be utilised to select different gamma ray energies for measurement. One method that is used to discriminate low-energy and high energy γ -ray emitters (e.g. ^{99m}Tc and ^{99}Mo) is to measure the sample with and without lead shielding around the source. With the shielding in place, predominantly the activity of the high-energy emitter that is recorded, while the total activity of both emitters is recorded in the absence of the shielding. This technique can be used to detect tens of kBq quantities of ^{99}Mo in the presence of tens or even hundreds of MBq of ^{99m}Tc (Cherry et al. 2012).

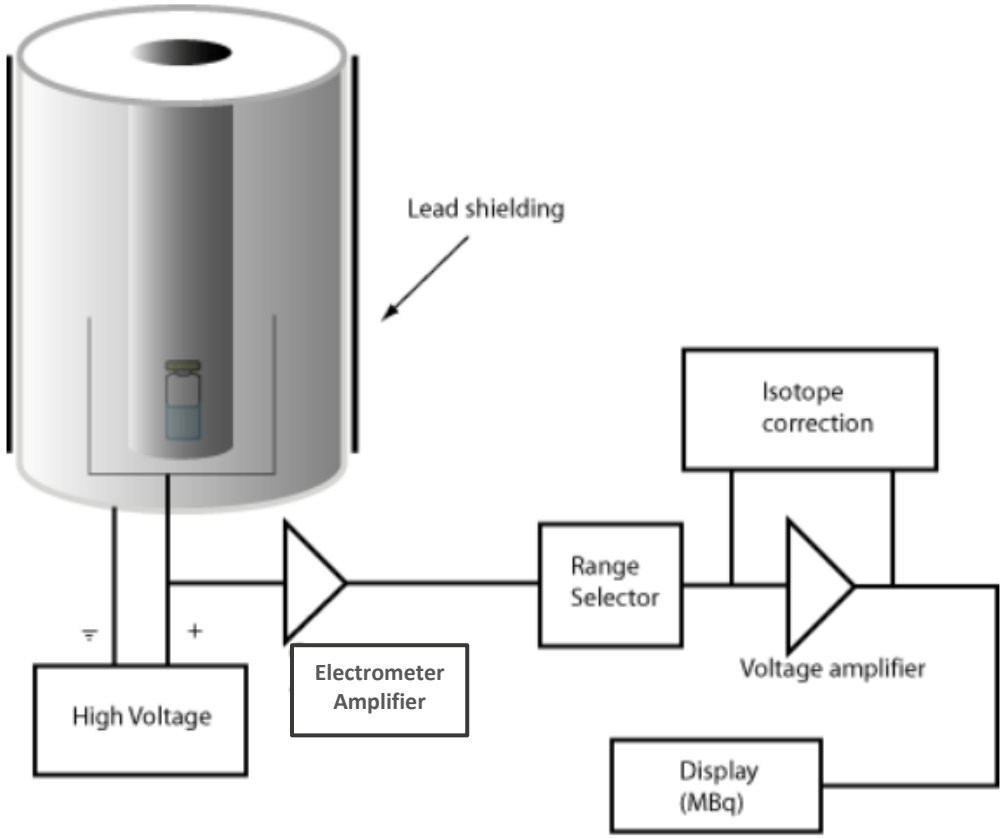

Figure 2-8: Schematic of a radionuclide calibrator (IAEA 2015)

In this study, a secondary standard radionuclide calibrator called Fidelis (Figure 2-9) was used to measure the activity of some radionuclides. This detector is manufactured by Southern Scientific Ltd. (Henfield, England) and comprises a well type ionisation chamber and electrometer connected to a laptop computer with associated software. The chamber is the same as the National Physical Laboratory (NPL) calibrator type 271 described by Woods in 1983 (Talboys 2016).

Figure 2-9: Fidelis secondary standard radionuclide calibrator (NPL) (Talboys 2016)

The Fidelis is a sealed, concentric cylinder type of activity calibrator and it is mainly constructed of aluminium alloy. The chamber is filled with dry nitrogen to a pressure of 1 MPa. The applied voltage between the cathode and anode within the chamber is 1450 V. The electrometer integrated into the base of the ionisation chamber is the new state-of-the-art, high resolution, PAM Electrometer Module (Talboys 2016).

The Fidelis calibrator is supplied with a database of calibration factors traceable to the NPL primary standardisations. When a specific radionuclide, container and volume are used, the corresponding calibration factor can be retrieved by the display software (Talboys 2016).

Before purchase of the Fidelis chamber in 2009 by the Medical Physics Department at the University Hospital of Wales, the detector was checked against the master chamber at NPL to ensure that the response of the instrument was within specification. Five radioactive sources were assayed in the chamber and compared with the NPL master chamber. The variation in current measurements was also checked for the Fidelis electronics and compared with the NPL electronics. It was found that the specification was met (Talboys 2016).

A quality assurance scheme for the Fidelis was established and maintained to ensure the stability of the chamber. The Fidelis has an in-built quality control routine that evaluates the amplifier offset, ambient background radiation and high voltage values. In addition, the calibrator response was checked using a 10 MBq ^{137}Cs sealed source, which was first assayed on the chamber by NPL (Talboys 2016).

The Fidelis calibrator is relatively expensive and is not a choice for the routine assay of radionuclides in a nuclear medicine department. For example, a regional medical physics department may have just one Fidelis calibrator but may need many field radionuclide calibrators for routine measurements. Field calibrators are produced by a number of manufacturers including Capintec, Biodex, Veenstra and PTW. The basic design of these calibrators matches that previously described (Talboys 2016).

The assay of ^{99}Mo activity in ^{99m}Tc eluate, called the molybdenum breakthrough test (MBT), was performed using a Capintec (CRC-15R) in the radiopharmacy at the University Hospital of Wales. This was done by measuring the sample with and without a few millimetres (6 mm) of lead shielding around the source. Predominantly, it is the activity of the high-energy radionuclide that is recorded with the shielding in place, whereas the total activity of both radionuclides is recorded with the shielding absent.

One of the main differences between the Fidelis secondary standard instrument and a field calibrator is the number of available calibration factors for the user to choose. Normally, a field calibrator will have one factor for a given radionuclide. This means that it does not take account of other variables that have an impact on the chosen calibration factor; these include the container material, the geometry of the container and also the volume of the solution. The Fidelis calibrator has calibration factors for a number of container and volume combinations and these can be applied to give a more accurate activity reading (Talboys 2016). In this study, a Schott vial with 4 ml of radioactive solution was chosen as the standard vial and volume combination for measuring activity in the Fidelis calibrator.

2.6.2 Scintillation detectors

Scintillation is a general term that refers to light emission and a scintillator is any material that emits a photon within the UV or visible light region when de-excitation takes place (i.e. an excited electron in the scintillator material returns to the ground state). The resulting scintillation photons may be detected by a photomultiplier tube (PMT) to produce an output electrical pulse (Reilly et al. 1991; Prekeges 2011).

Generally, scintillation detectors consist of a detector (scintillation crystal and PMT), power supply, preamplifier, amplifier and pulse analyser. The interaction of a gamma or x-ray photon with the crystal generates a scintillation. The PMT is a major part of this system and it is used to convert the scintillation photons to an electronic signal. The closest part of the photomultiplier tube to the scintillation crystal is called the photocathode. This is made of a very thin layer of a photoemissive material which has the ability to generate electrons when exposed to UV and visible light photons (Reilly et al. 1991; Knoll 2010; Prekeges 2011).

The electrons released by the photocathode enter a focusing grid, which provides a suitable electrical field to direct them towards the first of a series of dynodes. The electrons from the last dynode are collected by the anode which is located at the opposite end of the PMT to the cathode. The output current signal is still small, but it is amplified by subsequent electronics (Reilly et al. 1991; Prekeges 2011).

Scintillation detectors have relatively poor energy resolution of typically 5-10%. This is attributed to the events that must occur to convert an incident gamma photon into light and the subsequent formation of an electrical signal via many inefficient stages. In addition, the number of primary charge carriers (photoelectrons) generated in a typical radiation interaction is normally no more than a few thousand. This number is subject to a relatively large statistical variation, which further degrades energy resolution. However, scintillation crystals may be manufactured with large thickness and thus they have relatively large sensitivity (detection rate per unit activity) (Knoll 2010).

2.6.3 Semiconductor detectors

Usually a semiconductor material is a poor electrical conductor. However, when it is irradiated by ionising radiation, the electrical charge generated can be collected by an

external applied voltage, as it is with a gas. This is the operating principle of a semiconductor detector. This principle does not apply to a conducting material (e.g. a metal) because such a material would conduct a large amount of current even without the presence of ionising events. Insulators (e.g. glass) are also not appropriate detector materials, because they do not conduct current even in the presence of ionising radiation (Cherry et al. 2012).

2.6.3.1 Semiconductor properties

According to the band theory of solids, the band furthest from atomic nuclei that is filled with electrons is called the valence band. The next band further out is called the conduction band.

Electrons in the valence band are bound to a determined position within the material, while those in the conduction band are free electrons that can migrate through the material. If a material naturally has some electrons in the conduction band, it is an electrical conductor. If under normal circumstances, the material has no electrons in the conduction band, it is an electrical insulator or a semiconductor.

The classification of the material as an insulator or a semiconductor is determined by the size of the bandgap, which is the gap between the valence band and the conduction band. In insulators, this gap is usually 5 eV or more, while it is significantly less in semiconductors (Figure 2-10) (Lilley 2001; Knoll 2010).

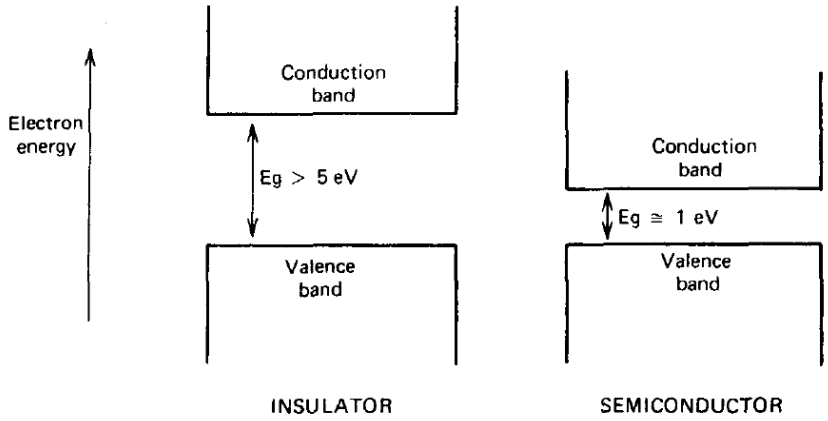

Figure 2-10: Band structure in both insulators and semiconductors (Knoll 2010)

The most commonly used materials for a semiconductor detector are silicon (Si) and germanium (Ge). In such detectors, one pair of charge carriers is produced per 3 to 5 eV of radiation energy absorbed. By comparison, approximately 34 eV is required to produce one such pair in air. Thus a semiconductor detector is a more efficient absorber of radiation than a gas-filled detector and it produces an electrical signal that is about 10 times larger per unit of radiation energy absorbed. This signal is large enough to allow the detection and counting of individual radiation events. The signal is produced by multiple excitations of electrons across the narrow band gap from the valence band to the conduction band, leaving holes in the valence band. In addition, a semiconductor detector has much better energy resolution (typically 1% or better) than a scintillation detector (Cherry et al. 2012).

In spite of these advantages, semiconductor detectors have a number of drawbacks that have limited their use in nuclear medicine applications. The first one is that both Si and Ge (especially Ge) conduct a considerable amount of thermally induced electrical current at room temperature. This generates a background noise current that interferes with the detection of radiation-induced currents. Thus, Si detectors (usually) and Ge detectors (always) must be operated at a low temperature (typically that of liquid nitrogen which is -196^{o}C) (Cherry et al. 2012).

A second problem related to the use of semiconductor detectors is the existence of impurities in Si and Ge crystals. Impurities (atoms of other elements) normally disturb the regular arrangement of Si and Ge atoms in the crystal matrix of these materials. These disturbances generate electron traps that capture electrons released in ionisation events. This leads to a significant reduction in the electrical signal and, in turn, restricts the usefulness of semiconductor detectors for detection of gamma rays (Cherry et al. 2012).

To address the impurity problem in the semiconductor material, two types of compensating impurities may be introduced into the crystal matrix. The first type is called acceptor impurity, for which atoms of an element (such as boron) in group III of the periodic table are added. The boron atom has three valence electrons. Therefore, it requires one more electron to saturate the covalent bond with the crystalline silicon. Leaving the covalent bond unsaturated would mean leaving a hole in exactly the same way as when an electron is excited from the valence band to the conduction band, but

with slightly different energy characteristics. An electron filling this hole is slightly less firmly attached than a typical valence electron (Lilley 2001; Knoll 2010).

The other type is called donor impurity, for which atoms of an element (such as phosphorus) in group V of the periodic table are added. The phosphorus atom has one more valence electron than the surrounding atoms. Therefore, adding phosphorus to the silicon would leave one extra electron after the formation of all the covalent bonds. This extra electron occupies states that lie near to the conduction band and will not be strongly bound to the original impurity atom. It takes very little energy to dislodge it to form a conduction electron without a corresponding hole. Impurities such as phosphorus are referred to as donor impurities as they easily contribute electrons to the conduction band (Lilley 2001; Knoll 2010).

However, as a detector of ionising radiation, a semiconductor cannot simply consist of the material and two electrodes. It is necessary for p-type and n-type crystal material to be combined to create what is called a (p-n junction), or semiconductor diode. This diode is reversed biased so that no current passes through when no ionising radiation is applied. The reverse bias creates a region called the depletion region which is sensitive to ionising radiation (Khandaker 2011). However, with the use of normal pure silicon or germanium, it is difficult to achieve depletion depths beyond 2 or 3mm with diode semiconductors. In order to detect γ rays efficiency, a much greater thickness is required to do so. The thickness (d) of the depletion region is given by the equation (Knoll 2010):-

$$d = \left(\frac{2\epsilon V}{eN}\right)^{1/2} \qquad \textbf{(2-15)}$$

where V denotes the voltage of the reverse bias, ϵ is the dielectric constant, e is the electronic charge and N is the concentration of impurities within the semiconductor material. At a given applied voltage, a thicker depletion region can only be achieved by reducing the impurity concentration (Knoll 2010).

Detectors that are manufactured with high purity Ge semiconductor material are usually called intrinsic germanium or high-purity germanium (HPGe) detectors. In this type of detector, depletion depths of several centimetres are possible. HPGe detectors became commercially available in the early 1980s. The starting material is bulk geranium with high purity; this is further processed using a technique called zone refining. In this

technique, the impurity concentration in the material is continuously reduced by locally heating the germanium and slowly passing a melted zone from one end of the material to the other. The solubility of the impurities is greater in the molten germanium than in the solid one and so they tend to transfer into this molten zone and are gradually swept out of the sample. After many repetitions, impurity concentrations as low as 10^9 atoms/cm^3 can be achieved. The germanium that results from the use of this method is probably the most purified material that has ever been produced. The final product is large single crystal of germanium that is described as high purity n-type if the remaining low level impurities are donors or high purity p-type if the remaining low level impurities are acceptors (Knoll 2010).

2.7 Electronic components

Signal processing plays a key role in extracting useful information from radiation detectors. Figure 2-11 shows the main electronic components of a nuclear radiation counting instrument.

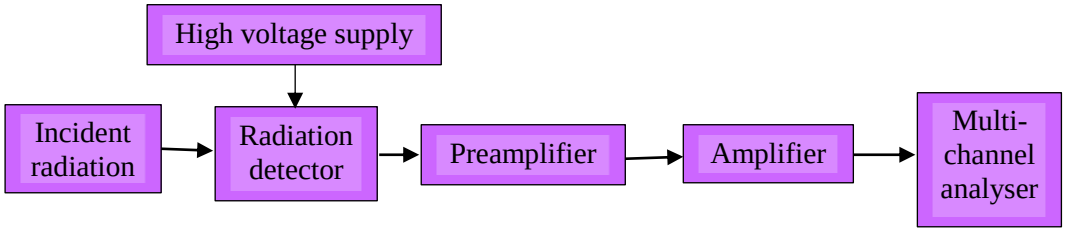

Figure 2-11: Schematic representation of the electronic components of a radiation detector (Cherry et al. 2012)

2.7.1 Preamplifier

The signal pulse produced as a result of radiation passage through a detector cannot be directly digitised and counted because it is noisy and has a very narrow width, small amplitude and a short duration. Thus a preamplification stage is crucial before any further signal processing. The main purposes of the preamplifier are as follows: providing optimum impedance matching between the detector and the rest of the electronic system, pulse shaping, minimising noise by filtering, and increasing the amplitude of the pulses (Sandi 2013).

The preamplifier must be as close as possible to the detector in order to reduce the distortion of the signal. It is desirable to reduce the capacitive loading on the preamplifier, and thus it is important to avoid using long connecting cables between it and the detector (Prekeges 2011).

2.7.2 Amplifier

The main functions of the amplifier are as follows: restoring the baseline, filtering the noise, fixing the gain of the signals (increasing the amplitude) and providing near-Gaussian pulse shaping. The millivolt output from the preamplifier is further amplified to a range of a few volts by the amplifier. The multiplication factor normally ranges between 1 and 1000, and this can be adjusted by coarse and fine gain controls on the electronics module (Prekeges 2011; Sandi 2013).

2.7.3 High-voltage (HV) supply

The HV supply provides the charge collection voltage for the detector. This device converts the alternating voltage provided by the line source into a constant or direct voltage (Cherry et al. 2012).

The collection of the charge carriers is incomplete when the bias voltage is low in the HPGe detector, due to recombination or trapping along the track of the secondary particle. Conversely, when the voltage is reasonably high, charge collection becomes complete and the pulse height no longer changes with further increase in the detector bias voltage. This voltage region is called the saturation region (Sandi 2013). However, small HV variations have little effect on the output pulse amplitude with semiconductor detectors (Cherry et al. 2012).

2.7.4 Multichannel Analyser (MCA)

The multichannel analyser (MCA) is a device that sorts out the incoming pulses according to their heights and counts the number at each height in a multichannel memory. The contents of each channel can then be displayed to give a pulse height spectrum (Sandi 2013).

The main part of the MCA is an analogue-to-digital converter (ADC), which measures and sorts out the incoming pulses based on their amplitudes (Cherry et al. 2012).

The ADC converts analogue signals (pulse amplitudes in volts), which have an infinite number of different values, into digital signals (channel number), which have a finite number of integer values. For each analyser channel, there is a related storage location in the MCA memory. The MCA memory counts and stores the number of pulses recorded in each analyser channel. The number of memory storage locations available determines the number of MCA channels. The sorting and storage of the energy information from radiation detectors with an MCA are used to record the pulse height spectrum (counts per channel versus channel number, or energy), as shown in Figure 2-12 (Cherry et al. 2012).

Each radiation counting system has a characteristic dead time or pulse resolving time τ which is defined as the time required by the ADC to process individual detected events. Conversely, live time is defined as the permitted time for the pulses to pass to be processed by the ADC. In this study, the acquisition time is always the live time.

At high counting rates, amplified pulses can occur so close together that they fall on top of each other (Figure 2-13 (a)). Thus, if a second pulse occurs before the disappearance of the first one, the two pulses will overlap be counted as one and form a single distorted pulse that is not representative of either. This problem is called pulse-pile up results in further counting or dead time losses (Cherry et al. 2012).

Counting losses can also occur due to another problem, which is baseline shift (Figure 2-13 (b)). This happens when a second pulse occurs during the negative component of the first one. Thus, the second pulse will be slightly depressed in amplitude, resulting in an inaccurate pulse amplitude and an apparent decrease (shift) in energy of the detected radiation event (Cherry et al. 2012).

The HPGe detector and associated electronics used in this project are described in more detail in chapter 4.

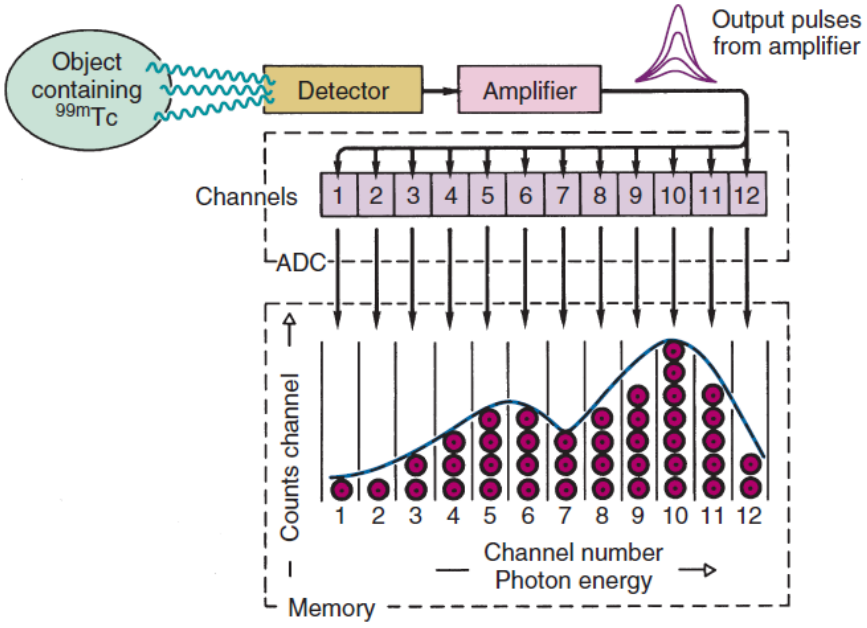

Figure 2-12: Pulse sorting of radiation events according to their amplitudes from an object containing ^{99m}Tc (Cherry et al. 2012)

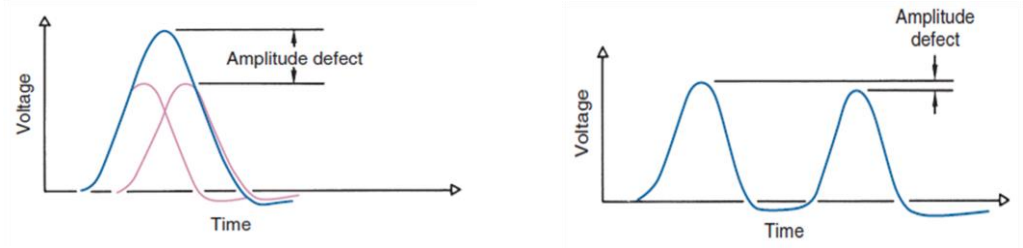

(a) (b)

Figure 2-13: Schematic representation of (a) Pulse pile-up effects and (b) baseline Shift

2.8 Pulse height spectrum

In gamma ray spectroscopy, when a monoenergetic gamma photon (with an energy less than 1.022 MeV) interacts with the detector, it deposits part or all of its energy in the material of the detector, mainly via photoelectric absorption and Compton scattering. The photoelectric interaction leads to the full deposition of the gamma ray energy in the detector (the characteristic x-ray is usually also absorbed in the detector). The amplitudes of the pulses from these events are proportional to the energy of the gamma photon. Ideally, this would give a single narrow line in the pulse-height spectrum, called the photopeak, at a location corresponding to the energy of the gamma photon. On the other hand, in Compton scattering, only part of the gamma energy is deposited in the detector material by the Compton recoil electron. If the scattered gamma photon is also absorbed in the detector, the interaction produces a pulse in the photopeak, whereas if it escapes, the energy deposited in the detector is less than the original photon energy (Cherry et al. 2012).

The deposited energy in the detector in a single Compton scattering event ranges between near zero up to a maximum value, depending on the angle of the scattering event.

Therefore, the ideal spectrum includes a distribution of pulse amplitudes ranging from nearly zero (small-angle scattering) amplitude up to some maximum amplitude corresponding to 180-degree Compton scattering events (Figure 2-14). This part of the spectrum is named the Compton region, while the sharp edge in the spectrum is called the Compton edge (Cherry et al. 2012).

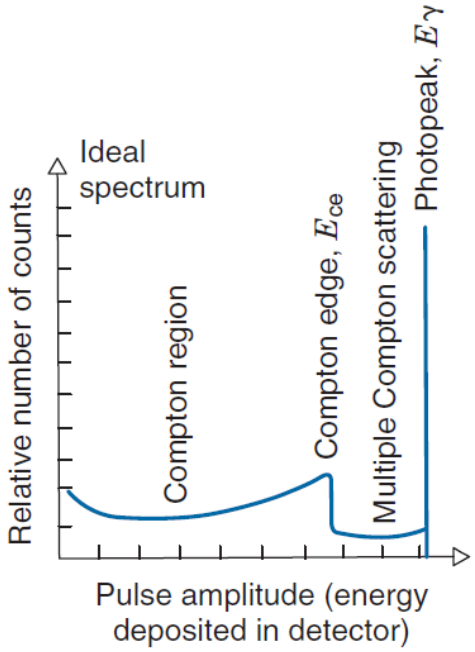

Figure 2-14: Distribution of pulses versus amplitude (or energy deposited in the detector)

2.9 Energy calibration

In germanium detectors, the horizontal scale of the pulse height spectrum must be calibrated in terms of the energy of gamma rays if different gamma peaks are to be determined in a spectrum. The purpose of energy calibration is to convert pulse height to energy using photopeaks with known gamma energies. Energy calibration uses a standard radioactive source with range of gamma energies that should not be broadly different from those to be measured in the unknown spectrum. Using multiple gamma peaks spread along the measured energy range is beneficial because most spectrometer systems demonstrate a nonlinear relation to some extent (Gilmore 2008; Knoll 2010).

In general, however, the relationship between channel number and energy deposited in the detector and is represented by a straight line. Thus the energy calibration equation is as follows:

$$E = m\,x + c \qquad \textbf{(2-16)}$$

where E denotes the energy (keV), m is the slope (keV/channel), x represents the channel number and c symbolises the intercept of the straight line.

2.10 Efficiency calibration

The full-energy peak (FEP) efficiency is a very important parameter in practical gamma ray spectrometry as it allows the determination of the activity of each radionuclide. The FEP efficiency is defined as the number of the photons emitted by the source contributing to the corresponding full-energy photopeak on the pulse height spectrum. It can be calculated from the ratio of the number of detected counts in a photopeak to the number of photons emitted by the radioactive source (Reguigui 2006; Gilmore 2008):-

$$\varepsilon = R/(S \times P_{\gamma}) \qquad \textbf{(2-17)}$$

where ε denotes the efficiency, R represents the full-energy peak count rate (counts/s), S is the source activity in disintegrations per s (Bq) and P_{γ} is the emission probability of the gamma rays being measured (Gilmore 2008).

Normally, the efficiency calibration curve is constructed by measuring different gamma sources of known activity and plotting efficiency versus gamma energy. There are some mixed radionuclide sources that are available for efficiency calibration in the UK and USA; these are the QCY and QCYK sources. The QCYK reference source includes about 12 gamma emitting radionuclides ranging from ^{241}Am (59.5 keV) to ^{88}Y (1836.05 keV).

Chapter 3

Production of Artificial Medical Radionuclides

3.1 Introduction

In the 1920s and 1930s, the first applications of radioactivity for medical tracer studies made use of natural radionuclides. However, because of their generally undesirable characteristics, e.g long half-life and alpha emission, they have found virtually no applications in medical diagnosis since that time.

Given that, the need for manufactured or artificial radionuclides was identified. In modern nuclear medicine practice, all the radionuclides that are used are artificial. They are made either by nuclear fission or by irradiating the nuclei of stable atoms with subnuclear particles (such as neutrons and protons) so as to cause nuclear reactions that change a stable nucleus into an unstable (radioactive) one. This chapter describes the main methods that are used to produce radionuclides for nuclear medicine. These methods comprise: irradiation or fission in a research reactor, irradiation in a particle accelerator (usually a cyclotron) and the use of a radionuclide generator (Table 3-1). The latter requires a research reactor or cyclotron source to produce the parent radionuclide.

Table 3-1: Common methods of radionuclide production (Synowiecki et al. 2018)

Radionuclide sources	Advantages	Disadvantages
Nuclear Reactors	- Production of neutron-rich radionuclides, particularly suitable for therapeutic use - High production efficiency - One research reactor has the ability to supply globally to large regions or centralised production	- Extremely high investment cost - High operational costs - Significant activities of long-lived radionuclides - Long out-of-service periods - Difficult to back-up in case of unforeseen downtime - Demanding logistics, often including air transportation - Public safety issues
Cyclotrons	- Production of proton rich radionuclides suitable for PET - High specific activity in most produced radionuclides - Small investment in comparison to nuclear reactor - Limited long-lived radioactive waste	- Regional network of cyclotrons and complex logistics required for short-lived radionuclide production - Production dependent on the beam energy
Generators	- Available on site, no need for complicated logistics - Mostly long shelf life - Easy to use - Limited radioactive waste a generator normally returned to manufacturer after use	- Radionuclides are supplied in cycles according to possible elution frequency and in-house use must be timed - Trace contaminants of long-lived parent nuclide in eluted product

3.2 Nuclear reactions and nuclear cross-sections

In general, neutrons and charged particles (such as protons) may interact with the atoms of a material either elastically or inelastically. In an elastic interaction, the total kinetic energy remains unchanged although some kinetic energy may be transferred from the incident particle to a target (such as an electron or nucleus) within the atom. For an inelastic process, on the other hand, the total kinetic energy is changed because of ionisation, excitation, the emission of photons or a combination of these effects (Anderson 1984).

There are four categories of charged particle interaction:

1. Elastic processes with electrons
2. Inelastic processes with electrons
3. Elastic processes with nuclei
4. Inelastic processes with nuclei

In the first two categories, the incident particles interact via the Coulomb force with atomic electrons. In the last two categories, the incident particles interact with atomic nuclei through either the Coulomb force or the strong nuclear force. Ionisations and excitations caused by fast charged particles belong to category 2; this is often called collisional energy loss. Bremsstrahlung emission (radiative energy loss) and nuclear reactions belong to category 4.

Neutrons, which have no electric charge, may also undergo elastic and inelastic interactions, but not with electrons because there is no Coulomb force between neutrons and electrons. However, neutrons may interact with nuclei through the strong force. Elastic interactions lead to neutron scattering. Inelastic neutron scattering is also possible, while other inelastic interactions between neutrons and nuclei include neutron capture reactions and the induction of nuclear fission.

Thus, both neutrons and charged particles may participate in nuclear reactions. In general, a nuclear reaction is a process in which the nucleus of an atom and a sub-atomic particle (such as a proton or a neutron) from outside the atom, collide to produce one or more nuclides that are different from the initial nuclide. A nuclear reaction must cause a transformation of at least one nuclide (the target) to another (the product); secondary radiation (particles or photons) may also be released. If a nucleus interacts with a

particle and they separate without changing the composition of any nuclide, the process is simply referred to as a type of nuclear scattering, rather than a nuclear reaction.

Nuclear reactions are often expressed in a symbolic form in which the incident particle and secondary particle or photon are separated by a comma and enclosed in brackets, with the target nucleus to the left of the brackets and the product nucleus to the right. For example, X(n,p)Y denotes a reaction in which a neutron (n) strikes a target nucleus X leading to the creation of a product nucleus Y and a proton (p). Both the target and product nuclei may be stable or radioactive (i.e. a radionuclide). If the reaction converts a stable target into a radioactive product, the process is often called activation. Other example reactions include (p,n), (n,γ) and (p,γ) and the incident particle may be an entity other than a proton, such as a deuteron (d) or an alpha particle (α).

In medical radionuclide production, nuclear reactions always involve a change in the number of either protons or neutrons as a target nucleus is changed to a product. Reactions that result in a change in the number of protons are desirable because the product is a different element, facilitating chemical separation from the target. This contrasts with a (n,γ) reaction (neutron capture), in which the product and target are isotopes of the same chemical element (Bailey et al. 2014).

The probability that a nuclear reaction will occur is often expressed in terms of the reaction cross-section, also called the excitation function. The concept may also be applied to other interactions, such as scattering. The cross-section is the effective area presented by a target nucleus to an incident particle; it is usually denoted by the symbol σ. The SI unit for σ is m^2, although the traditional and more commonly used unit is the barn ($1b=10^{-28}m^2$) or millibarn ($1mb = 10^{-31}m^2$). The cross-section depends on the target nucleus, the type of incident particle and the energy of the incident particle. Cross-section values determine the activity of a desired product radionuclide that may be generated in a reactor or cyclotron, and the activities of other unwanted radionuclides that are produced as impurities or contaminants. Irradiation conditions need to be optimised to maximise the former and minimise the latter.

Neutrons can penetrate target nuclei even at very low (thermal) energies, while charged particles need high kinetic energy to overcome the Coulomb barrier in order to achieve nuclear penetration. Figure 3-1 shows the general behaviour of the nuclear reaction cross-section as a function of incident particle energy for both protons and neutrons.

Because protons have to overcome the Coulomb barrier, there is an energy threshold below which reactions do not occur; such a threshold does not exist for neutrons (Bailey et al. 2014).

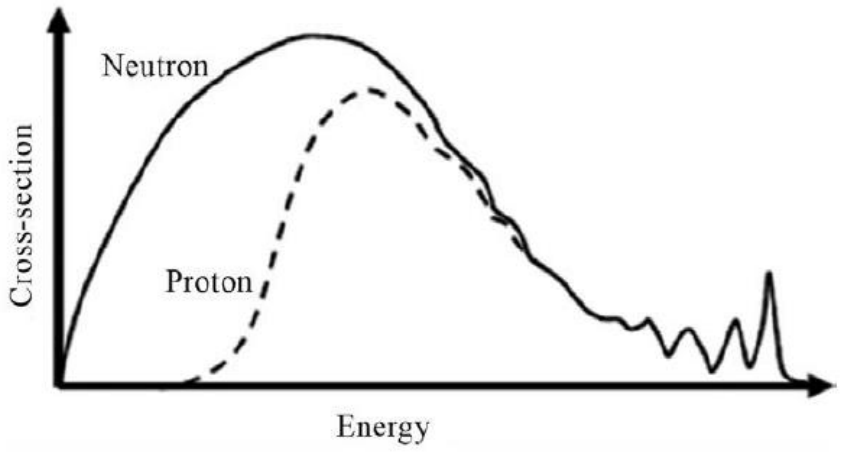

Figure 3-1: General behaviour of the nuclear reaction cross-section as a function of incident particle energy for protons and neutrons (Bailey et al. 2014)

3.2.1 Activation Rates

The activity produced when a sample is irradiated in a particle beam depends on the intensity of the particle beam, the number of target nuclei in the sample, and the reaction (or activation) cross-section i.e. the probability that a bombarding particle will interact with a target nucleus.

Suppose that a sample of a nuclide containing n target nuclei per unit volume (cm^{-3}), each having an activation cross-section σ (cm^2), is irradiated in a beam having a particle flux rate ϕ ($cm^{-2}\,s^{-1}$) (Figure 3-2). Assume that the thickness Δx (cm) of the sample is sufficiently small such that ϕ does not change much as the beam passes through it (Cherry et al. 2012).

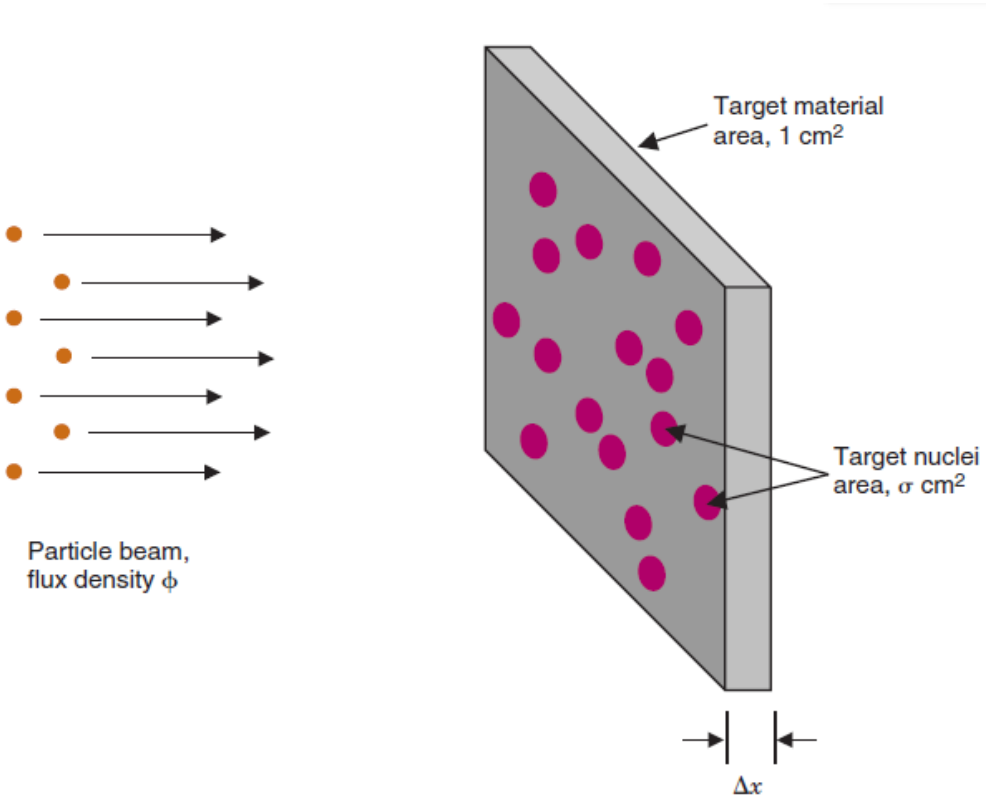

Figure 3-2: Activation targets in a particle beam (Cherry et al. 2012)

The number of targets per unit area (cm^{-2}) of the particle beam is $n\Delta x$ and they present a total target area $n\sigma\Delta x$ per unit area of the beam. Therefore, the fractional reduction of beam flux rate after passing through the target thickness Δx is given by:

$$\Delta\phi/\phi = n\sigma\Delta x \qquad (3\text{-}1)$$

The number of particles removed from the beam (i.e. the number of nuclei activated) per unit area of the beam area per unit time ($cm^{-2}\,s^{-1}$) is given by:

$$\Delta\phi = n\sigma\phi\Delta x \qquad (3\text{-}2)$$

Each atom of the target material has mass $W/(6.023\times10^{23})$ (g), where W is the atomic weight of the material and 6.023×10^{23} is Avogadro's number. Therefore, the total mass m of target material per unit area of the beam is:

$$m = n\Delta x W/(6.023\times10^{23}) \qquad (3\text{-}3)$$

Thus, the activation rate R per unit mass ($g^{-1}s^{-1}$) of target material is given by:

$$\mathbf{R = \Delta\phi/m} \qquad \textbf{(3-4)}$$

$$\mathbf{R} = \frac{(\mathbf{6.023\times10^{23}})\times\boldsymbol{\sigma}\times\boldsymbol{\phi}}{\boldsymbol{W}} \qquad \textbf{(3-5)}$$

The activation rate (Equation 3-5) can be used to calculate the rate at which target nuclei are activated in a particle beam per gram of target material in the beam, provided that the particle flux rate and the reaction cross-section are known (Cherry et al. 2012). The derivation assumes that the target nuclide is 100% abundant in the irradiated sample. If this is not the case, R is decreased by percentage abundance of the relevant isotope.

In practice, the activation rate is often less than that predicted by Equation 3-5 because there is significant attenuation of the particle beam as it passes through a relatively thick target material. Thus, some parts of the target are irradiated by a reduced flux rate. Furthermore, particles lose energy when traversing a thick target and this leads to a change in the activation cross-section.

3.3 Reactor-produced radionuclides

3.3.1 Reactor Principles

Figure 3-3 shows a schematic representation of a nuclear reactor. The core (fuel cells) of the reactor contains a quantity of fissionable material, normally natural uranium (^{235}U and ^{238}U) enriched in ^{235}U content. Uranium-235 undergoes spontaneous fission ($t_{1/2}$ ~7 $\times 10^8$years), splitting into two lighter nuclear fragments with roughly equal masses and emitting two or three high energy neutrons in the process (Figure 3-4) (Cherry et al. 2012).

The fuel cells are surrounded by a moderator material. The purpose of the moderator is to slow down the rather energetic fission neutrons. The resulting slow neutrons (also named thermal neutrons) are more efficient initiators of additional fission processes.

The most commonly used moderators are heavy water and graphite. Control rods are used to either expose or shield the fuel cells from each another. Both the fuel cells and control rods are carefully located to establish the critical conditions for a controlled chain reaction (Cherry et al. 2012).

In the nuclear research reactor, the objective is to arrange for the neutrons emitted in each spontaneous or stimulated fission process to initiate, on average, one additional fission, thus establishing a controlled nuclear chain reaction (Cherry et al. 2012).

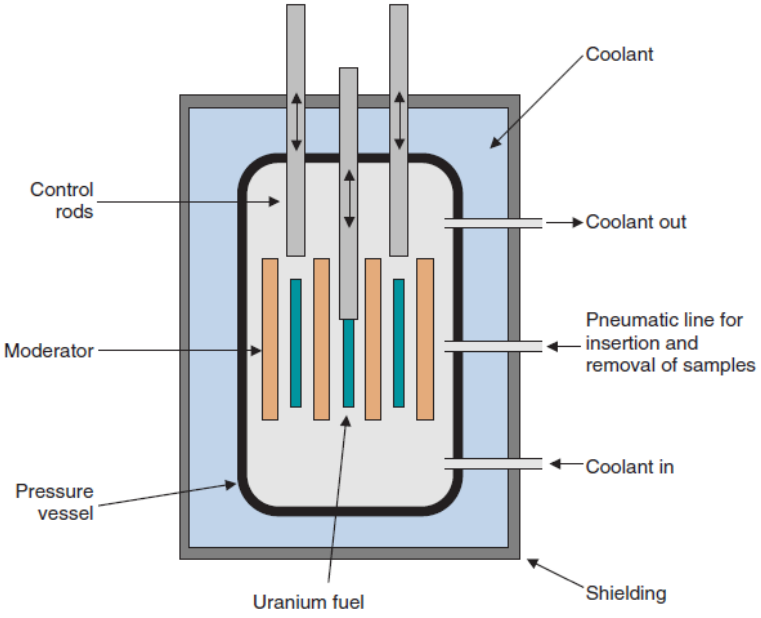

Figure 3-3: Schematic representation of a nuclear reactor core (Cherry et al. 2012)

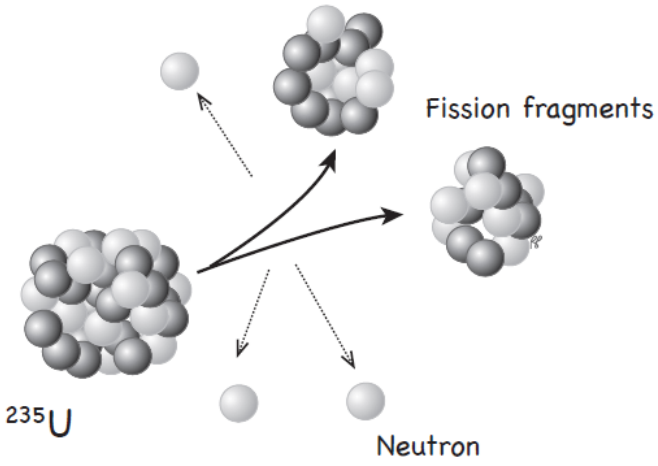

Figure 3-4: Fission process of the nucleus of ^{235}U (Powsner et al. 2013)

3.3.2 Fission Fragments

The fission process that occurs in a reactor can result in useful quantities of medically important radionuclides such as ^{99}Mo, the radionuclide used in a generator for producing ^{99m}Tc. ^{99}Mo is normally produced by the fission of ^{236}U which, in turn, splits into two fragments (Figure 3-5).

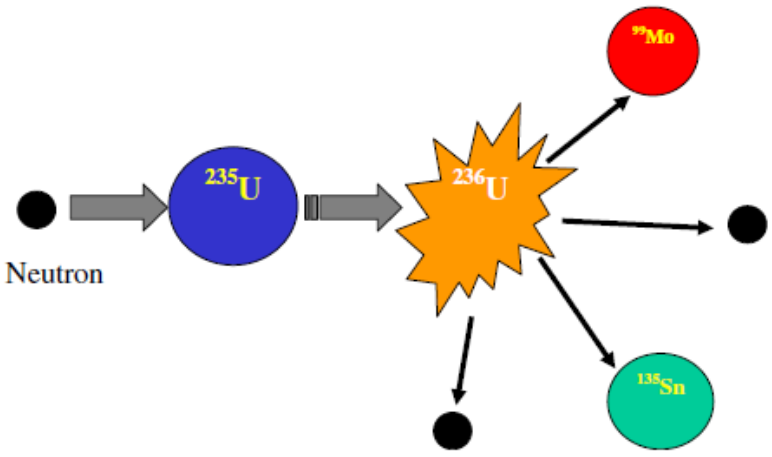

Figure 3-5: Schematic diagram of the fission process following neutron capture by ^{235}U to ^{236}U (Ruth 2009)

The fission products are always neutron-rich radionuclides and thus undergo radioactive decay by β^- emission, until a stable nuclide is produced. If one of the radioactive intermediates has an appropriately long half-life, it can be extracted from the fission products and utilised as a medical radionuclide. For example, ^{99}Mo ($t_{1/2} \approx 66$ hrs) plays a crucial role in producing technetium-99m, which is the most common radionuclide used in nuclear medicine procedures (Powsner et al. 2013):

$$^{99}_{39}\mathrm{Y} \xrightarrow{\beta^-(1.5\,\mathrm{s})} {}^{99}_{40}\mathrm{Zr} \xrightarrow{\beta^-(21\,\mathrm{s})} {}^{99}_{41}\mathrm{Nb} \xrightarrow{\beta^-(15\,\mathrm{s})} {}^{99}_{42}\mathrm{Mo}$$

Radionuclides produced by fission may be obtained carrier free, which means that no stable isotope of the element of interest is produced alongside. Therefore, the radionuclides can be produced with high specific activity (Cherry et al. 2012).

3.3.3 Neutron Activation

Neutrons have no net electrical charge. Therefore, they are neither attracted nor repelled by nuclei by Coulomb interaction. When neutrons (e.g. from a nuclear reactor core) hit a target material, nuclei of the target atoms capture some of the neutrons. As a result, a stable target nucleus may be converted into a radioactive nucleus. Such an event is called neutron activation. Two types of such reactions commonly occur (Cherry et al. 2012).

In the first reaction (n,γ), a target nucleus ($^{A}_{Z}X$) captures a neutron and is converted into a product ($^{A+1}_{Z}X$), which is formed in an excited state. The nucleus of this product immediately undergoes de-excitation to its ground state by emitting a prompt γ ray. The schematic representation of this reaction is as follows:

$$^{A}_{Z}X(n,\gamma)^{A+1}_{Z}X$$

The nuclei of the target and the product of this reaction are different isotopes of the same chemical element.

A second type of neutron activation is the (n,p) reaction. In this reaction, the nucleus of the target nuclide captures a neutron and promptly ejects a proton. This reaction is represented as follows:

$$^{A}_{Z}X(n,p)_{Z-1}{}^{A}X$$

In this reaction, the nuclei of the target and the product do not represent the same chemical element. This means that chemical separation is possible and the radioactive product is carrier-free i.e. does not contain a stable isotopes of the same element.

The (n,γ) reaction is the more common mode and the products of this reaction are not carrier free because isotopes of the same element cannot be separated chemically. The radionuclides produced by neutron activation tend to decay by β^- emission as neutrons are added to the nucleus of the target material and, in β^- decay, a neutron changes into proton.

3.4 Accelerator-produced radionuclides

3.4.1 Charged-Particle Accelerators

As its name suggests, a charged particle accelerator is used to accelerate electrically charged particles, such as protons, α particles ($^{4}_{2}He$ nuclei) and deuterons ($^{2}_{1}H$ nuclei), to a very high energy. Irradiating a target material with these particles may cause nuclear reactions that result in the formation of radionuclides. However, a major difference is that the particles must have very high energies, normally between 10 and 20 MeV, to exceed the repulsive Coulomb forces of the nucleus.

There are two common types of nuclear reaction that produce radionuclides using a charged-particle accelerator. The first one is a (p,n) reaction in which the nucleus of the target captures a proton and promptly emits a neutron. This reaction is represented as follows:

$$^{A}_{Z}X(p,n)_{Z+1}{}^{A}X$$

This reaction can be considered to be the opposite of the (n,p) reaction that is induced by neutrons as the irradiating particle in a reactor.

A second common reaction is the (d,n) reaction. In this reaction, the nucleus of the target material captures an accelerated deuteron (d) and immediately releases a neutron.

This results in a change of both the atomic number and the mass number. This reaction is represented as follows:

$$ {}^{A}_{Z}X(d,n)^{A+1}_{Z+1}X $$

Various types of device have been used to accelerate charged particles; these include Van de Graaff accelerators, linear accelerators and cyclotrons. The cyclotron is the most commonly used form of particle accelerator for the production of medically important radionuclides.

3.4.2 Cyclotron Principles

The first cyclotron to be used specifically for medical applications was installed at Washington University in St. Louis in 1941; radioactive isotopes of phosphorus, iron, arsenic and sulphur were produced (Mahmood and Jones 2002).

A cyclotron consists of two hollow halves of a closed cylinder (called dees due to their shape) placed between the poles of a large electromagnet (Figure 3-6). The dees are separated from each other by a narrow gap. The charged particles are generated by an ion source (normally an electrical arc device in a gas) that is positioned near the centre of the dees. All these components are placed in a vacuum tank (Cherry et al. 2012; Powsner et al. 2013).

During cyclotron operation, particles are generated by the ion source in bursts and a high frequency alternating voltage is applied across the dees; this is generated by a high-frequency oscillator (typically operating at 30 kV, 25-30 MHz). After the injection of the charged particles into the gap between the dees, they are accelerated directly toward one of the dees by the electrical field generated by the applied voltage. Inside the dee there is no electrical field, but as the particles are in a magnetic field, they move in a circular path around to the opposite side of the dee.

Each time the charged particles pass through the gap, they gain energy. Thus the orbital radius increases at each pass and the charged particles follow an outwardly spiralling path. When the particles acquire sufficient kinetic energy and reach the maximum orbital radius, they are directed and deflected onto a target material placed directly in the orbiting beam path (Cherry et al. 2012; Powsner et al. 2013).

Cyclotron-produced radionuclides tend to decay by either EC or $\beta+$ emission as a positive charge is added to the nucleus of the target material in the activation process. Furthermore, addition of positive charge to the nucleus of the target atom changes its atomic number. Thus, products generated using a cyclotron are usually carrier free because chemical separation is possible (Cherry et al. 2012).

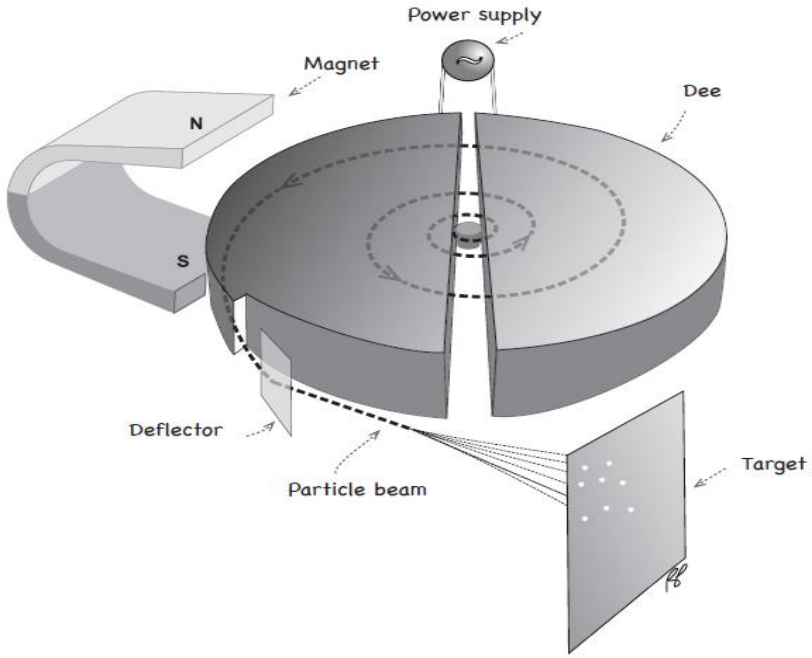

Figure 3-6: Internal parts of cyclotron (Powsner et al. 2013)

A cyclotron may be used to produce many radionuclides of clinical importance (Figure 3-7), including short-lived positron emitters such as ^{11}C ($t_{1/2}$ = 20.4 min), ^{13}N ($t_{1/2}$ = 9.97 min), and ^{15}O ($t_{1/2}$ = 2.03 min), that are of special interest in PET. These radionuclides are important constituents of biological substances, and they can be used to label a wide range of biologically relevant tracers. These particular positron-emitting radionuclides must be prepared on site with a specified biomedical cyclotron due to their very short lifetimes (Cherry et al. 2012).

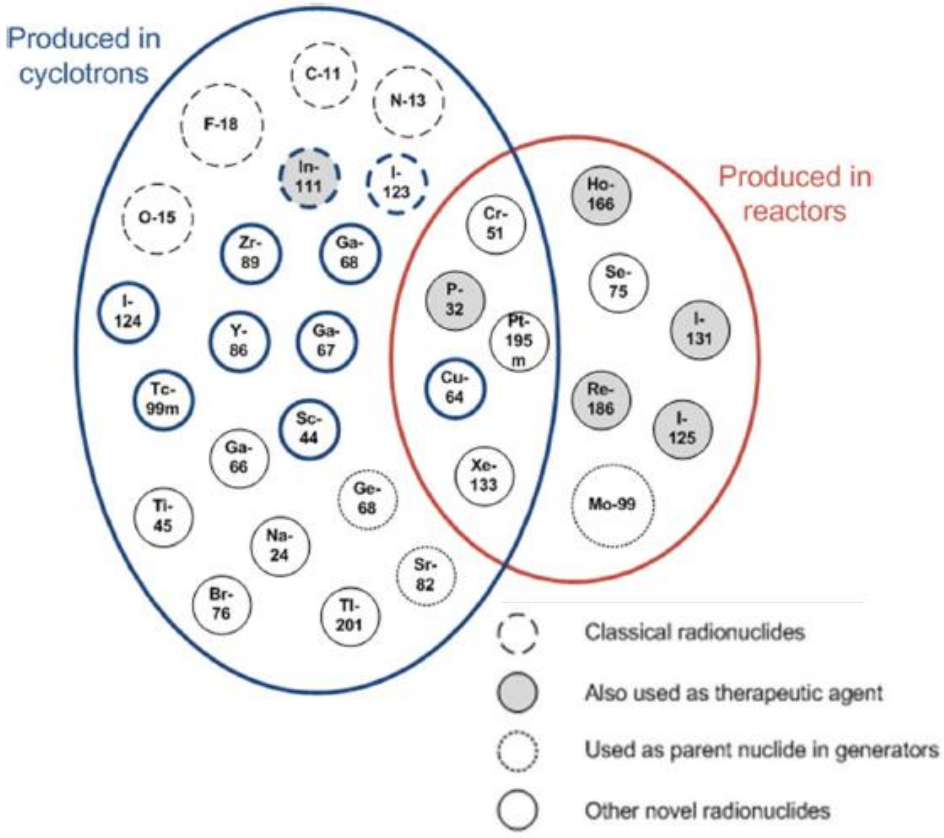

Figure 3-7: Radionuclides used in nuclear medicine diagnostics (Synowiecki et al. 2018)

3.4.2.1 Energy degradation in a cyclotron

Most cyclotrons deliver charged particles at a fixed kinetic energy, but this may not be optimal in that the cross-section for the desired reaction may be relatively small giving a low yield of the required radionuclide. In addition, cross-sections for competing reactions that produce radionuclidic impurities may be unacceptably large. In practice, the approach is to procure a cyclotron that operates at an energy greater than that required for production of the desired range of radionuclides and to reduce or degrade the particle energy to optimise the production of each one. This energy degradation is achieved by passing the particle beam through a thin metallic foil (the degrader).

The mechanisms of charged particle energy degradation have already been described; they comprise elastic and inelastic interactions with atomic electrons and nuclei (section 3.2). For a particular type and energy of particle, the energy loss is determined by the composition and thickness of the foil. It is related to the stopping power of the foil

material; this is the energy loss per unit path length of the particles in the material. It is collisional loss (due to ionisation and excitation) that tends to dominate and the collisional stopping power depends on the velocity and electric charge of the particles and the electron density of the material through which they travel (Anderson 1984). Nuclear reactions may also take place in the foil leading to its activation; this creates additional radioactive waste and an additional radiation hazard when the irradiated target is processed.

At typical energies used for radioisotope production, a particle will undergo more than a million collisions before it comes to rest. Because if the statistical nature of these interactions, the exact type and number of collisions and the exact path of an individual particle are not predictable. This means that charged particles having the same initial energy do not travel the same distance through the absorbing material. There is a distribution of ranges centred on the mean value and this phenomenon is known as straggling. Similarly, particles that are initially monoenergetic have a range of kinetic energies after traversing a particular thickness of material such as a degrader foil (IAEA 2012). Thus, the use of energy degraders to optimise radionuclide production presents significant challenges.

If the target material is solid, the energy degradation foil is placed in the beam path in front of the target within the vacuum tank of the cyclotron. Liquid and gaseous target materials must be contained in a suitable target vessel with a thin foil entrance window through which the particles must pass in order to interact with the target. The entrance foil may also act as the energy degrader or this function may be performed by another foil placed in front of the window. As the target absorbs particle energy, its temperature increases; in the case of liquid and gaseous target materials, the pressure also increases. Window foils must be thick enough to withstand high temperature and pressure without excessive attenuation and energy degradation of the particle beam (IAEA 2012).

Window and energy degradation foils may be made from a range of materials including metallic elements such as aluminium, niobium and titanium and Havar, a non-magnetic cobalt-based alloy. Desirable properties of foil materials include low chemical reactivity, high tensile strength and high melting point (IAEA 2012). Details of the foils used for the cyclotron-produced radionuclides investigated as part of the work for this thesis are given in Chapters 7 and 8.

3.5 Radionuclide generators

A radionuclide generator is a closed system consisting of an apparatus that contains a parent-daughter radionuclide pair, for which the half-life of the parent is much longer than the half-life of the daughter. It allows for separation and extraction of the daughter from the parent; the daughter product can be extracted repeatedly.

A radionuclide generator can be used to produce various radionuclides that are of interest in nuclear medicine. The most important and common generator is the ^{99}Mo-^{99m}Tc system, due to the widespread use of ^{99m}Tc for radionuclide imaging. There are alternative methods of producing ^{99m}Tc (Table 3-2), but the generator is the most common one.

Table 3-2: ^{99m}Tc production methods (Synowiecki et al. 2018)

Reaction	Method	Currently available	Status and further development
$^{235}U(n,f)^{99}Mo \rightarrow ^{99m}Tc$	Reactor + generator	Worldwide	Well-established, availability will shrink with closure of some nuclear research reactors
$^{100}Mo(p,2n)^{99m}Tc$	Small medical or intermediate cyclotron	In Canada	Possible worldwide implementation with decreasing nuclear reactor capacity
$^{96}Zr(\alpha,n)^{99}Mo \rightarrow ^{99m}Tc$	α beam cyclotron + generator	No	Will not be implemented, method not competitive, α-beam required, low yields
$^{100}Mo(\gamma,n)^{99}Mo \rightarrow ^{99m}Tc$	Linear accelerator +generator	No	Under development in Canada, USA and the Netherlands
$^{98}Mo(n,\gamma)^{99}Mo \rightarrow ^{99m}Tc$	Reactor + generator	In USA and Japan	Auxiliary method used in nuclear reactors, will shrink with closure of some nuclear research reactors
$^{100}Mo(p,2n)^{99m}Tc$	Laser (simulation study (Bychenkov et al. 2014))	No	Theoretically feasible. Further research required

3.5.1 Production of molybdenum-99

The original method of producing ^{99}Mo involved by the irradiation of metallic molybdenum or molybdenum trioxide Mo_2O_3 (natural or enriched with ^{98}Mo) by thermal neutrons in a nuclear reactor. The cost of the target material is high. In addition, activation of metallic impurities existing in the target material results in the production of radionuclidic impurities. However, this neutron activation method has some advantages:

1. Post-irradiation processing is minimal
2. Radionuclidic contamination is limited by the purity of the target material.
3. The quantity of radioactive waste is small

The disadvantage of this method is the low specific activity of ^{99}Mo ($<3.7\times10^{11}$ Bq/g). This is why ^{99}Mo is now generated by the fission of uranium-235 as this method gives significantly higher specific activity ($>3.7\times10^{14}$ Bq/g). In this case, uranium-235 is bombarded with thermal neutrons in a nuclear reactor and ^{99}Mo is separated from the fission products. The reaction may be represented as follows (Thrall et al. 2001; Zolle 2007):

$$\text{U-235 (n-fission)} \longrightarrow \text{Mo-99}$$

indicating neutron irradiation causing fission. This method has some disadvantages: the post-irradiation processing facilities are expensive and costly, it requires chemical separation of β emitters and highly toxic α emitters and large quantities of long-lived radioactive waste material is produced.

3.5.2 Design of the generator

The generator is a closed system in which chemically purified ^{99}Mo obtained from the fission reaction is incorporated onto an alumina (Al_2O_3) anion exchange column (Figure 3-8). The pH within the column is normally adjusted to an acid level to enhance the binding ability. The loaded column is placed in container made of lead to provide radiation shielding. Tubes are attached to both ends of the column to allow it to be eluted or “miked” with saline (sodium chloride solution) to remove ^{99m}Tc but leave ^{99}Mo (in

the form of MoO_4^{-2}) firmly attached to the aluminium oxide (Thrall et al. 2001; Zolle 2007; Jones et al. 2013).

^{99m}Tc is finally produced as a sodium pertechnetate solution ($Na^{99m}TcO_4$), and this the starting point for a wide range of ^{99m}Tc radiopharmaceuticals. However, in this solution ^{99m}Tc exists in the most stable oxidation state, and it does not directly bind to biological molecules or ligands (compounds that form complexes by binding to other metals). Therefore, in the production of radiopharmaceuticals, it is important to use reducing agents to form ^{99m}Tc with lower oxidation states (Sampson 1994; Saha 2010; Eckelman 2009).

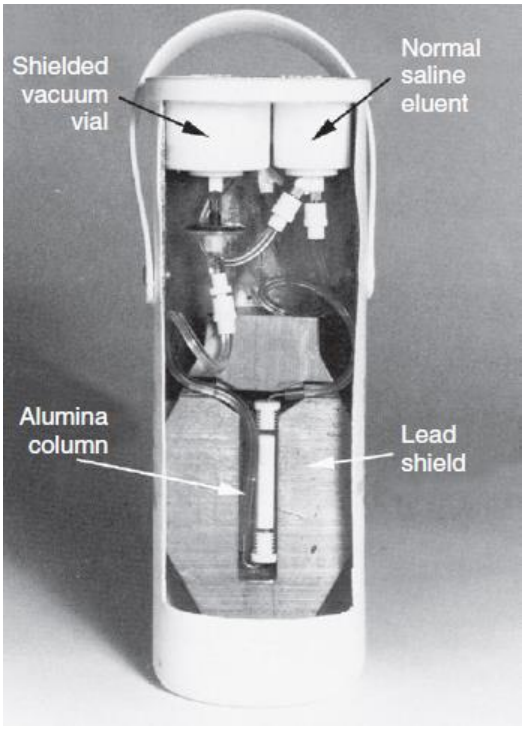

Figure 3-8: Cut-away view of a $^{99}Mo/^{99m}Tc$ generator (Cherry et al. 2012)

3.5.3 Activity decay and growth in a $^{99}Mo/^{99m}Tc$ generator

The variation in activity of the ^{99}Mo and ^{99m}Tc pair is an example of transient equilibrium (Figure 3-9). This happens when the half-life of the parent radionuclide for example ^{99}Mo ($t_{1/2}$ = 66 hr)) is longer (nearly 10 times) than that of the daughter (^{99m}Tc ($t_{1/2}$ = 6 hr)) but is not "infinite". In this case, and when the branching ratio (B.R.) is equal to 1, the activity of the daughter product (A_d) increases due to the decay of its parent reaches a maximum value, eventually exceeds the activity of the parent

radionuclide (A_p) and then decreases and follows the decay of the parent. The parent and daughter radionuclides are said to be in transient equilibrium when this stage of "parallel" decay rates occurs. According to Bateman equation, the activity of the parent and the daughter radionuclides is as follows:

$$A_p(t) = A_p(0)\, e^{-\lambda_p t} \tag{3-6}$$

$$A_d(t) = \left\{\left[A_p(0)\, \frac{\lambda_d}{\lambda_d - \lambda_p} \times \left(e^{-\lambda_p t} - e^{-\lambda_d t}\right) \times B.R.\right]\right\} + A_d(0)\, e^{-\lambda_d t} \tag{3-7}$$

where, λ_p and λ_d are the decay constants for parent and daughter radionuclides, respectively. In spite of the fact that the activities of both parent and daughter are decreasing, the ratio of parent-to-daughter activity remains constant. The ratio of daughter-to-parent activity in transient equilibrium (Cherry et al. 2012) is given by:

$$A_d/A_p = [t_p/(t_p - t_d)] \times B.R. \tag{3-8}$$

where t_p and t_d are the half-lives of parent and daughter respectively. The time at which maximum daughter activity is available is given by:

$$T_{max} = [1.44 t_p t_d /(t_p - t_d)] \ln(t_p / t_d) \tag{3-9}$$

In the case of ^{99m}Tc, the activity reaches its maximum after approximately four half-lives (23 hrs) and as the branching ratio is not equal to 1, the time-activity curve for this radionuclide is somewhat lower than that in Figure 3-9. Not all of the parent ^{99}Mo atoms decay to ^{99m}Tc (Figure 3-10), but only a fraction (B.R. = 0.876) (Cherry et al. 2012).

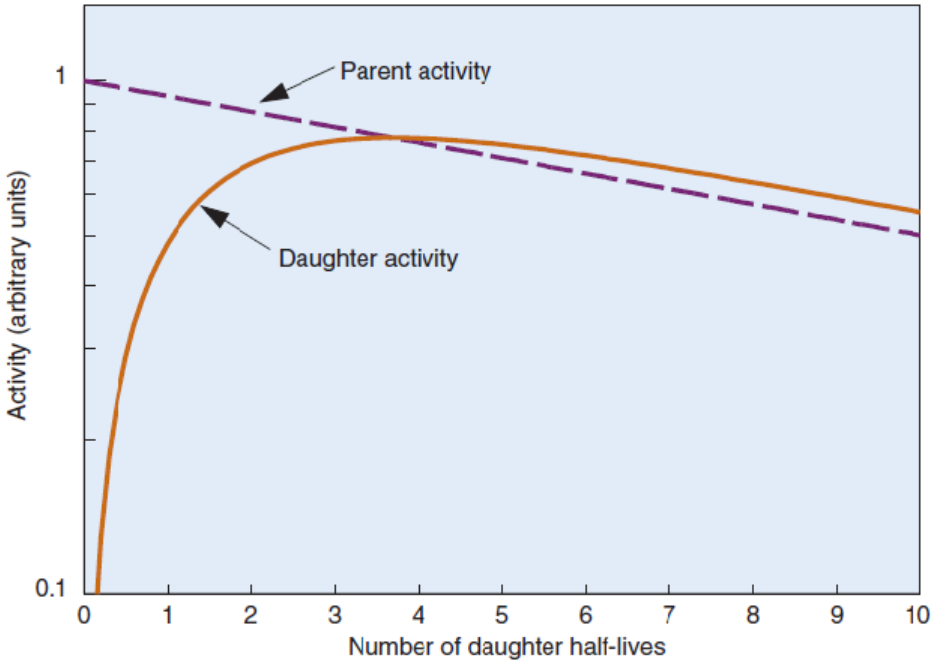

Figure 3-9: Decay and build-up of activity for parent radionuclide with half-life of t_p and daughter radionuclide with half-life of t_d respectively, for $t_p = 10\ t_d$ (Cherry et al. 2012)

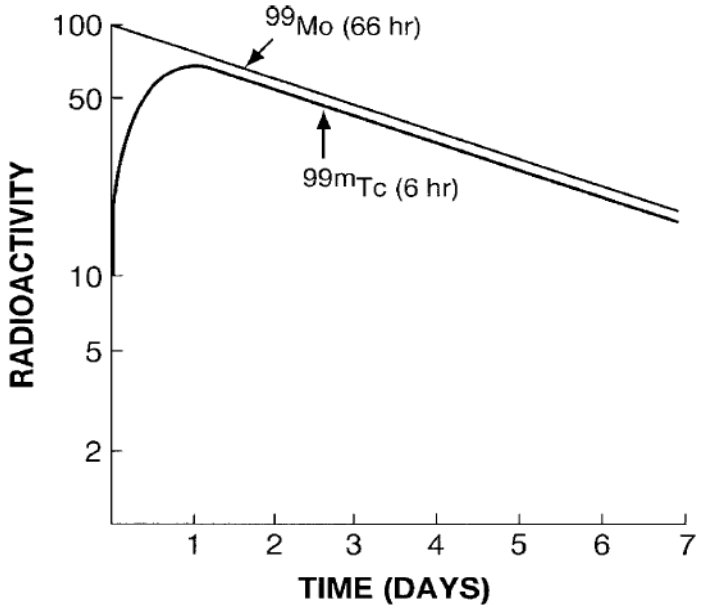

Figure 3-10: Plot of logarithm of ^{99}Mo and ^{99m}Tc activities versus time demonstrating transient equilibrium (Saha 2010)

3.5.4 The generator eluate

The $^{99}Mo/^{99m}Tc$ generator normally provides ^{99m}Tc eluate on daily basis. The eluate should be clear, colourless and contain the radionuclide in the form of a simple salt. Typically, the eluate should contain no radionuclide impurities and should be sterile and pyrogen free. However, in some cases, ^{99}Mo may be extracted with ^{99m}Tc from the column during the elution process; thus is called ^{99}Mo breakthrough. The contamination of ^{99}Mo is limited by the European Pharmacopeia to 0.1% of the total eluate activity. This contamination may be ascribed to imperfections in the generator production or to the possible occurrence of some mechanical defects within it (Dantas et al. 2005; Momennezhad et al. 2010).

The existence of ^{99}Mo in the eluate has many disadvantages. For example, it will administer an undesirable and unnecessary radiation dose to patients. This high dose is due to the beta particle emission and higher energies of the emitted γ-photons. Moreover, the occurrence of the ^{99}Mo within the eluate has a detrimental effect on radionuclide image quality and on the ^{99m}Tc spectrum. This is generally the case for any impurity possessing a gamma energy higher than that of the main radionuclide (Dantas et al. 2005; Momennezhad et al. 2010).

Therefore, performing quality control is vital in order to ensure the radionuclide purity of the eluate. Vials with excessive ^{99}Mo contamination must be discarded (Momennezhad et al. 2010).

3.6 The production of radionuclidic impurities

The purity requirements of a radionuclide product are specified by its eventual use. If the radionuclide is intended to be used for industrial applications, the requirements would not be very strict. On the other hand, when a radio-labelled product is prepared for use in the human body, high standards of purity have to be maintained (Shivarudrappa and Vimalnath 2005).

To produce the main radionuclide with a high radionuclidic purity, is necessary to reduce radiocontaminants. Radionuclidic and other impurities (such as radiochemical impurities) may be reduced by proper choice of post irradiation radiochemical and purification methods, using techniques such as dissolution, precipitation, distillation,

solvent extraction, ion-exchange chromatography, electrochemical oxidation reduction, etc. The impurity limitations of the desired radionuclide for use in nuclear medicine applications are very strict.

^{131}I is an important radionuclide that is used extensively in the diagnosis and treatment of thyroid disorders, including thyroid cancer. ^{131}I is produced by neutron irradiation of natural tellurium metal in a nuclear reactor (see chapter 6). ^{131}I is produced by neutron activation of the natural ^{130}Te isotope. Activation of other Te isotopes, such as ^{126}Te and ^{128}Te, would result in the formation of the stable ^{127}I and long-lived ^{129}I ($t_{1/2}$=1.57×10^7 years) isotopes. The presence of iodine impurities in ^{131}I produced and would result in post manufacture handling and safe disposal problems (Shivarudrappa and Vimalnath 2005).

Another example of radioactive impurities in the main radionuclide is the formation of ^{145}Sm, ^{151}Sm, ^{153}Sm and ^{155}Sm radioisotopes along with the production of ^{153}Sm. The radioisotope ^{153}Sm is used in nuclear medicine applications for palliative treatment of bone pain in metastatic bone cancer patients. ^{153}Sm is usually produced by irradiation of a natural or enriched Sm_2O_3 target in a reactor. Natural Sm_2O_3 consists of several isotopes of Sm, which result in the formation of the previously mentioned radiocontaminants along with the production of ^{153}Sm. The radioactive decay of ^{155}Sm eventually leads to the formation of ^{155}Eu radionuclidic impurity (Shivarudrappa and Vimalnath 2005).

Waiting a suitable time after irradiation for short-lived impurities to decay can be one way to reduce the radioactive contamination, but using an appropriate high purity target for the production of radionuclides of interest is the usual practice (Shivarudrappa and Vimalnath 2005). However, it is not always possible to eliminate radionuclidic impurities even with the highest isotopic enrichment and the most precise particle energy selection. In such cases, all that can be done is to choose an irradiation energy with which the production of the radioactive contaminant is near a minimum. An example of this is the production of ^{124}I impurity along with ^{123}I as a main radionuclide (Schlyer et al. 2009).

Examples of competing reactions that produce impurities along with the desired radionuclides are shown in Table 3-3.

Table 3-3: Desired radionuclides and impurities produced by competing reactions (Mahmood and Jones 2002)

Product radionuclide, half-life	Nuclear reaction	Competing reactions for impurities	Impurity half-life
^{48}V, 16 d	^{48}Ti(p, n)	^{49}Ti(p, n)^{49}V	337 d
	^{47}Ti(d, n)	^{48}Ti(d, n)^{49}V	337 d
^{55}Fe, 2.73 y	^{55}Mn(p,n)	^{55}Mn(p,pn) ^{54}Mn	312 d
^{55}Co, 17.5 h	^{56}Fe(p,2n)	^{56}Fe(p,n)^{56}Co	77.3 d
^{62}Zn, 9.2 h	^{63}Cu(p,2n)	^{65}Cu(p,n)^{65}Zn	244 d
		^{65}Cu(p,pn)^{64}Cu	12.7 h
^{123}I, 13 h	^{124}Te(p,2n)	^{124}Te(p,n)^{124}I	4.2 d
^{89}Zr, 3 d	^{89}Y(p,n)	^{89}Y(p,2n) ^{88}Zr	83 d

3.7 Radiopharmaceuticals

A radiopharmaceutical is a combination of a pharmaceutical with a suitable radionuclide produced in a particular way. In order for a radiotracer (radiopharmaceutical) to be ideal and safe for use in humans, it must satisfy quality standards that include the following (Hendee et al. 2005; Thrall et al. 2001; Ruth 2009):

- Readily available at a low cost.

- A pure gamma emitter for diagnostic applications, that is no α and β emissions as such particles contribute radiation dose to the patient while not giving any diagnostic information. However, beta-emitting radionuclides are appropriate for therapeutic purposes.

- Have a short effective half-life so that it is eliminated from the body as quickly as possible. However, it should be long enough to allow the investigation to be performed.

- Have a high target to non-target ratio so that the resulting image has a high contrast, while the background does not blur the image.

- Possess proper metabolic activity in that it follows or is trapped by the metabolic process of interest.

- Have chemical stability *in vitro* for storage before use and *in vivo* so that the radionuclide is not dissociated from the pharmaceutical once it is inside the human body.

- Should be sterile and free from micro-organisms (pyrogens) that can cause fevers.

The safety of radiopharmaceuticals is also determined by the following criteria (Cherry et al. 2012):

- Radionuclidic purity, which is the fraction of the total radioactivity in a sample that is in the form of the specified radionuclide. As mentioned earlier, radionuclidic contaminants arise in the production of radionuclides and can be significant in some situations. They may increase the radiation dose to the patient or increase the detector dead time, and thus they may result in incorrect counting rate or pixel intensities in images. Of concern in radionuclide generator systems is contamination with the long-lived parent radionuclides, such as the existence of ^{99}Mo in ^{99m}Tc eluate.

- Radiochemical purity, which is the fraction of the radioactivity in the sample that is present in the required chemical form. Radiochemical impurities usually arise from competing chemical reactions in the radiolabelling process or from decomposition of the sample. Radiochemical impurities are problematic as they reduce the efficacy of diagnostic investigations. The distribution of such impurities in the body generally differs from that of the main radiopharmaceutical and thus adds a background to the image.

The time course of the radiopharmaceutical in the body must also be considered. Some radiopharmaceuticals have rapid uptake (by the target organ) and clearance (from the body), whereas others circulate in blood with only slow uptake. The rate of clearance of the radiopharmaceutical is characterised by the biological half-life (t_b). This has nothing to do with radioactivity, but it reflects the time taken for half of the radiopharmaceutical to be excreted by an organ or the body. The biological half-life,

together with the physical half-life ($t_{1/2}$)of the radionuclide, determine a quantity called the effective half-life (t_e), this is the time required for one-half of the initial radioactivity to disappear from an organ or the whole body both by excretion and by physical decay. The effective half-life is always shorter than either the physical or the biological half-life and is calculated using the formula (Cherry et al. 2012; Powsner et al. 2013):

$$\frac{1}{t_e} = \frac{1}{t_b} + \frac{1}{t_{1/2}}$$

3.8 Labelling Strategies

The use of compounds labelled with radionuclides has grown considerably in medical, biochemical and related fields due to very active research in radiochemistry and radiopharmaceutical preparation. There are two distinct techniques for labelling small molecules with radionuclides. In direct substitution, a stable atom in the molecule is replaced with a radioactive atom of the same element. The compound has exactly the same biological characteristics as the unlabelled compound. This gives the opportunity for many compounds of biological relevance to be labelled and studied *in vivo* utilising radioactive isotopes of elements that are widely found in nature (e.g. carbon, hydrogen, nitrogen and oxygen). An example is replacing a ^{12}C atom in glucose with a ^{11}C atom to create ^{11}C-glucose. This radiopharmaceutical will distribute and metabolise in the body exactly in the same way as unlabelled glucose (Cherry et al. 2012).

The second approach is to create analogues. This involves modifying the original compound to simplify the analysis of a biologic system. Analogues allow the use of radioactive isotopes of elements (e.g. fluorine and iodine) that are not so widely available in nature but that otherwise have beneficial imaging characteristics. Analogues also allow chemists to beneficially modify the biological characteristics of a molecule by changing the rates of uptake, clearance or metabolism. For example, replacing the hydroxyl (OH) group on the second carbon in glucose with ^{18}F ($t_{1/2}$≈110 min) results in FDG, an analogue of glucose. This has the advantage of putting a longer-lived radioactive tag onto glucose compared with ^{11}C ($t_{1/2}$≈20 min). Of even greater importance is the fact that FDG undergoes only the first step in the metabolic pathway for glucose, thus making data analysis much more straightforward. FDG is now a widely used radiopharmaceutical for measuring glucose metabolism. The disadvantage of

analogues is that they behave differently from the original compounds, and these differences need to be carefully understood if the analogue is used to provide a measure of the biological function of the native molecule (Cherry et al. 2012).

An alternative way to label materials (that is possible only for larger biomolecules) is to keep the radioactive label away from the biologically active site of the molecule. Thus large molecules (e.g. antibodies, peptides and proteins) may be labelled with many different radionuclides, with minimal effect on their biological properties (Cherry et al. 2012).

Chapter 4

HPGe Detector Construction, Operation and Characterisation

4.1 Introduction

High-purity germanium (HPGe) detectors are important instruments in high-resolution gamma spectroscopy and they are one of the most widely used tools in radiation detection research .Applications of gamma-ray spectroscopy rely on the stability of the efficiency of detectors over the duration of the experiment.

This chapter describes the construction, operation and characterisation of a semiconductor detector based on a HPGe crystal with particular emphasis on the absolute detection efficiency as a function of energy. The detection efficiency is regarded as one of the most important properties of any radiation measurement instrument. High detection efficiency is desirable to give the greatest possible count rate for a given amount of radioactivity.

4.2 Construction and operation a HPGe detector

The operational principle of a HPGe detector is a reverse-biased semiconductor diode (Figure 4-1). When the incoming radiation interacts with the semiconductor crystal, it generates electron-hole pairs. The released charges are collected by electrodes at the surface of the crystal. The number of electron-hole pairs created, and hence the magnitude of the output charge pulse, is proportional to the amount of energy deposited in the detector by the radiation (Sandi 2013).

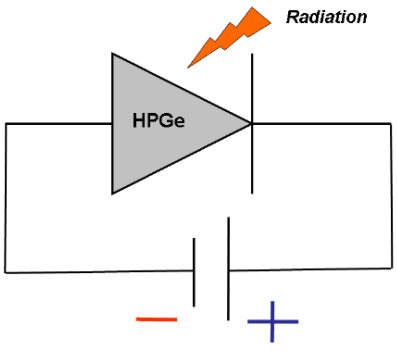

Figure 4-1: Representation of a reverse-biased semiconductor diode (Sandi 2013)

HPGe detectors are made of either N-type or P-type material, often in the form of a hollow cylinder (coaxial configuration). The type of material determines how the contacts are applied (Figure 4-2). For N-type material, a thick lithium contact is placed

on the inside surface (the N+ contact) and a thin, ion-implanted contact (the P+ contact) is placed on the outer surface. For P-type material, the contacts are reversed (Twomey 2003; Sandi 2013).

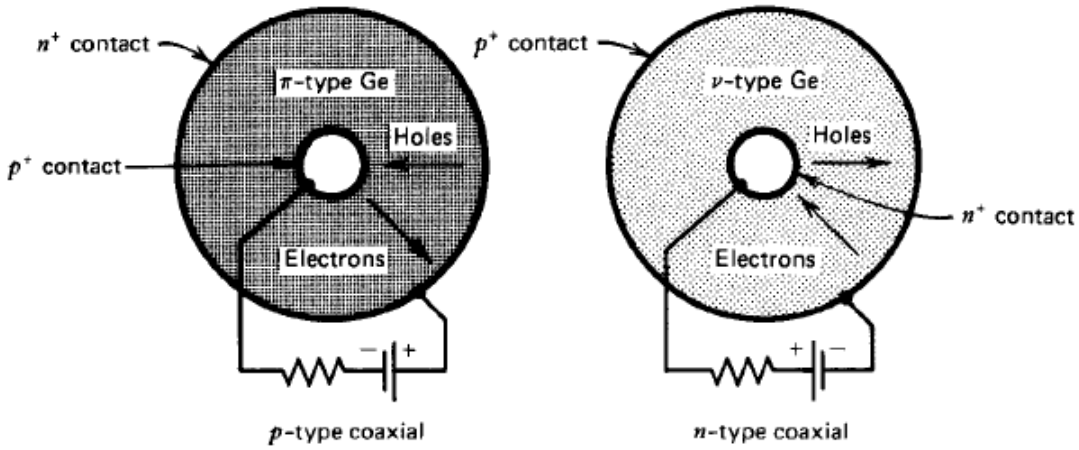

Figure 4-2: Coaxial N-type and P-type HPGe detector with the corresponding electrodes (Knoll 2010)

HPGe detectors have excellent energy resolution, which is attributed to the small value of the forbidden energy gap (0.7 eV). Thus HPGe detectors are highly desirable for detecting and identifying complex gamma ray spectra that include many photopeaks. This good resolution gives HPGe detectors a superior ability to identify discrete peaks of weak radioactive sources that may be superimposed on the noise of the spectral continuum. Such peaks would remain unresolved with a scintillation detector (

Figure **4-3**) (Knoll 2010).

The energy resolution is related to the temperature of the material. The resolution deteriorates if the temperature of the HPGe detector is high. This results in a decreased forbidden energy gap and a corresponding increased thermal noise and leakage current (Sandi 2013).

At sufficiently low temperature (usually that of liquid nitrogen), the thermal generation of intrinsic carriers (electrons and holes) in the germanium crystal becomes negligible, the forbidden energy gap is optimised and the leakage current decreases to the low value that is required for superior performance. Given that, it is crucial to keep the germanium crystal cooled at liquid nitrogen temperature, although alternatives using electrical cooling systems are also commercially available (Sandi 2013).

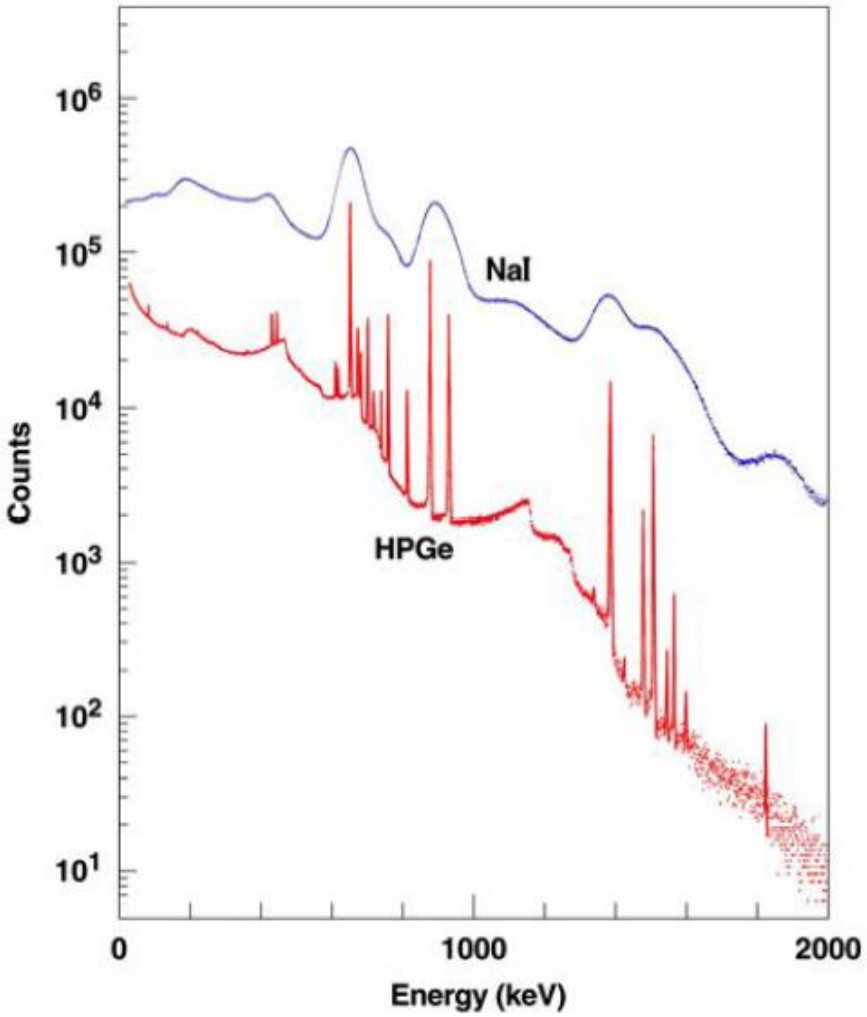

Figure 4-3: Energy resolution difference between HPGe detector and NaI (T1) detector (Nelson et al. 2009)

The germanium crystal is encased in a vacuum-tight cryostat (Figure 4-4) to reduce thermal conduction between the crystal and the surroundings and to decrease the possible contamination of internal components due to impurity gases. The cryostat is typically mounted on a liquid nitrogen Dewar vessel, in which the cryostat is cooled by thermal conductivity through a thermal finger in contact with the liquid nitrogen (Sandi 2013; Byun 2017).

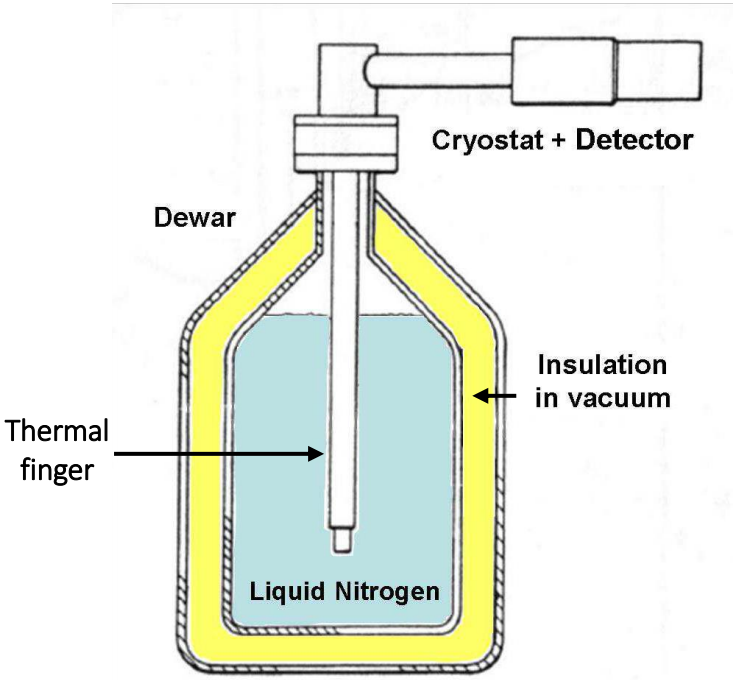

Figure 4-4: Coupling between cryostat, thermal finger and liquid nitrogen (Sandi 2013)

All the cryostat materials around the detector should be made of low Z materials to reduce the probability of photon scatter. Thus materials such as magnesium, beryllium and Teflon are used whenever possible (Byun 2017).

4.3 HPGe detector at the University Hospital of Wales

In this thesis, a special type of HPGe detector named LO-AX was used because of its availability. It was provided by ORTEC (Wokingham, England). ORTEC HPGe detectors have different names depending on the type of material used. The ORTEC name for a detector based on P-type material is GEM, whereas that for a detector based on N-type material is GMX. Very short N-type coaxial detectors are named LO-AX.

Figure 4-5 illustrates the two N-type detectors: LO-AX and GMX (Twomey 2003). P-type detectors (GEM) are most commonly used in counting laboratories. However, N-type coaxial (GMX) and LO-AX detectors work better at low photon energies because the efficiency is greater due to a thin electrode contact. They have slightly worse energy resolution at higher energies than GEM detectors (Twomey 2003).

In this study, a LO-AX detector with model number 70495/30-S and serial number 35-N30961B was used (Figure 4-6). Its germanium crystal had a diameter of 70.6 mm and a height of 29.5 mm. The detector had a thin entrance window made of beryllium with a thickness of 0.5mm. It was covered with two plastic caps: the original cap supplied by the manufacturer and another made by the workshop of the University Hospital of Wales to improve detector protection.

The LO-AX detector was surrounded by lead shield with a thickness of about 10 cm. An additional 0.1 cm thick shield of copper, covering the detector inside the lead shield, was added to reduce the intensity of the characteristic x-rays produced by the lead shield.

During the course of this study, the LO-AX detector was broken for the period April-June 2017. The liquid nitrogen had been allowed to evaporate and so the detector came to room temperature. This resulted in a loss of vacuum and a high leakage current. All the experimental work descried in this thesis was done with the detector after repair.

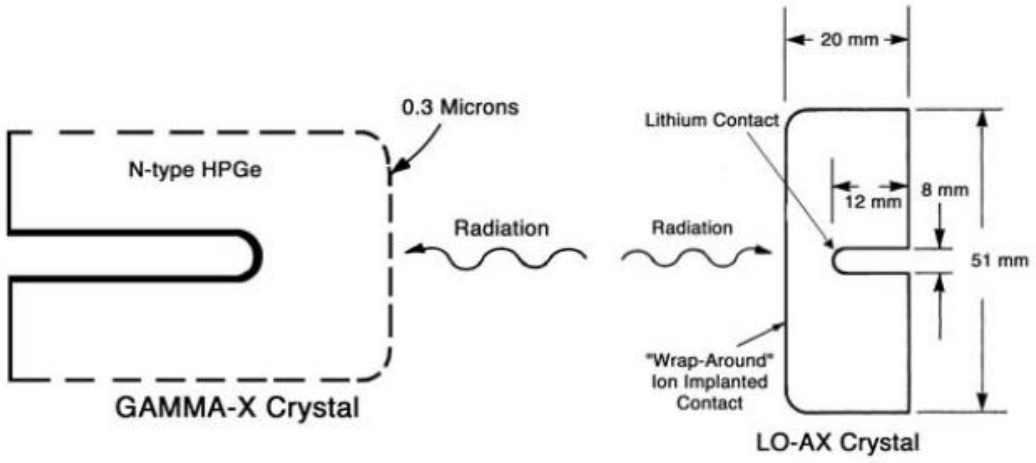

Figure 4-5: Typical ORTEC N-type HPGe crystal geometries: GMX (left) and LO-AX (right) (Twomey 2003)

Figure 4-6: HPGe detector at University Hospital of Wales showing the Dewar and shielding

4.4 Electronic components of the LO-AX HPGe detector

4.4.1 Preamplifier

Inside the cryostat, almost touching the detector, there was a charge-sensitive preamplifier (model 237N by Ortec). A low value capacitor was put just at the output of the detector in order to reduce the noise. This device resists very low temperatures without creating noise or deforming the signal. Thus, the system is able to maintain proportionality between the total collected charge in the detector and the output voltage (Sandi 2013).

4.4.2 Amplifier

The amplifier used with the detector was a Nuclear Instrumentation Module (NIM) model 2022 provided by Canberra (Farnborough, England). This has a 6-step shaping time selector (0.5, 1, 2, 4, 8 and 12 μs), a 6-step coarse gain selector (with factors of 10, 30, 100, 300, 1 k, 300 k) and a continuous fine gain selector (with factors from 0.3-1.3).

4.4.3 HV supply

The high voltage bias was provided by a Canberra NIM model 3106D, which is designed for semiconductor detector operation. It is particularly well suited for use with high resolution detector systems. The 3106D device accommodates all types of detectors requiring up to 6 kV bias voltage and up to 300 μA current. The output voltage is adjustable from ±30 V dc to ±6000 V dc. For detectors requiring a low voltage, a secondary output is available with a range of ±3 V to ±600 V. A three-digit volt meter measures and displays the output voltage with a resolution of 10 V on the normal output and 1 V on the secondary output. The Model 3106D has the ability to withstand any overload or short circuit condition for an indefinite period of time. For remote shut down, an inhibit input is available. The unit can be programmed by an internal jumper either to restart normal operation after fault removal or to require a manual reset (Canberra 2007).A high voltage of 4000 V was used in this work.

4.4.4 MCA

The ADC was a Canberra model 8701. This is a 100 MHz Wilkinson type ADC, designed to offer 8192 channels of resolution. It provides front panel, multi-turn, screwdriver adjustable potentiometers for the control of the low level discriminator, the high level discriminator, as well as the ADC zero. Its excellent linearity improves peak shape and resolution, thus improving the overall performance of the spectroscopy system. Gain, range and digital offset controls allow optimal use of limited MCA memory by choosing only a specific energy range of interest (Canberra 1997).

On the MCA, an energy range of 0-2 MeV and 4096 channels were used for the pulse height spectra acquired in this work.

4.5 Energy calibration

Energy calibration is used to derive a linear relationship between the amount of energy transferred to the detector *E* (keV) and the MCA channel number x. The calibration equation can be expressed as follows:

$$E = m\,x + c \qquad (4\text{-}1)$$

where m is the gradient (keV/channel) and c is the intercept of the straight line.

Energy calibration is normally performed before measurement, and it allows the gamma-ray spectrum to be interpreted in terms of energy rather than channel number or voltage (pulse height).

The electronic modules of a HPGe detector are not absolutely stable under all conditions due to temperature variations, and hence a slight drift of m and c values occurs with time. Therefore, frequent energy calibration is required. Energy calibration of the Lo-AX detector was performed on each day of use.

4.5.1 Method

Three standard energy calibration sources were used. These were ^{133}Ba (81 keV, 276 keV, 302 keV, 356 keV, 384 keV), ^{137}Cs (662 keV) and ^{60}Co (1173 and 1332 keV). These sources were placed together at a distance of 8 cm from the HPGe detector in order to give a suitable dead time loss.

A spectrum was acquired for a time of 1200 s, which gave at least 10,000 counts in the centroid channel of five of the gamma photopeaks. A high count reduces the fractional error (coefficient of variation) associated with the measurement, resulting in a smaller percentage uncertainty. The coefficient of variation is defined as:

$$Coefficient\ of\ variation\ (CoV)\ (\%) = \frac{\boldsymbol{standard\ deviation}}{\boldsymbol{total\ number\ of\ recorded\ counts}}\ 100\% \qquad (4\text{-}1)$$

Thus, if the total number of counts recorded is 10,000, the CoV will be reduced to just 1%.

4.5.2 Results

The relationship between energy and MCA channel number is essentially linear and a typical graph for the HPGe detector with all eight gamma photopeaks and a best-fit straight line drawn through the data points is shown in Figure 4-7. This line can be used to determine the energy of photons that are responsible for unknown photopeaks in the spectrum, such as those due to radionuclidic impurities in medical radionuclides.

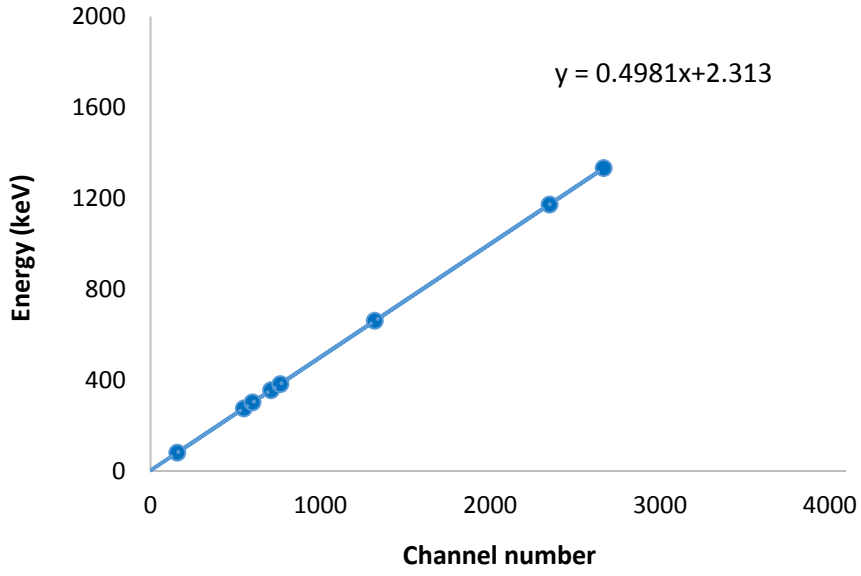

Figure 4-7: Typical energy calibration for the HPGe detector using three sources of known gamma energies

4.6 Back ground spectrum

All radiation detectors produce a background signal, the magnitude and variability of which depends on the size and type of the detector and the extent of the shielding around it. Various sources of natural radiation contribute to the background; these include (Elessawi 2010):

- Natural radioactivity (e.g radionuclides of potassium and thorium) in the component materials of the detector

- Natural radioactivity in the shielding, which is placed around the detector to minimise the background radiation from terrestrial radiation and cosmic rays.

- Natural radioactivity in the walls of the room in which the detector is located and other structures within that room

- Natural radioactivity in ambient air. The important sources are radon (^{222}Rn) and thoron (^{220}Rn) because of the presence of the radioactive gases.

The background spectrum for the HPGe detector in this study was acquired (Figure 4-8) using a vial of tap water under standard conditions (Schott vial and a volume of 4 ml). The acquisition live time was 1 hour. The gamma peak at 511 keV is the annihilation radiation peak. The net count of this peak is 34.

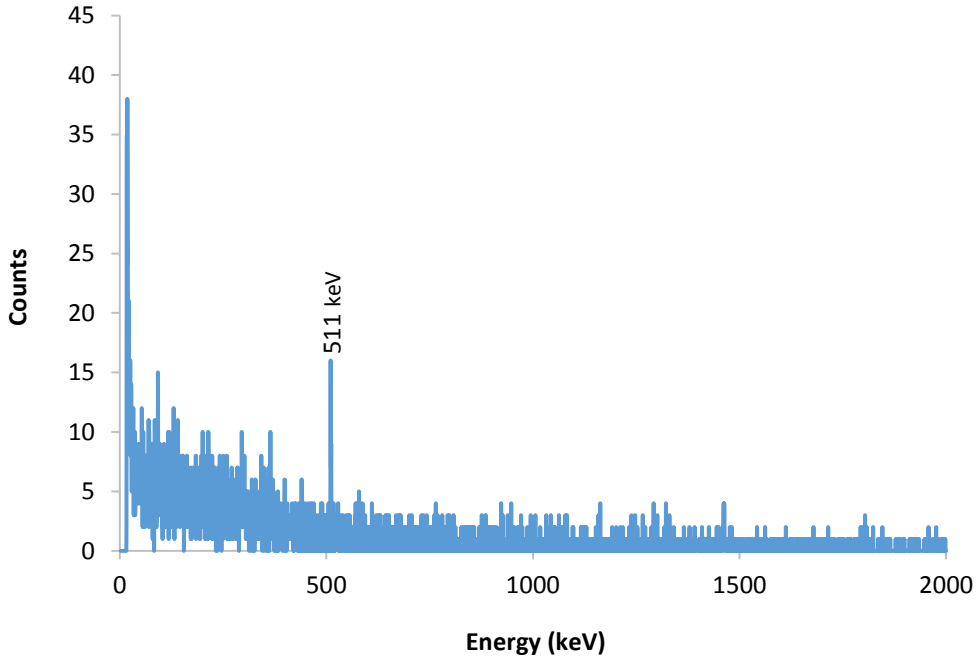

Figure 4-8: Background spectrum for the HPGe detector with an acquisition live time of 1 hour

4.7 Peak area and count rate calculation

Analysis of the recorded spectra to find photopeaks was done using the automatic peak-search routine implemented in the CANBERRA Genie-2000 software package. All peaks that exceeded a user defined sensitivity threshold were regarded as true gamma photopeaks. The sensitivity threshold is the number of standard deviations above

background that a feature must have for it to be regarded as a real peak. In this work, the threshold was set at 3. This meant that and if the average background in a special region was 10 000 counts, any feature with a magnitude less than 300 counts would be ignored. In this way, statistical fluctuations of the background continuum were rejected from the list of identified peaks.

A Gaussian curve was fitted to each identified photopeak using a non-linear least-squares method. The gross peak area was determined and the background continuum under the peak was automatically subtracted to give the net area (net counts). The net counts were divided by the live time to give the net count rate (NCR). The NCR was corrected to the beginning of the measurement period to account for decay of the radionuclide during counting; this was done using the following equation:

$$NCR_0 = \frac{\lambda C}{(1-e^{-\lambda t})} \qquad (4\text{-}2)$$

where NCR_o is the count rate at the beginning of the measurement, C is the net counts accumulated in the photopeak, λ is the decay constant and t is the acquisition live time (Nir-El 2013).

4.8 HPGe detector stability

For a detection system to be stable, the count-rate for a given radionuclide source should not vary with time of the measurement after correction for radioactive decay. A ^{137}Cs sealed source in the Medical Physics Department at the University Hospital of Wales was used in investigate the count-rate stability of HPGe detector.

4.8.1 Method

The source was used over two periods of time (before and after detector repair) from 2016 to 2018 to check the stability of HPGe detector. Before detector repair, measurements were made between November 2016 and March 2017, while after repair, the stability was checked from June 2017 to October 2018.

The source was placed at the centre of the detector cap. Spectra were acquired with a live time of 300 s on each occasion. Count-rates were determined for the photopeak using the automatic peak area facility and net count rates were corrected for radioactive

decay to the time of first measurement before repair. Linear regression analysis was used to investigate the variation of corrected count-rate with time.

4.8.2 Results

Figure 4-9 shows the variation of decay corrected net count-rate with time expressed as number of weeks. The blue regression line shows the HPGe stability before repair, whereas the red regression line shows the HPGe stability after repair.

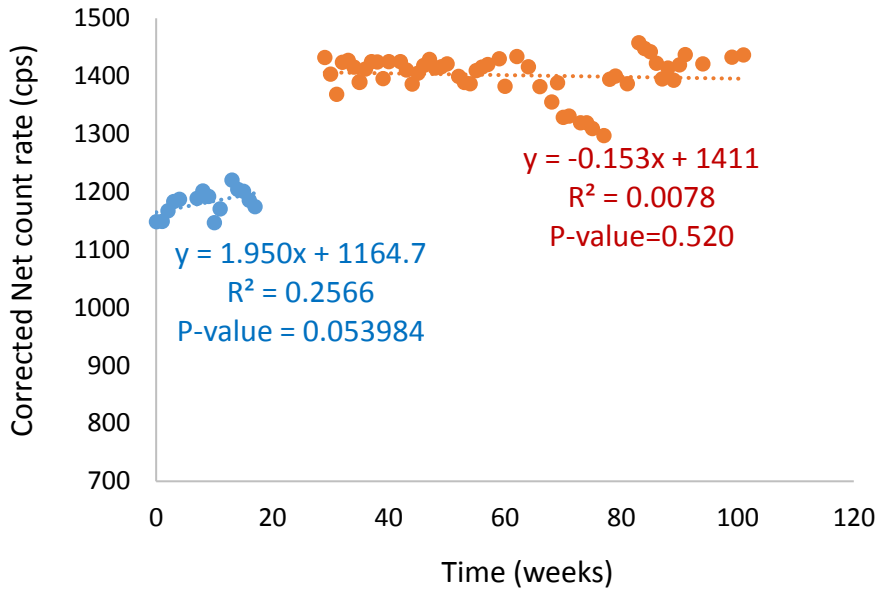

Figure 4-9: Stability of ^{137}Cs source count-rate for HPGe detector over two periods of time

4.8.3 Conclusion

Linear regression analysis of the relationship between net count-rate and time showed that the detector was stable (P>0.05) before and after repair. However before repair the count-rate shows an increasing trend with time. Furthermore, the sensitivity (count-rate per unit activity) of the detector increased following repair.

4.9 HPGe detection efficiency

Calculating HPGe detector efficiency is very important in this study in order to quantify the activity of the radionuclidic impurities (using equation (2-17)) that are produced along with the desired radionuclides.

4.9.1 Method

A set of seven gamma sources (Table 4-1) was used to estimate the absolute efficiency of the HPGe detector. Some of these sources were prepared 'in house' (^{125}I, ^{99m}Tc, ^{123}I, ^{131}I and ^{137}Cs) while the ^{54}Mn and ^{65}Zn sources were bought from a specialist supplier (Eckert & Ziegler Isotope Products, California). Each of these sources was separately prepared as an aqueous solution in a Schott vial with a volume of 4 ml adopted as a standard. One sample was prepared for each source, except ^{131}I for which two samples were prepared as a precaution. The in house sources were prepared from diluted stock solutions and their activities were determined using the Fidelis secondary standard calibrator, while the ^{54}Mn and ^{65}Zn sources were undiluted and their activities were calculated according to the data sheets provided with them.

Table 4-1: Gamma sources used to estimate the absolute efficiency of HPGe detector

Gamma source	Energy (keV)
^{125}I	35
^{99m}Tc	140
^{123}I	159
^{131}I	80, 284 and 364
^{137}Cs	662
^{54}Mn	834
^{65}Zn	511 and 1115

The activity of these samples ranged from 0.9 kBq to 12 kBq, which gave an acceptable dead time (less than 3%).

Each gamma source was individually positioned at the centre of the detector and a spectrum was acquired. This step was repeated 10 times for each radionuclide (except ^{131}I, for 25 experiments were done). At least 10,000 counts were acquired within each photopeak in the spectra of the efficiency calibration sources.

The stability of HPGe detector was tested for each photopeak of each source over the period of measurement. Linear regression analysis was used to investigate the variation

of sensitivity (NCR/activity) with time after correction for radioactive decay. In addition, the half-lives of some radionuclides were determined by plotting the logarithm of the count-rate against time over the period of the experiment without correction for radioactive decay.

Finally, the HPGe detector efficiency was calculated according to equation (2-17) using the mean net count-rate (after correction for both radioactive decay during counting time and decay over the 10 measurements).

4.9.2 Results

Figure 4-10 to Figure 4-22 show the sensitivity of the HPGe detector versus time for the seven radionuclides ^{125}I, ^{131}I, ^{99m}Tc, ^{123}I, ^{65}Zn, ^{137}Cs and ^{54}Mn respectively, while Figure 4-23 and Figure 4-24 demonstrate the determination of the half-lives of ^{99m}Tc, ^{123}I and ^{131}I.

A log-log plot was used to describe the variation of efficiency over the entire energy range. On this plot, the efficiency data were separated into two regions: low energy and high energy. In order to yield a stable mathematical solution free of oscillations, the low energy interval was fitted with a quadratic expression and the high energy interval with a linear function. The counting efficiency values for the seven sources are summarised in Table 4-2. The log-log of efficiency vs. energy is shown in Figure 4-25.

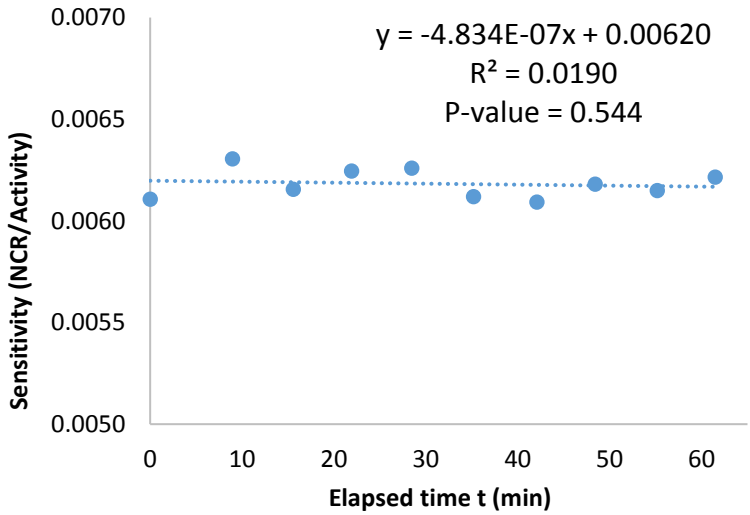

Figure 4-10: Sensitivity of HPGe detector with elapsed time for ^{125}I

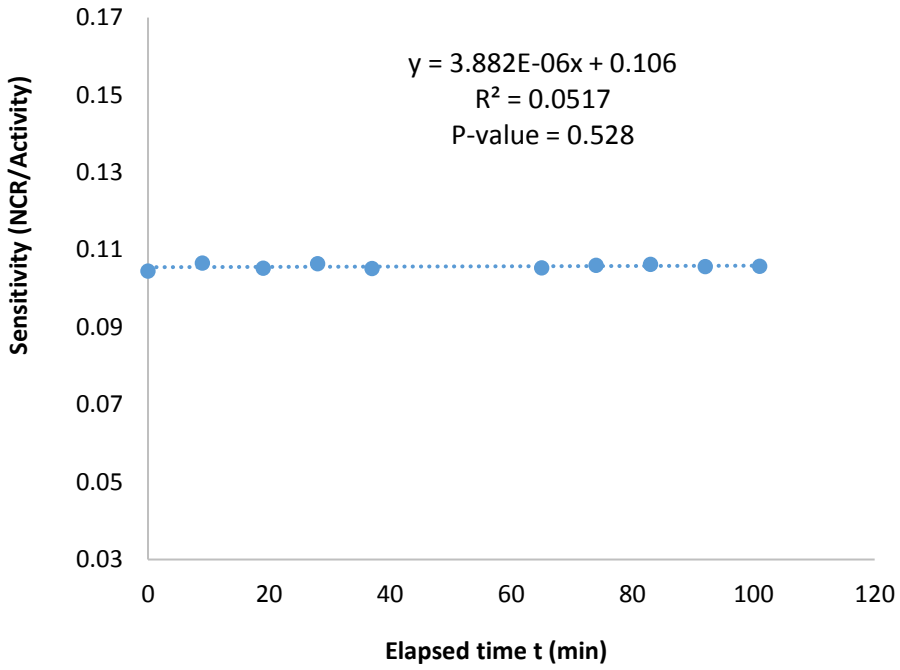

Figure 4-11: Sensitivity of HPGe detector with elapsed time for ^{99m}Tc

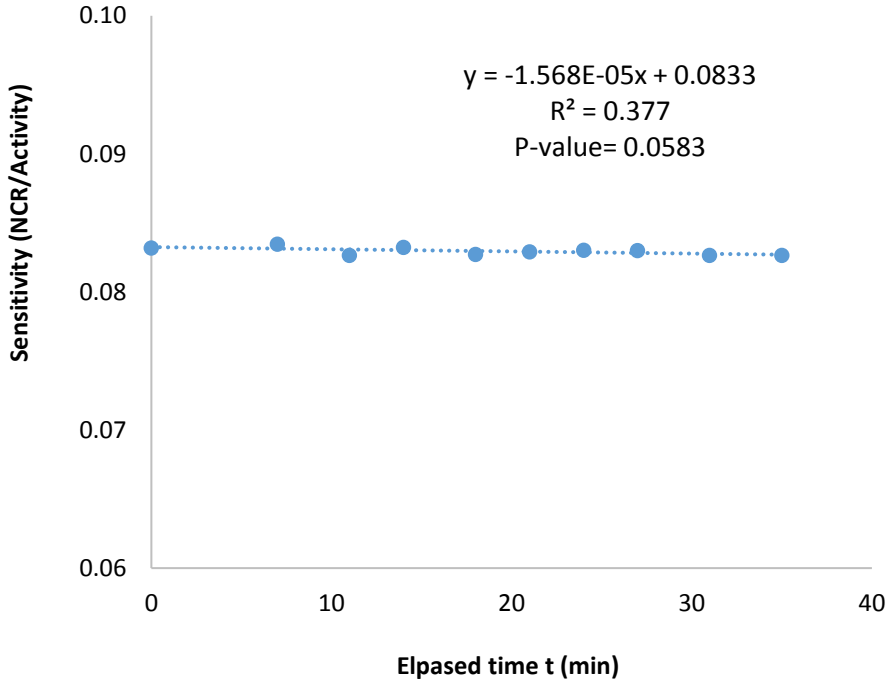

Figure 4-12: Sensitivity of HPGe detector with elapsed time for ^{123}I

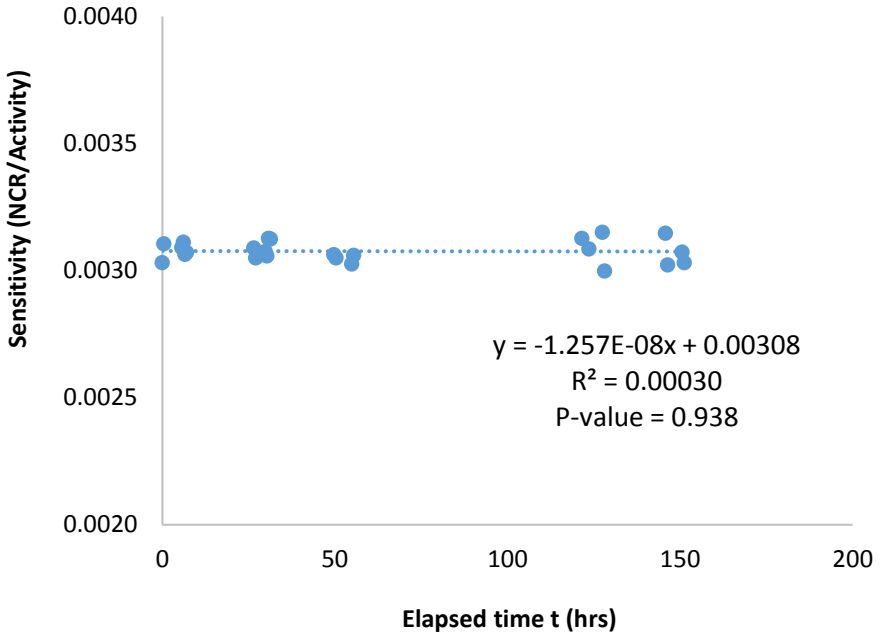

Figure 4-13: Sensitivity of HPGe detector with elapsed time for the 1st vial of ^{131}I (81 keV)

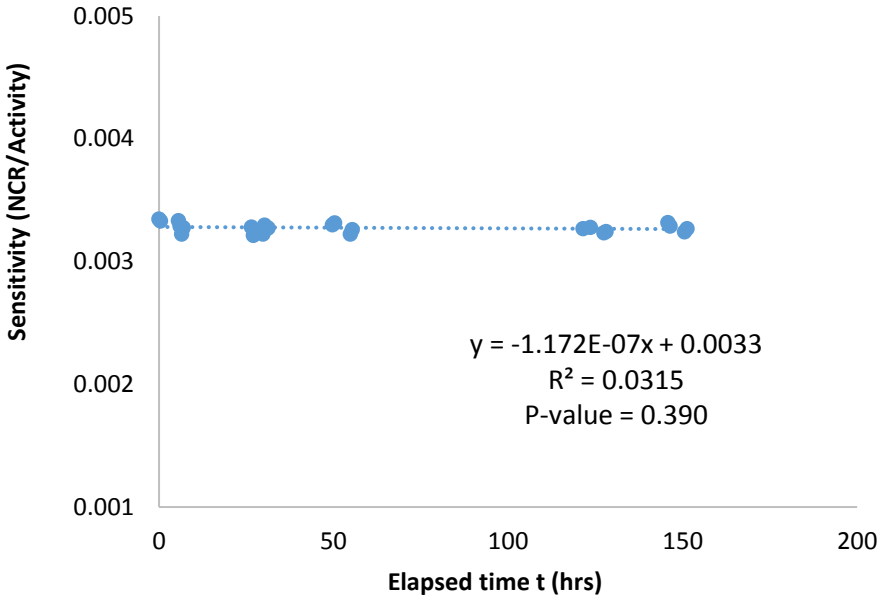

Figure 4-14: Sensitivity of HPGe detector with elapsed time for the 1st vial of ^{131}I (248 keV)

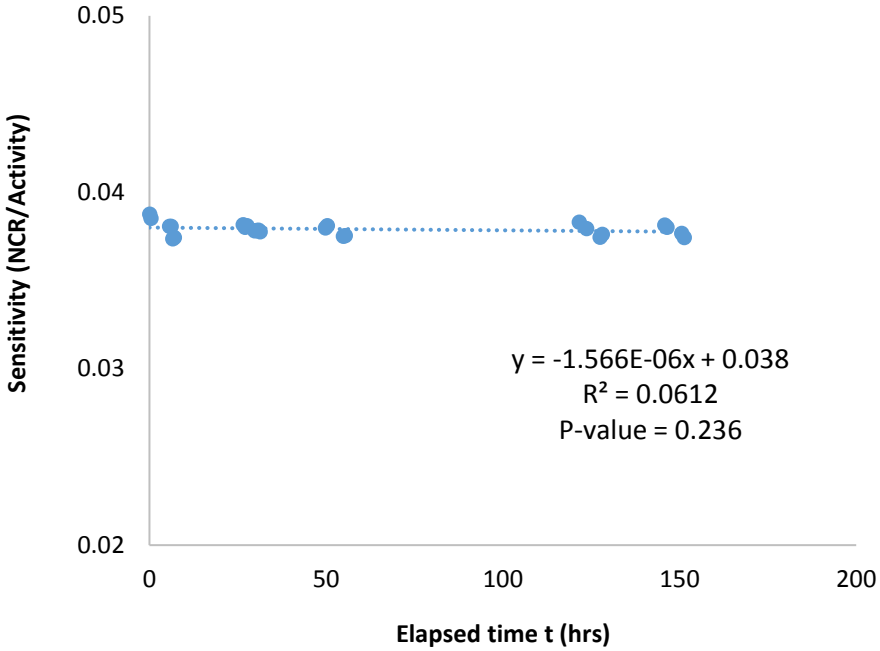

Figure 4-15: Sensitivity of HPGe detector with elapsed time for the 1st vial of ^{131}I (364 keV)

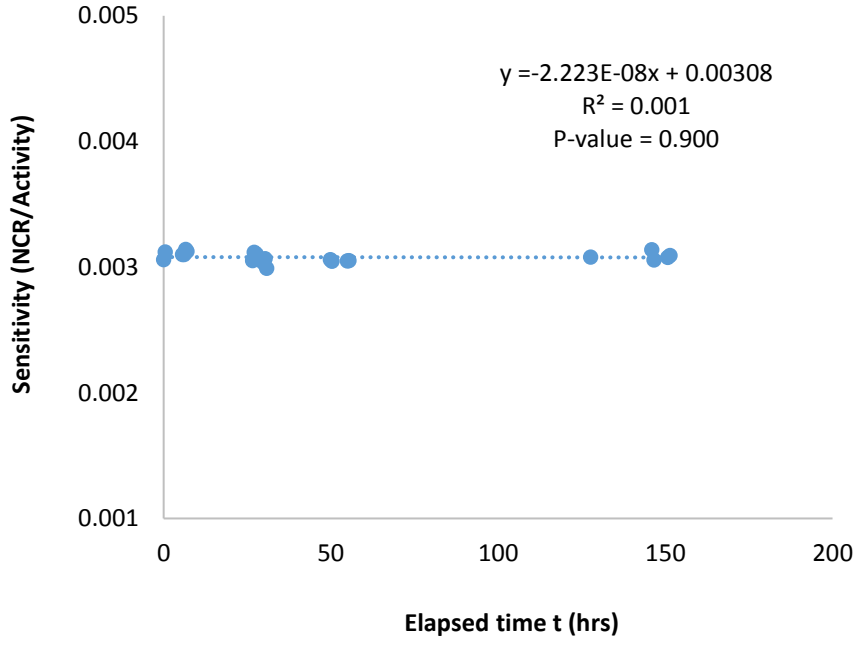

Figure 4-16: Sensitivity of HPGe detector with elapsed time for the 2nd vial of ^{131}I (81 keV)

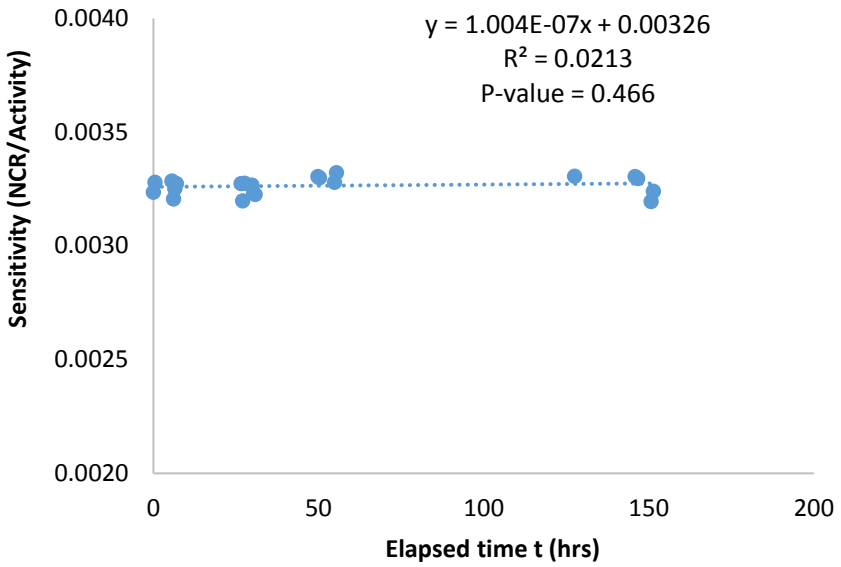

Figure 4-17: Sensitivity of HPGe detector with elapsed time for the 2nd vial of ^{131}I (284 keV)

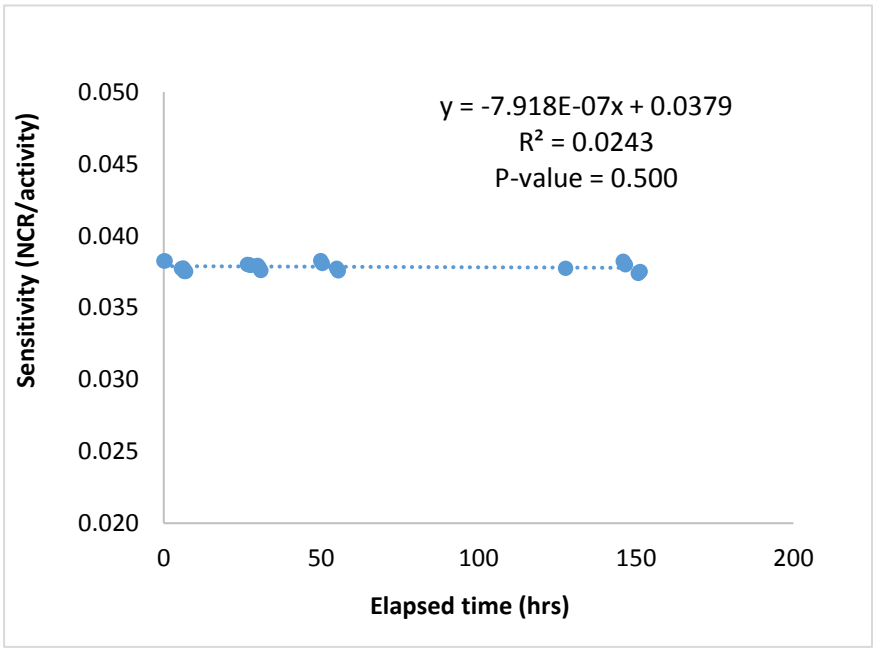

Figure 4-18: Sensitivity of HPGe detector with elapsed time for the 2nd vial of ^{131}I (364 keV)

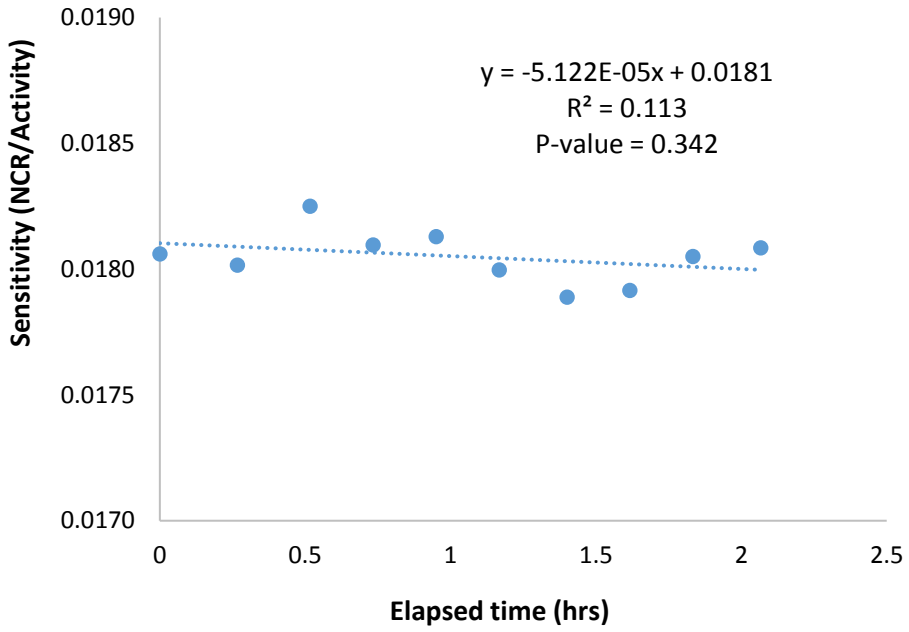

Figure 4-19: Sensitivity of HPGe detector with elapsed time for ^{137}Cs

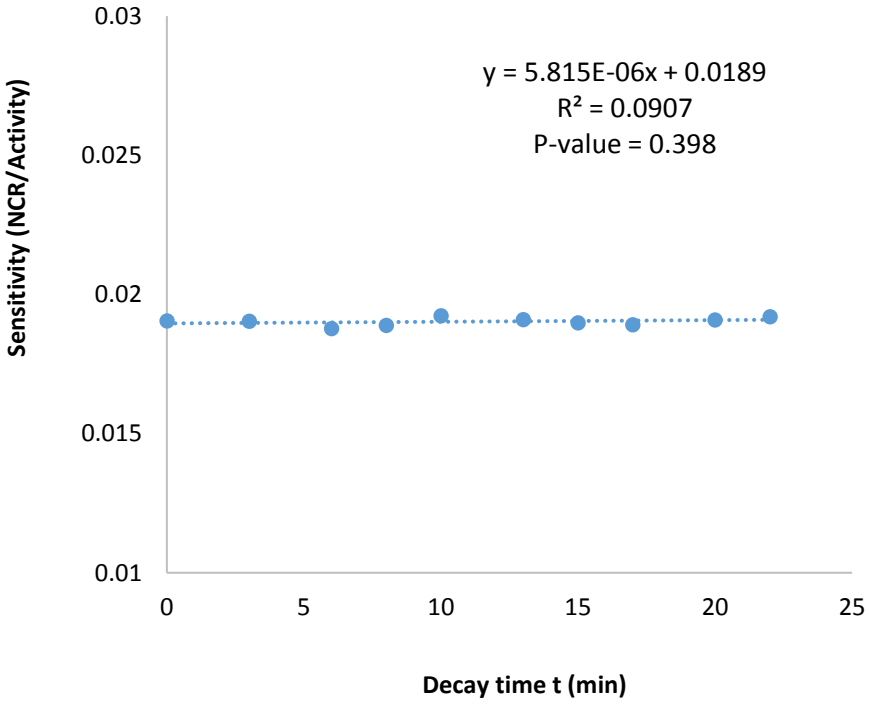

Figure 4-20: Sensitivity of HPGe detector with the elapsed time for ^{54}Mn

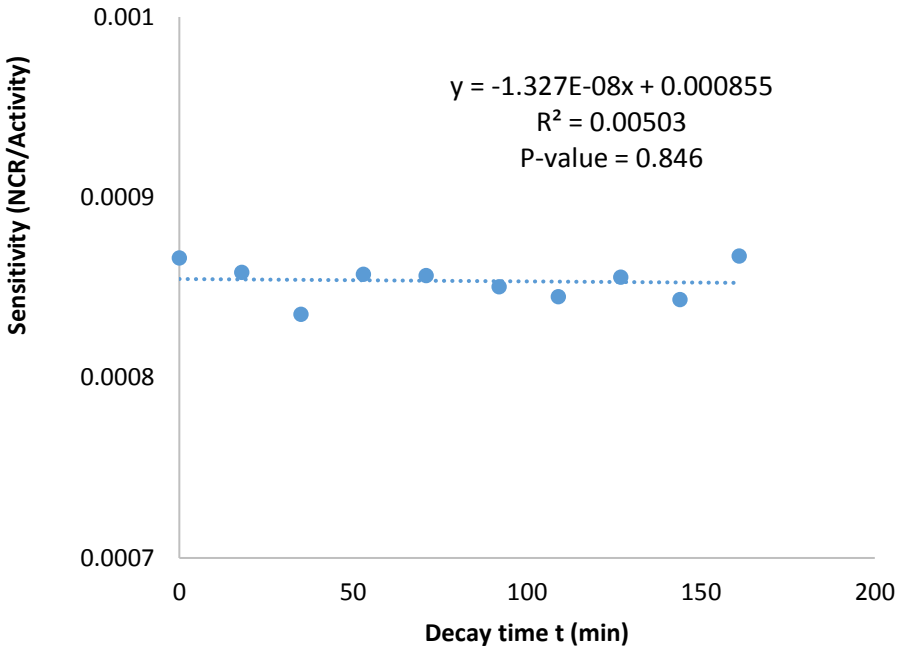

Figure 4-21: Sensitivity of HPGe detector with elapsed time for ^{65}Zn (511 keV)

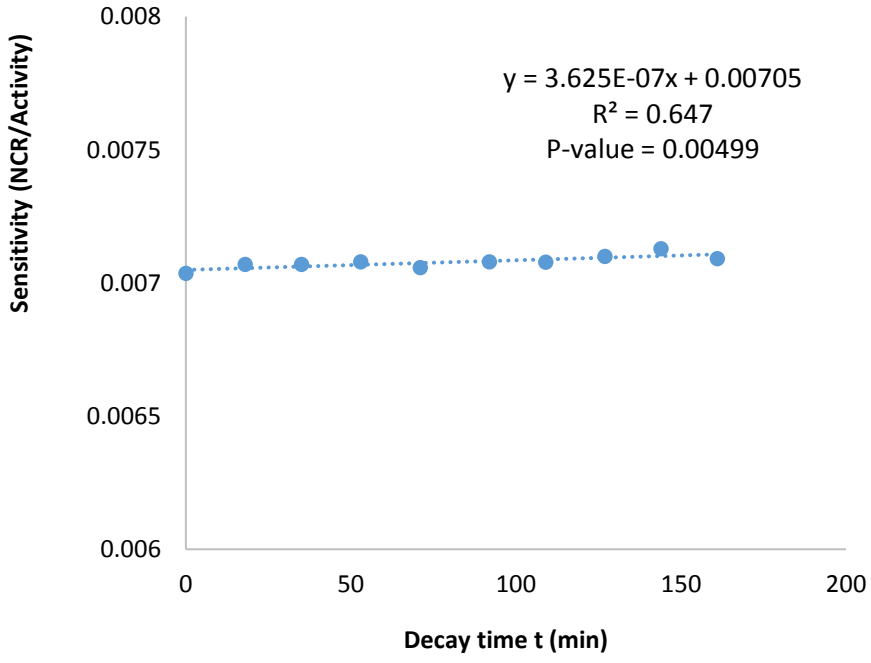

Figure 4-22: Sensitivity of HPGe detector with elapsed time for ^{65}Zn (1115 keV)

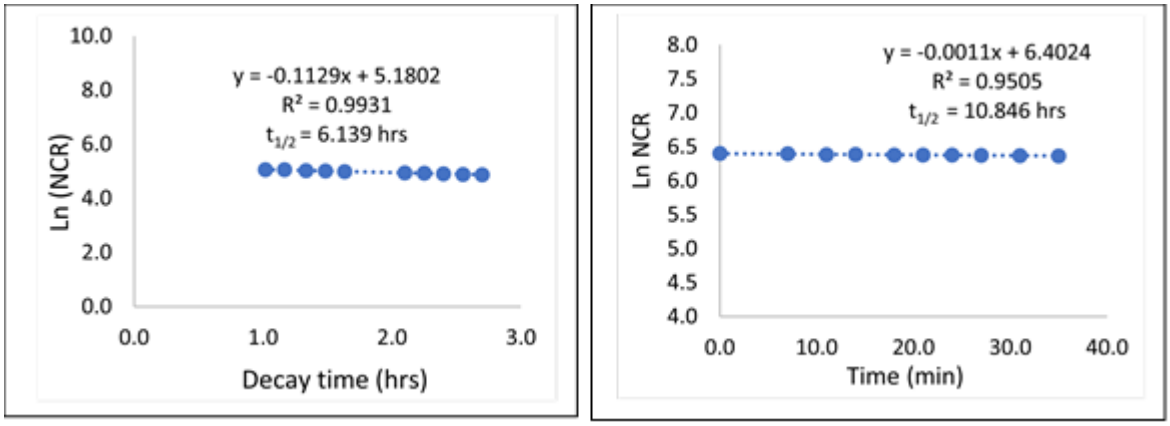

Figure 4-23: Half-life determination of ^{99m}Tc (6 hrs) and ^{123}I (13 hrs)

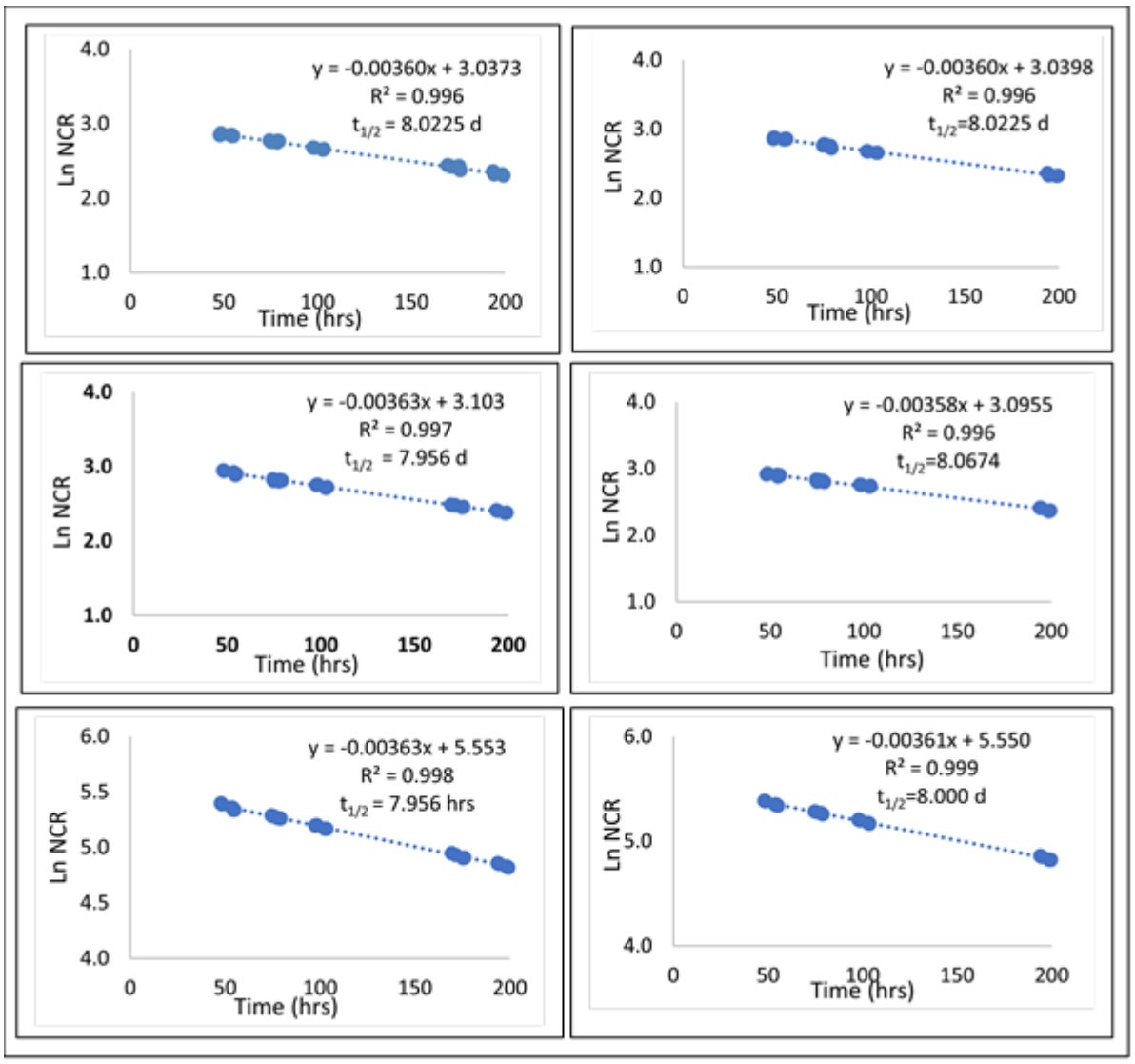

Figure 4-24: Determination of ^{131}I half-life (8.04 d). Figures on the left are for the first sample, while those at the right are for the second sample for the gamma peaks at 81 keV (top), 284 keV (middle) and 364 keV (bottom)

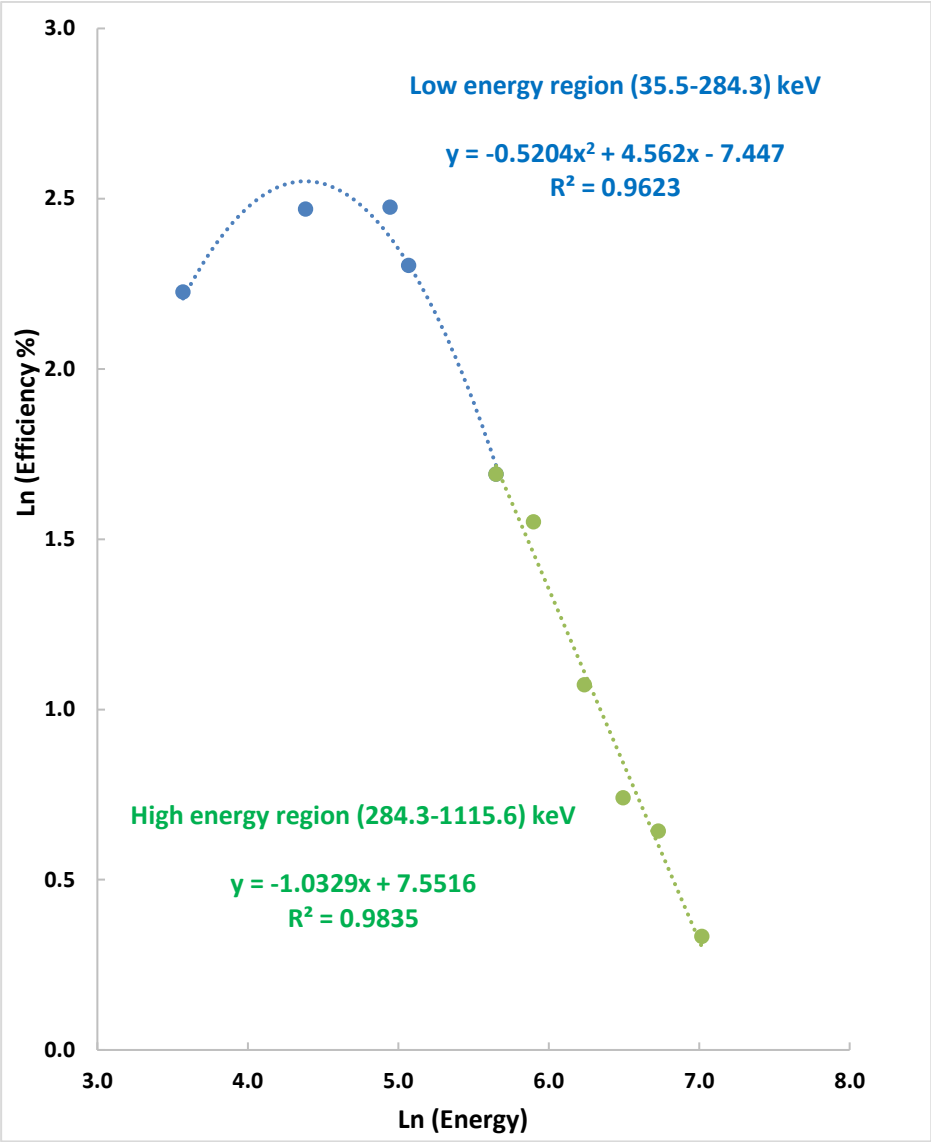

Figure 4-25: HPGe detector efficiency curve with a quadratic fit to the low energy region (35.5–284.3 keV) and a linear fit to the high energy region (284.3-1115 keV)

Table 4-2: Mean and Standard deviation (SD) values of efficiency at 10 photon energies obtained with 7 gamma sources

Gamma Source	Energy (keV)	Efficiency (%) Mean/SD	Ln Energy	Ln Efficiency Mean/SD
I-125	35.5	9.269 /0.107	3.569	2.227/0.012
I-131*	80.2	11.818/ 0.251	4.384	2.470/0.021
Tc-99m	140.5	11.892/0.070	4.945	2.476/0.006
I-123	159.0	10.019/0.034	5.069	2.304/0.003
I-131*	284.3	5.425/0.101	5.650	1.691/0.019
I-131*	364.5	4.720/0.077	5.899	1.552/0.016
Zn-65	511.0	2.923/0.035	6.236	1.073/0.012
Cs-137	661.6	2.099/0.012	6.495	0.741/0.006
Mn-54	834.9	1.903/0.014	6.727	0.643/0.007
Zn-65	1115.6	1.396/0.005	7.017	0.334/0.003

* Values for ^{131}I were obtained as a an average of two samples

4.9.3 Discussion

Linear regression analysis of the relationship between HPGe detector sensitivity and time indicated good stability (P>0.05) over the period of the experiments for all the gamma energies of the seven radionuclides except for the ^{65}Zn gamma photopeak at 1115 keV. This may be attributed to the mechanism by which the photons interact. However, the actual variation was relatively small, given that the corresponding percentage coefficient of variation (CoV) for repeated measurements of that gamma peak (0.35%) was less than that for the other gamma photopeak (1.20%) of the same nuclide (^{65}Zn).

Determination of the half-life was done only for the short-lived radioactive sources. It is difficult to measure the half-life of a very long-lived radionuclide as the change in disintegration rate may not be noticeable within a reasonable measurement period. To

obtain close agreement with the actual half-life, measurements should be repeated over a period that is approximately equal to the half-life itself (Billinghurst and Hreczuch 1976; Loveland et al. 2005). The calculated half-lives of both ^{99m}Tc and ^{131}I showed good agreement with the reference values. The measured half-life of ^{123}I, however, showed a relatively large percentage difference (-17.7%) compared with the actual value. This is attributed to the time of the experiment (about 1 hr), which was much less than one half-life of this radionuclide (13 hrs).

Figure **4-25** shows that at low photon energies ranging between 35 keV and 80 keV, the efficiency increased rapidly due to the photoelectric effect as the dominant mechanism. A maximum is reached at about 80 keV. Above that energy value, the detection efficiency decreased due to Compton scattering, which is the dominant interaction at higher energies.

The efficiency curve determined in this present study had a similar shape to that obtained by Sivers et al. (2014) (Figure 4-26). They used a LO-AX HPGe detector with exactly the same model number (70495/30-S). The main difference was that the calibration sources were placed directly at the entrance window of the detector, whereas in the present study the HPGe detector was covered with two plastic caps for detector protection. The presence of these two caps increased the attenuation, which resulted in reduced efficiency.

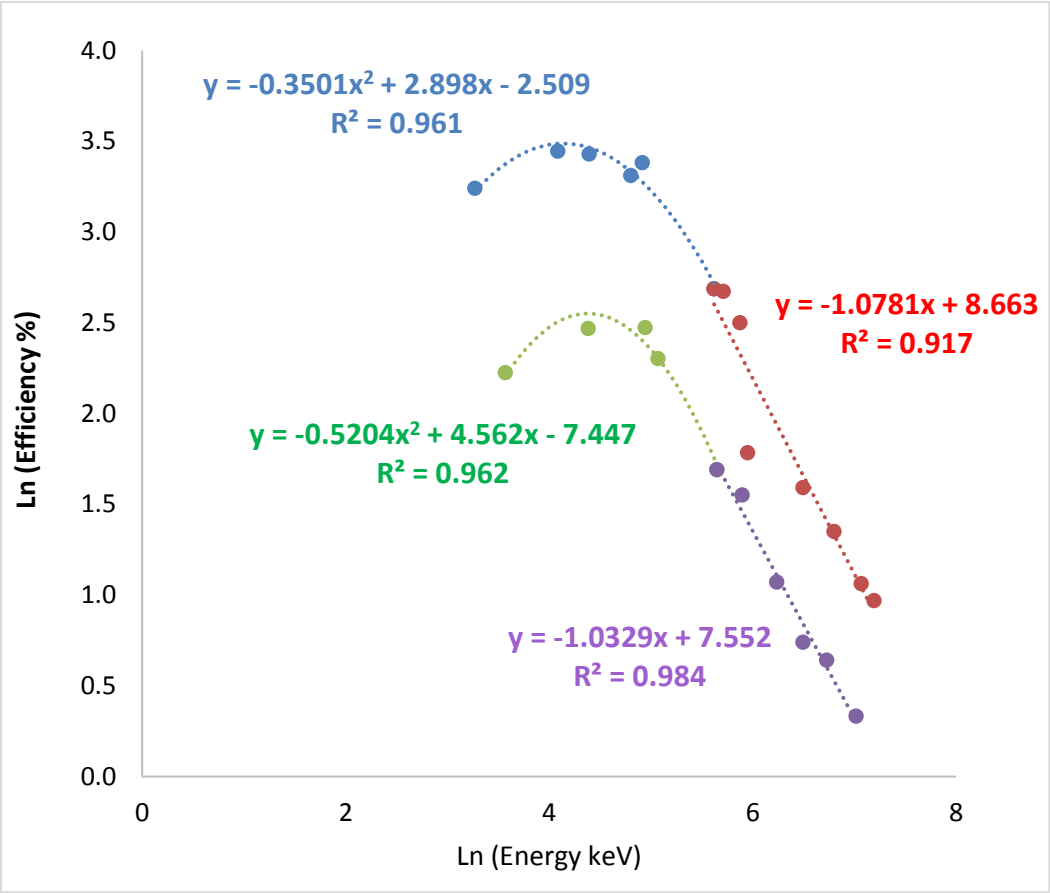

Figure 4-26: LO-AX HPGe detector efficiency curve obtained by Sivers et al. (2014) (top) and the present study (bottom)

4.10 Energy resolution

The ability of the system to distinguish between two gamma rays with a slight difference in energy is characterised by the energy resolution R, which is an important aspect of gamma ray spectrometry. R is defined as a ratio of the full width at half maximum (FWHM) of the photopeak to its gamma photon energy E and it is given by:

$$R = \frac{FWHM}{E} \times 100\% \qquad \textbf{(4-3)}$$

FWHM is the width of the distribution at a level corresponding to half-maximum of the peak value and is used as a measure of peak broadening. The energy resolution is expressed as a percentage and it is a dimensionless quantity (Cherry et al. 2012). It is obvious that the smaller the energy resolution, the better is the ability of the detector to distinguish between two photopeaks that are close in energy (Knoll 2010).

4.10.1 Method

The energy resolution of the LO-AX HPGe detector was determined for the seven radionuclides. It was measured using the FWHM values acquired using the automatic peak area method, as mentioned earlier in section 4.7.

4.10.2 Results

The FWHM and energy resolution values for the radionuclides are shown in Table 4-3 and FWHM is plotted against energy in Figure 4-27.

Table 4-3: Energy resolution for the seven relevant radionuclides using HPGe detecteor

Energy (keV)	FWHM (keV) Mean/SD	Resolution (%)
35.49	1.143/0.008	3.220
80.18	1.210/0.020	1.509
140.50	1.216/0.010	0.866
159.00	1.295/0.005	0.815
284.30	1.428/0.019	0.502
364.50	1.505/0.006	0.413
511.00	2.903/0.019	0.568
661.60	1.901/0.011	0.287
834.90	2.141/0.011	0.256
1115.60	2.467/0.010	0.221

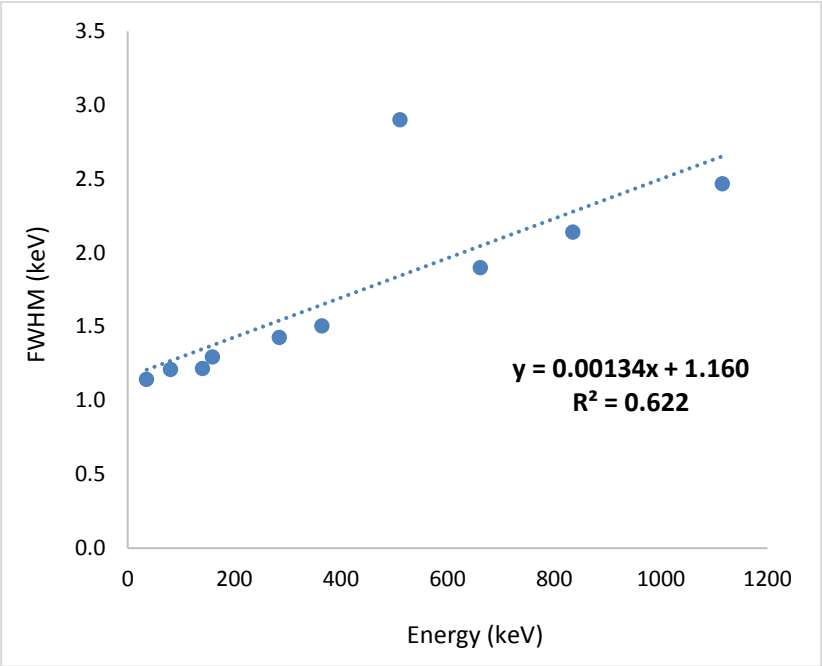

Figure 4-27: FWHM versus the energy of the seven radionuclides

4.10.3 Discussion

The HPGe detector shows a linear response to energy in the explored range. However, it is clear that the annihilation radiation photopeak at 511 keV has a greater FWHM than expected. This is due to the fact that annihilation radiation suffers greater Doppler broadening than other gamma radiation (Murray 1967), leading to an increase in the width of the photopeak. The difference in FWHM between the 511 keV peak and other gamma peaks is more apparent with high resolution detectors. With the 511 keV excluded, linear regression equation becomes:

$$y = 0.00124\times + 1.0815 \qquad (4\text{-}4)$$

The FWHM at 122 keV (^{57}Co) was 0.708 keV and the R^2 values increase to 0.998 in 1995 according to the detector manual provided by the supplier. However, the FWHM at this energy given by equation 4-4 is 1.233 keV, which means that the energy resolution has deteriorated since that time.

4.11 Coincidence summing

This phenomenon occurs when a radionuclide emits two or more gamma rays simultaneously per nuclear disintegration. This may result in simultaneous detection of these two gamma rays. Summing between x rays and gamma rays also can occur (Cherry et al. 2012). Coincidence summing was the effect of reducing the measured count-rate in photopeaks corresponding to the participating gamma rays.

Chapter 5

Radionuclidic Purity of Technetium-99m Generator Eluates

5.1 Introduction

This chapter describes the evaluation of the radionuclidic purity of ^{99m}Tc eluates obtained from ^{99}Mo/^{99m}Tc generators. Most of radiopharmaceuticals used for diagnostic imaging in nuclear medicine are labelled with ^{99m}Tc with generator eluate as a starting point. Quality control of these radiopharmaceuticals is important to get good images and to avoid unnecessary radiation dose to the patient.

5.2 Properties of ^{99m}Tc

Technetium (Tc) is an element that was discovered in 1937 by Perrier and Segrè. Tc has 21 isotopes, all of which are radioactive. They range from ^{90}Tc to ^{110}Tc. Technetium-110 has the shortest half-life (0.86s), whereas technetium-97 has the longest one (2.6×10^6 years). However, the isotope that is commonly used in diagnostic nuclear medicine is ^{99m}Tc (half-life=6 hours), which involves decay by gamma emission to the ^{99}Tc ground state (Figure 5-1 and Table 5-1). ^{99m}Tc is generated by the radioactive decay of its parent radionuclide (molybdenum-99) (Figure 5-2 and Table 5-2) (Kowalsky 2006; Zolle 2007; James 2007).

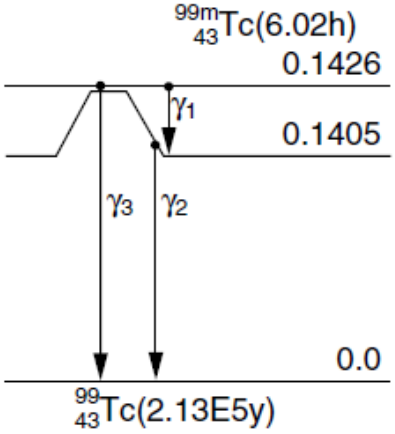

Figure 5-1: Decay scheme of ^{99m}Tc (Cherry et al. 2012)

Table 5-1: Emissions of ^{99m}Tc. y(i) is the yield per disintegration, E(i) is the energy of the emission, y(i)×E(i) is the product of the yield and the energy of the disintegration and ce are conversion electrons (Cherry et al. 2012)

Radiation	*y(i)* (Bq•s)$^{-1}$	*E(i)* (MeV)	*y(i)* × *E(i)*
ce-M, γ 1	9.14E-01	1.749E-03*	1.60E-03
ce-N$^+$, γ 1	7.57E-02	2.174E-03*	1.65E-04
γ 2	8.89E-01	1.405E-01	1.25E-01
ce-K, γ 2	8.79E-02	1.194E-01	1.05E-02
ce-L_1, γ 2	9.67E-03	1.374E-01	1.33E-03
ce-L_2, γ 2	6.10E-04	1.377E-01	8.40E-05
ce-L_3, γ 2	3.01E-04	1.378E-01	4.15E-05
ce-M, γ 2	1.92E-03	1.400E-01*	2.70E-04
ce-N$^+$, γ 2	3.71E-04	1.405E-01*	5.21E-05
ce-K, γ 3	6.91E-03	1.216E-01	8.41E-04
ce-L_1, γ 3	1.17E-03	1.396E-01	1.63E-04
ce-L_2, γ 3	2.43E-04	1.399E-01	3.39E-05
ce-L_3, γ 3	7.40E-04	1.400E-01	1.04E-04
ce-M, γ 3	4.19E-04	1.422E-01*	5.97E-05
Kα_1 X ray	4.03E-02	1.837E-02	7.39E-04
Kα_2 X ray	2.12E-02	1.825E-02	3.86E-04
Kβ_1 X ray	6.88E-03	2.062E-02	1.42E-04
Auger-KLL	1.45E-02	1.535E-02*	2.23E-04
Auger-KLX	5.76E-03	1.777E-02*	1.02E-04
Auger-LMM	7.10E-02	2.053E-03*	1.46E-04
Auger-LMX	3.05E-02	2.468E-03*	7.53E-05
Auger-MXY	1.11E 00	4.090E-04*	4.54E-04

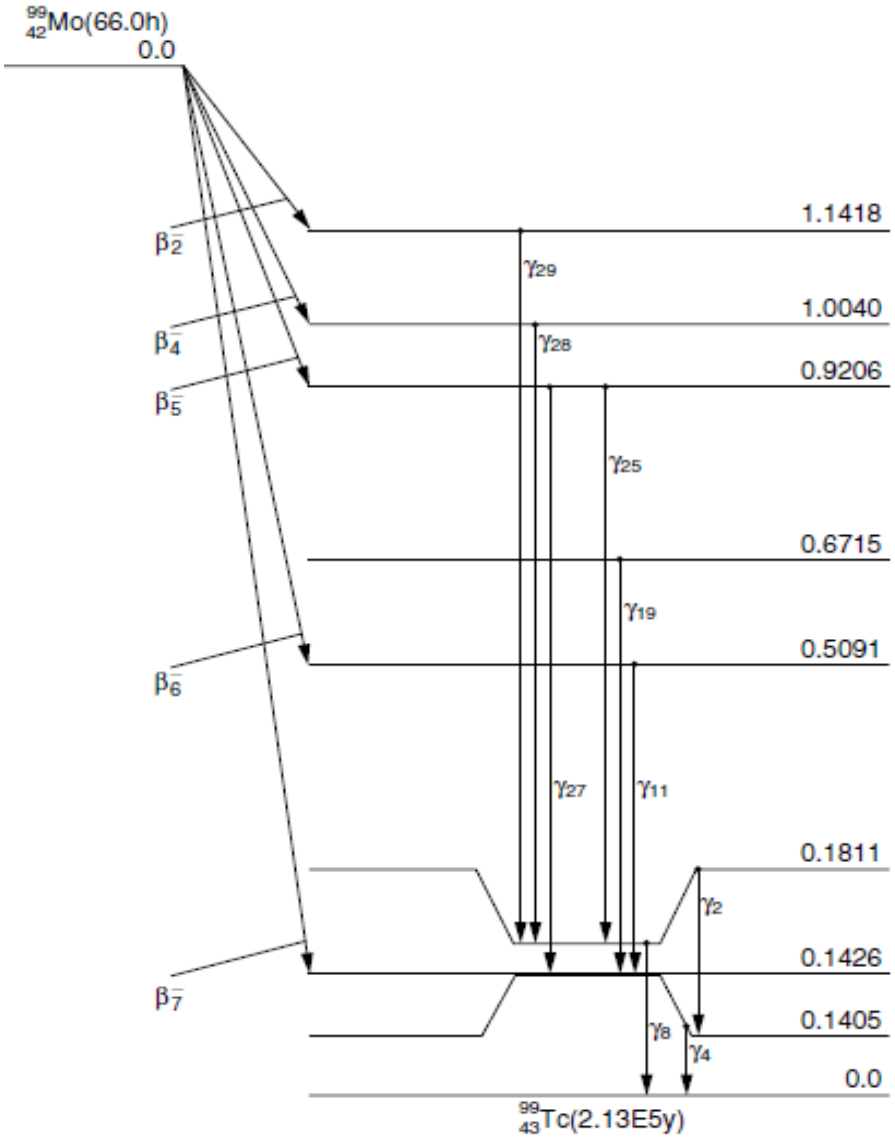

Figure 5-2: Decay scheme for ^{99}Mo (Cherry et al. 2012)

Table 5-2: Emissions of ^{99}Mo. y(i) is the yield per disintegration, E(i) is the energy of the emission, y(i)×E(i) is the product of the yield and the energy of the disintegration and ce are conversion electrons (Cherry et al. 2012)

Decay Mode(s): β^-			
Radiation	***y(i)*** **(Bq•s)$^{-1}$**	***E(i)*** **(MeV)**	***y(i)* × *E(i)***
β^- 5	1.66E-01	1.330E-01*	2.20E-02
β^- 6	1.17E-02	2.895E-01*	3.39E-03
β^- 7	8.20E-01	4.426E-01*	3.63E-01
γ 2	1.16E-02	4.059E-02	4.69E-04
ce-K, γ 2	3.77E-02	1.954E-02	7.38E-04
γ 4	4.95E-02	1.405E-01	6.95E-03
ce-K, γ 4	4.89E-03	1.194E-01	5.84E-04
γ 8	6.06E-02	1.811E-01	1.10E-02
ce-K, γ 8	7.62E-03	1.600E-01	1.22E-03
γ 11	1.19E-02	3.664E-01	4.37E-03
γ 19	5.45E-04	5.288E-01	2.88E-04
γ 24	2.60E-04	6.218E-01	1.61E-04
γ 25	1.22E-01	7.395E-01	9.02E-02
γ 27	4.32E-02	7.779E-01	3.36E-02
γ 28	1.33E-03	8.230E-01	1.09E-03
γ 29	9.76E-04	9.608E-01	9.37E-04
$K\alpha_1$ X ray	2.15E-02	1.837E-02	3.95E-04
$K\alpha_2$ X ray	1.13E-02	1.825E-02	2.06E-04

^{99m}Tc is used in about 85% of all diagnostic nuclear medicine procedures. About 40 million of these medical procedures are done worldwide each year; this includes 20 million in North America (Eckelman 2009). This widespread use is attributed to the availability of this radionuclide from generator systems and to its ideal nuclear properties, such as short half-life (Pillai 2008; Kowalsky 2006; Zolle 2007). The energy of the emitted gamma radiation (140 keV) is high enough to reduce attenuation within the body and ideal for detection by a scintillation crystal in a gamma camera, giving scintigraphic images with good spatial resolution (Saha 2010). Furthermore, because it is produced from a generator, it is readily available for local use (Kowalsky 2006).

The element technetium has several oxidative states depending on electron loss or gain (Sampson 1994; Banerjee et al. 2001; Kowalsky 2006; Zolle 2007). In its eluate, the ^{99}Mo/^{99m}Tc generator produces sodium pertechnetate with technetium its highest oxidative state (+7). Technetium may be compounded into a variety of chemical forms.

5.3 Clinical applications of ^{99m}Tc

In 1965, Richards and his followers at Brookhaven National Laboratories introduced the ^{99}Mo/^{99m}Tc generator for clinical use (Zolle 2007). In the following year, the application of ^{99m}Tc radiopharmaceuticals for clinical purposes increased significantly.

Technetium-99m radiopharmaceuticals are used in a wide range of diagnostic radionuclidic imaging procedures; these include evaluation of the function of the liver, kidney, brain and thyroid. They are also used in cancer imaging, such as the detection of neuroendocrine tumours and tumours within the bones and breast tissue (Pillai 2008; Willerson et al. 1975; Villanueva-Meyer et al. 1996; Zolle 2007; Saha 2010; Cervera 2009; Loutsios et al. 2015). Table 5-3 shows some of the technetium radiopharmaceuticals used for imaging and functional studies of organs.

One of the most common applications of ^{99m}Tc radiopharmaceuticals is myocardial imaging, which has been used on more than 40 million patients since 1991. One brand of ^{99m}Tc-MIBI (Cardiolite$^{(R)}$) generated sales of $304 million from January 2007 to September 2007, without including costs for physician input and the additional treatments that each scan required (Cervera 2009).

^{99m}Tc is a good radiolabel for peptides because the ^{99m}Tc chelate does not affect the biological activity if it is located properly in the peptide molecule and the pharmacokinetics of peptides match the physical half-life of ^{99m}Tc very well. Many peptides have been studied: somatostatin, VIP/PACAP, bombesin, CCK-B/gastrin, neurotensin, alpha-MSH, neuropeptide Y, GnRH/ LHRH, substance P and opioid peptides (Eckelman 2009).

^{99m}Tc pharmaceuticals based on coordination complexes with functionalised ligands are known as "Tc essentials". There are various different Tc essentials that are in clinical use (Figure 5-3). The optimal chelator should not change the *in vivo* characteristics of a biomolecule and the chelating unit should not affect the biomolecule potency (Zolle 2007).

Table 5-3: Technetium-99m radiopharmaceuticals for imaging and functional studies of organs with their absorbed and effective dose (Stabin et al. 1996; Schwochau 2000; Cherry et al. 2012)

Organ	Radiopharma-ceutical	Applications	Effective Dose (mSv/MBq)	Organ	Dose (mGy/MBq)
Brain	^{99m}Tc-HMPAO	Regional blood perfusion, cerebral stroke, ischemia, dementia, tumours and trauma hematoma	1.4×10^{-2}	Gallbladder Kidneys Bladder wall	5.1×10^{-2} 3.5×10^{-2} 2.8×10^{-2}
	^{99m}Tc-ECD	Regional blood perfusion, cerebral stroke and focal epilepsy	1.1×10^{-2}	Gallbladder LLI wall ULI Wall	2.7×10^{-2} 1.5×10^{-2} 1.7×10^{-2}
Thyroid	$Na^{99m}TcO_4$	Morphology, vascularity and function	1.1×10^{-2}	Bladder wall ULI wall LLI wall	3.6×10^{-2} 2.8×10^{-2} 2.7×10^{-2}
Lungs	^{99m}Tc-MAA	Blood perfusion and shunt diagnosis	1.3×10^{-2}	Muscle Lungs Uterus	6.7×10^{-2} 1.6×10^{-2} 9.8×10^{-3}
Liver and gall bladder	^{99m}Tc-disofenin	Liver and gall bladder function	2.5×10^{-2}	Gallbladder ULI Wall LLI Wall	1.1×10^{-1} 8.6×10^{-2} 6.0E-02
Kidneys	^{99m}Tc-MAG3	Tubular function and flow studies	1.2×10^{-2}	Bladder Wall Uterus LLI wall	1.4×10^{-1} 1.5×10^{-2} 7.1×10^{-3}
	^{99m}Tc-DMSA	Morphology and function diagnosis	1.6×10^{-2}	Brain Liver Bladder Wall	1.2×10^{-2} 1.9×10^{-1} 1.5×10^{-2}
Skeleton	^{99m}Tc-HMDP	Bone fracture, tumour, metastatic lesion, sarcoma and arthritis	6.1×10^{-3}	Red Marrow Bone Surfaces Bladder Wall	7.5×10^{-3} 5.2×10^{-2} 2.2×10^{-2}
Blood	^{99m}Tc-red blood cells	Ventricular functioning, cardiac output, vein thrombosis and internal bleeding	7.23×10^{-3}	Heart Wall Bladder Wall Spleen	1.6×10^{-2} 1.5×10^{-2} 1.2×10^{-2}

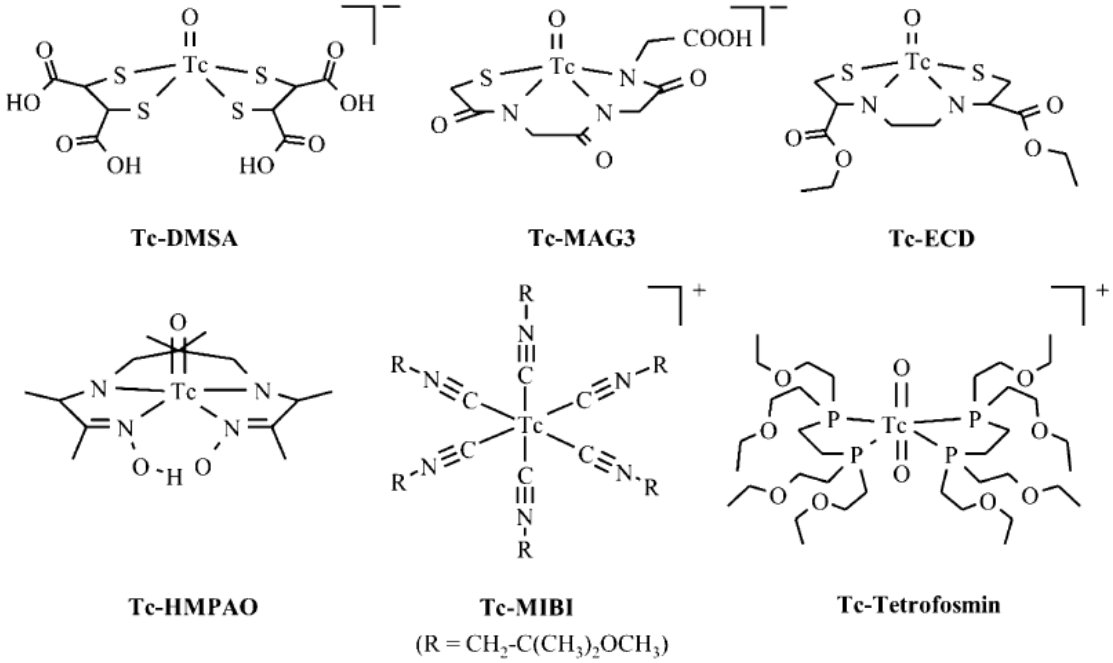

Figure 5-3: Tc essentials in clinical use (Zolle 2007)

5.4 Previous studies of the measurement of the radionuclidic purity of ^{99m}Tc eluates

There are several early studies in which lithium-drifted germanium(Ge(Li)) detectors had been used to evaluate the radionuclidic purity of ^{99m}Tc-eluates (Billinghurst et al. 1974; Anderson et al. 1974; Billinghurst and Hreczuch 1976; Finck and Mattsson 1976; Vinberg and Kristensen 1976; Vlček et al. 1979; Hoffmann et al. 1980; Hammermaier et al. 1986).

More recently, Andrade and Lima (2009) used the molybdenum breakthrough test with a radionuclide calibrator to assess the ^{99}Mo content in samples collected from the 1st, 3rd, 5th, 7th and 9th elutions of 20 generators with nominal 55.5 GBq and 70 GBq activities.

The results of this study showed that none of the measurements exceeded the limit recommended by the European Pharmacopoeia, which is 0.1%. However, no investigation was done to evaluate the relationship between the specified elutions and between the two types of generator.

Marengo et al. (1999) used the MBT and a HPGe detector to evaluate the radionuclidic purity of 245 generators supplied by seven different manufacturers (Amersham, CIS, Mallinckrodt, Medgenix, NeN Du Pont, Sorin Biomedica and Soreq). For more than 50 generators, the relationship between the purity of 1st and the 2nd elutions was assessed.

Following the MBT, the same eluates were re-examined after 7-15 days with a HPGe detector for a more accurate determination of the radionuclidic purity. ^{99}Mo, ^{103}Ru and ^{131}I were identified. The activities of ^{103}Ru and ^{131}I were found to be within the European Pharmacopoeia limit (5×10^{-3}%). However, it was found that the MBT gave approximate results and, in general, overestimated the ^{99}Mo activity. In addition, it was found that activity of ^{99}Mo in all eluates was below the European Pharmacopoeia limits and that there was no difference between the 1st and the 2nd elutions.

A few years later, Urbano et al. (2005) also used the MBT and high resolution gamma-spectrometry with HPGe to determine the radionuclidic purity of ^{99m}Tc eluates obtained from two different generators delivered weekly each Monday (nominal activity 10.75 GBq) and Wednesday (nominal activity 17.20 GBq). From each generator, 40 eluates were measured directly after generator delivery and after 24 hrs, while 22 eluates were measured 72 hrs after generator delivery. The relationship between the purity of the 1st, 2nd and 3rd elutions of each generator and the relationship between the purity of Monday and Wednesday generator elutions was investigated.

Following the MBT and for a more accurate determination of radionuclidic purity, 1 ml of the same eluate was re-analysed using high resolution gamma-spectrometry after 7 to 10 days to allow for ^{99m}Tc to decay.

It was found that the activity of ^{99}Mo was within the European Pharmacopoeia requirements. In general, its activity was very low compared with that of ^{99m}Tc. Thus, it was concluded that this impurity did not represent an additional dose risk for patients. No significant differences of purity were observed amongst the elutions, and between Monday and Wednesday generators.

Mushtaq et al. (2012) also found that there was no difference in ^{99}Mo breakthrough between low activity (23 GBq) and high activity (74 GBq) generators. For evaluation of the molybdenum content, a HPGe detector was used to analyse eluate samples from eight sets of generators with each activity. The samples were left for a long time for the

^{99m}Tc to decay to a sufficiently low level to permit the detection of radionuclidic impurities. Gamma spectra were then acquired and analysed.

A HPGe detector was also used by Tomarchio 2012 to determine the radionuclidic purity of the first eluate of ^{99}Mo/^{99m}Tc generators supplied by two manufacturers. The samples were positioned directly on the top of the detector, without any material between them and the detector end-cap. Spectra were acquired for the first sample from the first manufacturer with a counting live time of 65,500 s after a decay time of 11 days, whereas the live time for the second sample from the other manufacturer was 80,000 s with a decay time of 7 days.

^{99}Mo was the main the radio-contaminant highlighted in the spectrum of eluate from the first manufacturer, while the spectrum of the second manufacturer showed a presence of ^{103}Ru as a fission product related to the method of molybdenum production.

The literature indicates that field radionuclide calibrators were used to measure ^{99m}Tc activity for the evaluation of percentage radionuclidic impurity in generator eluates. As stated earlier (Chapter 2), field radionuclide calibrators do not take account of variables that have an impact on the chosen calibration factor; these include the container material, the geometry of the container and also the volume of the solution. Thus, the work described in this thesis used a secondary standard radionuclide calibrator (Fidelis), which has calibration factors for a number of container and volume combinations.

Furthermore, studies described in the literature evaluated the difference in radionuclidic impurity between the 1st, 2nd and 4th eluates, but the other eluates were not investigated. Thus in this study, impurity differences were investigated for up to six elutions of the same generator. The mathematical relationship between the percentage impurity and the eluate number was also determined.

5.5 Determination of ^{99}Mo contamination in ^{99m}Tc eluates

5.5.1 Generators

Tekcis ^{99}Mo/^{99m}Tc generators (Curium, Portsmouth, England) are supplied to the Medical Physics Department at University Hospital of Wales. Figure 5-4 and

Figure 5-5 show the external appearance of the generator and a schematic diagram of its interior respectively. Two generators are normally delivered each week: one every Monday with ^{99}Mo activity of 138 GBq and the other every Wednesday with an activity of 104 GBq. The Monday generator is usually eluted once a day over five consecutive working days. The Wednesday generator is eluted over three consecutive working days with further elutions on Sunday and the next two working days. Sunday elution is necessary because the eluate is used to prepare ^{99m}Tc-MAG3 and ^{99m}Tc-HMPAO. Table 5-4 shows the eluate number for both generators and the corresponding elution days.

Table 5-4: Eluate numbers and corresponding **elution days**

Eluate Number	**Monday generator**	**Wednesday generator**
1	Monday	Wednesday
2	Tuesday	Thursday
3	Wednesday	Friday
4	Thursday	Sunday
5	Friday	Monday
6	/	Tuesday

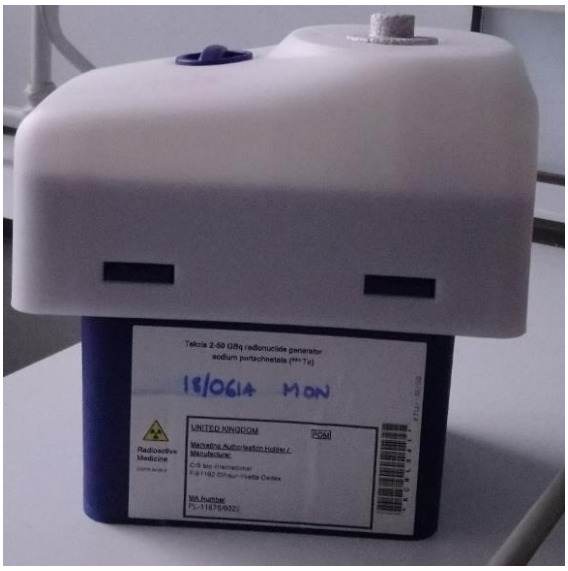

Figure 5-4: Tekcis (^{99}Mo/^{99m}Tc) generator supplied by Curium to the University Hospital of Wales

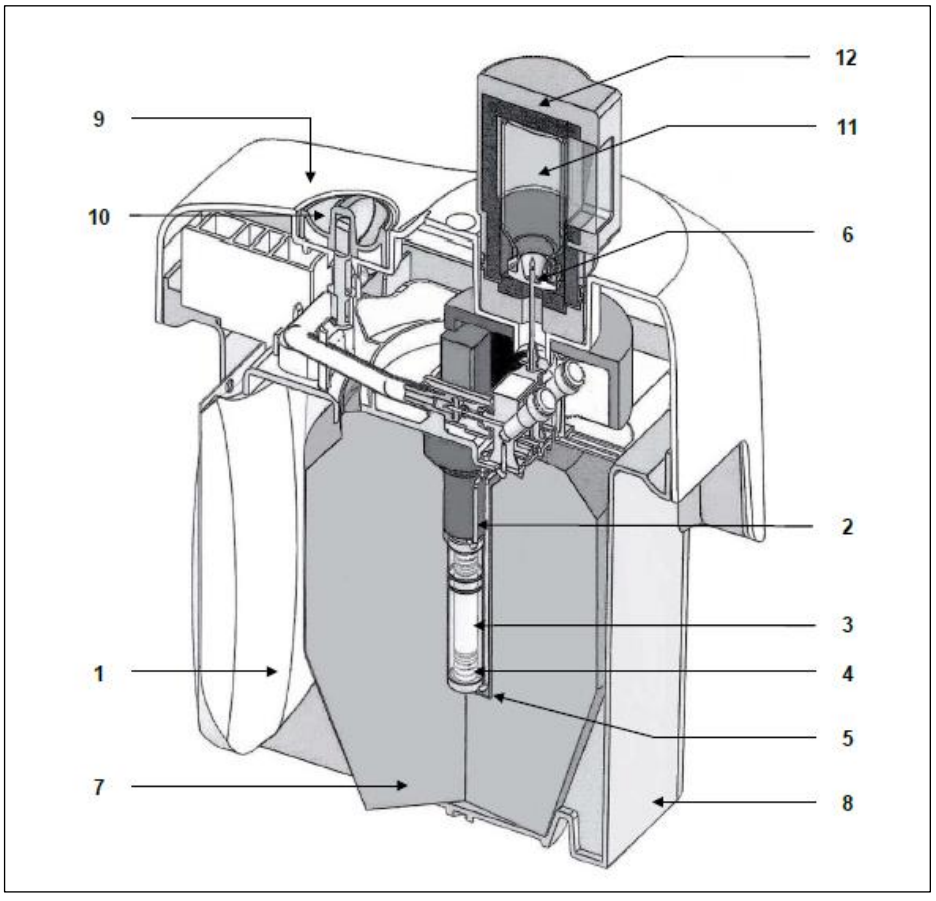

Figure 5-5: Schematic diagram of Tekcis generator: (1) bag of elution solution, (2) connection needle, (3) glass chromatography column, (4) silicone stopper, (5) stainless steel outlet needle, (6) elution needle, (7) tungsten shielding, (8) lower plastic shell, (9) upper plastic shell, (10) safety valve, (11) elution vial and (12) elution container

5.5.2 Method

The radionuclidic purity of 98 ^{99m}Tc eluates was evaluated, with 50 elutes from Monday generators and 48 elutes from Wednesday generators. Eluates from each working day, but not Sunday, were used.

Each sample comprised residual eluate after that day's radiopharmaceutical kit preparation. The volume of residual eluate varied from 0.5 to 13 ml, although it was always contained in a standard 15 ml eluate vial.

The ^{99m}Tc activity of most samples was measured on the day following elution as they had to be kept in the radiopharmacy for that time for regulatory reasons. The exceptions were the Friday eluates, for which activity was measured on the same day. The Fidelis radionuclide calibrator was used for this purpose.

Sample volumes were determined by weighing. For safety reasons, the weight of each eluate vial was measured using electronic weighing scales (model NA114, Oertling, Bermingham, England) after a few days to allow the ^{99m}Tc to decay. Each weighing was done five times and the average and standard deviation values calculated. Previously, 20 empty eluate vials had been weighed once using the same scales and the average empty weight determined. The eluate weight was obtained by subtracting the empty vial weight from that of the vial with residual eluate. The value of the eluate volume (ml) was set to be the same as the weight (g), assuming a density (mass divided by volume) of 1 g/ml.

The samples were then left for a further period of time to allow the ^{99m}Tc to decay to a sufficiently low value such that photopeaks due to radionuclidic impurities were not hidden in the background continuum created by the ^{99m}Tc 140 keV radiation in fresh radiation samples. This process gave an adequate dead time of less than 3%. The gamma-ray spectrum of each eluate vial was acquired using the HPGe detector. Spectra were examined to identify photopeaks due to the main radionuclide and possible radionuclidic impurities. The latter were identified from various sources including the scientific literature and information from the supplier. Details of the gamma emission energies and yields per disintegration were obtained from the (ICRP 1983). In this case, the main radionuclide was ^{99m}Tc and the expected impurities were ^{99}Mo and ^{103}Ru (Tomarchio 2012; Currium 2018).

The vials were examined separately by placing them in contact with the cap at the centre of the detector. The live time was varied depending on the residual volume, the activity of ^{99m}Tc in the vial and the ^{99}Mo activity. It was set to obtain at least 10,000 counts within the three strongest gamma photopeaks of ^{99}Mo (181 keV, 739 keV and 778 keV), with a corresponding statistical uncertainty (CoV) of 1% or less. These acquisitions gave about 6000 counts in the gamma photopeak of energy 366 keV, which was associated with an uncertainty of about 1.3%. Net count rate (NCR) in each gamma photopeak was then determined, corrected for decay during counting and the activity of ^{99}Mo calculated according to equation (2-17). However, the eluate and Schott vials did not have the same size and shape and the residual eluate volumes differed between the samples. Corrections to both ^{99m}Tc and ^{99}Mo activities were made for these two effects.

5.5.2.1 ^{99m}Tc activity correction

The dimensions of the eluate vial were different to those of the Schott vial used as a reference container in this work. Furthermore, the volume of the eluate differed from the 4 ml used as a reference volume. Thus, corrections had to be made for these different conditions. For the vial correction, 4 ml of ^{99m}Tc eluate from the same stock solution was dispensed into a Schott vial and an eluate vial. The volumes were confirmed by weighing. The eluate vial was placed in the eluate vial jig of the Fidelis radionuclide calibrator, activity readings were recorded every second for 1 minute (60 readings) and mean (SD) values calculated. The same procedure was applied to the Schott vial in the Fidelis Schott vial jig. In each case, the time of measurement was recorded.

The activity for the Schott vial was corrected for radioactive decay to the time of the eluate vial measurement. The ratio of eluate vial activity reading to Schott vial reading was calculated to give the vial correction factor C1.

To correct for the variation in eluate volume, a small volume of eluate was dispensed into an eluate vial and its volume increased by the addition of tap water. Again the exact volumes were determined by weighing. The initial volume of ^{99m}Tc eluate was about 0.2 ml and the second volume of the solution was about 0.5 ml. Subsequently, successive additions of about 0.5 ml were made up to a total volume of about 5 ml. The same procedure was repeated with successive additions of 1 ml up to a total volume of around 15 ml, giving a total of 21 different volumes. For each volume, activity was

measured using the Fidelis eluate jig and the mean (SD) of 60 readings calculated. The time of the measurement was also recorded.

The activity reading for each volume was corrected for radioactive decay to the time of the first measurement (volume of 0.2 ml). A set of eluate volume correction factors (C_2) was calculated by dividing the corrected activity at each volume by the activity reading at the reference volume of 4 ml. The values of C_2 were plotted against volume (ml) and a second degree polynomial equation was fitted to the data.

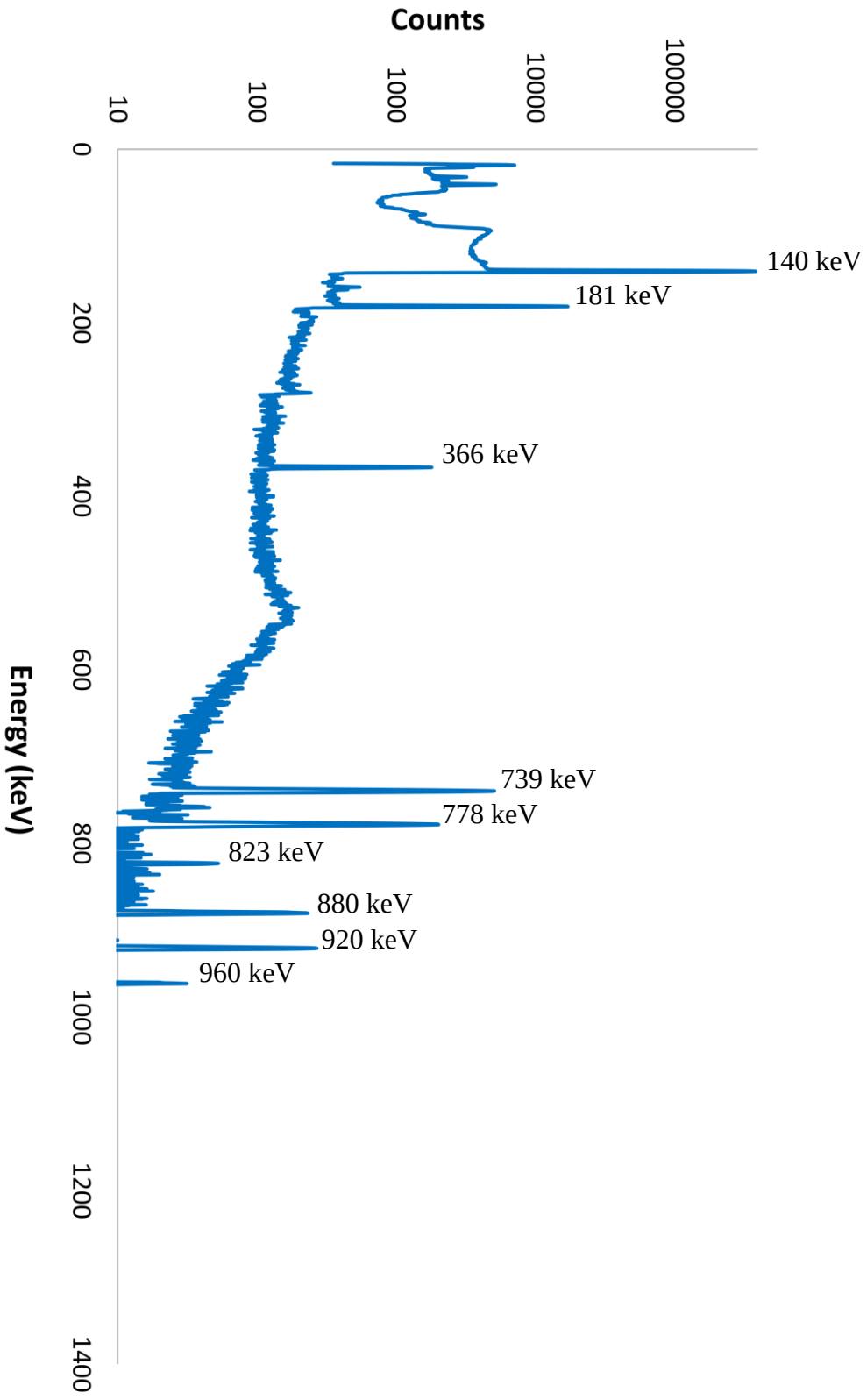

Figure 5-6: Actual ^{99m}Tc spectrum acquired using the HPGe detector showing the ^{99m}Tc peak (140 keV), ^{99}Mo peaks (181, 366, 739 and 778) keV and sum peaks

5.5.2.2 ^{99}Mo net count rate correction

Similar correction was needed for the values of NCR for ^{99}Mo. For the vial correction, the previously prepared Schott and eluate vials with 4 ml of eluate in each were separately placed on the HPGe detector. Spectra were acquired for a live time of 77400s (dead time was 0.09%) for the Schott vial and 61200s (dead time 0.11%) for the eluate vial,. NCR was calculated and the corrected for decay during counting for each of the four main gamma photopeaks of ^{99}Mo.

The Schott vial NCR values were corrected for radioactive decay to time of measurement of the eluate vial. Vial correction factors (C_3) were then calculated for each gamma photopeak by dividing the corrected NCR of the eluate vial by that of the Schott vial.

To obtain the ^{99}Mo NCR eluate volume correction factors, a procedure similar to that used for the ^{99m}Tc volume correction was used. An eluate vial with a fixed activity of ^{99}Mo was filled with 21 different volumes. Spectra were acquired using the HPGe detector for each volume with a live time of 900 s. The dead time was short (1.34%) for the first acquired spectrum. In each case, the NCR calculated, corrected for decay during counting and further corrected for radioactive decay to the time of acquisition of the first spectrum.

For each photopeak a set of ^{99}Mo NCR volume correction factors C_4 was obtained by dividing the corrected NCR at each volume by the corrected NCR at the reference volume of 4 ml. The values of C_4 were plotted against volume (ml) and a second degree polynomial equation was fitted to the data.

5.5.2.3 Comparison of ^{99m}Tc and ^{99}Mo activities measured in the radiopharmacy

For all the individual eluates, the corrected ^{99m}Tc and ^{99}Mo activity values measured using the Fidelis radionuclide calibrator and the LO-AX HPGe detector respectively were further corrected for radioactive decay to the corresponding time of generator elution in the radiopharmacy using equation (2-4).

For both radionuclides, the activity concentration of the residual eluates were expressed in MBq/ml. Using information from the radiopharmacy, the activities of the total

volume of eluate that would be in the vial at the time of elution were then determined. These were compared with the corresponding values obtained in the radiopharmacy using the Capintec calibrator.

5.5.2.4 Comparison of relative ^{99}Mo activity in eluates

For each eluate sample, the ^{99}Mo activity was expressed as a percentage of the ^{99m}Tc activity at the time of generator elution. Comparisons between eluates from the Monday generators and Wednesday generators and between successive eluates of each generator were made using the t-test. In addition, the relative ^{99}Mo activity was plotted against eluate number for each generator and the data analysed by logarithmic regression.

5.5.3 Results

5.5.3.1 ^{99m}Tc activity correction

The value of the vial correction factor C_1 obtained in the Fidelis calibrator was 0.999. The values of the volume correction factor C_2 obtained with a Schott vial are shown in Table 5-5 and plotted against volume in Figure 5-7. Also shown in the figure is the quadratic regression equation.

Table 5-5: Volume correction factors C_2 obtained with a Schott vial in the Fidelis calibrator

Volume (ml)	Volume correction factor C_2
0.2257	1.012
0.5389	1.012
1.0503	1.011
1.5607	1.008
2.0687	1.007
2.5714	1.001
3.0799	1.003
3.5972	1.001
4.0049	1.000
4.5194	0.998
5.0280	0.997
6.0338	0.994
7.0504	0.993
8.0651	0.991
9.0766	0.990
10.0911	0.989
11.0094	0.987
12.0301	0.989
13.0388	0.984
14.0555	0.985
15.0755	0.982

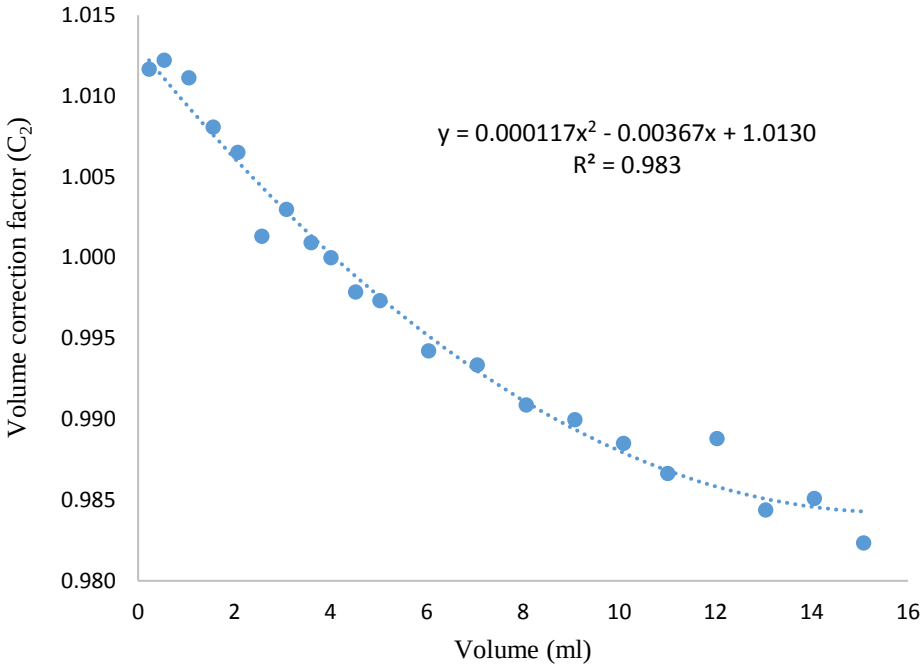

Figure 5-7: Volume correction factor (C_2) versus volume of ^{99m}Tc

5.5.3.2 ^{99}Mo net count rate correction

^{99}Mo NCR vial correction factors (C_3) obtained with the HPGe detector are shown in Table 5-6 for the four main photopeaks.

The values of the volume correction factor C4 obtained with a Schott vial for these photopeaks are shown in Table 5-7 and plotted against volume in Figure 5-8. The corresponding regression equations and R-squared values are shown in Table 5-8.

Table 5-6: ^{99}Mo NCR vial correction factors for four photopeaks

^{99}Mo gamma peak (keV)	Vial correction factor (C_3)
181	0.984
366	0.962
739	1.007
778	0.978

Table 5-7: Volume correction factors C_4 obtained with a Schott vial on the HPGe detector for ^{99}Mo photopeaks

Volume (ml)	Volume correction factor C4 for 181 keV	Volume correction factor C4 for 366 keV	Volume correction factor C4 for 739 keV	Volume correction factor C4 for 778 keV
0.210	1.186	1.276	1.200	1.227
0.522	1.179	1.190	1.190	1.201
1.051	1.176	1.251	1.194	1.215
1.563	1.134	1.176	1.157	1.185
2.008	1.103	1.138	1.119	1.139
2.504	1.079	1.148	1.083	1.130
3.001	1.056	1.050	1.063	1.075
3.500	1.016	1.046	1.041	1.039
3.999	1.000	1.000	1.000	1.000
4.504	0.969	0.994	0.993	0.956
5.003	0.954	0.882	0.975	0.958
5.937	0.889	0.887	0.946	0.904
7.022	0.866	0.853	0.876	0.878
8.006	0.809	0.832	0.858	0.838
9.011	0.786	0.783	0.802	0.785
10.013	0.744	0.761	0.793	0.751
11.003	0.714	0.745	0.743	0.721
12.023	0.676	0.659	0.724	0.685
13.018	0.658	0.666	0.711	0.674
14.016	0.632	0.645	0.695	0.651
15.026	0.609	0.601	0.659	0.602

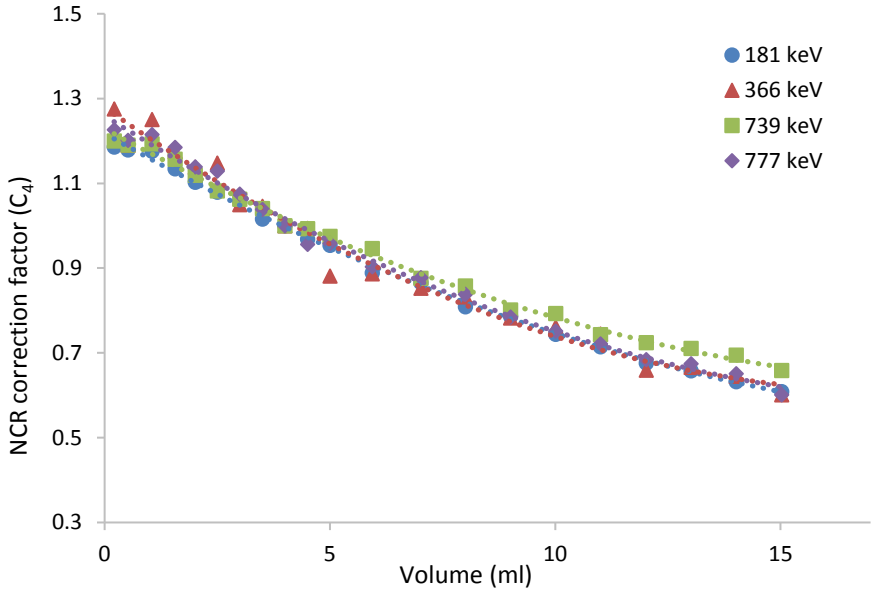

Figure 5-8: NCR volume correction factor C_4 versus volume for the 181 keV, 366 keV, 739 keV and 778 keV photopeaks of ^{99}Mo

Table 5-8: Quadratic regression equations and R-squared values for the relationship between NCR volume correction factor C_4 and volume for the 181 keV, 366 keV, 739 keV and 778 keV photopeaks of ^{99}Mo

Energy keV	Regression equation	R^2
181	$Y= 0.00132x^2 - 0.0605x + 1.218$	0.998
366	$Y= 0.00209x^2 - 0.0749x + 1.279$	0.981
739	$Y= 0.00142x^2 - 0.0588x + 1.229$	0.996
778	$Y= 0.00165x^2 - 0.0673x + 1.259$	0.993

5.5.3.3 ^{99m}Tc and ^{99}Mo activities in generator eluates

Table 5-9 shows the ^{99m}Tc activity (MBq) for the Monday and Wednesday generators as measured with the Fidelis and the Capintec radionuclide calibrators.

Table 5-10 shows the ^{99}Mo activity (MBq) for Monday and Wednesday eluates at elution time based on the HPGe detector gamma photopeaks at 181 keV, 366 keV, 739 keV and 778 keV, compared with the Capintec MBT reading, while Table 5-11 shows the corresponding values of the ^{99}Mo activity expressed as a percentage of the ^{99m}Tc activity.

Table 5-12 shows % ^{99}Mo activity by eluate number for different Monday generators whereas Table 5-13 shows same data for different Wednesday generators. The Mo activities were the average of those obtained at 366 and 778 keV.

Table 5-14 and

Table 5-15 show the t-test P-values for the comparison of % ^{99}Mo activity in different eluates of the Monday and Wednesday generators respectively.

Table 5-16 gives the t-test P-values for the comparison of corresponding eluates of the two generators.

Figure 5-9 show the percentage of ^{99}Mo to ^{99m}Tc activity versus the eluate number for the Monday and Wednesday generators. Each point on the curve represents the average of several measurements of the same eluate number, while the error bars represent standard error of the mean (SEM).

Table 5-9: Activity (MBq) of ^{99m}Tc for Monday and Wednesday eluates corrected to 4 ml in a Schott vial and corrected for decay to the time of elution

No. of eluate	Monday eluates			Wednesday eluates		
	N	Fidelis Mean (SD)	Capintec Mean (SD)	N	Fidelis Mean (SD)	Capintec Mean (SD)
Eluate 1	10	94291 (7119)	98390 (8916)	8	65341 (6139)	70688 (3386)
Eluate 2	8	74756 (8504)	78613 (970)	9	54238 (5216)	59611 (3143)
Eluate 3	10	59295 (5759)	59730 (4638)	10	42124 (4443)	44580 (3674)
Eluate 4	11	44585 (3545)	46045 (3567)	/	/	/
Eluate 5	11	33917 (3858)	35336 (4004)	10	20496 (1064)	21280 (976)
Eluate 6	/	/	/	11	15951 (953)	16552 (797)

Table 5-10: ^{99}Mo activity (MBq) for Monday and Wednesday eluates at elution time based on HPGe detector gamma peaks at 181 keV, 366 keV, 739 keV and 778 keV and the Capintec MBT reading

		Monday eluates (n=50)		Wednesday eluates (n=48)	
		Mean	SD	Mean	SD
HPGe	**181 keV**	0.485	0.485	0.305	0.375
	366 keV	0.562	0.567	0.342	0.417
	739 keV	0.423	0.419	0.261	0.319
	778 keV	0.549	0.547	0.335	0.406
Capintec	**^{99}Mo activity**	0.704	0.528	0.491	0.442

Table 5-11: ^{99}Mo activity as % of ^{99m}Tc activity for Monday and Wednesday eluates at elution time based on HPGe detector gamma photopeaks at 181 keV, 366 keV, 739 keV and 778 keV and the Capintec MBT reading

		Monday eluates (n=50)		Wednesday eluates (n=48)	
		Mean	**SD**	**Mean**	**SD**
HPGe	**181 keV**	0.00071	0.00047	0.00066	0.00054
	366 keV	0.00082	0.00055	0.00074	0.00060
	739 keV	0.00062	0.00041	0.00056	0.00046
	778 keV	0.00081	0.00053	0.00072	0.00057
Capintec	**MBT**	0.00131	0.00183	0.00116	0.00063

Table 5-12: ^{99}Mo Activity as % ^{99m}Tc activity for Monday eluates according to the eluate number for different generators

	Eluate Number				
Generator number	**1**	**2**	**3**	**4**	**5**
1	0.00050	0.00039	0.00039	0.00074	0.00048
2	0.00162	0.00131	0.00104	0.00012	0.00012
3	0.00029	0.00092	0.000153	0.00057	0.00033
4	0.00081	0.00066	0.00085	0.00042	0.00029
5	0.00140	0.00103	0.00067	0.00007	0.00059
6	0.00092	0.00081	0.00085	0.00106	0.00060
7	0.00194	0.00103	0.00104	0.00115	0.00021
8	0.00251	0.00065	0.00065	0.00167	0.00033
9	0.00100		0.00046	0.00044	0.00063
10	0.00253		0.00082	0.00079	0.00074
11				0.00138	0.00073
Mean	**0.00135**	**0.00085**	**0.00069**	**0.00077**	**0.00046**
SD	**0.00079**	**0.00029**	**0.00029**	**0.00051**	**0.00021**

Table 5-13: ^{99}Mo Activity as % of ^{99m}Tc activity for Wednesday eluates according to the eluate number for different generators

No.	1st	2nd	3rd	5th	6th
1	0.00151	0.00014	0.00015	0.00034	0.00043
2	0.00016	0.00019	0.00051	0.00036	0.00027
3	0.00012	0.00056	0.00118	0.00072	0.00055
4	0.00131	0.00135	0.00053	0.00031	0.00038
5	0.00222	0.00086	0.00038	0.00035	0.00030
6	0.00149	0.00109	0.00074	0.00048	0.00038
7	0.00152	0.00126	0.00050	0.00066	0.00040
8	0.00284	0.00209	0.00085	0.00033	0.00027
9		0.00123	0.00093	0.00042	0.00023
10			0.00080	0.00064	0.00024
11					0.00050
Mean	**0.00140**	**0.00097**	**0.00066**	**0.00046**	**0.00036**
SD	**0.00092**	**0.00062**	**0.00030**	**0.00015**	**0.00011**

Table 5-14: P-values of comparison between % ^{99}Mo activity in different Monday eluates (t-test)

Eluate Number	1	2	3	4
2	0.087			
3	0.030	0.263		
4	0.055	0.680	0.690	
5	0.006	0.003	0.048	0.088

Table 5-15: P-values of comparison between % ^{99}Mo activity in different Wednesday eluates (t-test)

Eluate Number	1	2	3	5
2	0.280			
3	0.061	0.187		
5	0.025	0.038	0.090	
6	0.016	0.018	0.013	0.092

Table 5-16: P-values of comparison between % activity of ^{99}Mo in corresponding Monday and Wednesday eluates (t-test)

Monday eluate number	Wednesday eluate number	P-value
1	1	0.915
2	2	0.595
3	3	0.796
5	5	1.000

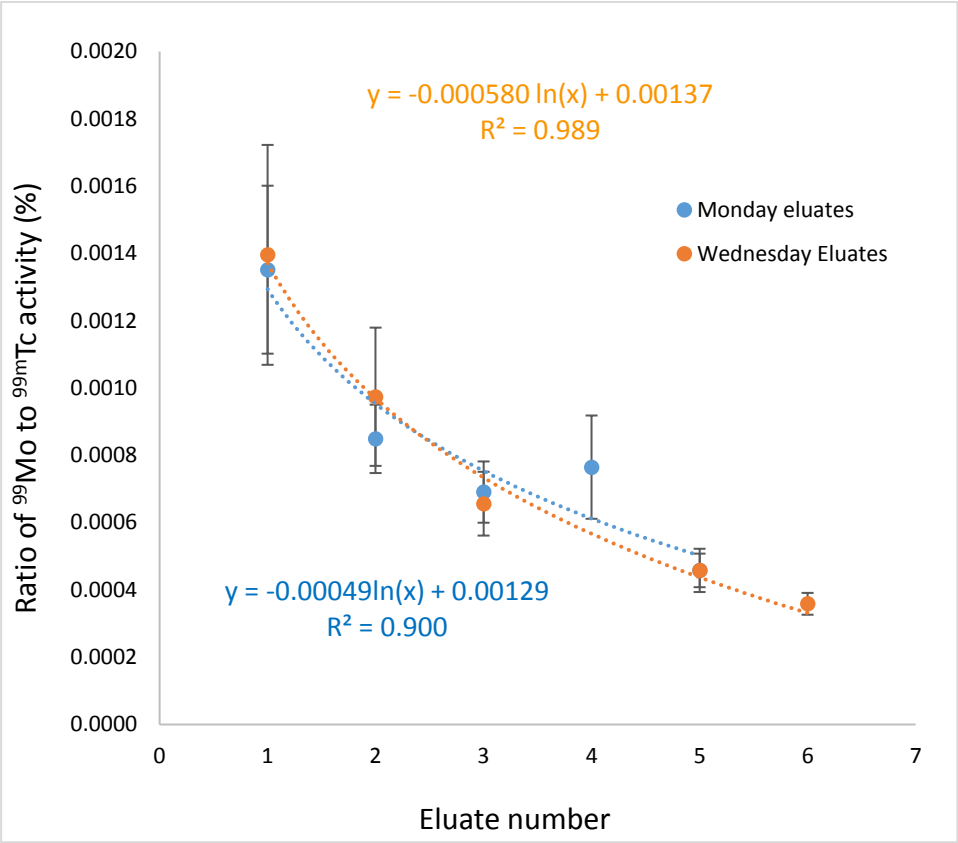

Figure 5-9: % ^{99}Mo activity versus eluate number for the Monday and Wednesday generators (mean± 1 SEM)

5.5.4 Discussion

In this study, the radionuclidic purity of 98 generator eluates was investigated. ^{99m}Tc activity was measured using a Fidelis secondary standard radionuclide calibrator that is used for testing the accuracy of field radionuclide calibrators such as those made by Capintec. Sample volume and vial geometry corrections were necessary as the Fidelis calibration factors are only available for specific geometries and volumes. It was shown that as the sample volume increased, the recorded activity decreased. This was due to the fact that the energy deposited within the calibrator ionisation chamber, and, in turn, the ionisation current decreased with volume.

Compared to the Fidelis calibrator readings, the Capintec field calibrator measurement of ^{99m}Tc activity gave approximate results and, in general, overestimated the ^{99m}Tc activity.

Similar behaviour was noticed as regards the effect of volume on the ^{99}Mo NCR using the LO-AX HPGe detector. It was shown that as a small volume of radioactive solution of fixed activity was diluted progressively by the addition of water, the counting rate recorded from the sample decreased.

Only photopeaks associated with the gamma emissions of ^{99m}Tc and ^{99}Mo were consistently observed in the eluate spectra (e,g. Figure 5-6). In addition to the main photopeaks, a number of sum peaks were also seen. The photopeaks and sum peaks are are listed in Table 5-17. For the measurement of ^{99}Mo activity, the photopeaks at 823keV and 960 keV were not used because of their low intensity.

Table 5-17: Photopeaks and sum peaks observed in the eluate spectra

Gamma energy (keV)	Yield	Description
140	0.889	^{99m}Tc photopeak
181	0.061	^{99}Mo photopeak
366	0.012	^{99}Mo photopeak
739	0.122	^{99}Mo photopeak
778	0.043	^{99}Mo photopeak
823	0.001	^{99}Mo photopeak
880	/	Sum of 140 keV and 739 keV photopeaks
920	/	Sum of 181 keV and 739 keV photopeaks
960	0.001	^{99}Mo photopeak

Using the HPGe detector, it was found that the greatest ^{99}Mo activity was registered by the gamma photopeaks at 366 keV and 778 keV. The difference in activity calculated using these two photopeaks was significant (t-test, $P<0.01$). However, it was only 2% and so the values were combined for the comparison of eluates and generators. The 739 keV photopeak registered the least ^{99}Mo activity with the 181 keV peak giving an intermediate value. In turn, the ratio of ^{99}Mo/^{99m}Tc activity based on the 366 keV and

778 keV peaks gave higher values than those for the other two peaks (181 keV and 739 keV). These effects are attributed to the existence of sum peaks in the ^{99}Mo spectrum.

Table 5-17 shows that the 739 keV photons contributed to two sum peaks resulting in the greatest decrease in count rate and, in turn, ^{99}Mo activity and activity ratio. On the other hand, the 181 keV photons contributed to just one sum peak leading to a smaller effect on count rate, activity and activity ratio. No sum peaks were identified involving the 366 keV and 778 keV photons. Thus, these photopeaks registered greater ^{99}Mo activities than these associated with the 181 and 739 keV photons.

Given the problem created by sum peaks, the determination of ^{99}Mo activity was based on data from the 366 keV and 778 keV peaks of the HPGe detector spectrum.

^{99}Mo activity obtained using the MBT with the Capintec calibrator gave approximate results and, in general, overestimated activity compared with the HPGe detector. This observation was similar to that reported in the literature although the differences found in this study were smaller by far. However, the activity of ^{99}Mo in all eluates using both devices were below the limit set by the European Pharmacopoeia. It is worth noting that determining the ^{99}Mo activity using a HPGe detector is much more accurate than using the MBT and a Capintec calibrator. In the latter, ^{99}Mo activity was estimated by multiplying the reading by a suitable correction factor to account for attenuation of 739–778 keV photons by the 6 mm lead shielding. Such attenuation correction was not needed using the HPGe detector as the elution vial was put directly at the centre of the detector and time had been allowed for almost complete decay of ^{99m}Tc.

No significant difference in ^{99}Mo activity was observed between corresponding eluates from the two generators ($P>0.05$, Table 5-16). This agrees with the results of previous studies published in the literature.

In addition, no significant difference ($P>0.05$) was observed between eluates 1 and 2, and eluates 2 and 3 from both generators; between eluates 3 and 4, eluates 4 and 5 and 1, 2 and 4 from the Monday generator and between eluates 3 and 5, eluates 5 and 6 and eluates 1 and 3 from the Wednesday generator (Table 5-14 and

Table 5-15). However, there was a significant difference ($P<0.05$) between other eluates: (a) eluates 1 with 5 and eluates 2 with 5 from both generators; (b) Monday eluates 1 and 3 and eluates 3 and 5 and (c) Wednesday eluates 1 and 6, eluates 2 with 6 and eluates 3 and 6.

Finally, it was found that the activity of ^{99}Mo as a percentage of ^{99m}Tc activity decreased logarithmically with the eluate number in both generators (Figure 5-9). This may happen because the chemical binding of some molybdate ions to the alumina column is relatively weak and these ions are preferentially removed with successive elutions. Another possibility is that there are some alumina particles that are loosely attached to the column and these are removed in the early elutions. This trend has not been reported previously.

5.6 Determination of ^{103}Ru contamination in ^{99m}Tc eluates

5.6.1 Method

The radio-contaminant ^{103}Ru (497 keV) was identified in a total of 21eluates of both the Monday and Wednesday generators. However, this radionuclide was not seen in the spectra of samples used to derive ^{99}Mo NCR vial and volume correction factors. Thus, the NCR correction factors used for ^{103}Ru were the same as those for the closest gamma peak of ^{99}Mo, which was 366 keV.

5.6.2 Results

Table 5-18 **s**hows the activity of ^{103}Ru (MBq) and its value as a percentage of ^{99m}Tc activity for both the Monday and Wednesday generators. Figure 5-10 shows a graph of the ^{103}Ru activity as a percentage of ^{99m}Tc activity versus the eluate number. Each point on the curve represents the average of several readings for the Monday and Wednesday eluates combined, while the error bars represent the standard error of the mean.

Table 5-18: Activity of ^{103}Ru (MBq) and its ratio to that of ^{99m}Tc for Monday and Wednesday generators

No. of eluate	Monday eluates			Wednesday eluates		
	N	^{103}Ru activity Mean (SD)	^{103}Ru/^{99m}Tc (%) Mean (SD)	N	^{103}Ru activity Mean (SD)	^{103}Ru/^{99m}Tc (%) Mean (SD)
Eluate 1	2	5.23×10^{-03} (3.41×10^{-03})	2.91×10^{-06} (8.51×10^{-06})	3	7.20×10^{-03} 5.81×10^{-03}	1.13×10^{-05} (1.02×10^{-05})
Eluate 2	1	9.02×10^{-04}	1.00×10^{-06}	1	2.11×10^{-03}	4.00×10^{-06}
Eluate 3	3	1.63×10^{-03} (1.50×10^{-03})	5.03×10^{-06} (6.93×10^{-08})	1	3.53×10^{-04}	7.69×10^{-07}
Eluate 4	1	1.99×10^{-03}	4.32×10^{-06}	/	/	/
Eluate 5	1	1.97×10^{-04}	5.96×10^{-07}	4	5.33×10^{-04} 7.08×10^{-04}	2.55×10^{-06} (3.43×10^{-06})
Eluate 6	/	/	/	4	1.41×10^{-04} 5.22×10^{-05}	8.71×10^{-07} (3.69×10^{-07})

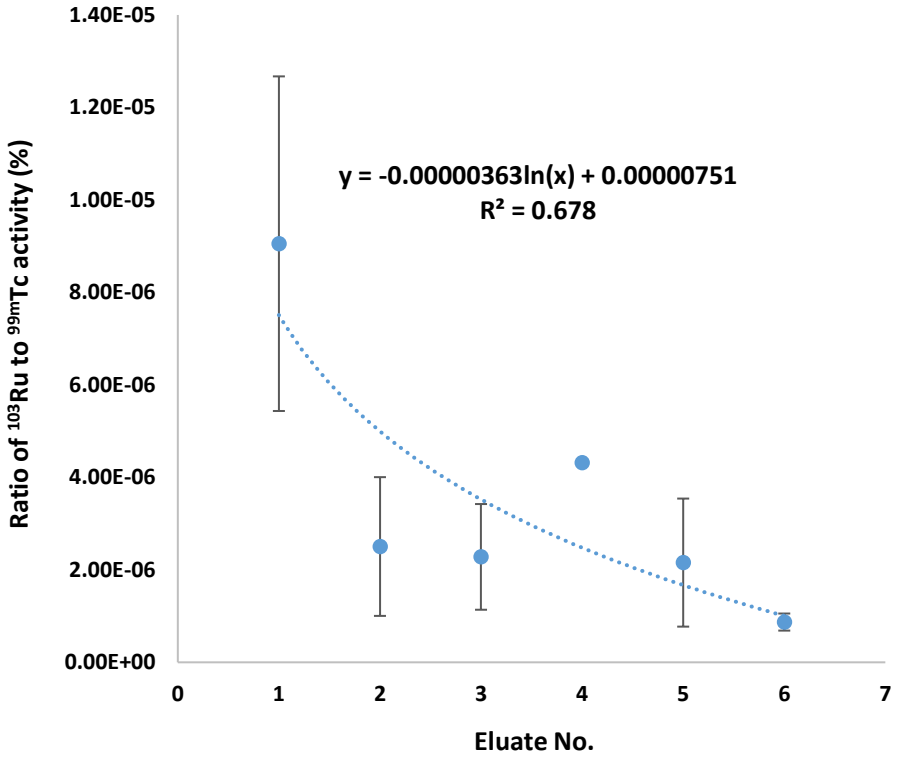

Figure 5-10: Variation of the ratio of ^{103}Ru activity to that of ^{99m}Tc versus eluate number combined for the Monday and Wednesday generators combined (mean±1 SEM)

5.6.3 Discussion

The fission product ^{103}Ru was identified in 21 out of 98 eluates for a combination of both generators. In all cases it was found that the ratio of ^{103}Ru activity to that of the main radionuclide ^{99m}Tc was within European Pharmacopoeia limits (5×10^{-03}%). However, the 497 keV photopeak had a relatively high statistical uncertainty of 7% as a maximum value.

In general, the ^{103}Ru/^{99m}Tc activity ratio decreased with the eluate number for the two generators. Following the approach for ^{99}Mo (Figure 5-9), the data were analysed by logarithmic regression (Figure 5-10). However, it may be that most of the ^{103}Ru is removed at the first elution with little or no change in relative activity thereafter.

Chapter 6

Radionuclidic Purity of Commercial Radioiodine Solutions

6.1 Introduction

This chapter describes the evaluation of the radionuclidic purity of radioactive sodium iodide solution (^{123}I and ^{131}I). Iodine is one of the halogen group of elements, these are fluorine (F), chlorine (Cl), bromine (Br), iodine (I) and astatine (At). In its elemental form, iodine appears as a greyish-purple, non-metallic solid. It is not very soluble in water. All the non-elemental forms of iodine can be readily converted to I_2 by exposure to heat and light. Iodine has 24 radioisotopes that are equally distributed on either side of one stable isotope, ^{127}I. The radioiodines that are most used in nuclear medicine are ^{123}I and ^{131}I (Rhodes and Croft 1978).

Radioactive isotopes of iodine were first used as tracers of thyroid function. Radioiodine was first used in 1941 in the Massachusetts General Hospital by Saul Hertz. Since then, radioiodine has been successfully used for many thousands of patients to treat hyperthyroidism and benign thyroid diseases (McCready 2017).

Sodium iodide labelled with ^{123}I and ^{131}I is the simplest inorganic pharmaceutical that incorporates radioactive iodine. In this chemical form, the two radioisotopes have been used for the diagnosis of thyroid dysfunction and the treatment of thyroid cancer for over 50 years, based on the ability of the thyroid gland to accumulate iodine. Sodium iodide (^{131}I) is also useful in treating hyperthyroidism (Graves' disease), by utilising emitted beta radiation.

As with other products, the quality control of radiopharmaceuticals labelled with radioiodine is important to avoid unnecessary radiation dose to the patient.

6.2 Properties of ^{123}I

^{123}I decays 100% via electron capture to ^{123}Te (Figure 6-1 and Table 6-1). It is a useful radionuclide for diagnostic applications due to its short half-life of 13.3 h and the fact that its principal gamma energy is 159 keV (Chilton and Witcofski 1986; Talboys 2016). In diagnostic nuclear medicine, this is the gamma radiation that is used as it falls within the energy range 80 – 400 keV, which is ideal for detection using a NaI(Tl) scintillation crystal.

However, there are other gamma emissions in the decay scheme. They are generally at higher energies than the predominant gamma emission but at a much reduced

abundance, about 100-1000 times less than that of the 159 keV. The decay of ^{123}I is also characterised by the emissions of K-alpha and K-beta characteristic x-rays at energies ranging between 27 and 31 keV.

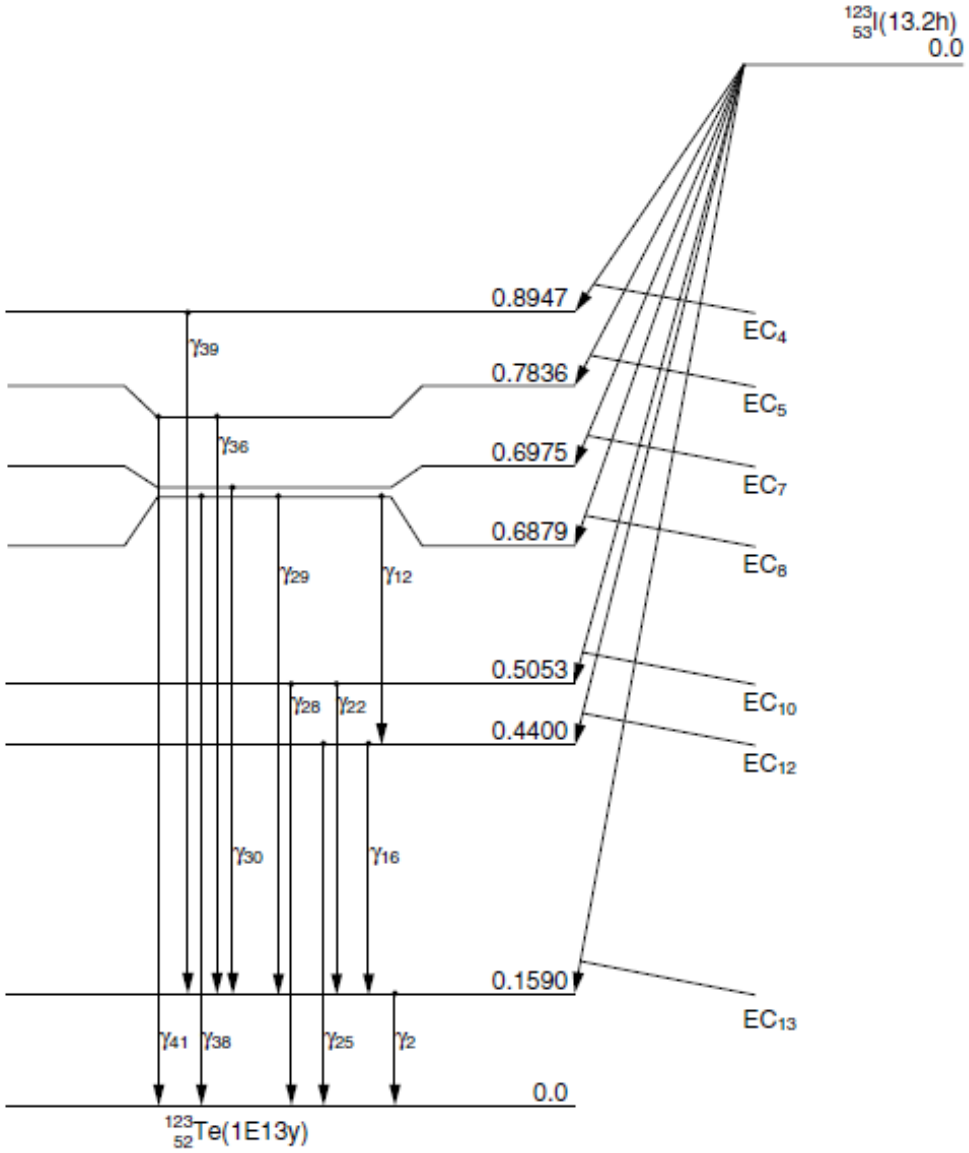

Figure 6-1: Decay scheme for ^{123}I (Cherry et al. 2012)

Table 6-1:Emissions of ^{123}I. y(i) is the yield per disintegration, E(i) is the energy of the emission, y(i)×E(i) is the product of the yield and the energy of the disintegration and ce are conversion electrons (Cherry et al. 2012)

Radiation	*y(i)* (Bq•s)$^{-1}$	*E(i)* (MeV)	*y(i)* × *E(i)*
γ 2	8.28E-01	1.590E-01	1.32E-01
ce-K, γ 2	1.35E-01	1.272E-01	1.72E-02
ce-L_{1}, γ 2	1.60E-02	1.540E-01	2.47E-03
ce-L_{2}, γ 2	1.09E-03	1.544E-01	1.69E-04
ce-L_{3}, γ 2	3.46E-04	1.546E-01	5.35E-05
ce-M, γ 2	3.46E-03	1.582E-01*	5.48E-04
ce-N^{+}, γ 2	8.27E-04	1.590E-01*	1.32E-04
γ 12	7.07E-04	2.480E-01	1.75E-04
γ 16	7.86E-04	2.810E-01	2.21E-04
γ 22	1.25E-03	3.463E-01	4.33E-04
γ 25	4.25E-03	4.400E-01	1.87E-03
γ 28	3.14E-03	5.053E-01	1.59E-03
γ 29	1.38E-02	5.290E-01	7.31E-03
ce-K, γ 29	9.90E-05	4.971E-01	4.92E-05
γ 30	3.79E-03	5.385E-01	2.04E-03
γ 36	8.28E-04	6.246E-01	5.17E-04
γ 38	2.66E-04	6.879E-01	1.83E-04
γ 39	6.12E-04	7.358E-01	4.50E-04
γ 41	5.90E-04	7.836E-01	4.62E-04
$K\alpha_1$ X ray	4.58E-01	2.747E-02	1.26E-02
$K\alpha_2$ X ray	2.46E-01	2.720E-02	6.70E-03
$K\beta_1$ X ray	8.66E-02	3.100E-02	2.69E-03
$K\beta_2$ X ray	2.66E-02	3.171E-02	8.43E-04
$K\beta_3$ X ray	4.46E-02	3.094E-02	1.38E-03

6.3 Clinical applications of ^{123}I

Iodine is one of the important elements for life, although the total amount in the human body (for an adult weighing 70 kg) is just 10–30 mg. It is a chemical element that exists as inorganic iodide ions, is ingested by the body via beverages and foods and localises mainly in the thyroid gland. The human thyroid gland is a small organ positioned in the throat region; its length is < 5cm and it weighs between 15 and 20 g, which is only about 1/3500 of the body weight of a reference 70 kg adult. The iodide ions are eventually utilised for the formation of thyroid hormones such as thyroxine and triiodothyronine. Iodine may also be found in trace amounts in the brain, heart and mammary glands (Kaiho 2015).

As the half-life of iodine-123 is about 13 h, the expiration date of its labelled pharmaceuticals is within 48 h of production. In other words, ^{123}I–labelled pharmaceuticals are manufactured on a particular day, delivered to hospitals the next day and used for clinical applications on the same day. Therefore, manufacturing methods should be as simple as possible (Kaiho 2015).

There are different types of ^{123}I radiopharmaceuticals that are used for different clinical applications (Table 6-2). However, inorganic sodium iodide ($Na^{123}I$) is the simplest type. $Na^{123}I$ is used for the diagnosis of thyroid dysfunction and thyroid tumours. It is usually administered orally (as capsules) to patients with activities ranging between 3.7 and 7.4 MBq, and imaging is normally done 3 to 24 h after administration.

Table 6-2: ^{123}I radiopharmaceuticals and their clinical applications (Kaiho 2015)

^{123}I- pharmaceuticals	**Clinical applications**
Iofetamine ^{123}I	Imaging agent (injection) used for the diagnosis of ischamic brain diseases
Ioflupane ^{123}I	Diagnostic imaging agent (injection) that has a high affinity for dopamine transporter (DAT). DAT is a membrane protein that is intensely expressed in the substantia nigra of the brain to reuptake dopamine released from nigrostriatal dopamine nerve terminals
Betamethyl-p-iodophenylpentadecanoic acid (BMIPP) ^{123}I	Diagnostic imaging agent (injection) for myocardial fatty acid metabolism
Iobenguane ^{123}I	Diagnosis of heart diseases Diagnosis of neuroblastomas Diagnosis of pheochromocytomas Detection of primary and metastatic pheochromocytomas and neuroblastomas Cardiac risk evaluation in heart failure patients
Iomazenil ^{123}I	Detection of epilepsy

When $Na^{123}I$ is administered orally to patients, radioactive iodide ions in the stomach gradually move into blood and accumulate chiefly in the thyroid gland (target organ). Within 24 h of administration, 10–40% of the radioactive iodine is located in the thyroid and is synthesised into thyroid hormones (such as thyroxine and triiodothyronine). In patients with hyperthyroidism, however, the thyroid uptake of radioactive iodine may be greater than 70%. The remaining radioactivity is excreted from the body in urine (Kaiho 2015).

$Na^{123}I$ is also available as an intravenous injection with activity between 3.7 and 14.8 MBq for an adult patient (70 kg). The lower activity is recommended for thyroid uptake studies, while the higher value is recommended for thyroid scintigraphy. However, the effective (whole body) dose depends on the uptake in the thyroid gland. Table 6-3, Table 6-4 and Table 6-5 show absorbed dose to a variety of organs for different thyroid

uptakes; six standard organs with the highest absorbed dose marked with * for (ICRP 1987).

Table 6-3: Absorbed and effective dose due to ^{123}I at a thyroid uptake of 15%

Organ	Absorbed dose per unit activity administered (mGy/MBq)				
	Adult	15 year	10 year	5 year	1 year
Adrenals	6.3E-03	8.3E-03	1.3E-02	2.0E-02	3.7E-02
*Bladder wall	7.6E-02	9.5E-02	1.4E-01	2.1E-01	3.8E-01
Bone surfaces	7.1E-03	9.1E-03	1.4E-02	2.2E-02	4.1E-02
Breast	4.7E-03	4.7E-03	7.3E-03	1.2E-02	2.3E-02
GI-tract:					
* Stomach wall	6.8E-02	8.5E-02	1.2E-01	2.0E-01	3.8E-01
* Small intest	4.3E-02	5.4E-02	9.1E-02	1.4E-01	2.7E-01
* ULI wall	1.8E-02	1.9E-02	2.9E-02	4.5E-02	7.7E-02
LLI wall	1.1E-02	1.4E-02	2.2E-02	3.3E-02	6.0E-02
Kidneys	1.0E-02	1.3E-02	1.8E-02	2.7E-02	4.6E-02
Liver	6.2E-03	7.6E-03	1.3E-02	2.1E-02	3.8E-02
Lungs	5.7E-03	7.2E-03	1.1E-02	1.8E-02	3.4E-02
Ovaries	1.2E-02	1.6E-02	2.5E-02	3.8E-02	6.8E-02
*Pancreas	1.4E-02	1.6E-02	2.4E-02	3.5E-02	6.1E-02
Red marrow	9.4E-03	1.2E-02	1.7E-02	2.5E-02	4.3E-02
Spleen	9.5E-03	1.1E-02	1.7E-02	2.5E-02	4.4E-02
Testes	5.3E-03	7.2E-03	1.2E-02	2.0E-02	3.8E-02
Thyroid	1.9E+00	3.0E+00	4.5E+00	9.8E+00	1.9E+01
Uterus	1.5E-02	1.9E-02	3.1E-02	4.9E-02	8.6E-02
Other tissue	6.8E-03	8.5E-03	1.3E-02	2.1E-02	3.9E-02
Effective Dose Equivalent (mSv/MBq)	**7.5E-02**	**1.1E-01**	**1.7E-01**	**3.5E-01**	**6.5E-01**

Table 6-4: Absorbed and effective dose due to ^{123}I at a thyroid uptake of 35%

Organ	Absorbed dose per unit activity administered (mGy/MBq)				
	Adult	15 year	10 year	5 year	1 year
Adrenals	6.5E-03	8.4E-03	1.3E-02	2.1E-02	3.8E-02
*Bladder wall	6.0E-02	7.4E-02	1.1E-01	1.6E-01	3.0E-01
Bone surfaces	7.9E-03	1.1E-02	1.6E-02	2.5E-02	4.6E-02
Breast	5.2E-03	5.2E-03	8.5E-03	1.5E-02	2.7E-02
GI-tract:					
* Stomach wall	6.8E-02	8.5E-02	1.2E-01	2.0E-01	3.8E-01
* Small intest	4.2E-02	5.4E-02	9.0E-02	1.4E-01	2.7E-01
* ULI wall	1.8E-02	1.9E-02	2.9E-02	4.5E-02	7.6E-02
LLI wall	1.0E-02	1.4E-02	2.1E-02	3.2E-02	5.8E-02
Kidneys	9.1E-03	1.1E-02	1.6E-02	2.4E-02	4.1E-02
Liver	6.3E-03	7.8E-03	1.3E-02	2.1E-02	4.0E-02
Lungs	6.5E-03	8.6E-03	1.4E-02	2.2E-02	4.2E-02
Ovaries	1.1E-02	1.5E-02	2.4E-02	3.7E-02	6.6E-02
*Pancreas	1.4E-02	1.6E-02	2.4E-02	3.6E-02	6.2E-02
Red marrow	1.0E-02	1.3E-02	1.9E-02	2.8E-02	4.8E-02
*Spleen	9.6E-03	1.1E-02	1.7E-02	2.5E-02	4.5E-02
Testes	5.0E-03	6.8E-03	1.1E-02	1.8E-02	3.5E-02
Thyroid	4.5E+00	7.0E+00	1.1E+01	2.3E+01	4.3E+01
Uterus	1.4E-02	1.7E-02	2.9E-02	4.4E-02	7.9E-02
Other tissue	8.0E-03	1.0E-02	1.6E-02	2.6E-02	4.9E-02
Effective Dose Equivalent (mSv/MBq)	**1.5E-01**	**2.3E-01**	**3.5E-01**	**7.4E-01**	**1.4E+00**

Table 6-5: Absorbed and effective dose due to ^{123}I at a thyroid uptake of 55%

Organ	Absorbed dose per unit activity administered (mGy/MBq)				
	Adult	15 year	10 year	5 year	1 year
Adrenals	6.5E-03	8.5E-03	1.4E-02	2.1E-02	3.9E-02
Bladder wall	4.3E-02	5.3E-02	7.9E-02	1.2E-01	2.2E-01
Bone surfaces	8.6E-03	1.2E-02	1.8E-02	2.8E-02	5.1E-02
Breast	5.6E-03	5.6E-03	9.5E-03	1.7E-02	3.1E-02
GI-tract:					
* Stomach wall	6.8E-02	8.5E-02	1.2E-01	2.0E-01	3.9E-01
* Small intest	4.2E-02	5.4E-02	9.1E-02	1.4E-01	2.7E-01
* ULI wall	1.8E-02	1.9E-02	2.9E-02	4.4E-02	7.6E-02
LLI wall	9.8E-03	1.3E-02	2.0E-02	3.0E-02	5.5E-02
Kidneys	9.1E-03	1.1E-02	1.6E-02	2.4E-02	4.1E-02
Liver	6.4E-03	7.9E-03	1.3E-02	2.2E-02	4.1E-02
Lungs	7.2E-03	9.7E-03	1.6E-02	2.6E-02	4.8E-02
Ovaries	1.1E-02	1.5E-02	2.3E-02	3.6E-02	6.4E-02
*Pancreas	1.4E-02	1.6E-02	2.5E-02	3.6E-02	6.3E-02
Red marrow	1.1E-02	1.5E-02	2.1E-02	3.0E-02	5.2E-02
*Spleen	9.7E-03	1.1E-02	1.7E-02	2.6E-02	4.6E-02
Testes	4.6E-03	6.2E-03	1.0E-02	1.6E-02	3.2E-02
Thyroid	7.0E+00	1.1E+01	1.7E+01	3.6E+01	6.8E+01
Uterus	1.2E-02	1.6E-02	2.6E-02	4.0E-02	7.2E-02
Other tissue	9.2E-03	1.2E-02	1.9E-02	3.1E-02	5.8E-02
Effective Dose Equivalent (mSv/MBq)	**2.3E-01**	**3.5E-01**	**5.3E-01**	**1.1E+00**	**2.1E+00**

6.4 Production of ^{123}I

The predominant method of ^{123}I production is the use of a cyclotron. ^{123}I can be produced by various nuclear reactions (Nikjou and Sadeghi 2018), but there are two main routes. The first is direct reactions, while the second is an indirect route via the decay of ^{123}Xe (Table 6-6) (Schlyer et al. 2009).

There are two common reactions to produce ^{123}I. The older one is ^{124}Te(p,2n) ^{123}I with a solid TeO_2 target from which the iodine could be distilled off under an inert gas flow at high temperature. This production method gives a relatively high yield of impurity. Besides the existence of a small quantity of ^{125}I impurity, it results in contamination with the higher energy radioisotope ^{124}I (β^+_{max}: 973.6 keV, annihilation radiation: 511 keV, gamma radiation: 603, 723, 1690 keV). Moreover, the radioiodine solution that is obtained is normally contaminated with traces of tellurium or tellurium oxide (TeO_2), which might sometimes significantly affect the labelling yield significantly (Eersels et al. 2005).

Table 6-6: Nuclear reactions to produce ^{123}I (Schlyer et al. 2009)

Nuclear reaction	Useful particle energy range (MeV)	Natural abundance of target material (%)
^{122}Te(d, n)^{123}I	14–8	2.4
^{123}Te(p, n)^{123}I	15–8	0.87
^{124}Te(p, 2n)^{123}I	26–20	4.6
^{121}Sb(^{4}He, 2n)^{123}I	15–25	57.4
^{123}Sb(^{3}He, 3n)^{123}I	20–30	42.6
^{124}Xe(p, pn)^{123}Xe:^{123}I	15–30	0.10
^{127}I(p, 5n)^{123}Xe:^{123}I	55+	100
^{127}I(d, 6n)^{123}Xe:^{123}I	83	100

The current method of ^{123}I production, which results in the least contamination with radioactive impurities, is the proton bombardment of highly enriched ^{124}Xe (Figure 6-2). The percentage activity of radionuclidic impurities, such as ^{125}I and ^{121}Te, is less than 0.05% with this technique (Eersels et al. 2005).

In this method, a target chamber is filled with ^{124}Xe under high pressure and irradiated with a beam of protons. After bombardment, the gas is kept in the chambe,r for several hours to allow for the radioactive decay of ^{123}Xe to ^{123}I (Eersels et al. 2005). The reaction requires an incident proton energy range between 20 and 30 MeV (Synowiecki et al. 2018).

The ^{123}I samples used in this study were produced by this method with a proton beam energy of 30 MeV and beam current of 270 µA.

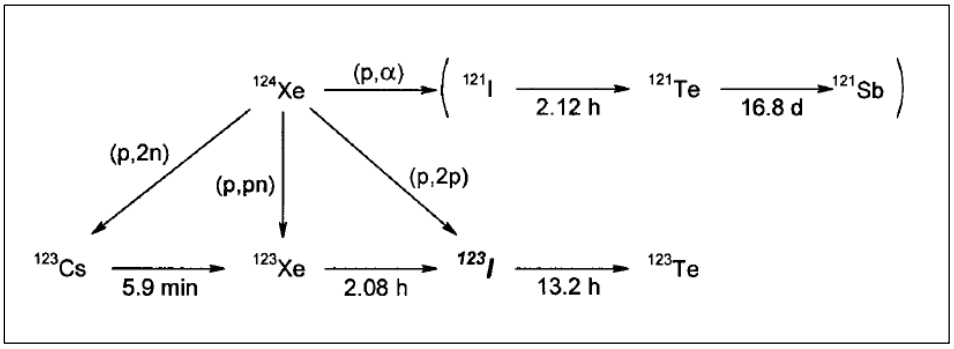

Figure 6-2: Production of ^{123}I from enriched ^{124}Xe (Eersels et al. 2005)

6.5 Previous studies of the measurement of the radionuclidic purity of ^{123}I

Undesirable contaminant radionuclides associated with the different ^{123}I production reactions degrade the resolution of gamma camera images and increase the absorbed radiation dose (Goolden et al. 1968; Wellman and Anger 1971; Baker et al. 1976; Hughes et al. 1979; Graham and Zielinski 1979; Hušák et al. 1980; Polak et al. 1983; Palmer and Rao 1985).

Each nuclear reaction has its own set of radionuclidic impurities that is produced alongside the main radionuclide ^{123}I. However, as mentioned earlier, the ^{123}I used in this study was produced using a proton reaction with isotopically enriched ^{124}Xe as a target gas. Thus, only studies dealing with this specific reaction will be discussed.

Several studies investigated this production method without addressing the radionuclidic purity of the product. For example, Sumiya and Sciani (2008) produced high-purity ^{123}I through the reactions ^{124}Xe(p, 2n)^{123}Cs with decay to ^{123}Xe and ^{123}I, and ^{124}Xe(p, pn)^{123}Xe with decay to ^{123}I. The target gas was irradiated with protons of energy 30 MeV. The target system consisted of a chamber made of copper coated with a thin layer of nickel. The cooling system comprised circuits of water and helium. After the irradiation, the target was left to cool in order for radioactive to decay to take place.

Lapolli et al. (2017) also produced ultrapure ^{123}I with the same reaction. An automated system was designed for the this purpose; it consisted of a target port, water cooling system, helium cooling system, cryogenic system, removal of ^{123}I and cleaning and

drying of the irradiation system. In this way, ^{123}I was successfully produced in a short time.

There are other studies in which the radionuclidic purity of ^{123}I has been assayed. Firouzbakht et al. (1987) found that the radionuclidic purity of ^{123}I depended on the experimental methods to recover it. ^{123}I was produced by the proton irradiation of enriched ^{124}Xe (isotopic enrichment of 20% and 40%) with an energy range of 15 to 34 MeV. Product yield was obtained using two procedures. The first involved the use of two different types of target cells, which after several methodological steps, were finally rinsed with NaOH. After allowing ^{123}Xe to decay in the vessel, the cells and the solutions were counted with a Ge(Li) detector to evaluate the concentration of ^{123}I and contaminants. In the second procedure, the xenon gas was removed from the cells after half an hour. It was found that the latter procedure gave ^{123}I without contamination (less than 0.1%), whereas the first procedure yielded a significant amount of ^{127}Cs and ^{129}Cs contaminants. These impurities arose from heavier isotopes of xenon in the 40% enriched gas.

Venikov et al. (1991) identified the level of radioactive contaminants (^{121}Te and ^{123}Te) in ^{123}I produced by proton-induced reactions. Again the target material was highly enriched ^{124}Xe (>99%). The energy and current of the proton beam were 35 MeV and 20 μA respectively. The ^{123}I was produced in the Institute of Atomic Energy (IAE), Moscow using target technology that involved cryogenic extraction of the product from the gas target. In the cryogenic facility, the irradiated xenon was transferred into a decay vessel located in a Dewar containing liquid nitrogen. The temperature in this vessel was raised to room temperature during the transfer; as ^{123}Xe decayed to ^{123}1, the latter radionuclide was absorbed onto the vessel walls.

The vessel was then cooled for an optimum time of 6.6 hrs. During cooling, the irradiated gas in this vessel was transferred to the initial one using the cryogenic technology, while the decay vessel with ^{123}1 on its internal walls was separated remotely. The ^{123}1 was thrown off into a container and then transferred to the radiochemical laboratory for use in labelling radiopharmaceuticals.

Product analysis revealed the existence of radionuclidic impurities with extremely low content. These impurities were ^{121}Te and ^{123}Te ($\leq 10^{-4}$%) and ^{125}I ($<10^{-3}$%).

Tárkányi et al. (1991) also determined the activity of ^{121}Te impurity in ^{123}I produced by two proton induced reactions in ^{124}Xe: (p, 2n) and (p, pn). The target vessels were stainless steel cells filled with ^{124}Xe at a specific pressure. These cells were irradiated in a cyclotron with different proton energies. The contents of the irradiated cells were left to decay for about 20 hrs, the cells were connected to a vacuum line and the irradiated ^{124}Xe gas was removed cryogenically. The activity of the radioiodine on the walls of the cells was determined 15-24 hrs after end of bombardment (EOB) using a Ge(Li) detector coupled to an Ortec 4k MCA. Photopeak analysis was done using Maestro II software. The distance between the detector and the gas cell was > 20cm.

Regarding the purity of the radioiodine solution, it was found that the contaminant ^{121}I was not identified in samples irradiated with proton energies ≤ 35 MeV. However, in production runs at proton energies 22-30 MeV, ^{121}Te, which is the decay product of ^{121}I, was present at an percentage activity of 5×10^{-05}% of ^{123}I and its level increased with increasing proton beam energy.

Venikov et al. (1993) determined the activity of ^{125}I impurity for a proton induced nuclear reaction in ^{124}Xe. The initial proton energies were 37, 35.1, 32 and 28.9 MeV. The impurity measurement was done at 6.6 hrs after the EOB of highly enriched ^{124}Xe (99% with 1% of ^{126}Xe). This contaminant activity was estimated for two processes. In the first, the irradiated gas was left in the target vessel to give the maximum activity of ^{123}I. In the second process, after the EOB, the irradiated gas was pushed to a decay vessel and left there for 6.6 hrs again obtain the maximum activity of ^{123}I. The activity in the gas capsules was assessed using a Ge(Li) detector. The activity of contaminant ^{125}I was higher for the second process than for the first one. For the first process, the estimation revealed that for the presence of 1% of ^{126}Xe in the target gas, the ^{125}I contaminant activity was <0.005% at the time of maximum activity of ^{123}I.

Hermanne et al. (2011) showed that ^{121}I ($t_{1/2}$ =2.12h) is unavoidable contaminant in the production of ^{123}I due to the ^{124}Xe(p,α) reaction. In this study ^{123}I was produced by proton irradiation of highly enriched ^{124}Xe in dedicated gas target set-ups, and utilising the decay chain ^{123}Cs–^{123}Xe–^{123}I. Measurements of ^{123}I were done using HPGe gamma-ray spectroscopy and gamma photopeaks were evaluated using Canberra GENIE analysis software. The activity of contaminant ^{121}Te ,which is a daughter of the short-lived ^{121}I, was derived for realistic production conditions. It was found that this activity of ^{121}Te, depended on different parameters such as target thickness, irradiation time,

^{123}I separation time and time of ^{123}I use after separation (AST). However, no specific permissible limits of ^{121}Te contamination are recommended by the European Pharmacopoeia.

Nikjou and Sadeghi (2018) investigated the activities of ^{122}I, ^{123}Xe and ^{122}Xe in ^{123}I. Several nuclear reactions were evaluated, one of which was the proton reaction ^{124}Xe(p,2n)^{123}Cs. The activity of ^{123}I produced via this reaction was theoretically calculated and compared with the experimental value. The theoretical percentages of the impurities were also estimated. The contaminant values were ^{122}I ($t_{1/2}$= 3 min) 0.001%, ^{123}Xe ($t_{1/2}$= 2 hrs) 39.77%, ^{122}Xe ($t_{1/2}$= 20 hrs) 14.65%. The contamination activity of both ^{121}I (which decreased with time) and ^{121}Te (which increased with time) were presented as functions of AST. A 1% ^{121}I contamination activity decreased to a permissible 5×10^{-4} % at AST=52 h.

As regards contaminants within the ^{123}I samples investigated in this present study, the product leaflet provided by the supplier (GE Healthcare) indicated that the main radionuclidic impurities were ^{125}I and ^{121}Te with values less than 0.05% at calibration time, exactly the same as the value repeated by Eersels et al. (2005).

The aim of this portion of the thesis is to investigate the activity of these contaminants and to look for other radioactive impurities in ^{123}I.

6.6 Assessment of the radionuclidic purity of ^{123}I delivered to the University Hospital of Wales

6.6.1 Method

Sodium iodide (^{123}I) was supplied by GE Healthcare to the Medical Physics Department at the University Hospital of Wales once each fortnight. The solution was provided in a special vial with a volume of 10 ml with a reference activity of 370 MBq. After the required volume of solution had been used for clinical purposes, the residual volume (if there was some left) was taken for the assessment of radionuclidic impurities.

The residual volume had to be prepared to the same standards as used for HPGe efficiency calibration i.e. contained in a standard vial (Schott vial) with a standard volume (4 ml). Dilution was done for one sample as the available residual volume was

less than 4 ml and for some of the other samples to avoid a long waiting time for the ^{123}I to decay until a suitably low dead-time was achieved with the HPGe detector.

Ten ^{123}I samples were prepared in-house. For each one, an empty Schott vial was weighed 5 times using the electronic weighing scales (Oertling NA 114) and 4 ml of sodium iodide (^{123}I) solution was dispensed into the vial using a pipette. The weight of the vial was measured again to determine the exact volume dispensed. For the samples that required dilution, 2 ml of sodium iodide (^{123}I) solution was dispensed into a pre-weighed Schott vial. The vial was weighed again to calculate the solution volume accurately and to determine precisely how much tap water needed to be added to the vial to make the volume up to 4 ml.

The ^{123}I activity of the samples prepared under standard conditions was determined using the Fidelis secondary standard radionuclide calibrator. No correction was required as an appropriate calibration factor corresponding to the standard conditions was available.

Each sample was left to decay for a sufficient time to be measurable in the HPGe detector with a reasonable dead time. Vials were put at the centre of the capped detector. The live time was set to obtain 10,000 counts within the photopeaks of the main impurities, which were ^{125}I and ^{121}Te as mentioned by the supplier in the product leaflet (GE Healthcare 2011). Spectra were acquired, contaminants were identified, NCRs (c/s) were calculated and corrected for decay during counting. In addition to ^{125}I and ^{121}Te, the impurities ^{96}Tc, ^{126}I and ^{124}I were also identified together with trace amounts of ^{95m}Tc (Gilbert 2018).The HPGe detector efficiency at each contaminant gamma energy was calculated. From equation 2-17, the activity of the impurities within the sodium iodide (^{123}I) solution was determined.

The activities of both the main radionuclide ^{123}I and the identified impurities were decay corrected to the reference time in the product delivery note and the contaminant activity expressed as a percentage of ^{123}I activity. The mean and the standard deviation (SD) were calculated for the ten samples.

6.6.2 Result

Figure 6-3 shows a typical spectrum of a sodium iodide (^{123}I) solution recorded with the HPGe detector. The main photopeaks and sum peaks are listed in Table 6-7.

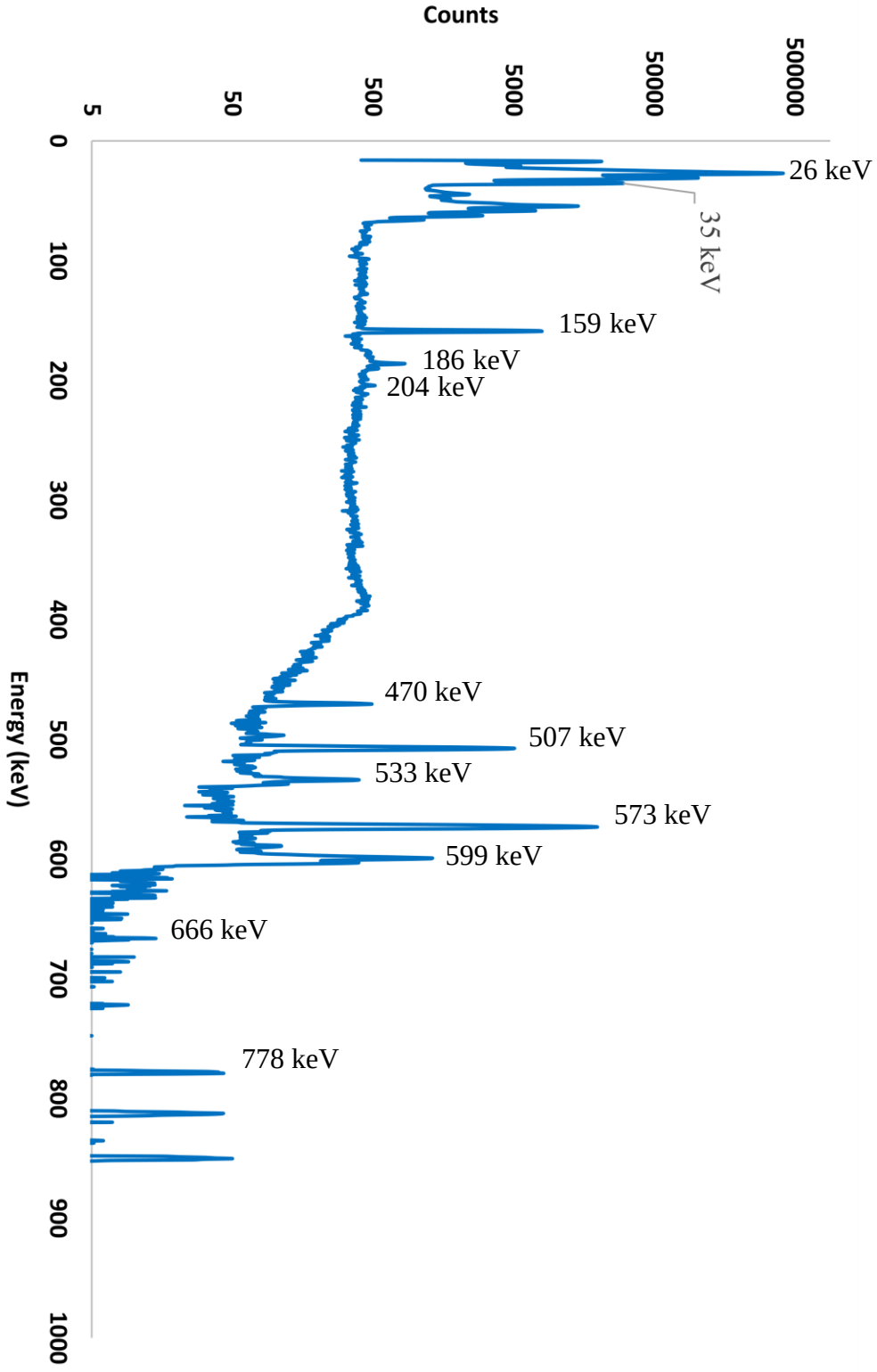

Figure 6-3: Typical sodium iodide (^{123}I) spectrum recorded with the HPGe detector

Table 6-7: Observed photopeaks and sum peaks in the spectrum of ^{131}I

Gamma energy (keV)	Yield	Description
≈ 26	0.615	^{121}Te x-ray photopeak
≈ 27	0.704	^{123}I x-ray photopeak
35	0.0667	^{125}I radionuclidic impurity photopeak
159	0.828	^{123}I Main radionuclide photopeak
186	/	^{123}I sum peak (159 keV and 27 keV x-ray)
204	0.619	^{95m}Tc radionuclidic impurity photopeak
470	0.0141	^{121}Te radionuclidic impurity photopeak
507	0.177	^{121}Te radionuclidic impurity photopeak
533	/	^{121}Te sum peak (507 keV and 26 keV x-ray)
573	0.803	^{121}Te radionuclidic impurity photopeak
599	/	^{121}Te sum peak (573 keV ^{121}Te and 26 keV x-ray)
666	0.331	^{126}I radionuclidic impurity photopeak
778	0.101	^{96}Tc radionuclidic impurity photopeak

Table 6-8 shows the ^{125}I activity (measured with the HPGe detector) as the percentage of the ^{123}I activity (measured with Fidelis calibrator).

Table 6-9 and Table 6-10 show the corresponding data for ^{121}Te (based on its two gamma peaks at 573 keV and 507 keV). The percentage difference between the activities derived from these two photopeaks was just 1.05 %.

Table 6-11, Table 6-12 and Table 6-13 show the activities of ^{126}I, ^{124}I and ^{96}Tc as a percentage of ^{123}I activity respectively. Traces of another contaminants (^{95m}Tc, 204 keV) were also seen in some samples. Table 6-14 show the corresponding data for this radioactive impurity.

Table 6-8: ^{125}I activity as a percentage of ^{123}I activity

Sample no.	Net Peak Area	NCR (cps)	Corrected NCR	^{125}I activity (HPGe) (MBq)	^{123}I activity (Fidelis) (MBq)	% ^{125}I/^{123}I
1	84927	34.0	34.0	0.006	35.3	0.0169
2	122588	81.7	81.7	0.021	155.4	0.0138
3	80656	80.7	80.7	0.019	156.4	0.0121
4	119358	91.8	91.8	0.023	155.2	0.0150
5	155063	77.5	77.5	0.019	157.3	0.0121
6	91314	60.9	60.9	0.011	77.9	0.0143
7	78841	52.6	52.6	0.010	80.1	0.0120
8	78105	65.1	65.1	0.012	77.8	0.0155
9	91018	75.8	75.9	0.014	77.4	0.0180
10	81211	62.5	62.5	0.011	77.2	0.0149
Mean						**0.0145**
SD						**0.0021**

Table 6-9: ^{121}Te activity (based on 573 keV photopeak) as a percentage of ^{123}I activity

Sample no.	Net Peak Area	NCR (cps)	Corrected NCR	^{121}Te activity (HPGe) (MBq)	^{123}I activity (Fidelis) (MBq)	% ^{121}Te /^{123}I
1	62273	24.9	24.9	0.0015	35.3	0.00437
2	52261	34.8	34.9	0.0090	155.4	0.00577
3	44653	44.7	44.7	0.0077	156.4	0.00490
4	45319	34.9	34.9	0.0080	155.2	0.00513
5	80036	40.0	40.0	0.0080	157.3	0.00511
6	83717	55.8	55.8	0.0040	77.9	0.00518
7	108595	72.4	72.4	0.0052	80.1	0.00654
8	68756	57.3	57.3	0.0043	77.8	0.00554
9	63837	53.2	53.2	0.0038	77.4	0.00497
10	77148	59.3	59.4	0.0043	77.2	0.00557
Mean						**0.00531**
SD						**0.00059**

Table 6-10: ^{121}Te activity (based on 507 keV photopeak) as a percentage of ^{123}I activity

Sample no.	Net Peak Area	NCR (cps)	Corrected NCR	^{121}Te activity (HPGe) (MBq)	^{123}I activity (Fidelis) (MBq)	% ^{121}Te /^{123}I
1	15631	6.3	6.3	0.0016	35.3	0.00439
2	12860	8.6	8.6	0.0088	155.4	0.00569
3	11033	11.0	11.0	0.0076	156.4	0.00484
4	11174	8.6	8.6	0.0079	155.2	0.00507
5	19958	10.0	10.0	0.0080	157.3	0.00510
6	20570	13.7	13.7	0.0040	77.9	0.00510
7	26723	17.8	17.8	0.0052	80.1	0.00644
8	17208	14.3	14.3	0.0043	77.8	0.00555
9	15879	13.2	13.2	0.0038	77.4	0.00495
10	18853	14.5	14.5	0.0042	77.2	0.00545
Mean						**0.00526**
SD						**0.00056**

Table 6-11: ^{126}I activity as a percentage of ^{123}I activity

Sample no.	Net Peak Area	NCR (cps)	Corrected NCR	^{126}I activity (HPGe) (MBq)	^{123}I activity (Fidelis) (MBq)	% ^{126}I /^{123}I
1	43.6	0.017	0.017	3.35×10^{-6}	35.3	9.48×10^{-6}
2	16.9	0.011	0.011	1.39×10^{-5}	155.4	8.95×10^{-6}
4	22.0	0.017	0.017	1.79×10^{-5}	156.4	1.15×10^{-6}
5	24.7	0.012	0.012	1.10×10^{-5}	155.2	7.01×10^{-6}
6	40.3	0.027	0.027	6.32×10^{-6}	157.3	8.11×10^{-6}
8	17.1	0.014	0.014	3.53×10^{-6}	77.9	4.54×10^{-6}
9	39.6	0.033	0.033	7.76×10^{-6}	80.1	1.00×10^{-5}
10	36.1	0.028	0.028	6.55×10^{-6}	77.8	8.48×10^{-6}
Mean						**8.51×10^{-6}**
SD						**2.09×10^{-6}**

Table 6-12: ^{124}I activity as a percentage of ^{123}I activity

Sample no.	Net Peak Area	NCR (cps)	Corrected NCR	^{124}I activity (HPGe) (MBq)	^{123}I activity (Fidelis) (MBq)	% ^{124}I /^{123}I
1	58.8	0.024	0.024	3.62×10^{-5}	35.3	1.03×10^{-4}
6	302.9	0.202	0.202	5.85×10^{-4}	77.9	7.51×10^{-4}
7	22.1	0.015	0.015	4.27×10^{-5}	80.1	0.53×10^{-4}
8	18.5	0.015	0.015	5.23×10^{-5}	77.8	0.67×10^{-4}
Mean						**2.43×10^{-4}**
SD						**3.39×10^{-4}**

Table 6-13: ^{96}Tc activity as a percentage of ^{123}I activity

Sample no.	Net Peak Area	NCR (cps)	Corrected NCR	^{96}Tc activity (HPGe) (MBq)	^{123}I activity (Fidelis) (MBq)	% ^{96}Tc /^{123}I
1	342.6	0.137	0.137	2.24×10^{-5}	35.3	6.34×10^{-5}
6	295.0	0.197	0.197	5.96×10^{-5}	77.9	7.64×10^{-5}
7	230.8	0.154	0.154	4.67×10^{-5}	80.1	5.82×10^{-5}
8	40.3	0.034	0.034	1.19×10^{-5}	77.8	1.53×10^{-5}
9	198.2	0.165	0.165	5.00×10^{-5}	77.4	6.46×10^{-5}
10	187.7	0.144	0.145	4.39×10^{-5}	77.2	5.69×10^{-5}
Mean						**5.58×10^{-5}**
SD						**2.10×10^{-5}**

Table 6-14: ^{95m}Tc activity as a percentage of ^{123}I activity

Sample no.	Net Peak Area	NCR (cps)	Corrected NCR	^{95m}Tc activity (HPGe) (MBq)	^{123}I activity (Fidelis) (MBq)	% ^{95m}Tc /^{123}I
3	178.3	0.178	0.178	5.11×10^{-6}	156.359	3.27×10^{-6}
5	311.3	0.156	0.156	4.66×10^{-6}	157.307	2.96×10^{-6}
10	274.0	0.211	0.211	4.75×10^{-6}	77.184	6.15×10^{-6}
Mean						**4.13×10^{-6}**
SD						**1.76×10^{-6}**

6.6.3 Discussion

Ten samples of ^{123}I sodium iodide were prepared in standard vials and volumes similar to those used for the efficiency calibration of the HPGe detector.

Various ^{123}I radionuclidic impurities were identified in this study; these were: ^{125}I, ^{121}Te, ^{126}I, ^{124}I, ^{96}Tc, ^{95m}Tc. The first two impurities have been reported in the literature. However, there have been no reports of the existence of ^{126}I, ^{124}I, ^{96}Tc, ^{95m}Tc as impurities produced by proton reactions in isotopically enriched ^{124}Xe.

The ^{125}I impurity had the highest percentage activity and it was identified in all samples of this study. The mean value was 0.0145 % of ^{123}I activity and this was within the limit given by the supplier. However, it was higher than values reported in the literature due to different irradiation conditions such as proton energy.

The existence of the ^{125}I contaminant was attributed to the reaction: ^{126}Xe (p,pn) ^{125}Xe with ^{125}Xe ($t_{1/2}$=17.1 hrs) decaying to ^{125}I ($t_{1/2}$=60 d). Here ^{126}Xe was an impurity within the target gas ^{124}Xe.

The existence of ^{121}Te as a contaminant has also been reported in the literature. The two gamma photopeaks of ^{121}Te were analysed in this study (573 keV and 507 keV). There was a significant difference ($P<0.05$) between the activities derived from these two peaks of ^{121}Te. This is likely to be due to the existence of sum peaks. However, the percentage difference between the activites was just 1.05%. Thus, the use of both peaks was judged to be valid for the estimation of ^{121}Te contamination in the ^{123}I samples.

^{121}Te was identified in all samples of this study. The mean activity of this contaminant was 0.0053 % of the ^{123}I main radionuclide activity, which is within the limit given in the leaflet provided by the supplier. Similar to ^{125}I, the level of this contaminant was higher than reported in the literature, again due to different irradiation conditions. The existence of this impurity in this study was attributed to the reaction ^{124}Xe (p,α) with ^{121}I ^{121}I ($t_{1/2}$=2.12 hrs)decaying ^{121}Te ($t_{1/2}$=16.8 d).

It was mentioned in the product delivery note (GE Healthcare 2011) that the existence of these two impurities (^{125}I and ^{121}Te) increases the effective dose by approximately 0.6% at the calibration time.

The percentage activities of ^{126}I and ^{124}I were 8.51×10^{-6} and 2.43×10^{-4} respectively. As mentioned earlier, these contaminants have not been reported in the literature on proton reactions in isotopically enriched ^{124}Xe. It is worth mentioning that these two impurities were not identified in all the samples; ^{126}I was noted in 8 samples, whereas ^{124}I was seen in just 4 samples out of 10.

^{96}Tc and ^{95m}Tc have also not been reported in the literature. Their percentage activities were 5.58×10^{-5} and 4.13×10^{-6} respectively. Their existence as trace impurities was ascribed to the activation of the target chamber and the entrance foil during bombardment. Again, these two impurities were not identified in all the samples; ^{96}Tc was noted in 6 samples, whereas ^{95m}Tc was identified in just three.

6.7 Properties of ^{131}I

This reactor-produced radioisotope was discovered at the University of California in 1938. ^{131}I is by far the most widely used radioiodine isotope for therapeutic applications on patients suffering from hyperthyroidism, persons who have long lives ahead of them (Rhodes and Croft 1978; Neacsu et al. 2013). It is also used for the treatment of thyroid cancer. It is suitable for therapeutic applications because it is a beta-emitting radionuclide, with a principal beta emission energy of about 610 keV. The beta particles normally have a range of 0.5–2 mm in human tissues (Chilton and Witcofski 1986).

This radioiodine has many gamma photopeaks; the predominant one having energy 364 keV (Figure 6-4 and Table 6-15), the half-life is 8.1 days. This value of half-life makes ^{131}I convenient for radiolabelling compounds for slow-uptake target organs.

Conversely, the short half-life of ^{123}I limits it usefulness for those compounds that have a prolonged clearance process from the blood (Chilton and Witcofski 1986).

Iodine enters the human body through ingestion, inhalation or penetration through the skin. Once in the body, it is concentrated in the thyroid gland. A high activity of ^{131}I in a contaminated environment from radioactive fallout gives a high radiation dose to the thyroid. Thus, there is an increased chance of radiogenic thyroid cancer occurring in later life or at least the possibility of thyroiditis (Rivkees et al. 1998).

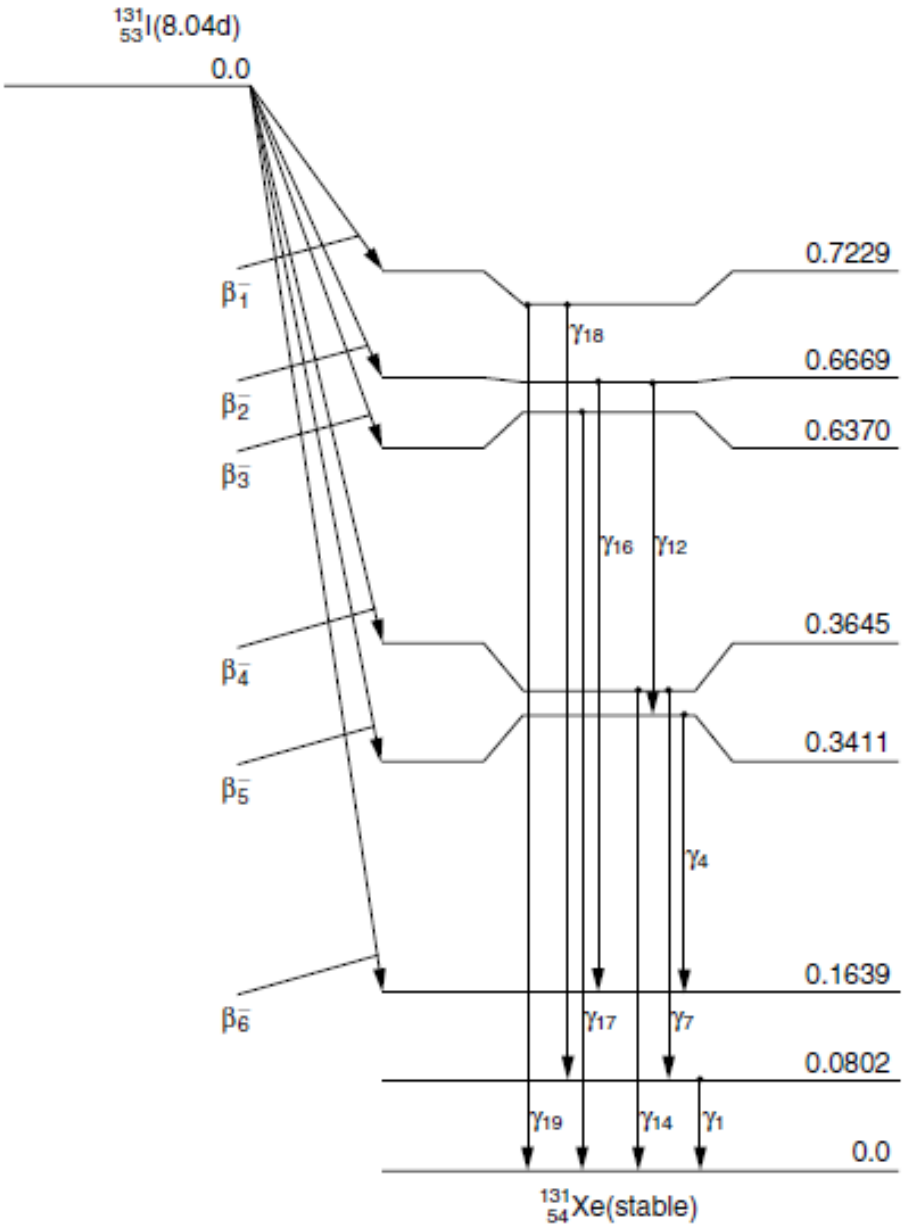

Figure 6-4: Decay scheme of ^{131}I with energies in MeV (Cherry et al. 2012)

Table 6-15: Emissions of ^{131}I where y(i) is the yield per disintegration, E(i) is the energy of the emission, y(i)×E(i) is the product of the yield and the energy of the disintegration and ce represents conversion electrons (Cherry et al. 2012)

Radiation	*y(i)* $(Bq \cdot s)^{-1}$	*E(i)* (MeV)	*y(i)* × *E(i)*
β^- 1	2.13E-02	6.935E-02*	1.48E-03
β^- 2	6.20E-03	8.693E-02*	5.39E-04
β^- 3	7.36E-02	9.660E-02*	7.11E-03
β^- 4	8.94E-01	1.915E-01*	1.71E-01
β^- 6	4.20E-03	2.832E-01*	1.19E-03
γ 1	2.62E-02	8.018E-02	2.10E-03
ce-K, γ 1	3.63E-02	4.562E-02	1.66E-03
ce-L_1, γ 1	4.30E-03	7.473E-02	3.21E-04
γ 4	2.65E-03	1.772E-01	4.70E-04
γ 7	6.06E-02	2.843E-01	1.72E-02
ce-K, γ 7	2.48E-03	2.497E-01	6.20E-04
γ 12	2.51E-03	3.258E-01	8.18E-04
γ 14	8.12E-01	3.645E-01	2.96E-01
ce-K, γ 14	1.55E-02	3.299E-01	5.10E-03
ce-L_1, γ 14	1.71E-03	3.590E-01	6.13E-04
γ 16	3.61E-03	5.030E-01	1.82E-03
γ 17	7.27E-02	6.370E-01	4.63E-02
γ 18	2.20E-03	6.427E-01	1.41E-03
γ 19	1.80E-02	7.229E-01	1.30E-02
$K\alpha_1$ X ray	2.59E-02	2.978E-02	7.72E-04
$K\alpha_2$ X ray	1.40E-02	2.946E-02	4.12E-04

6.8 Clinical applications of ^{131}I

Sodium iodide ^{131}I has been utilised for both diagnostic and therapeutic purposes. It has been used for 60 years in the treatment of thyroid hyperfunction. For diagnostic procedures, it may be given as a tracer to study radioiodine kinetics. Thyroid uptake obtained with such a tracer dose can be used to calculate the activity required for radioiodine therapy. In the management of thyroid carcinoma, sodium iodide is used to detect thyroid remnants and metastases (after ablation).

Radioiodide thyroid therapy is useful for:

- Graves' disease, toxic multinodular goitre or autonomous nodules
- Papillary and follicular thyroid carcinoma including metastatic disease.

Sodium iodide ^{131}I is available as capsules and as an injection. It is normally administered orally in activities ranging between 0.185 and 3.7 MBq for diagnostic

purposes. For therapy, it is administered orally in multiple doses greater than 1000 times the comparable diagnostic activity (up to 7.4 GBq per dose) (Kaiho 2015).

When ^{131}I is administered intravenously, the recommended activity for an adult patient with a weight of 70 kg ranges between 0.2 and 3.7 MBq for thyroid uptake studies and 7.4 and 11 MBq for thyroid imaging. A maximum activity of 400 MBq is used for the identification of metastases and thyroid remnants after thyroid ablation.

There are other ^{131}I radiopharmaceuticals such as tositumomab, which is one of the few successful examples of a radioimmunotherapy agent. It was approved in the United States in 2004 as the world's first pharmaceutical for radioimmunotherapy. Tositumomab is a monoclonal antibody (MoAb) and the ^{131}I label is suitable for radioimmunotherapy due to the fact that its half-life is similar to the biological half-life of MoAbs *in vivo* (Kaiho 2015).

6.8.1 Production of ^{131}I

^{131}I can be obtained by two different methods: the irradiation of a tellurium target (^{130}Te) in a nuclear reactor or by separation from uranium (^{235}U) fission fragments (Neacsu et al. 2013).

6.8.1.1 ^{131}I production by irradiation of ^{130}Te

The nuclear reactions for producing ^{131}I by the irradiation of ^{130}Te in a nuclear reactor have been given by Neacsu et al. (2013) (Figure 6-5). The target material can be either tellurium dioxide (TeO_2) or metallic tellurium (Te). Table 6-16 shows the abundance of different tellurium isotopes in target material with natural composition.

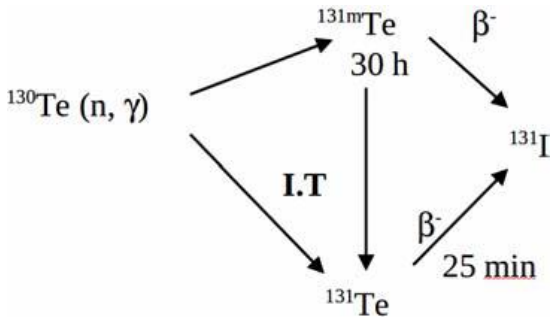

Figure 6-5: Nuclear reactions in a tellurium target for iodine-131 production (Neacsu et al. 2013)

Table 6-16: Abundance of different tellurium isotopes in natural target material

Tellurium Isotope	Isotopic abundance [%]
^{120}Te	0.09
^{122}Te	2.47
^{123}Te	0.89
^{124}Te	4.74
^{125}Te	7.03
^{126}Te	18.72
^{128}Te	31.75
^{130}Te	34.24

As the natural target material contains different tellurium isotopes (not just ^{130}Te), its irradiation can result in the production of radionuclidic impurities or stable isotopes, which are presented in Table 6-17.

Table 6-17: Tellurium isotope impurities produced by the irradiation of natural tellurium

Target isotope	Isotope produced by irradiation	$t_{1/2}$	Disintegration products
^{120}Te	^{121m}Te	130 days	^{121}Te $\rightarrow$ ^{121}Sb (stable)
	^{121}Te	17 days	
^{122}Te	^{123m}Te	104 days	^{123}Te (stable)
^{123}Te	^{124}Te	stable	
^{124}Te	^{125m}Te	58 days	^{125}Te (stable)
^{125}Te	^{126}Te	stable	
^{126}Te	^{127m}Te	104 days	^{127}Te $\rightarrow$ ^{127}I (stable)
	^{127}Te	9.3 hrs	
^{128}Te	^{129m}Te	33 years	^{129}Te $\rightarrow$ ^{129}I (stable)
	^{129}Te	7.4 min	

6.8.1.2 ^{131}I production by separation from the uranium (^{235}U) fission fragments

There are many routes by which ^{131}I is produced as a fission product. One possibility is the following reaction:

$$^{235}_{92}U\ (n, f)\ ^{131}_{53}\mathrm{I} + \ ^{101}_{39}Y + 4\ n \quad \text{.....Equation 6-1}$$

However, it is also produced by the radioactive decay of other fission products. In this method, ^{131}I is normally separated by a complicated radiochemical process followed by advanced purification. As regards potential impurities, ^{235}U fission generates more than 300 different radionuclides that appear in nearly 90 decay chains. During the fission process, many iodine isotopes are generated (Table 6-18). These nuclides are isolated along with ^{131}I during the process of chemical purification. For stable or long lived nuclides, the yields are very small and do not reach a value that may cause a significant decrease in the specific activity of ^{131}I. After purification, ^{131}I is usually contaminated with two short lived radionuclides: ^{133}I and ^{135}I. The ratio of the activities of both these radionuclides to that of the main radionuclide ^{131}I quickly decreases with time, and in turn the contamination level decreases.

Table 6-18: Iodine isotopes generated during the fission process

Isotope	$t_{1/2}$	Fission yield (%)
^{127}I	stable	0.13
^{129}I	1.7×10^7 years	0.8
^{131}I	8.1 days	3.1
^{132}I	2.3 hrs	4.7
^{133}I	20.8 hrs	6.62
^{134}I	52.5 minutes	8.06
^{135}I	6.7 hrs	6.3

The sodium iodide (^{131}I) samples included in this study were produced by this method as reported by the supplier. It was also reported that the only possible radionuclidic impurities were other iodine isotopes and the specified radionuclidic purity was greater than 99.9 %.

6.8.2 Previous studies of the measurement of the radionuclidic purity of ^{131}I

There are not many studies dealing with the evaluation of the radionuclidic purity of ^{131}I. However, such an investigation was done by Iwahara et al. (2001) using gamma-ray spectrometry with a germanium detector. No impurities were found in their ^{131}I samples.

Neacsu et al. (2013) assessed the radionuclidic purity of sodium iodide (^{131}I) solution and sodium iodide (^{131}I) capsules used for diagnosis purposes. A HPGe detector with a built-in amplifier and coupled to a MCA was used to do the evaluation. A basic gamma-ray spectrometry system was employed (Canberra S 502C-GENIE 2000).. The sample was either the radiopharmaceutical sodium iodide (^{131}I) solution, or a solution obtained by dissolution a sodium iodide (^{131}I) capsule in distilled water. A volume of 10 μL was dropped onto a paper stripe, which was placed in a glass container with a rubber stopper to prevent detector contamination. This container was placed at the centre of the detector and the spectrum was acquired with a measuring time of 1000 s. The distance between the sample and the detector was determined according to the sample activity so that the dead time was less than 10%

It was found that more than 99.9% of the total sample activity was ascribed to the presence of ^{131}I, while less than 0.1% was attributed to the presence of ^{133}I and ^{135}I and other possible radioactive contaminants. However, these suspected contaminants were not identified as visible in the acquired gamma radiation spectrum.

6.8.3 Assessment of radionuclidic purity of ^{131}I delivered to University Hospital of Wales

6.8.3.1 Method

A similar procedure to that implemented for sodium iodide (^{123}I) was used. Sodium iodide (^{131}I) was also supplied by GE Healthcare to the Medical Physics Department at the University Hospital of Wales once each fortnight. The solution was provided in a special vial with a volume of 10 ml with a reference activity of 1850 MBq. After the required volume of solution had been used for clinical purposes, the residual volume (if there was some left) was taken for the assessment of radionuclidic impurities.

The preparation of the ^{131}I samples was done in-house. Five samples in a standard Schott vial with a standard 4ml volume were prepared. For each one, an empty Schott vial was weighed 5 times using the electronic weighing scales (Oertling NA 114). In most cases, the original vial was essentially empty. Therefore, it was washed very well using tap water and 4 ml of the diluted sodium iodide (^{131}I) solution was dispensed into the weighed Schott vial. The weight was measured again to obtain the exact volume in the vial.

The ^{131}I activity of the samples prepared in this way was determined using the Fidelis secondary standard radionuclide calibrator. The samples were then left to decay for a sufficient time to be measurable in the HPGe detector with reasonable dead time. Spectra were acquired for about an hour.

6.8.3.2 Results

Figure 6-6 shows a typical spectrum of a sodium iodide (^{131}I) solution recorded with the HPGe detector. This spectrum shows gamma photopeaks of the main radionuclide ^{131}I (80, 163, 177, 284, 325, 364, 405, 503, 637 and 723 keV) and one peak with an energy of 314 keV.

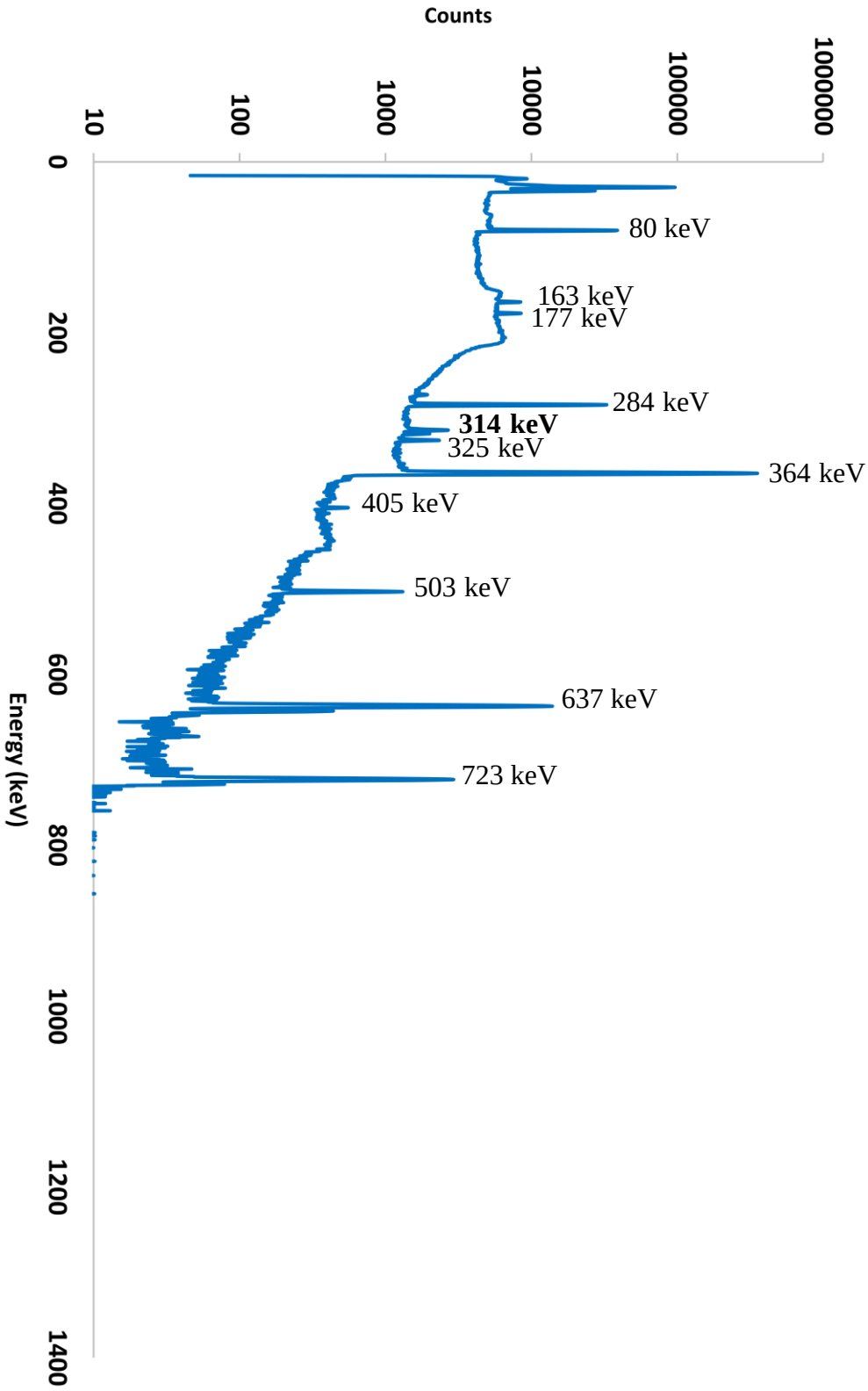

Figure 6-6: Typical spectrum of sodium iodide (^{131}I) recorded with the HPGe detector

6.8.3.3 Discussion

No identifiable impurities were found within the sodium iodide ^{131}I spectra. This agreed with the literature. However, a peak at 314 keV, which was not associated with the decay of ^{131}I, was seen in all the spectra. Its origin was not identified. It might be possible to obtain further information by repeated measurement of one sample and determining the half-life of the decrease of the NCR of this peak with time.

Chapter 7

Radionuclidic Purity of Cyclotron-Produced Gallium-68

7.1 Introduction

Gallium-68 is a positron emitting radionuclide that is having a great impact in nuclear medicine. In particular, it is used to good effect in positron emission tomography (PET) imaging, which is a non-invasive medical imaging technology that can produce relatively high resolution images of physiologic function with clinical application in cardiology, oncology and neurology.

An important feature of the decay of ^{68}Ga is its high positron abundance. In recent years, the radionuclide has been used for different clinical applications in PET imaging, such as the diagnosis of malignancies, especially neuroendocrine tumours (NETs) (Jalilian 2016). This gives an indication of the great importance and future impact zof^{68}Ga radiopharmaceuticals in human health.

As with other radionuclide imaging, the quality control of radiopharmaceuticals labelled with ^{68}Ga is important to avoid unnecessary radiation dose to the patients due to the presence of long-lived impurities as will be explained later in this chapter.

7.2 Properties of ^{68}Ga

Gallium (Ga) was discovered by a French chemist called Paul E. Lecoq de Boisbaudran in Paris (1875) using a spectroscope. Gallium has 24 different isotopes with mass numbers between 61 and 84. Of these isotopes, two are stable; these are ^{69}Ga and ^{71}Ga with natural abundances of 60.1% and 39.9% respectively. Among the available Ga radioisotopes, three are well known and widely used in the field of nuclear medicine (^{66}Ga, ^{67}Ga and ^{68}Ga). Of these, Ga-68 has the appropriate positron emission for use in PET imaging. The physical properties of ^{68}Ga make it an interesting radionuclide for developing new PET tracers (Jalilian 2016). Gallium-68 decays with a half-life of 67.71 min by a combination of EC and positron emission to the ground state of ^{68}Zn (Figure 7-1 and Table 7-1).

Different ^{68}Ga-labeled compounds have been developed for use in medical applications where the physical half-life of this radionuclide corresponds well with the biological half-life of synthetic peptides. The development of ^{68}Ga radiopharmaceuticals has occurred in parallel with the development of peptide-based pharmaceuticals during the last two decades. ^{68}Ga-labelled tetraazacyclododecane-

tetraacetic acid (DOTA) combined with somatostatin analogue octreotide (NOC) (^{68}Ga-DOTANOC) is an example of one of these ^{68}Ga radiopharmaceuticals (Jalilian 2016).

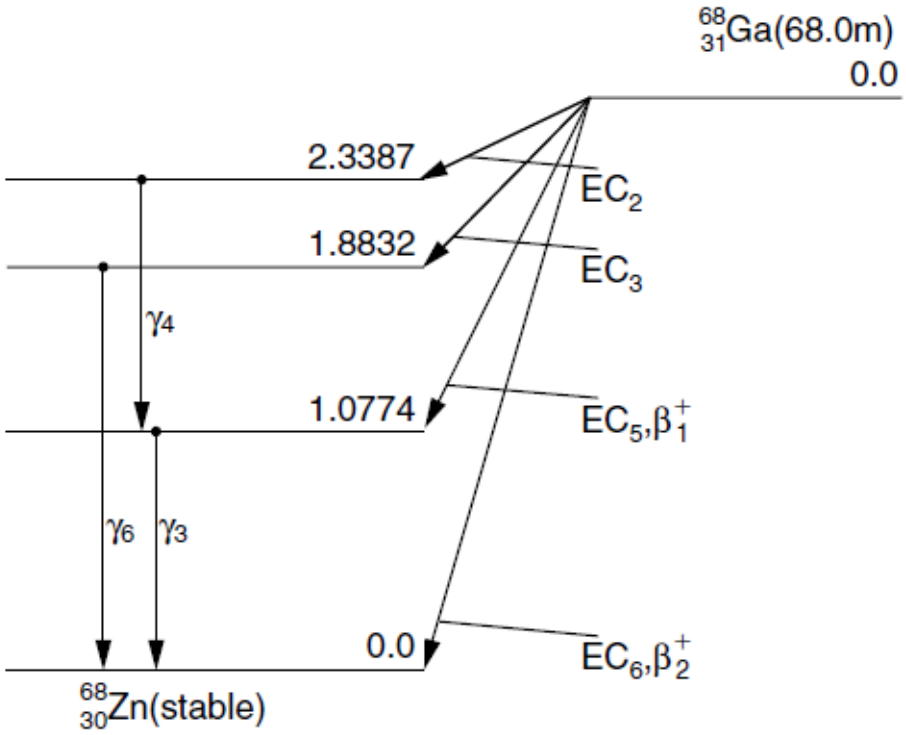

Figure 7-1: Decay scheme of gallium-68 (Cherry et al. 2012)

Radiation	*y(i)* (Bq•s)$^{-1}$	*E(i)* (MeV)	*y(i)* × *E(i)*
β^+ 1	1.08E-02	3.526E-01*	3.80E-03
β^+ 2	8.79E-01	8.358E-01*	7.35E-01
γ±	1.78E 00	5.110E-01	9.10E-01
γ 3	3.30E-02	1.077E 00	3.56E-02
γ 4	9.90E-04	1.261E 00	1.25E-03
γ 6	1.43E-03	1.883E 00	2.69E-03

Table 7-1: Emissions of ^{68}Ga. y(i) is the yield per disintegration, E(i) is the energy of the emission and y(i)×E(i) is the product of the yield and the energy of the disintegration (Cherry et al. 2012)

7.3 Clinical applications of ^{68}Ga

An important aspect of the development of ^{68}Ga radiopharmaceuticals is the theranostic properties of the radionuclide. Theranostics is a combination of therapeutic (‘thera’-) emissions such as beta particles, alpha particles or Auger electrons, and diagnostic (-‘nostic’) emissions such as gamma radiation or positrons. Key advantages of these properties include the personalisation of therapy based on the uptake of the lower-dose diagnostic radiopharmaceutical. This includes the optimisation of radiation dose based on personal dosimetry, and the selection of patients who have a high chance of responding to therapy (Jalilian 2016).

One of the earliest ^{68}Ga radiopharmaceuticals to be used in clinical procedures was ^{68}Ga-citrate. It has been known as an infection and inflammation imaging agent for several decades. Researchers have demonstrated the application of this radiopharmaceutical in inflammation due to atherosclerotic plaques in animal models.

Over the last decade, the use of ^{68}Ga-labelled DOTA conjugated with somatostatin (SST) peptide derivative groups, including active octapeptides (Octreotride, OC) and related peptide analogues, such as TOC (Tyr^3-OC), TATE (Tyr^3-Thr^8-OC) and NOC (NaI^3-OC) for the diagnosis of NETs has been reported extensively. The application of these radiopharmaceuticals for planning and monitoring the therapy of NETs has increased. It is beneficial to implement ^{68}Ga based PET imaging agents worldwide in order to increase the therapy capability of this radionuclide (Jalilian 2016).

Of these radiopharmaceuticals, ^{68}Ga-DOTATOC was the first to be utilised in the detection of malignancies. ^{68}Ga-DOTATOC was demonstrated to be a highly accurate in the diagnosis of NETs, meningiomas, thyroid malignancies and prostatic cancers as well as many other tumours. However, DOTATOC imaging has some limitations for non-cancerous tissues in the pancreas and pituitary gland, and in chronic inflammatory conditions (Jalilian 2016).

Another SST ligand developed for PET applications is ^{68}Ga-DOTATATE. Recent studies revealed that ^{68}Ga-DOTATOC and ^{68}Ga-DOTATATE perform equally well for cancer staging and patient selection for peptide receptor radionuclide therapy. However, ^{68}Ga-DOTATATE may be preferable due to a slight difference in healthy organ distribution and excretion. In many NET studies, ^{68}Ga-DOTATATE has shown high specificity and sensitivity. Also initial results have demonstrated that ^{68}Ga-

DOTATATE has a higher lesion uptake even in well differentiated thyroid cancer patients and may be preferable to ^{68}Ga-DOTANOC (Jalilian 2016).

^{68}Ga-DOTANOC (Figure 7-2) is yet another peptide-based chelator used in clinical procedures. Recent studies have indicated that ^{68}Ga-DOTANOC PET imaging may provide better images in a shorter acquisition time than ^{111}In-DTPA-octreotide in the assessment of NETs. Furthermore, this radiopharmaceutical detected considerably more lesions than ^{68}Ga-DOTATATE in patients with NETs. However, the clinical relevance of these finding has to been proven in larger studies (Jalilian 2016).

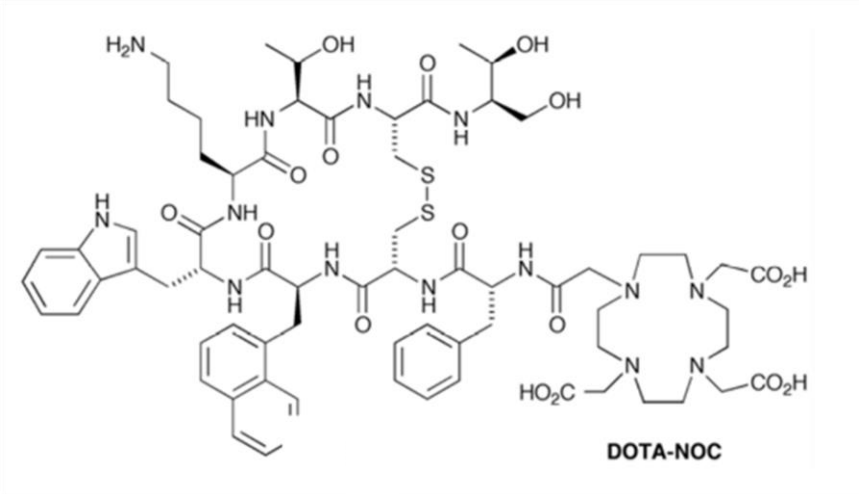

Figure 7-2: Chemical structure of ^{68}Ga-DOTANOC (Jalilian 2016)

Several other ^{68}Ga radiopharmaceuticals are under investigation in addition to SST analogues. The development of ^{68}Ga non-peptide tracers could have considerable benefit. They can be used as bone seeking agents, inflammation markers (for tumour diagnosis) or myocardial perfusion imaging tracers. However, application of these agents needs further research (Jalilian 2016). Table 7-2 shows some of the ^{68}Ga radiopharmaceuticals with their diagnostic applications (Kilian 2014).

Table 7-2: ^{68}Ga tracers and their diagnostic applications (Kilian 2014)

Ligand	Diagnostic applications
^{68}Ga-phosphonates	Bone metastases
^{68}Ga-EDTA (ethylenediaminetetraacetic acid)	Renal function
^{68}Ga- BAPEN (Trisdimethoxysalicylaldimine-aminopropyl-ethylenediamine)	Cardiac function
^{68}Ga-MAA (macroaggregated albumin)	Lung function
^{68}Ga-IDA (iminodiacetic acid)	Hepatobiliary function
^{68}Ga- citrate	Infection

7.4 Production of ^{68}Ga

There are two different ways to produce ^{68}Ga. The most common method is through the decay of its parent germanium-68 (half-life=271 days) in a generator. The other (and preferred) method is through the use of a cyclotron.

In a ^{68}Ge/^{68}Ga generator, the parent radionuclide ^{68}Ge continuously decays to ^{68}Ga by electron capture. Germanium-68 may be produced via several nuclear reactions (Table 7-3), all of which use charged particles in a particle accelerator. However, the most common reaction pathway is ^{nat,69}Ga(p,xn)^{68}Ge via cyclotrons with proton energy > 20 MeV (IAEA 2010).

Table 7-3 : Nuclear reactions that produce ^{68}Ge (IAEA 2010)

Reaction No.	Particle	Target nucleus	Nuclear reaction
1	Proton	^{69}Ga	(p,2n)
2	Deuteron	^{69}Ga	(d,3n)
3	Helium-4	^{66}Zn	(α,2n)
4	Proton	^{nat}Ga (^{69,71}Ga)	(p,xn), x = 2, 4
5	Helium-3	^{66,67,68}Zn	(^{3}He,xn), x = 1, 2, 3

In a generator, germanium is normally embedded in a sorbent material that is eluted with an HCl solution to recover gallium in its ionic form (Ga^{3+}) (Ferreira 2013). Producing ^{68}Ga via this method has some limitations; in contrast to the ease of this generator use, the production of ^{68}Ge is complex and time-consuming. Furthermore, breakthrough of the long-lived ^{68}Ge parent radionuclide into the eluted ^{68}Ga remains a concern due to the long half-life of the former. Moreover, the activity of ^{68}Ga produced each day is restricted, which is especially problematic with the increasing demand for ^{68}Ga for both clinical and research applications. All these reasons trigger the need for an alternative production method using a cyclotron (Pandey et al. 2014; Alves et al. 2017).

^{68}Ga production via irradiation of Zn using a cyclotron is the preferred method as it gives a relatively large product yield. Several radioisotopes of gallium with longer half-lives are also produced when irradiating natural Zn. Thus it is necessary to irradiate enriched ^{68}Zn. However, the irradiation of ^{68}Zn by protons still results in the production of undesired long-lived radioactive impurities such as ^{67}Ga, depending on irradiating proton energy (Alves et al. 2017).

The ^{68}Zn target material can be either solid or liquid. The use of a solid target has the advantage of producing ^{68}Ga with a high yield. However, a high yield is achieved at the expense of some important practical difficulties in the form of long and complex processes taking from a few hours up to 20 h. The approach requires considerable optimisation studies and additional quality control before target irradiation to ensure that it is appropriate for ^{68}Ga production and to avoid contaminant production (Alves et al. 2017).

In order to avoid the technical difficulties associated with the irradiation of solid targets, an alternative production method has been suggested. This involves bombarding a liquid target containing a solution of enriched target material. The liquid target is normally prepared by dissolving the enriched material in a nitrate solution which is then diluted with nitric acid (Alves et al. 2017).

PETIC was the first organisation in the UK to produce ^{68}Ga in a cyclotron (Cyclone 18/9, IBA, Louvain-la-Neuve, Belgium) (Figure 7-3)) using a liquid target in the form of ^{68}Zn nitrate solution (density of 33 g/l). This cyclotron was specially intended for large hospitals and medical research centres. It is optimised to produce both protons

(18 MeV) and deuterons (9 MeV). However, this type of cyclotron is unable to perform irradiation with alpha particles.

The cyclotron incorporates a large vacuum tank and the target vessel contains a foil separating the vacuum region from a region of helium coolant in front of the target. For ^{68}Ga production, two types of target windows were used for energy degradation: titanium and Havar. However, another type of window was used for zirconium-89 production (Chapter 8).

In general, liquid-target radiometal production technology is not yet mature and requires more experiments to optimise production yield. The literature review in this chapter will just deal with studies of ^{68}Zn in the form of a liquid material; these are recent and few in number.

Figure 7-3: The IBA Cyclone 18/9 cyclotron in PETIC, Cardiff

7.5 Previous studies of the assessment of the radionuclidic purity of ^{68}Ga

Ferreira (2013) produced ^{68}Ga in a low energy cyclotron via the nuclear reaction $^{68}Zn(p,n)^{68}Ga$. A Monte Carlo simulation was performed using SRIM (Stopping and Range of Ions in Matter) software to determine the irradiation conditions. The energy of the irradiating beam was 28 MeV and the target material was $ZnCl_2$ solution with 98% purity. The activity measurements were done using a radionuclide calibrator that was set to measure ^{68}Ga. As there was no available way to store the calibrator output in a computer, the activity of the sample as a function of time was determined by filming the display screen for several hours (10h-40h). The data were then inserted into a computer file for analysis. It was found that the contaminants produced alongside ^{68}Ga were ^{66}Ga (through the reaction $^{66}Zn(p,n)^{66}Ga$) and ^{13}N (through the reaction $^{16}O(p,\alpha)^{13}N$). The measured half-life (10min) of the latter radionuclide (^{13}N) showed good agreement with the expected value (9.96 min), whereas that of ^{66}Ga did not (54% difference, expected $t_{1/2}$=569 min and measured $t_{1/2}$=260 min). It was claimed that this was due to the fact that the measurement time (10h) was very close to one half-life of ^{66}Ga. With a longer measurement time (23h), the difference from the expected value was lower (18%).

In the same year, zinc chloride solution was also used as a target material for the production of ^{68}Ga by Moreira (2013). Irradiation under different conditions was done with a Cyclone 18/9 cyclotron (IBA, Louvain-la-Neuve, Belgium), using 18 MeV protons. The beam energy was degraded using a niobium window foil with a thickness of 0.125 mm. According to a SRIM simulation, the attenuated proton beam had an energy of 16.28 MeV on reaching the target solution. After irradiation, the activity of the ^{68}Ga product was measured using a COMECER® PET radionuclide calibrator. For the identification of specific gamma radiation from other radionuclides, a CRC®-55tW well counter, with a NaI crystal detector, was used. Count rates were recorded over a period of 23 hours, with a time lapse of 2 minutes between each measurement. ^{66}Ga, ^{67}Ga and ^{13}N were identified and the time-activity curve was used to determine the half-life of the gallium isotopes. The experimental and theoretical half-life values of the identified isotopes were approximately equal.

Pandey et al. (2014) produced ^{68}Ga by irradiating ^{68}Zn nitrate solution (isotopic enrichment of 99.23%) with a proton beam of energy ~14 MeV. Energy degradation was done using dual foils of aluminium and a Havar window. A Havar window has very high strength at high temperatures and excellent corrosion resistance. It withstands the high pressure and temperatures generated at the target by bombardment with protons. An HPGe gamma spectrometer was used to measure the radionuclide purity, while a radionuclide calibrator was used to measure the activity of the main radionuclide.

A purified sample of ^{68}Ga was subjected to HPGe spectrometry 36 h after EOB. The spectrum revealed some photopeaks associated with the impurity ^{67}Ga, whose activity on decay correction to EOB was estimated to be <0.07% of the total ^{68}Ga activity. The presence of ^{67}Ga impurity can be attributed to two possible nuclear reactions: ^{68}Zn $(p,2n)^{67}Ga$ and ^{67}Zn $(p,n)^{67}Ga$.

^{68}Zn nitrate solution was also used to produce ^{68}Ga by Alves et al. (2017). The liquid target solution was prepared by dissolving enriched material in a nitrate solution which was then diluted in nitric acid. The energy of the irradiating proton beam was 18 MeV. As the cyclotron delivered a fixed energy proton beam, it was crucial to degrade the beam energy to reduce the production of long-lived impurities. For this purpose, a target window consisting of two foils was used; these comprised a Havar window followed by a thick niobium window in contact with the liquid target solution. Pure niobium was chosen due to its chemical inertness, which prevented the creation of additional metallic contaminants.

Particular attention was paid to isotopic impurities with a longer half-life than ^{68}Ga, namely ^{66}Ga and ^{67}Ga, both of which were found in the final purified solution of ^{68}Ga (Table 7-4). Activity was measured using a calibrated HPGe detector. The dead-time was kept to 4% or less and the photopeak areas were determined using a software package called Gamma Vision.

Despite degrading the energy of the irradiating beam to minimise the activity of ^{67}Ga and using enriched ^{68}Zn (with a reduced amount of ^{66}Zn) to minimise the activity of ^{66}Ga due to the reaction $^{66}Zn(p, n)^{66}Ga$, both of these longer-lived radionuclides were found in the final product. Therefore its purity was seen to deteriorate over time.

Table 7-4: Experimental measurements of ^{68}Ga purity (%) at EOB

Target window	^{67}Ga	^{66}Ga
35 μm Havar and 35 μm niobium	0.48	0.009
35 μm Havar and 250 μm niobium	0.042	0.0037

7.6 Assessment of the radionuclidic purity of ^{68}Ga produced by PETIC

7.6.1 Method

As mentioned earlier, ^{68}Ga was produced in PETIC using ^{68}Zn nitrate solution as a target material.

After irradiation, ^{68}Ga samples were purified by loading the irradiated target solution onto a strong cation exchange resin column to separate ^{68}Ga from ^{68}Zn and other impurities. The column was washed with 5 ml of water to remove radionuclides such as ^{11}C, ^{13}N and ^{18}F and then eluted with 30 mL of 0.5M HBr in 80% acetone to remove zinc ions. This was followed by 5 ml of water to remove any traces of HBr and acetone. Subsequently, ^{68}Ga cations were eluted with 6 mL of 3M HCl, mixed with concentrated HCl (to increase molarity) and passed through an anion exchange column. ^{68}Ga was absorbed on the column and a flow of inert gas was applied to dry the column and remove any traces of HCl. Finally, ^{68}Ga was eluted from the column with 0.1M HCl to obtain a final product in the form of $^{68}GaCl_3$ in a vial.

Pairs of liquid samples (each with a volume of 4 ml in a Schott vial) were prepared before and after chemical purification of the target material for three validation productions.

^{68}Ga activity in these samples was measured in a Capintec CRC 25R radionuclide calibrator rather than the Fidelis calibrator, as the latter had no identified calibration factor for ^{68}Ga. After decay of the primary radionuclide, gamma spectra were acquired with the energy and efficiency-calibrated HPGe detector. Samples were placed

individually in direct contact with the centre of the detector end-cap. Each of the six samples was measured several times.

Spectra were analysed using the Canberra Genie 2000 MCA software to give net counts for recognised photopeaks. The live time was set initially at 1300s and this was increased to a maximum of about 7200s as the samples decayed. NCR was then calculated and corrected for radioactive decay during spectrum acquisition. The identification of impurities was based on information obtained from the scientific literature and experience gained from the study of ^{89}Zr (Chapter 8). For identified impurities, NCR was converted to activity according to Equation (2-17).

The activities of the main radionuclide ^{68}Ga and the identified impurities were decay corrected to EOB and the impurity activity expressed as a percentage of the ^{68}Ga activity. Mean and the standard deviation (SD) values were calculated.

Determination of half-life was done by plotting the logarithm of the contaminant NCR (before decay correction to EOB) versus time and applying linear regression.

7.6.2 Results

A typical spectrum from a gallium-68 solution recorded with the HPGe detector is shown in Figure 7-4. ^{67}Ga, ^{66}Ga and ^{56}Co were identified as radioactive impurities. Table 7-5 shows the mean and the SD activity of the main radioactive impurity (^{67}Ga) in MBq and as a percentage of ^{68}Ga activity for three productions. Figure 7-5 and Figure 7-6 show graphs of the logarithm of NCR versus decay time for the identified ^{67}Ga peaks of the pre-purification and post-purification samples respectively from the first production. Table 7-6 and Table 7-7 show the corresponding regression equations, R-squared values and the calculated half-life of ^{67}Ga for the pre-purification and post-purification samples respectively.

Table 7-8 shows the mean and the SD activity of ^{66}Ga radioactive impurity in MBq and as a percentage of ^{68}Ga activity for two productions. It was not identified in the third production.

Figure **7-7** shows a graph of the logarithm of corrected NCR versus decay time and the calculated half-life for this impurity in the pre-purification sample of the first

production. Table 7-9 shows the mean and the SD activity of ^{56}Co radioactive impurity in MBq and as a percentage of ^{68}Ga activity for three productions.

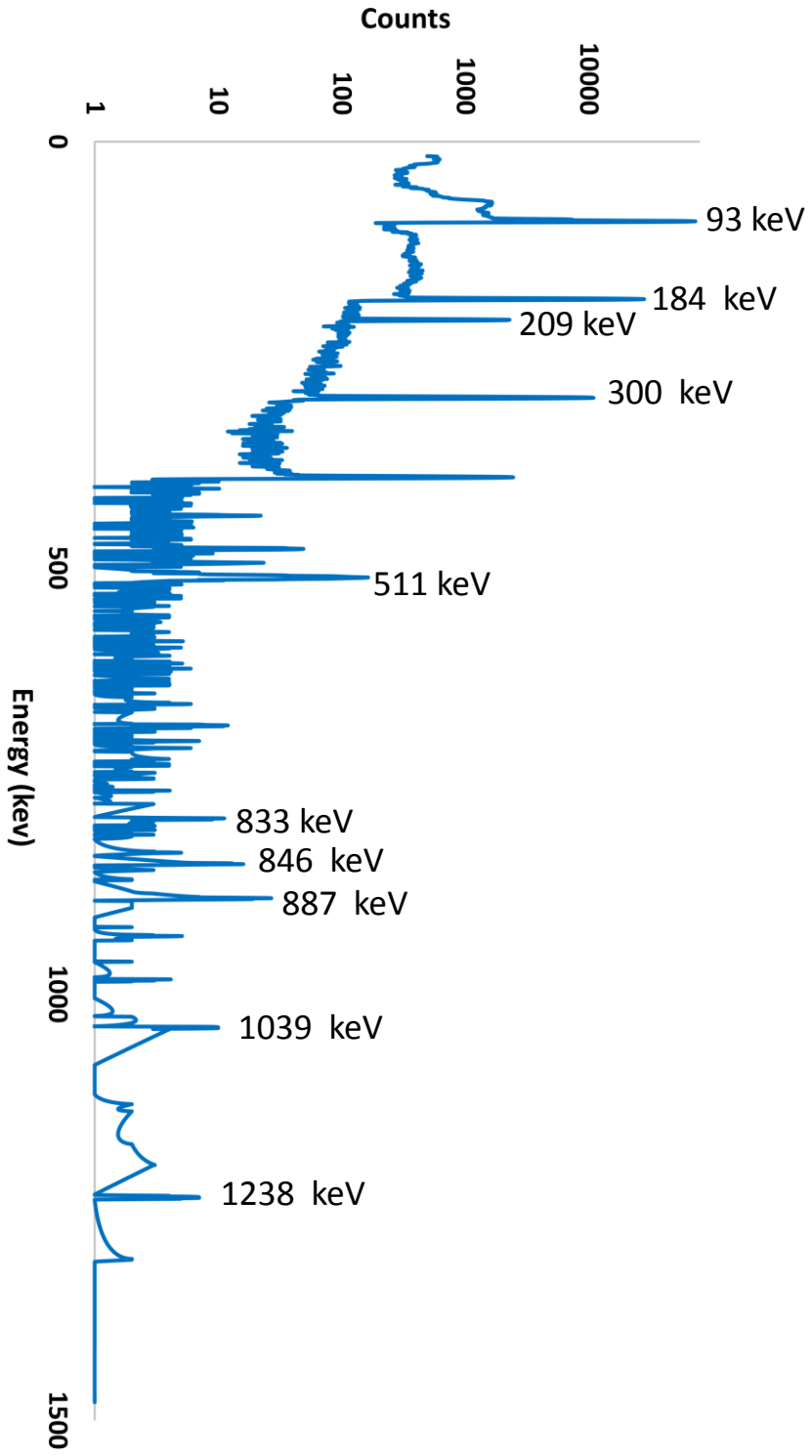

Figure 7-4: Typical ^{68}Ga spectrum recorded with the HPGe detector, showing the predominant gamma peaks of the main radiocontaminants ^{67}Ga (93 keV, 184 keV, 209 keV, 300 keV), ^{66}Ga gamma peaks (833 keV and 1039 keV) and ^{56}Co (846 keV and 1238 keV)

Table 7-5: Mean and SD activity of ^{67}Ga in MBq and as a percentage of ^{68}Ga activity for three productions

Production No.		1				2				3			
		Pre-purification		Post-purification		Pre-purification		Post-purification		Pre-purification		Post-purification	
^{68}Ga Activity (MBq)		1.80		12.70		1.70		4.90		1.63		2.32	
^{67}Ga peaks		Activity (MBq)	Ratio % $^{67}Ga/^{68}Ga$	Activity (MBq)	Ratio % $^{67}Ga/^{68}Ga$	Activity (MBq)	Ratio % $^{67}Ga/^{68}Ga$	Activity (MBq)	Ratio % $^{67}Ga/^{68}Ga$	Activity (MBq)	Ratio % $^{67}Ga/^{68}Ga$	Activity (MBq)	Ratio % $^{67}Ga/^{68}Ga$
93 keV	**Mean**	**1.39×10^{-2}**	**7.75×10^{-1}**	**5.88×10^{-2}**	**4.63×10^{-1}**	**3.21×10^{-3}**	**1.88×10^{-1}**	**1.10×10^{-2}**	**2.25×10^{-1}**	**3.57×10^{-3}**	**2.19×10^{-1}**	**5.65×10^{-3}**	**2.43×10^{-1}**
	SD	3.59×10^{-5}	2.00×10^{-3}	3.26×10^{-4}	2.57×10^{-3}	7.28×10^{-6}	4.27×10^{-4}	8.81×10^{-4}	1.80×10^{-2}	6.05×10^{-6}	3.71×10^{-4}	6.12×10^{-4}	2.63×10^{-2}
184 keV	**Mean**	**1.43×10^{-2}**	**7.98×10^{-1}**	**6.07×10^{-2}**	**4.78×10^{-1}**	**3.31×10^{-3}**	**1.94×10^{-1}**	**1.13×10^{-2}**	**2.30×10^{-1}**	**3.68×10^{-3}**	**2.26×10^{-1}**	**5.80×10^{-3}**	**2.50×10^{-1}**
	SD	7.51×10^{-5}	4.18×10^{-3}	3.18×10^{-4}	2.50×10^{-3}	2.01×10^{-5}	1.18×10^{-3}	9.08×10^{-4}	1.85×10^{-2}	1.15×10^{-5}	7.08×10^{-4}	6.32×10^{-4}	2.72×10^{-2}
209 keV	**Mean**	**1.18×10^{-2}**	**6.58×10^{-1}**	**5.36×10^{-2}**	**4.22×10^{-1}**	**2.83×10^{-3}**	**1.66×10^{-1}**	**9.65×10^{-3}**	**1.97×10^{-1}**	**3.15×10^{-3}**	**1.93×10^{-1}**	**5.08×10^{-3}**	**2.19×10^{-1}**
	SD	6.46×10^{-5}	3.59×10^{-3}	4.44×10^{-4}	3.50×10^{-3}	1.28×10^{-5}	7.51×10^{-4}	7.82×10^{-4}	1.59×10^{-2}	6.22×10^{-5}	3.82×10^{-3}	3.48×10^{-4}	1.50×10^{-2}
300 keV	**Mean**	**1.36×10^{-2}**	**7.58×10^{-1}**	**5.89×10^{-2}**	**4.64×10^{-1}**	**3.15×10^{-3}**	**1.85×10^{-1}**	**1.08×10^{-2}**	**2.20×10^{-1}**	**3.49×10^{-3}**	**2.14×10^{-1}**	**5.59×10^{-3}**	**2.41×10^{-1}**
	SD	9.44×10^{-5}	5.25×10^{-3}	4.86×10^{-4}	3.83×10^{-3}	4.27×10^{-5}	2.50×10^{-3}	8.57×10^{-4}	1.75×10^{-2}	1.07×10^{-5}	6.54×10^{-4}	5.15×10^{-4}	2.22×10^{-2}
887 keV	**Ave.**	**1.48×10^{-2}**	**8.26×10^{-1}**	**6.25×10^{-2}**	**4.92×10^{-1}**	**3.20×10^{-3}**	**1.88×10^{-1}**	**1.11×10^{-2}**	**2.27×10^{-1}**	**3.66×10^{-3}**	**2.24×10^{-1}**	**5.91×10^{-3}**	**2.54×10^{-1}**
	SD	7.59×10^{-4}	4.22×10^{-2}	1.27×10^{-3}	1.00×10^{-2}	8.60×10^{-5}	5.05×10^{-3}	8.59×10^{-5}	1.75×10^{-3}	3.14×10^{-4}	1.93×10^{-2}	5.77×10^{-4}	2.49×10^{-2}

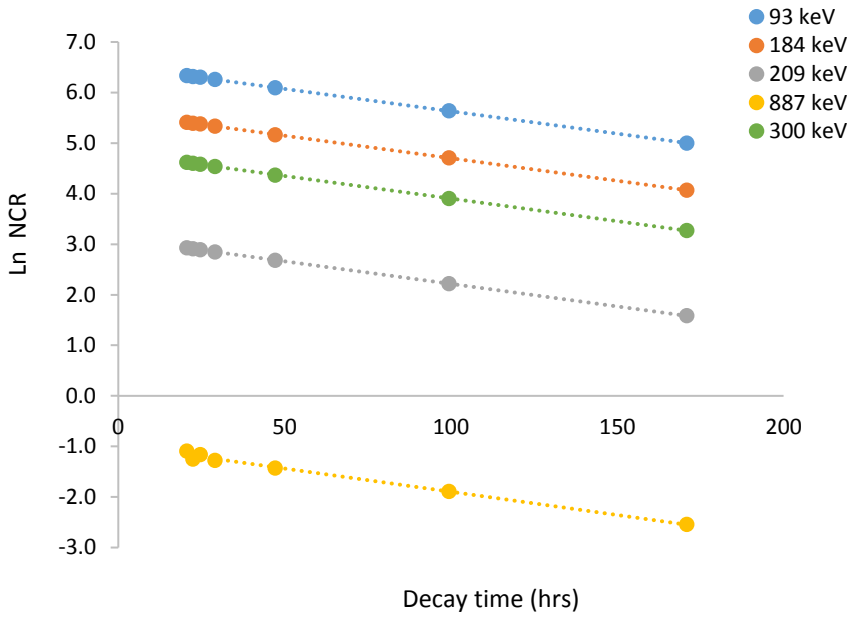

Figure 7-5: Determination of ^{67}Ga half-life (78.26 hrs) from its gamma photopeaks for the pre-purification sample of the first production (7 measurements)

Table 7-6: Linear regression equations and calculated $t_{1/2}$ values of ^{67}Ga for the pre-purification sample of the first production

Energy (keV)	Regression equation	R^2	Calculated $t_{1/2}$(hrs)= ln(2)/slope(λ)
93	Y= -0.00885x + 6.515	0.999	78.28
184	Y= -0.00892x + 5.592	0.999	77.72
209	Y= -0.00892x + 3.108	0.999	77.68
300	Y= -0.00895x + 4.797	0.999	77.46
887	Y= -0.00919x - 0.978	0.992	75.42
Mean(SD)			**77.31 (1.10)**

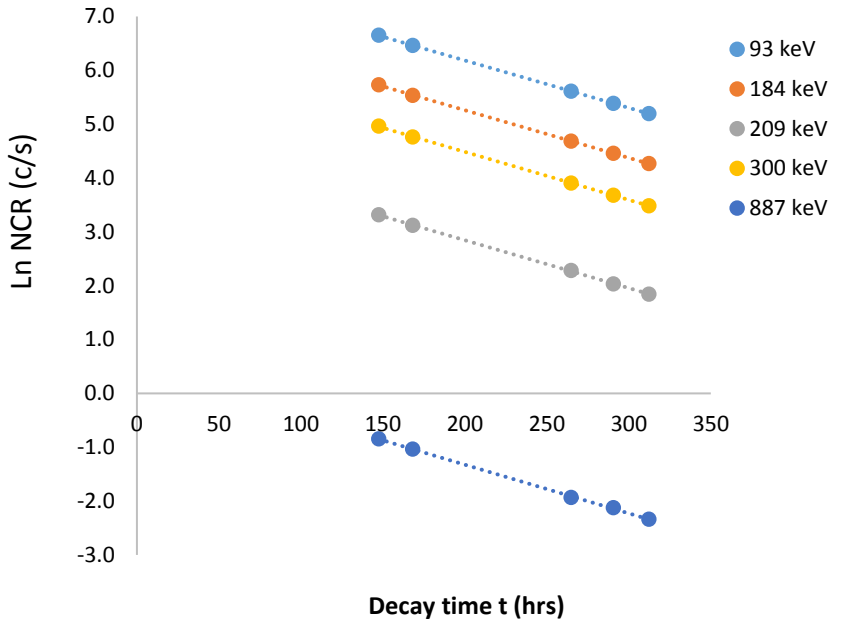

Figure 7-6: Determination of ^{67}Ga half-life (78.26 hrs) from its gamma photopeaks for a post-purification sample of the first production (5 measurements)

Table 7-7: Linear regression equations and calculated $t_{1/2}$ values of ^{67}Ga for the post-purification sample of the first production

Energy (keV)	Regression equation	R^2	Calculated $t_{1/2}$(hrs) = ln(2)/slope(λ)
93	Y= -0.00880x + 7.943	0.999	78.76
184	Y= -0.00885x + 7.030	0.999	77.30
209	Y= -0.00889x + 4.622	0.999	77.98
300	Y= -0.00892x + 6.269	0.999	77.72
887	Y= = -0.00904x + 0.484	0.999	76.66
Mean(SD)			**77.68 (0.78)**

Table 7-8: Mean and SD activity of ^{66}Ga in MBq and as a percentage of ^{68}Ga activity for two productions

Production No.		1				2			
		Pre-purification		Post-purification		Pre-purification		Post-purification	
^{68}Ga Activity (MBq)		1.80		12.70		1.704		4.90	
^{66}Ga peaks		Activity (MBq)	Ratio %)$^{66}Ga/^{68}Ga$	Activity (MBq)	Ratio % $^{66}Ga/^{68}Ga$	Activity (MBq)	Ratio % $^{66}Ga/^{68}Ga$	Activity (MBq)	Ratio % $^{66}Ga/^{68}Ga$
833 keV	Mean	$\mathbf{9.56\times10^{-5}}$	$\mathbf{5.32\times10^{-3}}$	/	/	$\mathbf{5.12\times10^{-5}}$	$\mathbf{3.00\times10^{-3}}$	$1.11\times\mathbf{10^{-4}}$	$\mathbf{2.27\times10^{-3}}$
	SD	3.01×10^{-5}	1.68×10^{-3}	/	/	/	/	/	/
1039 keV	Mean	$\mathbf{1.10\times10^{-4}}$	$\mathbf{6.11\times10^{-3}}$	/	/	$\mathbf{4.42\times10^{-5}}$	$\mathbf{2.59\times10^{-3}}$	$\mathbf{1.40\times10^{-4}}$	$\mathbf{2.85\times10^{-3}}$
	SD	1.00×10^{-5}	5.57×10^{-4}	/	/	3.88×10^{-6}	2.28×10^{-4}	5.82×10^{-6}	1.19×10^{-4}

/ means that the photopeak was not identified in this sample

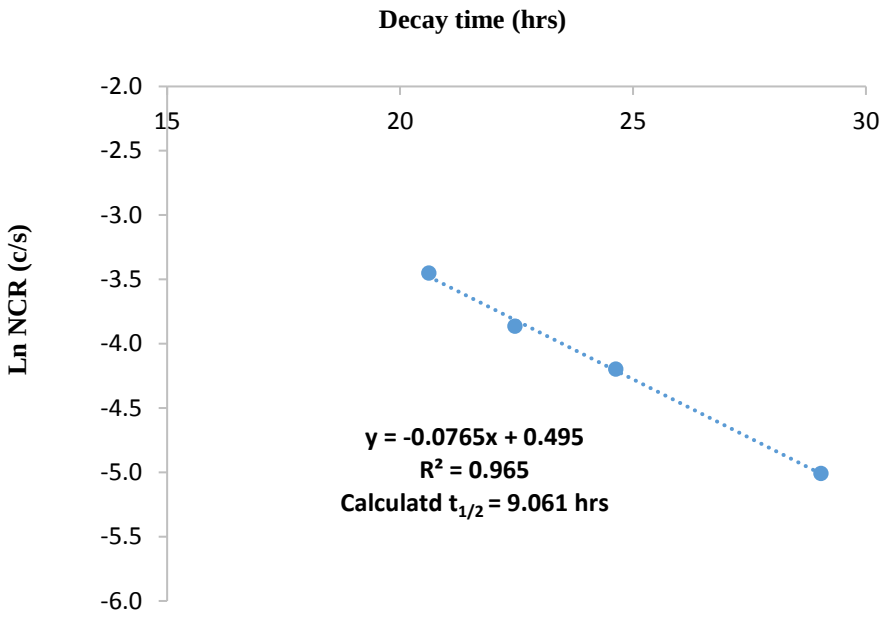

Figure 7-7: Determination of ^{66}Ga half-life (9.4 hrs) from its gamma photopeak (1039 keV) for the pre-purification sample of the first production

Table 7-9: Mean and SD activity of ^{56}Co in MBq and as a percentage of ^{68}Ga activity for three productions

Production No.		1				2				3			
		Pre-purification		Post-purification		Pre-purification		Post-purification		Pre-purification		Post-purification	
^{68}Ga Activity (MBq)		1.80		12.70		1.70		4.90		1.63		2.32	
^{56}Co peaks		Activity (MBq)	Ratio % $^{56}Co/^{68}Ga$	Activity (MBq)	Ratio % $^{56}Co/^{68}Ga$	Activity (MBq)	Ratio % $^{56}Co/^{68}Ga$	Act. (MBq)	Rat. %	Activity (MBq)	Ratio %	Act. (MBq)	Rat. %
846 keV	**Mean**	**8.65×10^{-6}**	**4.82×10^{-4}**	**2.11×10^{-7}**	**1.66×10^{-6}**	**1.94×10^{-6}**	**1.14×10^{-4}**	/	/	**2.27×10^{-6}**	**1.39×10^{-4}**	/	/
	SD	2.94×10^{-7}	1.64×10^{-5}	3.13×10^{-8}	2.47×10^{-7}	3.41×10^{-7}	2.00×10^{-5}	/	/	3.45×10^{-7}	2.12×10^{-5}		
1238 keV	**Mean**	**4.27×10^{-6}**	**2.38×10^{-4}**	/	/	**2.54×10^{-6}**	**1.49×10^{-4}**	/	/	**2.46×10^{-6}**	**1.51×10^{-4}**	/	/
	SD	2.28×10^{-7}	1.27×10^{-5}			7.19×10^{-7}	4.22×10^{-5}	/	/	1.67×10^{-7}	1.02×10^{-5}		
1039 keV	**Mean**	**8.60×10^{-6}**	**4.78×10^{-4}**	/	/	/	/	/	/	/	/	/	/
	SD	1.57×10^{-6}	8.76×10^{-5}					/	/	/	/		

7.6.3 Discussion

^{67}Ga (gamma energy 93, 184, 209, 300 and 887 keV), ^{66}Ga (833 keV and 1039 keV) and ^{56}Co (846 keV, 1038 keV and 1238 keV) were identified as impurity radionuclides in ^{68}Ga solutions. However, ^{67}Ga was considered to be the main impurity because it had the greater relative activity and this is in agreement with results mentioned in the literature. The presence of ^{67}Ga in this study was confirmed (in both pre- and post-purification samples of the first production) by determination of its half-life for all the identified photopeaks. The values obtained showed good agreement with the actual half-life (78.26 hrs).

For the first production, the activity of this impurity (^{67}Ga) as a percentage of ^{68}Ga activity at EOB varied between 0.66% and 0.83% for the pre-purification sample, while for the post-purification the range was 0.42% to 0.49%. This subtle difference may be attributed to the peak summing effect.

However, the relative activity of ^{67}Ga was less in the 2nd and 3rd productions. In the pre-purification samples, the range was 0.17%-0.23%, whereas for the post-purification samples it was 0.20%-0.25%. This difference is thought to be due to changes in irradiation conditions (e.g the proton energy) having a genuine effect on the activity of the impurity produced. After the three productions were completed, maintenance of the cyclotron revealed that the titanium window was broken for some reason. This was thought to be behind the changes in irradiation conditions, which in turn affected the percentage of impurity activity.

^{66}Ga was the other significant radioactive contaminant identified in the ^{68}Ga solutions. Its existence was confirmed by the determination of experimental half-life (9.06 hrs) which agreed with the actual value (9.4 hrs, % diff. = -3.606%). The ratio of ^{66}Ga activity to ^{68}Ga activity for the first production was about 0.006% before purification but this radionuclide was not identified in the purified sample. For the second production, the relative activity of ^{66}Ga was about 0.003% for both pre-purification and post-purification samples.

Regarding ^{56}Co, the relative activity in the first production was about 0.0005% for the pre-purification sample and only traces were identified in the post-purification sample. For the second and third productions, the relative activity was 0.0001% pre-

purification in both cases, with no trace of ^{56}Co found in the purified samples. This means that the chemical purification was effective, as the aim of his process is to remove elements with different chemical properties to those of the required nuclide. This impurity (^{56}Co) has not been reported in the literature. It is thought that this radioactive contaminant was generated during irradiation of the Havar window.

Chapter 8

Radionuclidic Purity of Cyclotron-Produced Zirconium-89

8.1 Introduction

The development of radiopharmaceuticals in the form of biological targeting agents such as proteins, antibodies, peptides and nanoparticles with a wide range of biological half-lives requires the production of new radionuclides with physical half-lives compatible with these biological properties. ^{89}Zr is one of these radionuclides that has emerged as a promising radiometal for targeted molecular imaging using PET in both animal models and humans. This radionuclide is particularly important for cancer research as it is well-suited for the *in vivo* targeting of macromolecules and nanoparticles to the surfaces of cancer cells.

The demand for ^{89}Zr for research purposes is increasing because this radionuclide remains in tumour cells after its administration so that time series studies are possible without administering further radiopharmaceuticals.

Once again, quality control of radiopharmaceuticals labelled with ^{89}Zr is important to avoid unnecessary dose to the patient.

8.2 Properties of ^{89}Zr

Zirconium is a group IVB transition metal. It was discovered in 1789 by the German chemist Martin Heinrich Klaproth, who prepared zirconium oxide from the mineral zircon, $ZrSiO_4$. Zirconium exists only in the 4+ oxidation state in aqueous solutions (Vugts et al. 2013).

Zirconium-89 has proven to be very useful in drug development, for instance for new antibody therapies. This is due to its long half-life (≈78 hrs) that is appropriate for studying the biodistribution of long-circulating proteins and antibodies. It also has balanced physical decay properties (Figure 8-1 and Table 8-1), i.e. sufficiently small positron energy to give good PET image resolution and acceptable patient radiation dose (Synowiecki et al. 2018).

Zirconium-89 decays through β^+ emission and electron capture into ^{89}Y. The characteristic x-rays are of very low energies at about 15 keV. The decay is followed by a prompt gamma ray at 909 keV. Thus the detection of 511 keV annihilation photons is relatively unaffected by both the gamma photon and the characteristic x-

rays because of the large energy differences. This helps to improve image quality (Alfuraih et al. 2013).

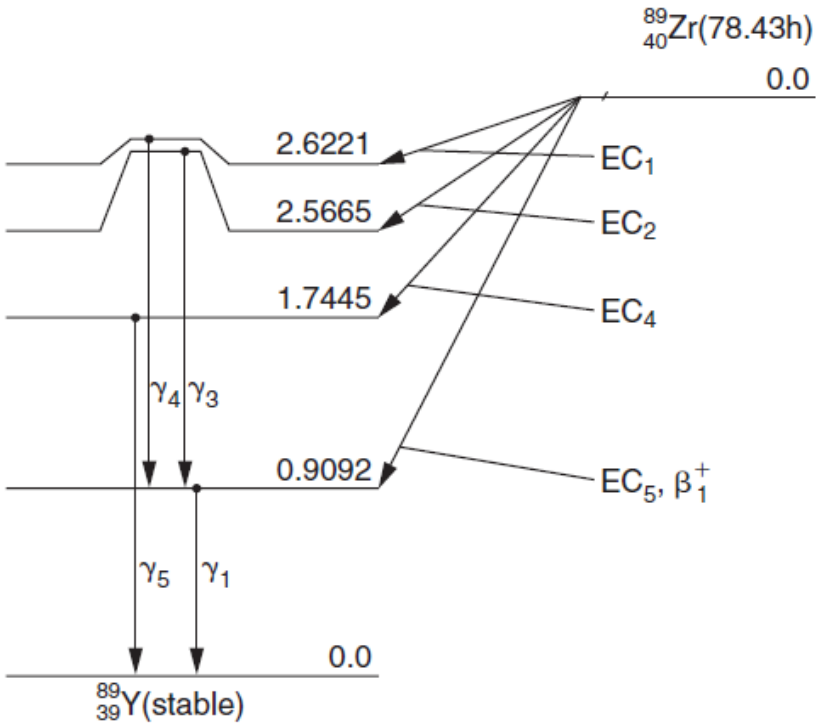

Figure 8-1: Decay scheme for ^{89}Zr (Cherry et al. 2012)

Table 8-1: Emissions of ^{89}Zr: y(i) is the yield per disintegration, E(i) is the energy of the emission, y(i)×E(i) is the product of the yield and the energy of the disintegration and ce are conversion electrons (Cherry et al. 2012)

Radiation	*y(i)* (Bq•s)$^{-1}$	*E(i)* (MeV)	*y(i)* × *E(i)*
β^+ 1	2.26E-01	3.949E-01*	8.94E-02
γ±	4.53E-01	5.110E-01	2.31E-01
γ 1	9.99E-01	9.092E-01	9.08E-01
ce-K_2, γ 1	7.44E-03	8.922E-01	6.63E-03
ce-L_1, γ 1	8.26E-04	9.068E-01	7.49E-04
γ 3	9.99E-04	1.657E 00	1.66E-03
γ 4	7.69E-03	1.713E 00	1.32E-02
γ 5	1.30E-03	1.744E 00	2.26E-03
$K\alpha_1$ X ray	2.69E-01	1.496E-02	4.03E-03
$K\alpha_2$ X ray	1.40E-01	1.488E-02	2.09E-03

8.3 Clinical applications of ^{89}Zr

Recently, there has been increased interest in using positron emitters such as ^{89}Zr for immuno-PET. Immuno-PET is an attractive novel tumour imaging option, which integrates the use of PET and monoclonal antibodies (mAbs). Immuno-PET has the potential to improve diagnostic tumour identification by combining the high sensitivity and resolution of PET/CT with the specificity of a mAb localisation. In fact, each mAb that targets a specific tumour cell is a candidate for use in immuno-PET, allowing the development of a new generation of mAb-based imaging methods. Immuno-PET might also play a role in the characterisation, efficient selection and optimisation of novel high-potential mAbs for diagnosis and therapy (Kasbollah et al. 2013).

^{89}Zr has good physical characteristics for immuno-PET and has been recommended for use in quantifying slow processes such as the deposition of mAbs in tissue and tumour. Over the last few years, several ^{89}Zr-labeled antibodies directed against different tumour types have been assessed in preclinical and clinical studies (Table 8-2). Intact antibodies need about 2–4 days to penetrate into a solid tumour. As the half-life of ^{89}Zr is about 3 days, it is considered to be compatible with the time needed for these mAbs to achieve optimal results (Kasbollah et al. 2013).

However, there is a need for an efficient chelator in order to prevent the release of $^{89}Zr^{4+}$ from the antibodies, because the free radionuclide can accumulate in bone mineral and can associate with plasma proteins. This results in depositing a significant radiation dose to the bone marrow. A compatible chelator system is crucial to minimise the disassociation of ^{89}Zr from the antibodies. Over the years, different chelators have been utilised with different degrees of success; examples include diethylenetriaminepentaacetic acid (DTPA), ethylenediaminetetraacetic acid (EDTA) and desferoxamine (DFO) (van de Watering et al. 2014).

Table 8-2: Overview of ^{89}Zr-labeled antibodies used in pre-clinical and clinical studies (van de Watering et al. 2014)

Target	Type of tumour
CD147	Pancreas
CD20	Non-Hodgkin's lymphoma
CD44v6	Head and neck squamous cell carcinoma
EGFR	Multiple
EGP-1	Prostate
GPC3	Liver
HER1	Colorectal
HER2	Breast and ovarian
IGF-1R	Triple negative breast cancer
MET	Head and neck squamous cell carcinoma and gastric
MN/CA	Renal cell carcinoma
PSMA	Prostate
PIGF	Liver
VEGF	Breast, head, and neck squamous cell carcinoma and ovarian

DFO was thought to be the most successful chelator of Zr^{4+} as it showed good stability, releasing less than 0.2% of Zr^{4+} after 24 h in serum and less than 2% after seven days. However, several proof-of-principle pre-clinical studies indicated that the *in vivo* stability of this complex remains an issue as free ^{89}Zr was observed in bone (van de Watering et al. 2014).

Therefore, there remains a need for novel chelators that allow more stable complexation of ^{89}Zr with antibodies. Pandya et al. (2017) reported that ^{89}Zr–DOTA is superior to ^{89}Zr–DFO, which is considered to be the "gold standard" in the clinical development of ^{89}Zr-radiopharmaceuticals. These results may pave the way to enhance the development of radiolabelled agents for accurate medical applications.

8.4 Production of ^{89}Zr

Three nuclear reactions have been explored for ^{89}Zr production in a cyclotron. The first reaction ($^{nat}Sr(\alpha,xn)^{89}Zr$) is not applicable as PETIC is unable to perform α irradiation. The second reaction, deuteron bombardment of ^{89}Y, is also not feasible as the cyclotron in PETIC can only accelerate deuterons to an energy of 9 MeV, which is not sufficiently high to implement this reaction (Dabkowski et al. 2015).

$^{89}Y(p,n)^{89}Zr$ is regarded as the best nuclear reaction for ^{89}Zr production executed on a medium to small cyclotron. The fact that natural yttrium consists of only ^{89}Y affords an extra advantage in the production of ^{89}Zr with a proton biomedical cyclotron; the target does not require costly enriched target material (Infantino et al. 2011).

The yttrium target material can be either a foil or sputtered material with copper backing to improve heat dissipation during irradiation. Additionally, it could be yttrium metal or Y_2O_3 in powder form (Severin et al. 2011).

In PETIC, the yttrium target material was a foil with a thickness of 150μm. This foil was positioned in an aluminium solid target holder (Figure 8-2). The irradiating proton energy was 18 MeV. This energy was degraded to ≈ 13.4 MeV using a niobium foil window (Figure 8-3) with a thickness of 300μm.

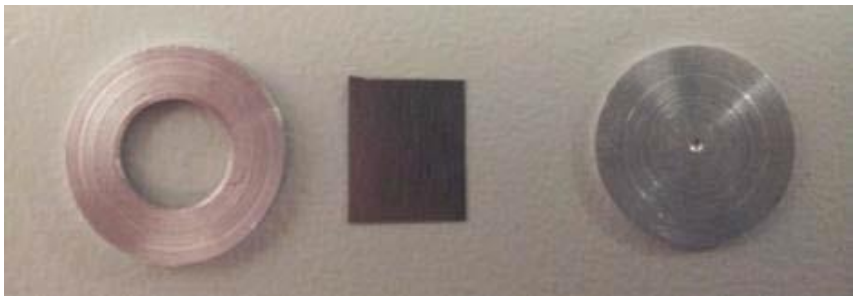

Figure 8-2: Aluminium solid target holder with ^{89}Y target foil (in the centre)

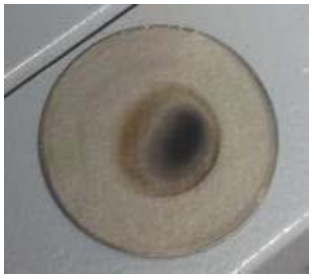

Figure 8-3: Niobium vacuum chamber window for proton energy degradation- the dark area is the beam trace

After irradiation, the yttrium target was removed from the aluminium holder and dissolved in 2 to 6 M HCl and 30% H_2O_2 heated to 110 ^oC; it was washed with HCl and water through a specific separation column. Hydroxamate functionalised ion exchange resin was used to separate the ^{89}Zr product from yttrium target material. The ^{89}Zr was eluted as zirconium-oxalate with 1.0 M oxalic acid.

To produce ^{89}Zr-chloride, the ^{89}Zr-oxalate was passed through a NaCl activated cartridge. The cartridge was then washed and the ^{89}Zr-chloride eluted.

8.5 Previous studies of the assessment of the radionuclidic purity of ^{89}Zr

Ciarmatori et al. (2011) produced ^{89}Zr via the $^{89}Y(p,n)^{89}Zr$ nuclear reaction. Irradiation was performed using a 16.5 MeV cyclotron. Yttrium metallic foils (of thickness 150 μm) were used as a target material. The target was firmly positioned in a copper backing support having a central cavity and covered by an aluminum disc with a thickness of 500μm. The aluminum disc was used for energy degradation and for protection of the yttrium target foil from possible motion. After irradiation, the yttrium foil was dissolved in HCl and 3 samples were prepared from the solution.

For radionuclidic purity assessment, the samples were measured in a calibrated HPGe detector after a sufficient waiting time to avoid pulse pile-up. Sample spectra were acquired for 14000 s and analysed using Canberra Genie 2000 software; the accuracy of the activity values was in the range 5-7%. The only significant radioactive impurity produced was ^{56}Co. The activity of this radionuclide at EOB was 530 ± 60 Bq, while that for the main radionuclide (^{89}Zr) was about 200×10^6 Bq. This meant that the ratio of the radio-contaminant to ^{89}Zr was about 0.00000265, which was considered to be negligible. The production of ^{56}Co was most likely due to the interaction of protons with ^{56}Fe, a small amount of which was present in the yttrium target.

In the same year, Walther et al. (2011) produced ^{89}Zr in an IBA Cyclone 18/9 cyclotron using the same foil thickness of 150μm. However, the production was done by proton irradiation with a greater energy of 18 MeV. The foil was positioned in an aluminum support and another aluminum foil was used as an energy degrader. This aluminum target set-up helped in facilitating the preparation of the target and avoiding the formation of undesired radionuclidic impurities in the crude product. The irradiating

energy was degraded from 18 MeV to 15 MeV, 12 MeV and finally to 10 MeV using vacuum aluminum foil (380 mm) and additional energy degrader foils with a thickness of 320 and 500 mm, respectively.

The radionuclidic purity of the samples (n=7) was measured using a HPGe detector. The samples were left for sufficient time (26–42 days), to allow most of the ^{89}Zr activity to decay.

Table 8-3 shows the ratios of the activity of radioactive impurities (^{88}Zr and ^{88}Y) to that of the main radionuclide (^{89}Zr).

Table 8-3: Activity ratio of $^{88}Zr/^{89}Zr$ and $^{88}Y/^{89}Zr$ as determined by HPGe detector (Walther et al. 2011)

Thickness of Al energy degrader foils	E_p (MeV)	n	Mean value $^{88}Zr/^{89}Zr$(%)	Mean value $^{88}Y/^{89}Zr$(%)
Vacuum foil 380μm	15	1	4.0	0.164
380+320μm	12	3	0.249±0.0025	0.041±0.0035
380+500μm	10	3	0.004±0.0008	0.001±0.00006

Infantino et al. (2011) used a Monte Carlo code (FLUKA) to stimulate the production of ^{89}Zr with a prototype solid target. ^{89}Zr was produced by the irradiation of a ^{89}Y target foil through the reaction $^{89}Y(p,n)^{89}Zr$ using 16.5 MeV protons. An aluminum foil with a thickness of 500μm was used for energy degradation, while the thickness of the target foil was 300μm. This foil was positioned in a deep cavity carved in a copper holder. Simulations were done both with and without the presence of the aluminum degrader. With the degrader, the energy of protons entering the target foil was 12.6 MeV.

Results of the simulated irradiations without the aluminum energy degrader predicted significant contamination from ^{88}Zr, with limited activity of ^{86}Y and ^{90}Y as expected. However, only ^{89}Zr was produced with the use of the aluminum degrader because it reduced the energy of the beam entering the target to below 13 MeV, thus excluding the reaction $^{89}Y(p, 2n)^{88}Zr$ that occurs at 13 MeV.

Monte Carlo simulation was also used by Alfuraih et al. (2013) to predict the production of ^{89}Zr and associated contaminants using a cyclotron. In the simulations, the thickness of the ^{89}Y foil target varied between 0.1 and 0.5 mm, whereas the thickness of the Al degrader varied from 0 (i.e no degrader) to 1 mm. The irradiating energy was the same as that in the previous study (16.5 MeV). ^{88}Zr and ^{88}Y were identified as radioactive contaminants and their activities were reduced using the 0.5 mm degrader: ^{88}Y from 0.4 or 0.6 MBq to 4 Bq and ^{88}Zr from 5 or 10 MBq to less than 1 Bq.

Wooten et al. (2013) irradiated a thicker (640μm) yttrium foil with protons of energy about 14.7 MeV to produce ^{89}Zr. The foil was positioned in a target holder made of niobium. This element was selected due to its high melting temperature and high chemical inertness. The final product was purified and produced as a solution. For the evaluation of the radionuclidic impurities, the solution was diluted to a volume of 2 ml and this sample was measured with a HPGe detector for 10 minutes within one ^{89}Zr half-life of the original bombardment. To identify longer-lived radioactive impurities, the sample was allowed to decay for several ^{89}Zr half-lives (≈22 days) and a spectrum was acquired for 12 h. ^{88}Zr was identified as the only radio-contaminant with a percentage activity of 0.002% of the total.

Lin et al. (2016) also used yttrium-89 foil of the same thickness (640μm), but with different irradiation conditions. The foil was positioned and locked inside a target holder. Initial tests were done with a proton beam energy of 15.2 MeV. After analysis of radionuclide impurities, the incident proton energy was reduced to 14.5 MeV. After irradiation, ^{89}Zr-oxalate and ^{89}Zr-chloride were prepared. The radionuclidic impurity assessment of these samples was done with a HPGe detector after preparing the samples in special tubes with a volume of 1 ml. The samples were counted for 4 hrs after EOB.

It was observed that with an irradiation energy of 15.2 MeV, there was a slight radioactive contamination (<0.01%) of ^{88}Y and/or ^{88}Zr. However, with a reduced proton energy of 14.5MeV, no gamma-rays other than these from ^{89}Zr were identified indicating a higher radionuclidic purity at EOB.

In PETIC, Dabkowski et al. (2015) produced ^{89}Zr using different thicknesses of niobium window foil as degraders. The proton energy of the IBA Cyclone 18/9

cyclotron was degraded from 18 MeV to ≈ 9.8 MeV using a thickness of 500 and to ≈ 11.6 MeV using a thickness of 400 μm. The target material was yttrium as a foil with a thickness of 150μm.

The activity of the produced ^{89}Zr was measured using a Capintec CRC 25R radionuclide calibrator at least 4 h after EOB, to allow for the decay of the short-lived radionuclide ^{89m}Zr, which is produced alongside ^{89}Zr. The activity was then decay corrected to EOB. Assessment of the long-lived radioactive impurities was done using EG&G Ortec NaI and HPGe detectors.

It was found that ^{89}Zr produced with a 500 μm thick niobium degrader was not accompanied by long-lived impurities such as ^{88}Zr or ^{88}Y. Similarly, ^{89}Zr produced with a 400 μm thick niobium degrader showed no evidence of the existence of these long lived impurities (^{88}Zr and ^{88}Y) in the acquired spectrum.

Dias et al. (2018) irradiated yttrium foil with protons of energy 13.8 MeV to produce ^{89}Zr. The energy was degraded using an aluminum ring. After irradiation, the sample was dissolved in HCl. The radionuclidic purity of the unpurified sample was assessed using a HPGe detector calibrated for both energy and efficiency. The spectrum was acquired 72hrs after EOB with a measurement time of 30 min and a dead time of <5%. Two gamma peaks were observed in the spectrum; these were at 511 keV and 909 keV and both seemed to be related to ^{89}Zr.

8.6 Assessment of radionuclidic purity of ^{89}Zr delivered to University Hospital of Wales produced by PETIC

8.6.1 Method

The purpose of the work described in this section is to confirm the ability of PETIC to limit the production of radionuclidic impurities in ^{89}Zr to negligible levels. Several ^{89}Zr validation productions were made, for which the produced ^{89}Zr was not ready to be used in patients.

^{89}Y foil with a thickness of 150 μm was used as a target material positioned in an aluminium holder and irradiated with a proton beam of energy about 13.4 MeV in an

IBA Cyclone 18/9 cyclotron. For energy degradation, a niobium window with a thickness of 300μm was used.

After the irradiation of the yttrium disc, ^{89}Zr was automatically separated by dissolving the disc in HCl and H_2O_2 heated to 110℃, allowing the solution to cool to room temperature then washing it with HCl and water through a separation column. Hydroxamate functionalised ion exchangers were used for separation of the ^{89}Zr product from the yttrium target material. The ^{89}Zr was eluted as Zr-oxalate with 1.0 M oxalic acid.

The same procedure as was used for ^{68}Ga was followed to measure the activity of the main product (^{89}Zr) and impurities. Liquid samples of the standard 4 ml volume in a standard Schott vial were prepared before and after chemical purification of the target material. This was done for two validation productions. The activity of ^{89}Zr in the samples was measured with the Capintec CRC 25R radionuclide calibrator. The samples were left for sufficient time (about a month) to allow the main radionuclide (^{89}Zr) to decay. For each sample, series of gamma spectra were acquired over a long period of time (a maximum time of about 75 days) with the energy and efficiency calibrated LO-AX HPGe detector.

Spectra were analysed using the same method as mentioned previously. Radionuclidic impurities were identified using information from the scientific literature and for each photopeak, NCR was calculated and corrected for radioactive decay during spectrum acquisition. For the identified impurities, NCR was corrected for radioactive decay to EOB and converted to activity according to Equation (2-17). Contaminant activity was expressed as a percentage of ^{89}Zr activity at EOB. Mean and the standard deviation (SD) values were calculated. Determination of radionuclide half-life was done by plotting the logarithm of the NCR (without decay correction) over the period of the experiment.

8.6.2 Results

Figure 8-4 shows a typical spectrum of a ^{89}Zr solution recorded with the HPGe detector. The following impurities were identified: ^{88}Zr, ^{88}Y and ^{56}Co. Table 8-4, Table 8-5 and Table 8-6 show the mean and the SD activity (MBq) of these three

radionuclides respectively, and the activity as a percentage of that of the main radionuclide (^{89}Zr), for two productions.

Figure 8-5 shows the determination of ^{88}Zr half-life (83.4 days) from its 392 keV gamma photopeak for both pre- and post-purification samples of the first production, while

Table 8-7 shows the corresponding linear regression equations and the calculated $t_{1/2}$ values. The equivalent data for the second production are shown in Figure 8-9 and Table 8-8.

Figure 8-6 and Figure 8-7 show the variation with time of ln (NCR) for the ^{88}Y 898 keV and 1836 keV photopeaks respectively for both pre- and post-purification samples of the first production. The equivalent data for the second production are shown in Figure 8-10 and Figure 8-11.

Figure 8-8 shows the determination of ^{56}Co half-life (78.76 days) from its gamma peaks (846 keV and 1238 keV) for the pre-purification sample of the first production, while Figure 8-12 shows the corresponding data for the second production.

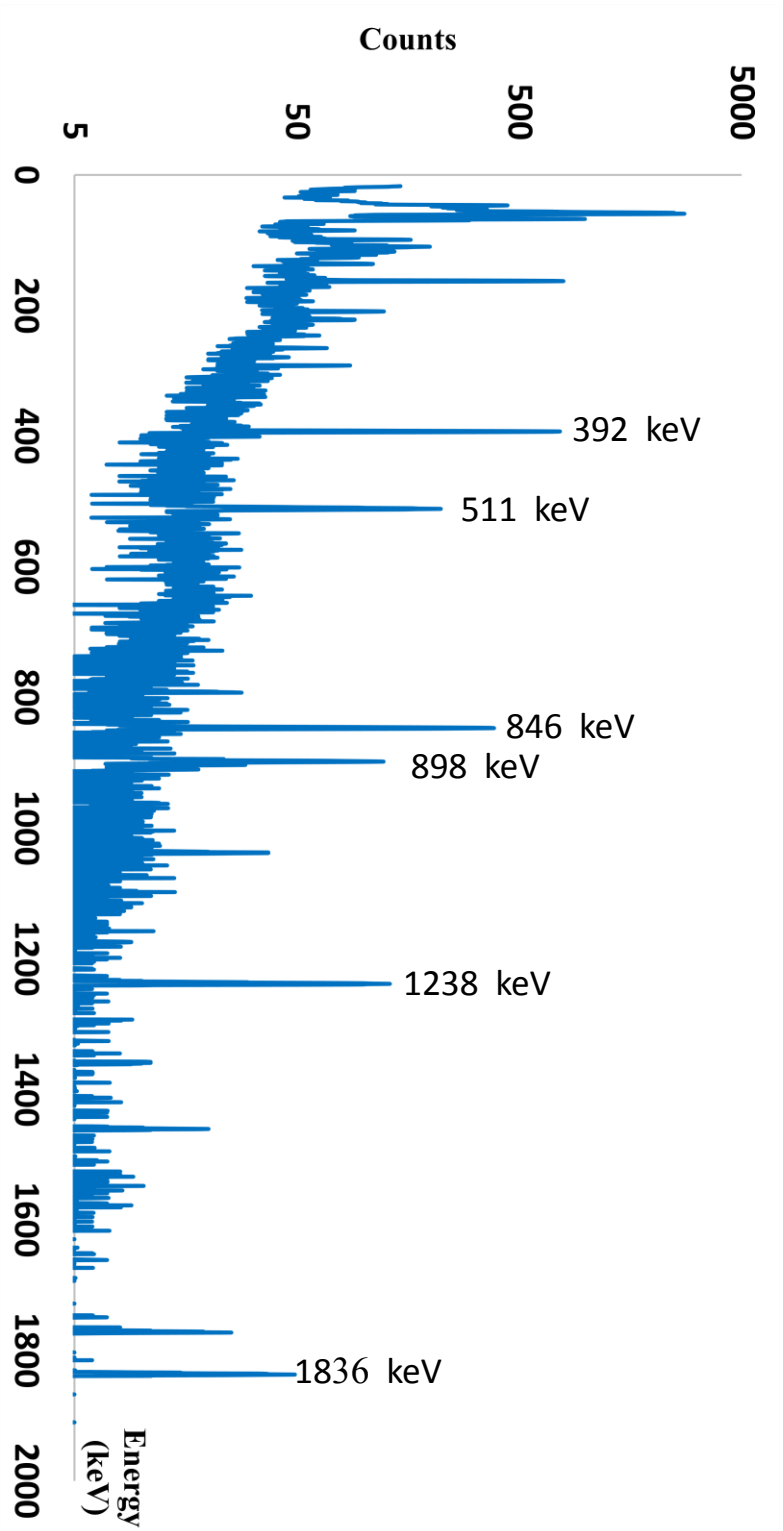

Figure 8-4: Typical ^{89}Zr spectrum recorded with the HPGe detector showing the annihilation radiation peak (511 keV) and the predominant gamma photopeaks of the main radio-contaminants: ^{88}Zr (392keV), ^{56}Co (846 keV and 1238 keV) and ^{88}Y (898 keV and 1836 keV)

Table 8-5: Mean (SD) activity (MBq) of ^{88}Zr and its value as a percentage of ^{89}Zr activity for two productions

Production No.		1				2			
		Pre-purification		Post-purification		Pre-purification		Post-purification	
^{89}Zr Activity at EOB (MBq)		4.30		9.19		1.85		2.50	
^{88}Zr photopeak		Activity (MBq)	% Activity ^{88}Zr/^{89}Zr	Activity (MBq)	%Activity ^{88}Zr/^{89}Zr	Activity (MBq)	%Activity ^{88}Zr/^{89}Zr	Activity (MBq)	%Activity ^{88}Zr/^{89}Zr
392 keV	Mean	5.06×10^{-5}	1.18×10^{-3}	8.73×10^{-5}	9.50×10^{-4}	1.19×10^{-5}	6.45×10^{-4}	1.33×10^{-5}	5.33×10^{-4}
	SD	9.59×10^{-7}	2.23×10^{-5}	2.42×10^{-6}	2.63×10^{-5}	5.18×10^{-7}	2.80×10^{-5}	4.62×10^{-7}	1.85×10^{-5}

Table 8-4: Mean (SD) activity (MBq) of ^{88}Y and its value as a percentage of ^{89}Zr activity for two productions

Production No.	1				2			
	Pre-purification		Post-purification		Pre-purification		Post-purification	
^{89}Zr Activity at EOB (MBq)	4.30		9.19		1.85		2.50	
^{88}Y photopeaks	Activity (MBq)	% Activity ^{88}Y /^{89}Zr	Activity (MBq)	% Activity ^{88}Y /^{89}Zr	Activity (MBq)	% Activity ^{88}Y /^{89}Zr	Activity (MBq)	% Activity ^{88}Y /^{89}Zr
898 keV	/	/	1.97×10^{-5}	2.15×10^{-4}	/	/	/	/
1836 keV	1.48×10^{-5}	3.44×10^{-4}	1.90×10^{-5}	2.07×10^{-4}	1.99×10^{-6}	1.07×10^{-4}	1.32×10^{-6}	5.30×10^{-5}

898 keV photopeak was only seen in the post-purification sample of the first production

Table 8-6: Mean (SD) activity (MBq) of ^{56}Co and its value as a percentage of ^{89}Zr activity for two productions

Production No.		1				2			
		Pre-purification		Post-purification		Pre-purification		Post-purification	
^{89}Zr Activity at EOB (MBq)		4.30		9.19		1.85		2.50	
^{56}Co peaks		Activity (MBq)	%Activity $^{56}Co/^{89}Zr$	Activity (MBq)	%Activity ^{56}Co /^{89}Zr	Activity (MBq)	%Activity ^{56}Co /^{89}Zr	Activity (MBq)	%Activity ^{56}Co /^{89}Zr
846 keV	Mean	1.03×10^{-4}	2.39×10^{-3}	/	/	1.77×10^{-5}	9.59×10^{-4}	/	/
	SD	3.63×10^{-6}	8.44×10^{-5}	/	/	3.23×10^{-7}	1.75×10^{-5}	/	/
1238 keV	Mean	9.76×10^{-5}	2.27×10^{-3}	/	/	1.64×10^{-5}	8.85×10^{-4}	/	/
	SD	2.22×10^{-6}	5.167×10^{-5}	/	/	3.841×10^{-7}	2.08×10^{-5}	/	/

No ^{56}Co photopeaks were seen in the purified samples

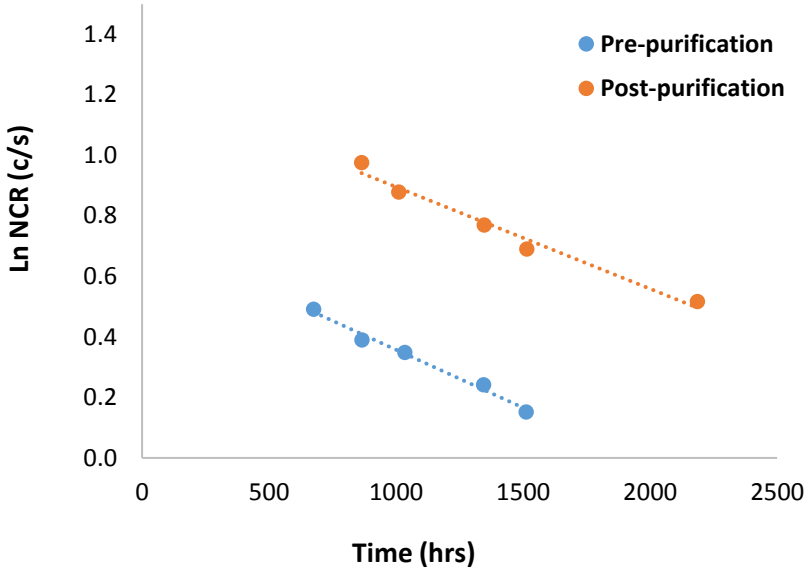

Figure 8-5: Determination of ^{88}Zr half-life (83.4 days) from its 392 keV gamma photopeak for both pre- and post-purification samples of the first production (5 measurements)

Table 8-7: Regression equations and calculated $t_{1/2}$ values of ^{88}Zr for both pre- and post-purification samples of the first production

1st production	**Regression equation**	**R^2**	**Calculated $t_{1/2}$ (days)= ln(2)/slope(λ)**
Pre-purification	Y= -0.000383x + 0.741	0.988	75.39
Post-purification	Y= = -0.000337x + 1.232	0.976	85.78

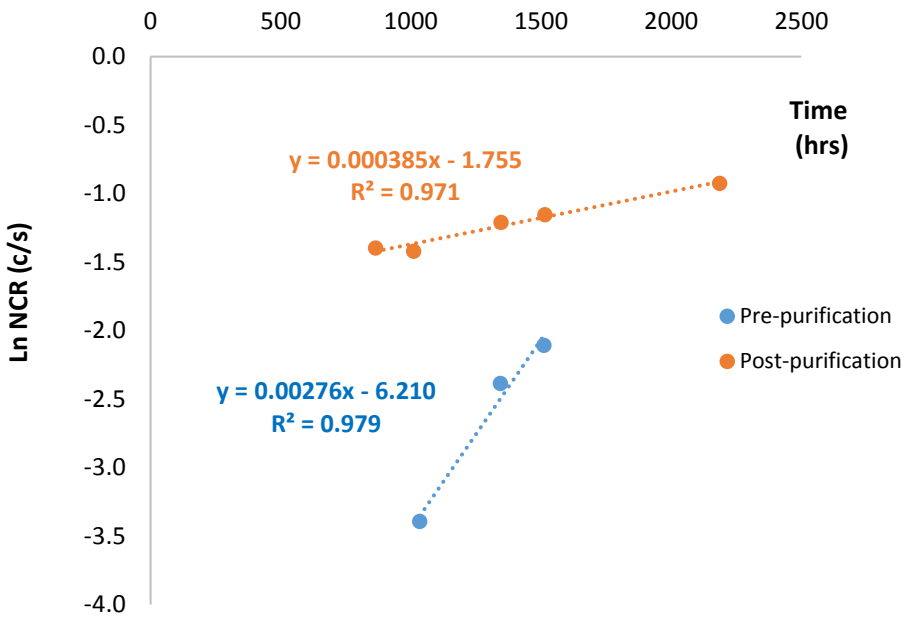

Figure 8-6: Ln (NCR) of ^{88}Y 898 keV photopeak versus time for both pre- and post-purification samples of the first production (5 measurements)

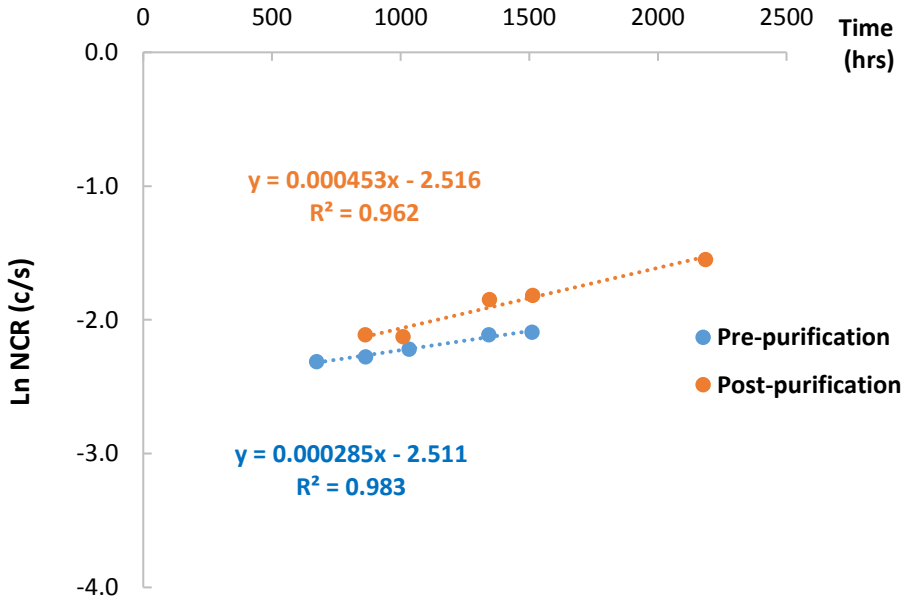

Figure 8-7: Ln (NCR) of ^{88}Y 1836 keV photopeak versus time for both pre- and post-purification samples of the first production (5 measurements)

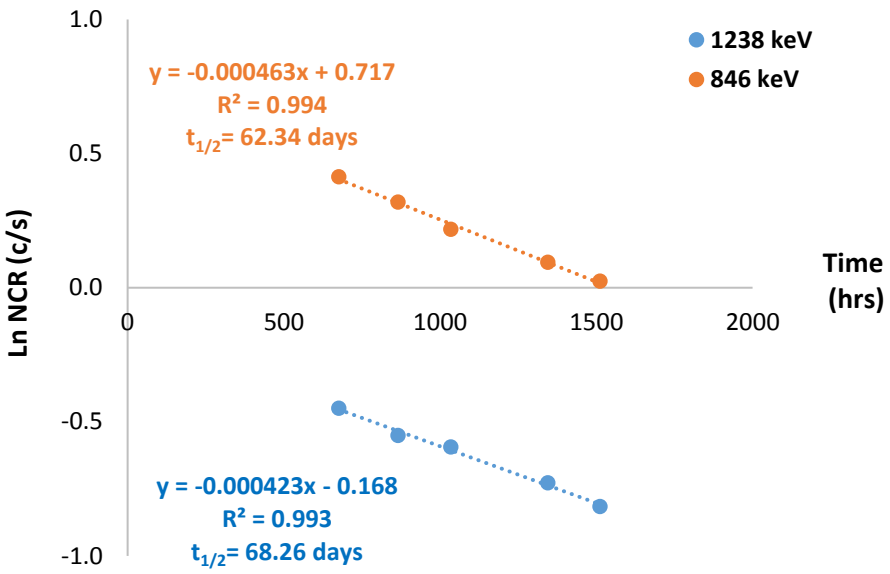

Figure 8-8: Determination of ^{56}Co half-life (78.76 days) from its gamma photopeaks (846 keV and 1238 keV) for the pre-purification sample of the first production

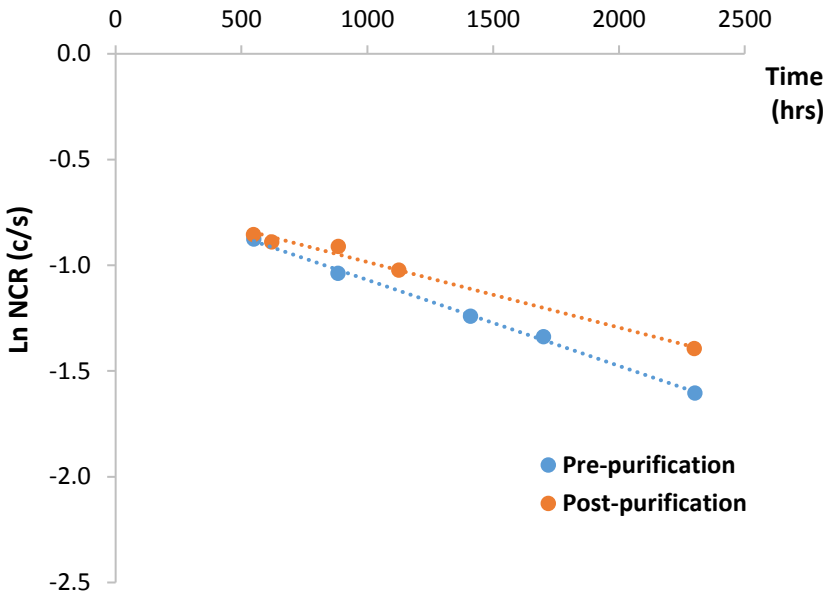

Figure 8-9: Determination of ^{88}Zr half-life (83.4 days) from its 392 keV gamma photopeak for both pre- and post-purification samples of the second production (5 measurements)

Table 8-8: Regression equations and calculated $t_{1/2}$ values of ^{88}Zr for both pre- and post-purification samples of the 2nd production

2nd production	Regression equation	R^2	Calculated $t_{1/2}$ (days)= ln(2)/slope(λ)
Pre-purification	Y= -0.000407x - 0.662	0.998	71.027
Post-purification	Y= 0.000310x - 0.674	0.989	93.171

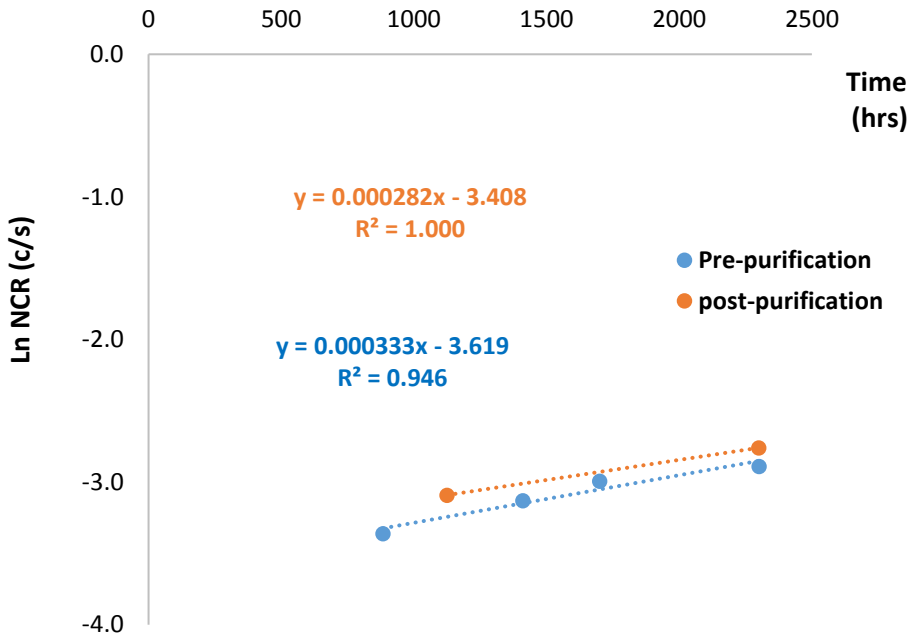

Figure 8-10: Ln (NCR) of ^{88}Y 898 keV photopeak versus the time for both pre- and post-purification samples of the second production (4 measurements)

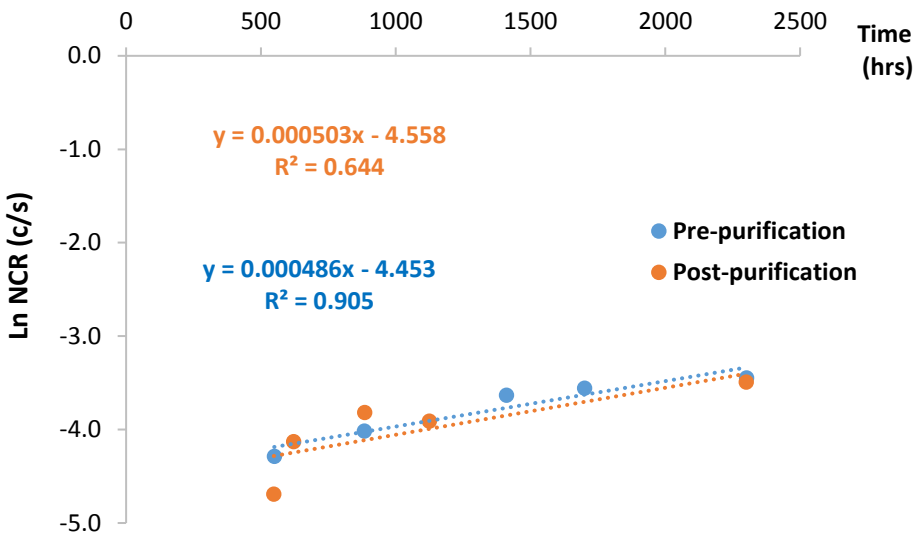

Figure 8-11: Ln (NCR) of ^{88}Y 1836 keV photopeak versus time for both pre- and post-purification samples of the second production (5 measurements)

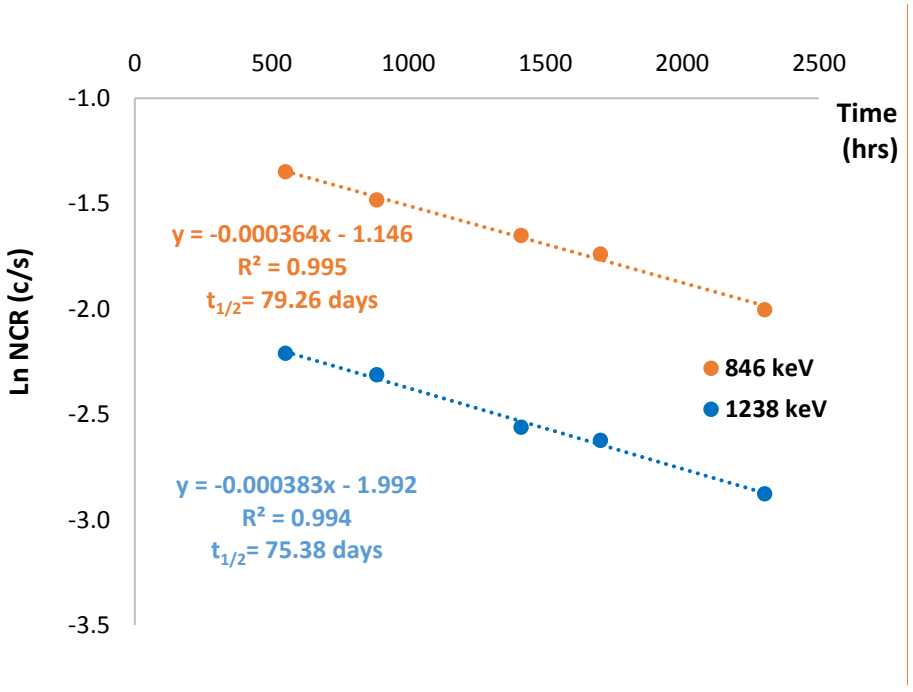

Figure 8-12: Determination of ^{56}Co half-life (78.76 days) from its gamma photopeaks (846 keV and 1238 keV) for the pre-purification sample of the second production (5 measurements)

8.6.3 Discussion

The results show that three radioactive impurities were identified in the ^{89}Zr solutions: ^{88}Zr, ^{88}Y and ^{56}Co. However, ^{88}Zr was the main impurity amongst them and this is in agreement with the literature. This radioactive contaminant was identified in both pre- and post-purification samples and for both productions. The presence of this radionuclide was confirmed by a determination of its half-life; over the period of the experiments, the logarithm of the counting rate decreased linearly with time, giving deviations of -9.6% and 2.9% from the expected half-life value for pre-and post-purification samples respectively. Values of ^{88}Zr activity as a percentage of ^{89}Zr activity were 0.0012 and 0.0010 for the pre-and post-purification samples respectively in the first production, while those for the 2nd production were 0.0006 and 0.0005 respectively. These ratios are less than those reported in the literature. However, it is difficult to compare values of radioactive contaminant activity with those of other researchers because the literature is sparse and shows great inconsistency. This is due to the fact that researchers have used different parameters, such as the thickness of the foil target, the material of the degrader, the thickness of the degrader and the proton energy used to irradiate the target.

The second identified radioactive contaminant (^{88}Y) was also seen in both pre-and post-purification samples and for both productions. However, its existence was not confirmed by a determination of its half-life as the logarithm of the counting rate increased with time over the period of the experiments (for both of its gamma peaks at 898 keV and 1836 keV). This is due to the presence of the first impurity (^{88}Zr), which exclusively decays to ^{88}Y by electron capture. Thus, the percentage activity of ^{88}Y was estimated from the first NCR readings as these were expected to be the closest to the actual values. These values were 0.0001-0.0003% for pre-purification samples and about 0.00005-0.0002% for post-purification samples.

The third identified radioactive impurity was ^{56}Co. This radionuclide was identified in just the pre-purification samples for both the first and the second productions, which means that the chemical purification was effective as the aim of this process is to remove elements with different chemical properties compared with the required nuclide. The existence of ^{56}Co was confirmed by a determination of its half-life from the NCR of the gamma photopeaks at 846 keV and 1238 keV. Over the period of the

experiments, the logarithm of the count rate decreased linearly with time, giving differences from the expected half-life value of -20.8% and -13.3% for the 846 keV and 1238 keV photopeaks respectively in the first production. The corresponding values for the second production were 0.6% and -4.3% respectively. The ratio of ^{56}Co activity to ^{89}Zr activity was about 0.001-0.002%. The presence of this impurity is most likely due to the interaction of protons with ^{56}Fe present in the yttrium target ($^{56}Fe(p,n)^{56}Co$).

Chapter 9

Discussion, Conclusion and Future Work

9.1 Introduction

This project investigated the presence of the radioactive impurities that are produced alongside the main radionuclides used for diagnostic or therapeutic applications. This results in degradation of the spatial resolution of diagnostic images and an increase in the absorbed radiation dose to the patient.

9.2 HPGe detector at the University Hospital of Wales

A HPGe detector was used in this study to detect, identify and quantify radioactive impurities in some available radionuclides. The type of the HPGe detector was an Ortec LO-AX device at the University Hospital of Wales, Cardiff. The detector was repaired during the course of the study, but all the experimental measurements reported in this thesis were made after repair.

9.2.1 Peak area and count rate calculation

In order to achieve precise and accurate photopeak detection and counting, an automatic peak-search routine was used. This method was implemented in a CANBERRA Genie-2000 software package. The software automatically subtracts the background, giving the net area of the peak (net counts). The net count rate (NCR) was then calculated by dividing the net counts by the counting live time. The calculated NCR was corrected to the beginning of the measurement to account for radioactive decay during the counting time

9.2.2 HPGe energy calibration

Energy calibration was performed on each day that measurements were made. Three standard energy calibration sources were used. These were ^{133}Ba, ^{137}Cs and ^{60}Co. The sources were placed together at a distance of 8 cm from the HPGe detector to limit the dead time. The relationship between energy and MCA channel number was found to be essentially linear.

9.2.3 HPGe detector stability

A long-lived ^{137}Cs sealed source was used to investigate the count rate stability of the HPGe detector over the period of the study. For the detection system to be stable, the count rate for a given radionuclide should not change with time after correction for radioactive decay. Linear regression analysis of NCR with time showed that the detector was stable after repair.

9.2.4 HPGe detection efficiency

Seven gamma emitters were used to estimate the absolute efficiency of the HPGe detector; these were ^{125}I, ^{99m}Tc, ^{123}I, ^{131}I, ^{137}Cs, ^{54}Mn and ^{65}Zn. Each of these sources was separately prepared as an aqueous solution in a Schott vial with a volume of 4 ml adopted as a standard. Some of these sources were prepared in house, while others were bought. The samples were prepared with different activities ranging between 0.9 kBq and 12 kBq, which gave a reasonable dead time (less than 3%).

The stability of the HPGe detector was tested for each gamma source. Investigation of sensitivity (NCR/Activity) variation with the time was done using linear regression analysis. It was found that the sensitivity of the HPGe detector was stable ($P>0.05$) over the period of each experiment for all the radionuclides except for ^{65}Zn (second gamma peak at 1115 keV). However, the actual variation at that gamma line was small (CoV=0.35%), which was even less than that for the other gamma line of the same nuclide (1.2% for 511 keV).

Half-life quantification of some sources was done by plotting the logarithm of the uncorrected NCR against time over the period of the experiment. The half-life determinations were done only for the short-lived radionuclides. It is difficult to do this for long-lived radionuclides, for which the variation in disintegration rate may not be noticeable within a reasonably short period of time. The determined half-lives of ^{99m}Tc and ^{131}I revealed good agreement with the actual values, while the calculated half-life of ^{123}I showed a difference of -17.67% from the actual value. This was due to the relatively short duration of the experiments (about 1 hr), which was much less than one half-life of this radionuclide (13 hrs). It is likely that counting for a longer period would improve the agreement between the experimental and actual values.

A curve of efficiency vs. photon energy was displayed using a log-log plot and separate curves fitted to the low and high energy regions. Due to the photoelectric effect, the efficiency increased rapidly at very low energies reaching a maximum at about 80 keV. Above this energy, the detection efficiency decreased due to Compton scattering, which is the dominant interaction at high energy.

The efficiency curve obtained in this study showed a similar trend to that of a previous work in which exactly the same make and model of HPGe detector was used.

9.2.5 HPGe energy resolution

The energy resolution of the LO-AX HPGe detector was determined for the seven radionuclides. In general, the FWHM showed a linear response with energy in the explored range. However, the photopeak at 511 keV had a higher FWHM than expected. This is attributed to the fact that it is produced by annihilation radiation, unlike gamma rays produced by radioactive decay, therefore subject to greater Doppler broadening. The difference in FWHM between the annihilation radiation peak and other gamma peaks is more apparent with high resolution detectors, such as germanium detectors, than with low resolution detectors such as sodium iodide detectors.

The FWHM at 122 keV (^{57}Co) was 0.708 keV back to 1995 as mentioned in the detector manual provided by the supplier. However, at the present time the FWHM at this energy is 1.233 keV, which means that the resolution has worsened since that time.

9.3 Radionuclidic purity of ^{99m}Tc eluates

The radionuclidic purity of 98 ^{99m}Tc eluates was assessed. These samples were eluted from two different size of generator. The first was delivered every Monday with a ^{99}Mo activity of 138 GBq and the other was delivered every Wednesday with an activity of 104 GBq. Fifty elutes were taken from the Monday generator and forty eight elutes from the Wednesday generator. The Monday generator was normally eluted once a day over five consecutive working days starting from Monday, while for the Wednesday generator, the first three eluates were obtained over three consecutive

working days starting from Wednesday, and a further two eluates were obtained on consecutive days after the weekend.

The activity of ^{99m}Tc for each eluate was measured on the day after elution using a Fidelis secondary standard radionuclide calibrator that is used for testing the accuracy of field radionuclide calibrators such as those made by Capintec. The eluate volume (ml) was calculated by subtracting the empty vial weight from that of the vial containing the eluate and assuming a density of 1 g/ml.

9.3.1 ^{99m}Tc activity reading correction

The dimensions of the eluate vial were different to those used as a standard (Schott vial). Moreover, the volume of the eluate differed from the 4 ml used as a reference volume. Thus, corrections were made for these different measurement conditions.

For the vial correction, 4 ml of ^{99m}Tc eluate from the same stock solution was dispensed into a Schott and an eluate vial. The volumes were confirmed by weighing. Both vials were separately placed in the Fidelis radionuclide calibrator, activity readings were recorded every second for 1 minute (60 readings) and mean (SD) values calculated. The activity for the Schott vial was corrected for radioactive decay to the time of the eluate vial measurement. The ratio of eluate vial activity reading to Schott vial reading was calculated to give the vial correction factor C_1, which was 0.999.

For the eluate volume correction, a small volume of eluate was dispensed into an eluate vial and its volume increased by the addition of tap water to a total volume of around 15 ml, giving a total of 21 different volumes. For each volume, activity was measured using the Fidelis calibrator and the mean (SD) of 60 readings calculated. The time of the measurement was also recorded.

The activity reading for each volume was corrected for radioactive decay to the time of the first measurement. A set of eluate volume correction factors (C_2) was calculated by dividing the corrected activity at each volume by the activity reading at the reference volume of 4 ml. The values of C_2 were plotted against volume (ml) and a second-degree polynomial equation was fitted to the data. It was shown that as the volume of the solution in an eluate vial increased, the ^{99m}Tc activity recorded by the Fidelis calibrator decreased.

9.3.2 ^{99}Mo net count rate reading correction

Similar corrections were needed for the NCR values for ^{99}Mo. For the vial correction, the previous prepared Schott and eluate vials with 4 ml of eluate in each were separately placed on the HPGe detector. Spectra were acquired, NCR calculated and corrected for decay during counting for each of the four main gamma photopeaks of ^{99}Mo (181, 366, 739 and 778 keV).

The Schott vial readings were corrected for radioactive decay to the measurement time of the eluate vial. Vial correction factors (C_3) then calculated for each gamma photopeak by dividing the corrected NCR of the eluate vial by that of the Schott vial. Values in the range 0.962-1.007 were found.

To obtain the ^{99}Mo NCR eluate volume correction factors, a similar procedure was followed to that for the ^{99m}Tc activity volume correction. Spectra were acquired using the HPGe detector for each volume. The counting live time was set to 900s. In each case, NCR was calculated and corrected for decay during counting and further corrected for radioactive decay to the time of acquisition of the first spectrum.

A set of ^{99}Mo NCR volume correction factors C_4 was obtained by dividing the corrected NCR at each volume by the corrected NCR at the reference volume of 4 ml. The values of C_4 were plotted against volume (ml) and a second-degree polynomial equation was fitted to the data. It was shown that the count rate recorded from the sample progressively decreased with increasing volume.

9.3.3 Determination of ^{99}Mo activity

The corrected ^{99m}Tc and ^{99}Mo activity readings measured using the Fidelis radionuclide calibrator and the LO-AX HPGe detector respectively were further corrected for radioactive decay to the corresponding time of generator elution in the radiopharmacy. For both radionuclides, the activity concentration of the residual eluates were expressed in MBq/ml. The activities of the total volume of eluate that would be in the vial at the time of elution were then determined.

It was found that measuring ^{99m}Tc activity and ^{99}Mo activity using a Capintec calibrator gave approximate results and, in general, overestimated both. ^{99}Mo activity values using the HPGe detector, and in turn the percentage of ^{99}Mo to ^{99m}Tc activity,

were determined using the two gamma lines at 366 keV and 778 keV, which gave the least significant activity difference (2%) amongst all the gamma lines for both generators ($P<0.01$). The 739 keV line registered the least ^{99}Mo activity, while the 181 keV line gave intermediate values; these effects were due to the influence of sum peaks.

It was found that the ratio of $^{99}Mo/^{99m}Tc$ in all eluates was below the limit stated by the European Pharmacopoeia.

It was concluded that there was no significant difference between the relative activity of ^{99}Mo in the eluates from the Monday and the Wednesday generators ($P>0.05$). This was in agreement with the literature. However, one of the main contributions of this part of the study was an investigation of the relationship between the ratio of ^{99}Mo activity to ^{99m}Tc activity and eluate number. It was concluded that the ratio decreased logarithmically with eluate number for both generators.

The other main contribution was an investigation of the differences in activity ratio between all the eluates using the t-test. According to the literature, such investigation has been done for just eluates 1, 2 and 4. The results show a tendency for differences to be significant only between the early and late eluates (Table 9-1 and Table 9-2).

Table 9-1: Differences between % ^{99}Mo activity in Monday generator eluates. No means no significant difference while Sig. means significant difference ($p<0.05$)

Eluate Number	1	2	3	4
2	No			
3	Sig.	No		
4	No	No	No	
5	Sig.	Sig.	Sig.	No

Table 9-2: Differences between % ^{99}Mo activity in Wednesday generator eluates. No means no significant difference while Sig. means significant difference ($p<0.05$)

Eluate Number	1	2	3	5
2	No			
3	No	No		
5	Sig.	Sig.	No	
6	Sig.	Sig.	Sig.	No

9.3.4 Determination of ^{103}Ru contamination in ^{99m}Tc eluates

The radionuclide ^{103}Ru was observed in 21 of the 98 eluates from the two generators. As this radio-contaminant was not identified in the spectra of the eluate used for the NCR volume and vial correction, correction factors derived from the closest gamma line of ^{99}Mo (366 keV) were used.

In all cases it was found that the ratio of ^{103}Ru to that of the main radionuclide ^{99m}Tc was within European Pharmacopoeia requirements (5×10^{-3}%). However, the results had a high statistical uncertainty (7% maximum).

There was a large decrease in the percentage of ^{103}Ru/^{99m}Tc activity after the first elutions with little change thereafter.

9.4 Radionuclidic purity of iodine radiopharmaceuticals

Sodium iodide labelled with ^{123}I and ^{131}I is the simplest inorganic pharmaceutical that incorporates radioactive iodine. Investigation of the radioactive impurities in these radionuclides was done.

9.4.1 Radionuclidic purity of ^{123}I

Ten samples of ^{123}I sodium iodide solution were prepared in house. These samples were prepared to the same standards as used for HPGe detector efficiency calibration i.e. standard vial (Schott vial) with a standard volume (4 ml). The ^{123}I activity of the

prepared samples was determined using the Fidelis secondary standard radionuclide calibrator.

The acquired spectra showed the presence of the expected radionuclidic impurities; ^{125}I and ^{121}Te. However, the main contribution of this work was the identification of other impurities, which have not been reported in the literature; these were ^{126}I, ^{124}I, ^{96}Tc, ^{95m}Tc.

^{125}I was identified in all the samples included in this study and it was the impurity with the highest relative activity, 0.0145% of that of ^{123}I. This value was within the limits reported by the supplier.

The second impurity was ^{121}Te and this was also seen in all the samples. Ratio of the activity of this contaminant to ^{123}I activity was 0.00528%, which is also within the limit provided by the supplier. Two gamma lines of ^{121}Te were analysed in this study: 573keV and 507keV. These were the strongest lines. There was a significant difference in the activity obtained with these two lines ($P<0.05$) and this was attributed to the existence of sum peaks. However, the percentage difference between the activites was just 1.048%. Thus, both of them were included in the calculation of ^{121}Te contamination activity.

^{126}I and ^{124}I were identified in some of the samples: ^{126}I was found in 8 samples whereas ^{124}I was identified in just 4 of them. The activity ratio of these two impurities were calculated to be 8.51×10^{-6} % and 2.43×10^{-4} %respectively.

Similarly, ^{96}Tc and ^{95m}Tc were identified in some of the samples of this study. ^{96}Tc was identified in six samples, whereas ^{95m}Tc was identified in just three. The activity ratios of these two impurities were 5.58×10^{-5} % and 4.13×10^{-6} % respectively.

9.4.2 Radionuclidic purity of ^{131}I

Five samples of sodium iodide (^{131}I) solution were also prepared in standard vials and with standard volumes. No impurities were identified within the acquired spectra, in agreement with the literature. However, a gamma peak at 314 keV was seen in all the ^{131}I spectra. This was not one of the ^{131}I gamma peaks and its origin was not identified. It may be possible to gain further information by determining the half-life of the NCR of this peak by repeated measurements.

9.5 Radionuclidic purity of gallium-68 radiopharmaceuticals

Gallium-68 is a positron emitting radionuclide that is having a great impact in nuclear medicine. ^{68}Ga in this study was produced by PETIC for the first time in the UK using a liquid target in the form of ^{68}Zn nitrate solution. The main contribution of this part of the study was the identification of radioactive contaminants and the measurement of the ratio of their activities to ^{68}Ga activity.

Pairs of liquid samples (with the standard 4 ml of volume solution and in a Schott vial) were prepared before and after chemical purification of the target material for three validation productions.

In this case, the activity of the ^{68}Ga was measured using a Capintec CRC-25R radionuclide calibrator as there was no identified Fidelis calibration factor for ^{68}Ga.

The analysed HPGe detector spectra showed the presence of ^{67}Ga (gamma energy 93, 184, 209, 300 and 887 keV), ^{66}Ga (833 keV and 1039 keV) and ^{56}Co (846 keV, 1038 keV and 1238 keV) as impurity radionuclides. ^{67}Ga was the main impurity amongst them. The experimental half-life of this radionuclide showed good agreement with the actual value. The percentage activity of ^{67}Ga to ^{68}Ga for the first production was found to be between 0.66% and 0.83% at the EOB for the pre-purification sample, while it was 0.42%-0.49% for the same production after purification.

However, better productions were achieved at the second and third attempts with ^{67}Ga activity in the range 0.17%-0.19% and 0.19%-0.23% respectively for the pre-purification samples and 0.20% to 0.23% respectively for the post-purification samples.

The relative activity of ^{66}Ga was about 0.006% before purification for the first production and no trace was found in the purified sample. A smaller value (0.003%) was obtained in the second production for both the pre-purification and post-purification samples. The experimental half-life of this impurity showed good agreement with the actual value with a difference of only -3.6%.

This other impurity (^{56}Co) was not identified by other researchers. Its activity ratio was about 0.0005% in the first production for the pre-purification sample with only traces identified in the post-purification sample. Smaller ratios (0.0001%) were noticed in the second and third productions for pre-purification. No traces were found in the

purified samples which means that the chemical purification was effective as the aim of his process is to remove elements with different chemical properties compared with the required nuclide.

9.6 Radionuclidic purity of cyclotron-produced zirconium-89

^{89}Zr is a radiometal that has emerged as a promising label for targeted molecular imaging. The demand for ^{89}Zr for research purposes is increasing as this radionuclide remains in tumour cells after its administration so that time series studies are possible without administrating further radiopharmaceuticals.

The main contribution of this part of the study was confirm PETIC's ability to limit the production of long-lived radionuclidic impurities in ^{89}Zr to negligible levels. Pairs of ^{89}Zr liquid samples (with the standard 4 ml volume of solution in a Schott vial) were prepared before and after chemical purification of the target material for two validation productions. Like ^{68}Ga, the activity of ^{89}Zr was measured in a Capintec calibrator and for the same reason. The samples were left for a sufficiently long time to allow the main radionuclide (^{89}Zr) to decay.

The acquired HPGe detector spectra showed the presence of ^{88}Zr, ^{88}Y and ^{56}Co. However, ^{88}Zr was the main one amongst them. This radioactive contaminant was identified in both productions; its existence was confirmed by the experimental half-life which showed agreement with the expected value with differences of -9.6% and 2.9% for the two samples. The activity ratios of ^{88}Zr to the main radionuclide were 0.00112%and 0.00095% for the pre-and post-purification samples of the first production respectively, while those for the second production were 0.00065% and 0.00053% respectively.

^{88}Y was the other radioactive contaminant identified in both productions. However, it was difficult to determine its half-life as the logarithm of the counting rate showed an increase with the time over the period of the experiments. This was attributed to the existence of the first impurity (^{88}Zr), which exclusively decays to ^{88}Y. Therefore, the activity ratio of ^{88}Y was determined using the first acquired spectrum as this was expected to be the closest to the actual value. These ratios were 0.0001-0.0003% for

the pre-purification samples and about 0.00005-0.0002% for the post-purification samples.

The third radioactive impurity was ^{56}Co. It was identified just in pre-purification samples for both the first and the second production, which means that the chemical purification was effective as the aim of this process is to remove elements with different chemical properties compared with the required nuclide. The determination of its experimental half-life gave differences from the expected value of -20.8% and -13.3% based on the two photopeaks at 846 keV and 1238 keV respectively for the 1st production. The corresponding values were 0.63% and -4.29% for the 2nd production. The ratio of the activity of this radioactive cobalt to that of the main radionuclide (^{89}Zr) was about 0.001-0.002%.

9.7 Conclusion

The work described in this thesis includes several contributions to the advancement of knowledge as regards radioactive impurities in medical radionuclides and the methods used to identify and quantify such impurities. The radionuclides investigated comprised ^{99m}Tc generator eluates, commercial ^{123}I and ^{131}I sodium iodide solutions and cyclotron-produced ^{68}Ga and ^{89}Zr.

A LO-AX HPGe radiation detector (Ortec) was used for the experimental aspects of the work because of its availability at the University Hospital of Wales. This device is designed for the detection of relatively low energy photons (< 100 keV), but the gamma emissions from the radionuclides that were investigated ranged in energy from 35-1836 keV. Nevertheless, the detector provided adequate sensitivity for the detection of even the highest energy photons with the source placed in contact with the detector cap and the use of sufficiently long spectrum acquisition times. The efficiency calibration confirmed that the LO-AX detector may be used for high energy gamma radiation and showed good agreement with a previous study that used the same instrument. It also showed the usefulness of the Fidelis secondary standard radionuclide calibrator (Southern Scientific) in preparing radionuclide sources for detector calibration.

As expected, in all the eluates from the Tekcis ^{99m}Tc generators (Curium), the relative activity of ^{99}Mo expressed as a percentage of ^{99m}Tc activity was found to be within the limits recommended by the European Pharmacopeia. The HPGe detector gave more reliable results than the conventional molybdenum breakthrough test using a lead shield and a radionuclide calibrator. No significant difference in relative ^{99}Mo activity was found between corresponding elutions of the generators delivered on a Monday (138 GBq reference activity) and Wednesday (104 GBq reference activity). However, significant differences were noted between the early and late eluates from each generator. Overall, it was found that the relative ^{99}Mo activity decreased logarithmically with eluate number and this has not been reported previously. This suggests that as regards ^{99}Mo content, the later eluates are safer for patients than the earlier ones because they deliver lower additional radiation dose.

The radionuclide ^{103}Ru was also identified as an impurity in some ^{99m}Tc generator eluates, but at a much lower relative activity than ^{99}Mo and within European Pharmacopoeia limits. This means that it could not be detected by a conventional breakthrough test, only by gamma spectroscopy. The relative activity of ^{103}Ru decreased rapidly after the first elution; this suggests that, in effect, its presence may be eliminated by pre-elution of the generator.

For the commercial Na^{123}I solution (GE Healthcare), the main contaminants were ^{125}I and ^{121}Te, for both of which the relative activity was within European Pharmacopeia limits. However, also observed were trace activities of ^{124}I, ^{126}I, ^{95m}Tc and ^{96}Tc, which have not been reported in the literature. As these impurities were found only in some samples with very small relative activity and as their half-lives are similar to or shorter than the half-life of the longer-lived main impurity (^{125}I), they do not present a significant hazard to patients. For the commercial Na^{131}I solution (also GE Healthcare), no impurities were identified from the pulse height spectra. However, a gamma photopeak was noted at 314 keV; this is not related to ^{131}I and its origin is unknown.

The radionuclides ^{68}Ga and ^{89}Zr were produced with the Cyclone 18/9 cyclotron (IBA) in PETIC on the University Hospital of Wales site. The identified impurities were ^{67}Ga, ^{66}Ga and ^{56}Co for ^{68}Ga and ^{88}Zr, ^{88}Y and ^{56}Co for ^{89}Zr. In most cases, it was possible to confirm the identity of the contaminants through half-life measurement as

well as photopeak identification on pulse height spectra. For both main radionuclides, the relative activities of the impurities were within the PETIC goal of 2% or less. The results of this study may be used to optimise the irradiation conditions for the production of the two radionuclides. This is work that is still in progress as PETIC pursues its goal of developing clinically useful radiopharmaceuticals labelled with ^{68}Ga and ^{89}Zr.

9.8 Future work

The study has identified possibilities for future work as indicated below.

- It would be beneficial to extend the efficiency calibration of the LO-AX HPGe detector using radionuclides that provide a wider range of photon energies and a greater number of energies at about 80 keV, where the efficiency curve reaches a maximum. This would improve the usefulness of the detector for a variety of applications at the University Hospital of Wales.
- In some nuclear medicine applications, the ^{99m}Tc generator eluate (in the chemical form of sodium pertechnetate) is administered directly to patients. In these cases, the patients would also receive any radionuclidic contaminants that may be present in the eluate. However, it would be interesting to measure the radionuclidic purity of more complex ^{99m}Tc labelled radiopharmaceuticals (as opposed to generator eluates) to see whether the ^{99}Mo and ^{103}Ru impurities are excluded by the radio-labelling process.
- Further work is needed to identify the origin of the 314 keV photopeak in the Na^{131}I spectra. A possible approach would be to do repeated measurements over a period of time on individual samples to see whether a half-life could be determined from the change in net count rate.
- The cyclotron production of ^{68}Ga and ^{89}Zr is still under development by PETIC. There is considerable scope to refine the process by identifying and quantifying impurity radionuclides after each modification of the proton irradiation conditions. In due course, the approach could also be applied to determine the radionuclidic purity of an extended range of cyclotron-produced radionuclides and the final radiolabelled radiopharmaceuticals.

There is a bright and exciting future for the application of high-resolution gamma spectroscopy in the advancement of radiopharmacy and nuclear medicine.

References

Al-Musawi, T.L. 2018. Caibration of a scanning whole body counter for measurement of the activity of gamma emitting radionuclides in the human body. PhD thesis. Cardiff University.

Alfuraih, A. et al. 2013. Optimization of ^{89}Zr production using Monte Carlo simulations. Journal of Radioanalytical and Nuclear Chemistry 296(2), pp. 1025–1029.

Allwood, M.C. and McCarthy, T.M. 1980. Microbial and pyrogenic contamination of molybdenum 99/technetium 99m radionuclide generators. International Journal of Pharmaceutics 4(3), pp. 185–193.

Alves, F. et al. 2017. Production of copper-64 and gallium-68 with a medical cyclotron using liquid targets. Modern Physics Letters A 32(17), p. 1740013.1-1740013.21.

Anderson, D.W. et al. 1974. Determination of impurity activities in fission-product generator eluate. Journal of Nuclear Medicine 15(10), pp. 889–892.

Anderson, D.W. 1984. Absorption of Ionizing Radiation. Baltimore: University Park Press.

Andrade, W.G. and Lima, F.F. 2009. Evaluation of the eluate quality of ^{99}Mo/^{99m}Tc generators in Recife, Brazil. Proceedings of the 2009 ternational Nuclear Atlantic Conference (INAL). Rio de Janeiro; Brazil, 27 September-2 October, 2009.

Bailey, D.L. et al. 2014. Nuclear Medicine Physics: A Handbook for Teachers and Students. Vienna: International Atomic Energy Agency.

Baker, G.A. et al. 1976. Significance of radiocontaminants in ^{123}I for dosimetry and scintillation camera imaging. Journal of Nuclear Medicine: 17(8), pp. 740–743.

Banerjee, S. et al. 2001. Evolution of Tc-99m in diagnostic radiopharmaceuticals. Seminars in Nuclear Medicine 31(4), pp. 260–277.

Billinghurst, M.W. et al. 1974. Radiochemical purity of ^{99m}Tc pertechnetate. Journal of Nuclear Medicine 15(4), pp. 266–269.

Billinghurst, M.W. and Hreczuch, F.W. 1976. Contamination from ^{131}I, ^{103}Ru, and ^{239}Np in the eluate of ^{99}Mo-^{99m}Tc generators loaded with (n, gamma)-produced ^{99}Mo. Journal of Nuclear Medicine 17(9), pp. 840–843.

Bychenkov, V.Y. et al. 2014. Tc-99m production with ultrashort intense laser pulses. Laser and Particle Beams 32(04), pp. 605–611.

Byun, S.H. 2017. Radioisotopes and Radiation Methodology, Med Phys 4R06/6R03.

Canberra 1997. Analog-to-Digital Converter, Model 8701, User's Manual,.

Canberra 2007. Model 3106D, Power Supply, User's manual.

Cervera, M. 2009. ^{99m}Tc production processes: an examination of proposals to ensure stable North American medical supplies. MSc dissertation: Colorado State University.

Cherry, S.R. et al. 2012. Physics in nuclear medicine. 4th ed. Philodelphia: Sounders.

Chilton, H.M. and Witcofski, R.L. 1986. Nuclear pharmacy : introduction to the clinical application of radiopharmaceuticals. Philadelphia: Lea & Febiger.

Ciarmatori, A. et al. 2011. Some experimental studies on ^{89}Zr production. Radiochimica Acta 99(10), pp. 631–634.

Currium 2018. Teckis 2-50 GBq radionuclide generator: summary of product characteristics. Partsmouth: Currium.

Dabkowski, A.M. et al. 2015. Optimization of cyclotron production for radiometal of zirconium 89. In: Acta physics polonica A. 127(5). pp. 1479–82.

Dantas, B.M. et al. 2005. Determination of ^{99}Mo contamination in a nuclear medicine patient submitted to a diagnostic procedure with ^{99m}Tc. Brazilian Archives of Biology and Technology 48(spe2), pp. 215–220.

Dias, G.M. et al. 2018. ^{89}Zr for antibody labeling and in vivo studies – a comparison between liquid and solid target production. Nuclear Medicine and Biology 58, pp. 1–7.

Eckelman, W.C. 2009. Unparalleled contribution of technetium-99m to medicine over 5 decades. JACC: Cardiovascular Imaging 2(3), pp. 364–368.

Eersels, J.L.H. et al. 2005. Manufacturing I-123-labelled radiopharmaceuticals: pitfalls and solutions. Journal of Labelled Compounds and Radiopharmaceuticals 48(4), pp. 241–257.

Elessawi, E.A. 2010. Measurement of caesium-137 in the human body using a whole body counter. PhD thesis. Cardiff University.

Ferreira, N.J.S. de S. 2013. Production of gallium-68 in a liquid cyclotron target: physics and viability. Master's thesis, Coimbra University.

Finck, R. and Mattsson, S. 1976. Long-lived radionuclide impurities in eluates from molybdenum-technetium generators and the associated absorbed dose to the patient. International Journal of Nuclear Medicine and Biology 3(2), pp. 89–97.

Firouzbakht, M.L. et al. 1987. Production of high purity iodine-123 from xenon-124 at energies between 15 and 34 MeV. Radiochimica Acta 41(1), pp. 1–4.

GE Healthcare 2011. Sodium iodide (^{123}I) injection 37 MBq/ml solution for injection. Little Chalfont: GE Healthcare.

Gilbert, S. 2018. Private communication.

Gilmore, G.R. 2008. Practical Gamma-Ray Spectrometry. 2nd ed. Chichester: John Wiley & Sons, Ltd.

Goolden, A.W.G. et al. 1968. The choice of a radioactive isotope for the investigation of thyroid disorders. British Journal of Radiology 41(481), pp. 20–25.

Graham, L. and Zielinski, F.W. 1979. Scintillation camera imaging with I-123. Radiology 130(2), pp. 519–523.

Grupen, P.D.C. 2010. Introduction to Radiation Protection. Berlin: Springer.

Hammermaier, A. et al. 1986. Chemical, radiochemical, and radionuclide purity of eluates from different commercial fission ^{99}Mo/^{99m}Tc generators. European Journal of Nuclear Medicine 12(1), pp. 41–46.

Hendee, W.R. et al. 2005. Radiation Therapy Physics. New Jersey: John Wiley and Sons.

Hermanne, A. et al. 2011. Limitation of the long-lived ^{121}Te contaminant in production of ^{123}I through the ^{124}Xe(p, x) route. Applied Radiation and Isotopes 69(2), pp. 358–368.

Hoffmann, P. et al. 1980. Determination of radionuclide purity by gamma-spectrometry. Journal of Radioanalytical Chemistry 57(2), pp. 363–372.

Hughes, J.A. et al. 1979. Potential errors caused by variable radionuclidic purity of iodine-123. Journal of Nuclear Medicine Technology 7(3), pp. 167–170.

Hušák, V. et al. 1980. Dosimetric aspects of application of ^{123}I-radiopharmaceuticals in nuclear medicine. Isotopenpraxis 16(11), pp. 361–365.

IAEA 2010. Production of long lived parent radionuclides for generators: ^{68}Ge, ^{82}Sr, ^{90}Sr and ^{188}W. Vienna: International Atomic Energy Agency.

IAEA 2012. Cyclotron produced radionuclides: operation and maintenance of gas and liquid targets (Radioisotopes and Radiopharmaceuticals Series No. 4). Vienna: International Atomic Energy Agency.

IAEA 2015. Principles of an isotope calibrator [Online] Available at: https://nucleus.iaea.org/HHW/Radiopharmacy/VirRad/Quality_Control_Procedures/Quality_Control_Module/Radioactivity_concentration/Measurement_tools/Isotope_Calibrator/Principles_of_an_isotope_calibrator/index.html [Accessed: 5 February 2019].

ICRP 1983. Radionuclide transformations: energy and intensity of emissions (Publication 38). Oxford: Pergaman Press.

ICRP 1987. Radiation dose to patients from padiopharmaceuticals (Publication 53). Oxford: Pergamon Press.

Infantino, A. et al. 2011. Prediction of ^{89}Zr production using the Monte Carlo code FLUKA. Applied Radiation and Isotopes 69(8), pp. 1134–1137.

Iwahara, A. et al. 2001. Intercomparison of ^{131}I and ^{99m}Tc activity measurements in Brazilian nuclear medicine services. Applied Radiation and Isotopes 54(3), pp. 489–496.

Jalilian, A.R. 2016. An overview on Ga-68 radiopharmaceuticals for positron emission tomography applications. Iranian Journal of Nuclear Medicine 24(1), pp. 1–10.

James, S. 2007. Rhenium and technetium radiopharmaceuticals: design and development for applicatons in nuclear medicine. PhD thesis, Syracuse University.

Jones, D.W. et al. 2013. Practical SPECT/CT in Nuclear Medicine. New York: Springer.

Kaiho, T. 2015. Iodine Chemistry and Applications. Hoboken: John Wiley & Sons.

Kasbollah, A. et al. 2013. Review on production of ^{89}Zr in a medical cyclotron for PET radiopharmaceuticals. Journal of Nuclear Medicine Technology 41(1), pp. 35–41.

Khandaker, M.U. 2011. High purity germanium detector in gamma-ray spectrometry. International Journal of Fundamental Physical Sciences 1(2), pp. 42–46.

Kilian, K. 2014. ^{68}Ga-DOTA and analogs: current status and future perspectives. Reports of Practical Oncology & Radiotherapy 19, pp. S13–S21.

Knoll, G.F. 2010. Radiation detection and measurement. 4th ed. New York: John Wiley & Sons.

Kowalsky, R.J. 2006. Technetium Radiopharmaceutical Chemistry. Albuquerque: University of New Mexico [Online] Available at: https://pharmacyce.unm.edu/nuclear_program/freelessonfiles/Vol12Lesson3.pdf%0A [Accessed: 6 August 2019].

Krane, K.S. 1988. Introductory nuclear physics. New York: John Wiley&Sons.

Lapolli, A.L. et al. 2017. A new ^{124}Xe irradiation system for ^{123}I routine production at the 30 MeV IPEN-CNEN/SP cyclotron. Proceedings of the 2017 International Nuclear Atlantic Conference (INAC). Belo Horizont; Brazil, 22-27 October, 2017.

Lilley, J. 2001. Nuclear Physics: Principles and Applications. John Wiley & Sons.

Lin, M. et al. 2016. Semi-automated production of ^{89}Zr-oxalate / ^{89}Zr-chloride and the potential of ^{89}Zr-chloride in radiopharmaceutical compounding. Applied Radiation and Isotopes 107, pp. 317–322.

Loutsios, C. et al. 2015. Clinical application of autologous technetium-99m-labelled eosinophils to detect focal eosinophilic inflammation in the lung. Thorax 70(11), pp. 1085–1086.

Loveland, W.D. et al. 2005. Modern Nuclear Chemistry. Hoboken: John Wiley & Sons.

Mahmood, A. and Jones, A. 2002. Technetium radiopharmaceuticals. In: Welch, M.I. and Redvanly, C.S. eds. Handbook of Radiopharmaceuticals: Radiochemistry and Applications. Chelchester John Wiley & Sons. pp. 323-362.

Marengo, M. et al. 1999. Quality control of ^{99}Mo/^{99m}Tc generators: results of a survey of the Radiopharmacy Working Group of the Italian Association of Nuclear Medicine (AIMN). Nuclear Medicine Communications 20(11), pp. 1077–1084.

McCready, V.R. 2017. Radioiodine – the success story of Nuclear Medicine. European Journal of Nuclear Medicine and Molecular Imaging 44(2), pp. 179–182.

Momennezhad, M. et al. 2010. Determination of ^{99}Mo contamination in ^{99m}Tc elute obtained from ^{99}Mo/^{99m}Tc- generator. Iranian Journal of Radiation Research 8(1), pp. 31–35.

Moreira, H.M.R. 2013. Cyclotron production of ^{68}Ga using a ^{68}Zn-based liquid target. Master's thesis, Coimbra University.

Murray, G. 1967. The Doppler broadening of annihilation radiation. Physics Letters B 24(6), pp. 268–269.

Mushtaq, A. et al. 2012. Evaluation of Pakgen ^{99m}Tc generators loaded with indigenous fission ^{99}Mo. Radiochimica Acta 100(10), pp. 793–801.

Neacsu, B. et al. 2013. Radionuclidic purity - An essential parameter in quality control of radiopharmaceuticals. Romanian Reports in Physics 65(1), pp. 155–167.

Nelson, K.E. et al. 2009. The effect of gamma-ray detector energy resolution on the ability to identify radioactive sources. Livermore CA: Lawrence Livermore National Laboratory. [Online] Available at: https://e-reports-ext.llnl.gov/pdf/370769.pdf [Accessed: 16 August 2019].

Nikjou, A. and Sadeghi, M. 2018. Overview and evaluation of different nuclear level density models for the ^{123}I radionuclide production. Applied Radiation and Isotopes 136, pp. 45–58.

Nir-El, Y. 2013. Correction for decay during counting in gamma spectrometry. Radiation Protection Dosimetry 153(3), pp. 400–401.

Palmer, D.W. and Rao, S.A. 1985. A simple method to quantitate iodine-124 contamination in iodine-123 radiopharmaceuticals. Journal of Nuclear Medicine. 26(8), pp. 936–940.

Pandey, M.K. et al. 2014. Cyclotron production of ^{68}Ga via the ^{68}Zn(p,n)^{68}Ga. American Journal of Nuclear Medicine and Molecular Imaging. 4(4), pp. 303–310.

Pandya, D.N. et al. 2017. Zirconium tetraazamacrocycle complexes display extraordinary stability and provide a new strategy for zirconium-89-based radiopharmaceutical development. Chemical Science 8(3), pp. 2309–2314.

Pearson, J.M. 1986. Nuclear physics : energy and matter. Bristol: A. Hilger.

Pillai, M.R.A. 2008. Technetium-99m radiopharmaceuticals: manufacture of kits. Vienna:IAEA [Online] Available at: https://www-pub.iaea.org/MTCD/publications/PDF/trs466_web.pdf [Accessed: 6 August 2019].

Polak et al. 1983. Performance of collimators used for tomographic imaging of I-123 contaminated with I-124. Journal of Nuclear Medicine 24(11), pp. 1065–1069.

Powsner, R.A. et al. 2013. Essentials of Nuclear Medicine Physics and Instrumentation. 3rd ed. Chichester: John Wiley & Sons.

Prekeges, J. 2011. Nuclear Medicine Instrumentation. 2nd ed. Burlington: Jones & Bartlett Learning.

Reguigui, N. 2006. Gamma ray spectrometry: practical information. Sidi Thabet: CNSTN [Online] Available at: https://www.researchgate.net/profile/Nafaa_Reguigui/publication/259533588_Gamma_Ray_Spectrometry/links/0046352c6cf29942b0000000.pdf [Accessed: 27 July 2019].

Reilly, D. et al. 1991. Passive nondestructive assay of nuclear materials (No. NUREG/CR--5550). Nuclear Regulatory Commission.

Rhodes, B.A. and Croft, B.Y. 1978. Basics of Radiopharmacy. Saint Louis : Mosby.

Rivkees, S.A. et al. 1998. The management of Graves' disease in children, with special emphasis on radioiodine treatment. Journal of Clinical Endocrinology & Metabolism 83(11), pp. 3767–3776.

Ruth, T.J. 2009. The uses of radiotracers in the life sciences. Reports on Progress in Physics 72(1), pp. 1–23.

Saha, G.B. 1996. The Chemistry of Tc-99m-Labeled Radiopharmaceuticals. The University of New Mexico, College of pharmacy.

Saha, G.B. 2010. Fundamentals of Nuclear Pharmacy. 6th ed. New York: Springer.

Sampson, C.B. 1994. Textbook of Radiopharmacy: Theory and Practice. 2nd ed. New York: Gordon and Breach.

Sandi, E.P. 2013. Advances in Gamma-Ray detection with modern scintillators and applications. PhD thesis, Madrid University.

Schlyer, D.J. et al. 2009. Cyclotron produced radionuclides: Physical characteristics and production methods. IAEA Technical Reports Series No. 468. Vienna: International Atomic Energy Agency.

Schwochau, K. 2000. Technetium Chemistry and radiopharmaceutical applications. weinbem: Wiley-VCH.

Severin, G.W. et al. 2011. ^{89}Zr radiochemistry for positron emission tomography. Medicinal Chemistry 7(5), pp. 389–394.

Shivarudrappa, V. and Vimalnath, K. 2005. High purity materials as targets for radioisotope production : Needs and challenges. Bulletin of Materials Science 28(4), pp. 325–330.

Sivers, M. et al. 2014. Low-level γ -ray spectrometry at the underground laboratory Garching. Applied Radiation and Isotopes 91, pp. 49–56.

Stabin, M.G. et al. 1996. Radiation dose estimates for radiopharmaceuticals (No. NUREG/CR-6345). Washington DC: Nuclear Regulatory Commission.

Sumiya, L.C.A. and Sciani, V. 2008. Evaluation of irradiation parameters of enriched ^{124}Xe target for ^{123}I production in cyclotrons. Applied Radiation and Isotopes 66(10), pp. 1337–1340.

Synowiecki, M.A. et al. 2018. Production of novel diagnostic radionuclides in small medical cyclotrons. EJNMMI Radiopharmacy and Chemistry 3(1), pp. 1–25.

Talboys, M. 2016. Monte Carlo simulation applied to uncertainties in iodine-123 assay and thyroid uptake measurement. PhD thesis, Cardiff University.

Tárkányi, F. et al. 1991. Excitation functions of (p,2n) and (p,pn) reactions and differential and integral yields of ^{123}I in proton induced nuclear reactions on highly enriched ^{124}Xe. International Journal of Radiation Applications and Instrumentation. Part A. Applied Radiation and Isotopes 42(3), pp. 221–228.

Thrall, J.H. et al. 2001. Nuclear medicine : the requisites. 3rd ed. St. Louis: Mosby.

Tomarchio, E. 2012. Gamma-ray spectrometric measurement of radionuclide purity of radiopharmaceuticals contained in bottle samples. Nuclear Technology and Radiation Protection 27(1), pp. 13–19.

Twomey, T.R. 2003. The Best Choice of High Purity Germanium (HPGe) Detector. ORTEC Oak Ridge, pp. 1–12.

Urbano, N. et al. 2005. Evaluation of fresh and old eluate of ^{99}Mo/^{99m}Tc generators used for labeling of different pharmaceutical kits. Journal of Radioanalytical and Nuclear Chemistry 265(1), pp. 7–10.

Venikov, N.I. et al. 1991. Production of high-purity ^{123}I on IAE cyclotron. Proceeding of the 12th International Conference on Cyclotrons and their Applications. Berlin; Germany, 8-12 May, 1989, pp. 535–537.

Venikov, N.I. et al. 1993. Excitation functions of proton-induced reactions on ^{126}Xe: ^{125}I impurity in ^{123}I. Applied Radiation and Isotopes 44(4), pp. 751–754.

Villanueva-Meyer, J. et al. 1996. Mammoscintigraphy with technetium-99m-sestamibi in suspected breast cancer. Journal of Nuclear Medicine 37(6), pp. 926–930.

Vinberg, N. and Kristensen, K. 1976. Comparative evaluation of ^{99m}Tc-generators. European Journal of Nuclear 1(4), pp. 219–233.

Vlček, J. et al. 1979. Results of regular study on radionuclidic purity of ^{99m}Tc obtained from ^{99}Mo-^{99m}Tc generators. European Journal of Nuclear Medicine 4(5), pp. 385–387.

Vugts, D.J. et al. 2013. ^{89}Zr-PET radiochemistry in the development and application of therapeutic monoclonal antibodies and other biologicals. Current Topics in Medicinal Chemistry 13(4), pp. 446–457.

Walther, M. et al. 2011. Implementation of ^{89}Zr production and in vivo imaging of B-cells in mice with ^{89}Zr-labeled anti-B-cell antibodies by small animal PET/CT. Applied Radiation and Isotopes 69(6), pp. 852–857.

van de Watering, F.C.J. et al. 2014. Zirconium-89 labeled antibodies: a new tool for molecular imaging in cancer patients. BioMed Research International 2014, pp. 1–13.

Wellman, H.N. and Anger, R.T. 1971. Radioiodine dosimetry and the use of radioiodines other than 131I in thyroid diagnosis. Seminars in Nuclear Medicine 1(3), pp. 356–378.

Willerson, J. et al. 1975. Acute subendocardial myocardial infarction in patients: its detection by technetium 99m stannous pyrophosphate myocardial scintigrams. 51(Circulation 51(3)), pp. 436–441.

Wooten, A.L. et al. 2013. Routine production of ^{89}Zr using an automated module. Applied Sciences 3(3), pp. 593–613.

Zolle, I. 2007. Performance and quality control of the ^{99}Mo/^{99m}Tc generator. In: Zolle, I. ed. technetium-99m pharmaceuticals. Berlin: Springer.